Nuclear Spin Relaxation and Diffusion Studies of Adsorption and Dynamics at the Catalyst-Liquid Interface

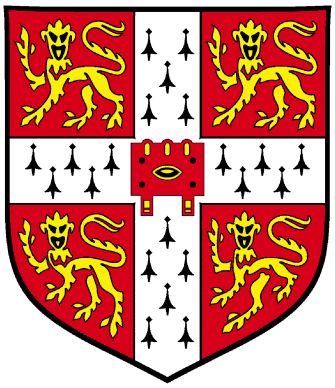

Neil John Owen Robinson

Department of Chemical Engineering and Biotechnology

University of Cambridge

This thesis is submitted for the degree of
Doctor of Philosophy

St Edmund's College
January 2019

Preface

This work is submitted for the degree of Doctor of Philosophy. It is the result of my own work, completed either at the Magnetic Resonance Research Centre, Department of Chemical Engineering and Biotechnology, University of Cambridge, or at the Department of Chemistry, University of Cambridge, between October 2014 and October 2017. This thesis includes nothing which is the outcome of work done in collaboration with others except where explicitly specified in the text. It is not substantially the same as any work that I have previously submitted, nor work that is concurrently submitted, for any degree, diploma or other qualification at the University of Cambridge, or any other University or similar institution. This thesis does not exceed 150 figures and 65000 words, including tables, equations, appendices and bibliographic entries.

Nuclear Spin Relaxation and Diffusion Studies of Adsorption and Dynamics at the Catalyst-Liquid Interface

Neil John Owen Robinson

The rational design of active materials for liquid-phase heterogeneous catalytic processes requires a detailed understanding of interactions occurring at the solid-liquid interface. The elucidation of such dynamics is of particular relevance to the study and development of solvated green chemical reaction processes, such as the production of chemicals and fuels from biomass. Nuclear spin relaxation time measurements have recently emerged as a novel tool for probing surface dynamics within such systems; herein, we detail the state-of-the-art of such measurements, and extend our current understanding of how such characteristics may be interpreted in terms of formal surface interaction phenomena.

Initially, a simple protocol is developed to illustrate the sensitivity of longitudinal nuclear spin relaxation to hydrogen-bond-mediated adsorption interactions occurring between a prototypical polar liquid (methanol) and a range of common mesoporous catalyst support materials (γ-Al_2O_3, θ-Al_2O_3, anatase-TiO_2 and SiO_2) exhibiting hydroxylated pore surfaces. Proton longitudinal relaxation time constant (T_1) measurements are shown to demonstrate significant sensitivity to changes in adsorption mechanism within these systems. Specifically, the acquired T_1 data indicates that the dynamics of methanol within the adsorbed surface layer is notably enhanced upon passivation of surface hydroxyl groups with alkyl chains, and tends towards that of the unrestricted bulk liquid. A complex analysis in which we account for the influence of changing pore morphology and surface layer structure upon passivation is found to be in agreement with these observations, validating the widely applied assumption that the surface relaxivity of polar adsorbates is sensitive to interactions with hydroxyl groups at the pores surface.

The ability of nuclear spin relaxation measurements to probe surface interaction strengths in a quantitative manner is then explored through the application of two-dimensional T_1-T_2 correlation experiments. The ratio of longitudinal–to–transverse relaxation time constants T_1/T_2 is readily obtained from such experiments, and is considered to provide a non-destructive indication of the surface affinities exhibited by species at the solid-liquid interface. We detail the application of such measurements to probe the surface interaction strengths of a homologous series of primary alcohols and cyclohexane within an industrial silica support material. The resulting T_1/T_2 values are shown to be in excellent agreement with the results of extensive density functional theory-based adsorption energy calculations, performed on single molecules interacting with an idealised silica surface. The observed correlation demonstrates the remarkable ability of this metric to provide a quantitative indication of adsorption energetics within liquid-saturated mesoporous media, and validates previous theoretical efforts to link adsorption energetics and the ratio T_1/T_2. Supplementary diffusion measurements illustrate that the effective self-diffusion coefficients obtained from these liquid/silica systems also exhibit sensitivity to interactions with the pore surface, leading to a reduction in alcohol mobility beyond that expected purely from the tortuosity of the porous material. For the first time, it is shown that a clear correlation between reduced diffusivity and T_1/T_2 ratio is evident.

Acknowledgements

No small number of people have played a role in the completion of this thesis. Indeed the limited space I have allocated here for such acknowledgements can barely hope to scratch the surface; I will, for the purposes of brevity, therefore limit my thanks to those whose influence has been most deeply felt.

Foremost, I am indebted to my supervisors, Dr Carmine D'Agostino (Department of Chemical Engineering and Biotechnology) and Professor Stephen J. Jenkins (Department of Chemistry), for providing me with the opportunity to carry out research here at the University of Cambridge. I am particularly grateful for their seemingly limitless time and encouragement, their heartfelt support, and their keen interest in my ideas. Special thanks are also directed to the Catalysis@Cambridge initiative for funding, without which none of this would have been possible. I must also express my gratitude to Professor Lynn Gladden, whose input and support has been invaluable, and to Drs Mick Mantle and Andy Sederman, for help and encouragement in all areas NMR. I am also beholden to many of the postdoctoral researchers, and to my contemporary research students, both at the Magnetic Resonance Research Centre and within the Surface Science group. Special mentions must go to Dr Christopher Robertson for our many insightful discussions over the years, and to Bianca Provost for her unwavering Canadian optimism.

Of course postgraduate life is not merely an exercise in academia. It is a pleasure to acknowledge the countless friends I have made here, especially those at St Edmund's college, and within the wider Chemical Engineering and Chemistry communities. In particular, my years living at Milton Road have provided a heart full of memories not easily forgotten. I will remember my time there most fondly.

Finally I must expressed my deepest gratitude to my family, whose support during the completion of this thesis has been heartfelt and unwavering.

Research outcomes

Publications

- 'Exploring catalyst passivation with NMR relaxation', Neil Robinson, Lynn F. Gladden and Carmine D'Agostino, *Faraday Discussions*, 2017, 204, 439-452.
- 'Direct correlation between adsorption energetics and nuclear spin relaxation in a liquid saturated catalyst material', Neil Robinson, Christopher Robertson, Lynn F. Gladden, Stephen J. Jenkins and Carmine D'Agostino, *ChemPhysChem*, 2018, 19, 2472-2479.
- 'NMR investigation into the influence of surface interactions on liquid diffusion in a mesoporous catalyst support', Neil Robinson and Carmine D'Agostino, *Topics in Catalysis*, 2019, Accepted.

Publications not detailed within this thesis

- 'Unravelling mass transport in hierarchically porous catalysts', Mark A. Isaacs, Neil Robinson, Brunella Barbero, Lee J. Durndell, Jinesh C. Manayil, Christopher M. A. Parlett, Carmine D'Agostino, Karen Wilson and Adam F. Lee, *J. Mater. Chem. A*, 2019, 7, 11814-11825.

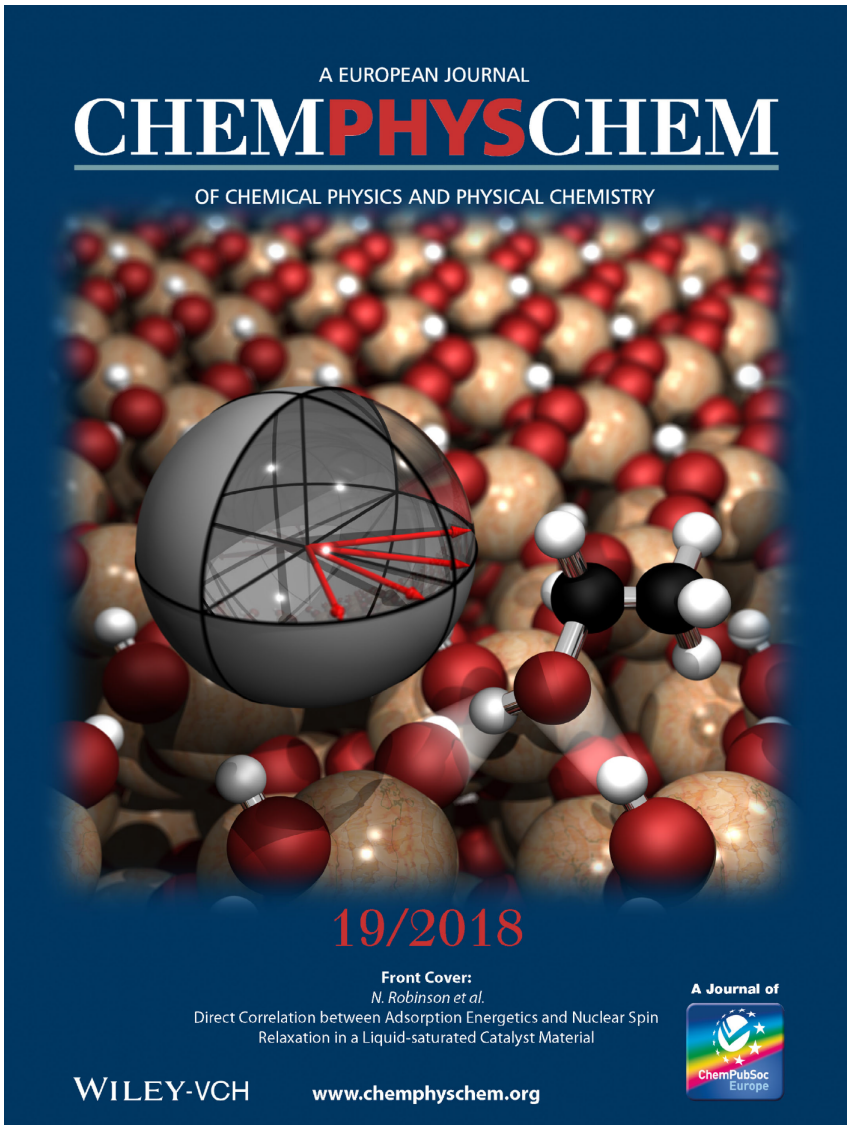
A EUROPEAN JOURNAL
CHEMPHYSCHEM
OF CHEMICAL PHYSICS AND PHYSICAL CHEMISTRY
19/2018
Front Cover:
N. Robinson et al.
Direct Correlation between Adsorption Energetics and Nuclear Spin Relaxation in a Liquid-saturated Catalyst Material
A Journal of
ChemPubSoc Europe
WILEY-VCH
www.chemphyschem.org

Contents

Chapter 1

Overture

Nuclear magnetic resonance (NMR) techniques are well-established across the physical, chemical and biological sciences. Foremost, NMR chemical shift-based analyses are known to be powerful spectroscopic methods for the elucidation of molecular and solid-state structures. NMR techniques are also prevalent across the field of medical physics in the form of magnetic resonance imaging, widely considered an invaluable aid to diagnostics both in human medicine and in the veterinary sciences. Perhaps unbeknown to the uninitiated, however, is the fact that such techniques are also widely applied across the engineering sciences, and as such are regularly employed to provide insight into fields as wide-ranging as membrane technology, battery development, and even the measurement of bubble size distributions. The key homology across these applications is that NMR-based measurements are both highly chemically selective and inherently non-invasive, and therefore offer experimentalists the opportunity to probe systems typically inaccessible to the vast majority of other analytical techniques. A rapidly developing sub-field within this discipline is the application of NMR analysis to understanding fluid behaviour in porous media. Such systems are of significant prevalence both within the natural world and to chemical industry, such as the dynamics of gas and oil in hydrocarbon-rich rocks, the hydration dynamics associated with plaster and cement drying processes, and the diffusion of water through biological cells. It is within this fascinating field that we will focus our efforts; specifically, it is the aim of this thesis to disseminate the state-of-the-art of NMR-based measurements for the evaluation of liquid dynamics within saturated porous materials of relevance to heterogeneous catalysis. The remainder of this thesis has the following structure:

Chapter 2 gives a detailed introduction to heterogeneous catalysis, and provides insight into the importance of surface interactions and mass transport processes. A range of surface-sensitive analysis techniques are contrasted and the requirement to develop novel, non-invasive methods to probe adsorption and surface dynamics is discussed.

Chapter 3 provides a detailed introduction to the theory of nuclear magnetic resonance, with specific emphasis placed on the measurement of nuclear spin relaxation and diffusion phenomena.

Chapter 4 details the utility of such measurements for the investigation of liquid-phase molecular dynamics within mesoporous media. An extensive account of how the measurement of nuclear spin characteristics can provide insight into surface-adsorbate interactions within liquid-saturated catalyst materials is provided, and the interpretation of diffusion measurements discussed.

Chapter 5 describes the utility of longitudinal nuclear spin relaxation measurements for the identification of adsorption mechanisms. Specifically, changes to the mobility of a prototypical polar adsorbate (methanol) upon the passivation of surface hydroxyl groups at the pore surface of a range of common mesoporous oxides highlight the ubiquity of surface-adsorbate hydrogen bonding interactions within such systems, and provide the first direct evidence that nuclear spin relaxation time measurements are sensitive to these interactions.

Chapter 6 details an extensive investigation into whether nuclear spin relaxation and self-diffusion measurements may be related to adsorption phenomena in a quantitative manner. This chapter focuses on the comparison of such measurements with extensive *ab initio* adsorption energy calculations performed at the level of dispersion-corrected periodic density functional theory. The results detailed in this chapter provide the first direct comparison of such calculations with nuclear spin relaxation measurements and provide the first molecular-level validation that relaxation time analysis may be interpreted as a quantitative probe of surface affinity.

Chapter 7 provides a summary of the main achievements detailed within this thesis and directs the reader towards relevant areas of further investigation.

Chapter 2

Introduction to catalysis and adsorbate dynamics

2.1 Microkinetics in catalysis

Consider the fictitious, thermodynamically favourable ($\Delta G_r < 0$) elementary reaction

$$\mathrm{A} + \mathrm{B} \xrightarrow{k} \mathrm{AB}. \tag{2.1}$$

Under a given set of experimental conditions this process will proceed at a rate $kc_\mathrm{A}c_\mathrm{B}$, where c_j indicates the concentration of species j, and must pass over an energy barrier, the magnitude of which is determined by the free energy of activation $\Delta^\ddagger G$. A free energy profile for this process is illustrated in Figure 2.1a; the saddle point of this profile constitutes formation of the transition state $[\mathrm{A}\cdots\mathrm{B}]^\ddagger$, which facilitates formation of the product AB. Standard transition state theory states that the rate constant k may be expressed in terms of the Eyring equation, [1]

$$k = \kappa\frac{k_B T}{h}\exp\left(\frac{-\Delta^\ddagger G}{RT}\right), \tag{2.2}$$

where k_B and h are the Boltzmann and Plank constants, respectively, T is the absolute temperature and R is the gas constant. The transmission coefficient $\kappa \leq 1$ defines the probability that the transition state proceeds to the product rather than reverting to the reagents. It follows that the reaction rate is directly dependent on the free energy of activation, as well as experimental parameters such as temperature and reagent concentration (or partial pressure).

Now let us consider the addition of a third elementary component C, whose interaction with A facilitates the formation of the product AB but is not consumed by the reaction itself. An example reaction pathway for how this process might proceed is given in Figure 2.1b. The initial reaction between A and C is again an activated process and proceeds through the transition state $[\mathrm{C}\cdots\mathrm{A}]^\ddagger$, forming the intermediate CA. The interaction of this intermediate with B is a second activated process, and through the transition state $[\mathrm{C}\cdots\mathrm{A}\cdots\mathrm{B}]^\ddagger$ forms the product AB, together with C in its initial form. The addition of this third component has therefore provided our simple chemical transformation with an alternative reaction pathway. If, as illustrated in Figure 2.1b, the activation energetics of this alternative pathway

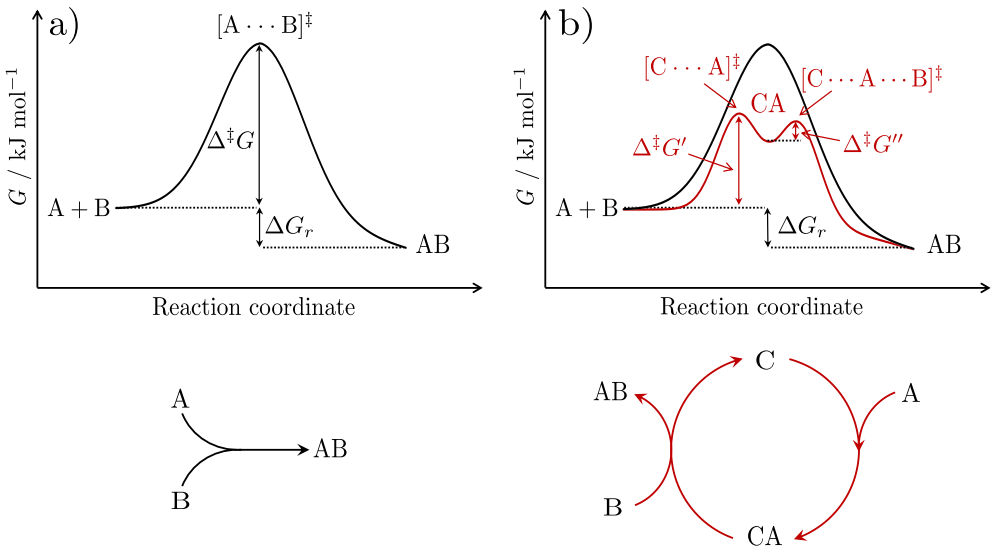

Figure 2.1: Free energy reaction profiles for the elementary reaction $A + B \rightarrow AB$. a) illustrates an uncatalysed free energy profile dictated by the free energy of activation $\Delta^{\ddagger}G$ and the free energy of reaction ΔG_r. b) illustrates the free energy profile for the same reaction when catalysed through the addition of a catalyst, C. The addition of this catalyst provides the reaction with an alternative free energy pathway in which the reaction kinetics depend on the reduced energy barriers $\Delta^{\ddagger}G'$ and $\Delta^{\ddagger}G''$. The reaction pathways below each energy profile illustrate the cyclic (non-stoichiometric) nature of catalytic reactions.

are reduced relative to those of the original free energy profile, then we may state that this reaction has been catalysed through the addition of C, which is termed a catalyst.

Catalysis – the study, development and application of catalysts – is of paramount importance to modern chemical industry. Indeed it is often estimated that more than 90 % of global chemical manufacturing processes employ a catalyst at some stage. [2, 3] Prevalent examples include the Haber-Bosch process for ammonia-based fertiliser production, the cracking of hydrocarbons from crude oil, the transformation of harmful exhaust emissions, and the polymerisation of unsaturated organic monomers such as ethene and styrene into plastics.

2.2 Modes of catalysis

2.2.1 Homogeneous catalysis

Homogeneous catalysts are present in the same phase as the reaction medium; typically in the liquid phase. The catalysts themselves often take the form of solvated organometallic complexes comprising catalytically active ligands surrounding a central metal ion. [4] Organometallic catalysts are well known for exhibiting high selectivities due to well-defined and highly tunable active sites. [2] For this reason their use is often seen in the pharmaceutical, fine chemical and food industries, where high enantiomeric excesses and minimal rates of by-product formation are a necessity. This subset of catalysts also includes organocatalysts [5] – organic molecules capable of facilitating chemical transformations within the aid of metal species – and enzymes (biocatalysts); protein structures which facilitate aqueous-phase processes, typically in biological systems. [6]

2.2.2 Heterogeneous catalysis

Heterogeneous catalysts occur in an alternative phase to that of the reaction medium; such catalysts take the form of solids and facilitate a vast array of gas- and liquid-phase reactions. [3] The active component of a heterogeneous catalyst is typically a metallic or metal alloy nanoparticulate species, which is finely dispersed and supported on the surface of a highly porous structure. [7] Organo and organometallic catalysts may also be supported on such structures. [8–11] Heterogeneous catalysts are known to lack the high selectivites of their homogeneous competitors, typically due to a lack of well-defined active sites on heterogeneous surfaces, often leading to a number of competing catalytic mechanisms. Such catalysts are therefore most commonly employed in the production of bulk, industrial-grade chemicals where higher concentrations of impurities can be tolerated. Despite the diminished selectivities typically achieved by heterogeneous catalysts, they remain popular in chemical industry due to their recyclable nature. Reactions catalysed by organometallic complexes or enzymes tend to be highly cost ineffective due to difficulties in catalyst retrieval and regeneration. Alternatively, heterogeneous

catalysts are easily separated from the reaction medium; for industrial-scale processes this provides large savings in terms of raw materials and catalyst synthesis, making heterogeneous rather than homogeneous processes economically desired. [2]

2.3 Surface processes in heterogeneous catalysis

In this thesis will we concentrate on the observation of surface dynamics of relevance to heterogeneous catalysis. Clearly adsorption processes – adhesion of chemical species to a solid surface – are of fundamental importance to heterogeneously catalysed reactions. Indeed, by definition such reactions are facilitated by surface-mediated reaction mechanisms. Below we introduce some of the fundamental surface processes which occur during such reactions.

2.3.1 Surface reaction mechanisms

Like all chemical transformations, heterogeneously catalysed reactions proceed *via* a particular reaction mechanism. For such mechanisms to be facilitated by the presence of a solid surface it follows that at least one reagent must become adsorbed; this concept leads us to the consideration of the two well-known limiting cases for such surface processes:

- The Langmuir-Hinshelwood mechanism (Figure 2.2a): All reagents adsorb and diffuse across the catalyst surface until they meet and react at an active site. The products then desorb and enter the mobile phase.

- The Eley-Rideal mechanism (Figure 2.2b): A single reagent is adsorbed at the catalyst surface and diffuses to the active site; here it is met by the other reagents directly from the mobile phase, facilitating the surface-mediated reaction. The products then desorb and enter the mobile phase.

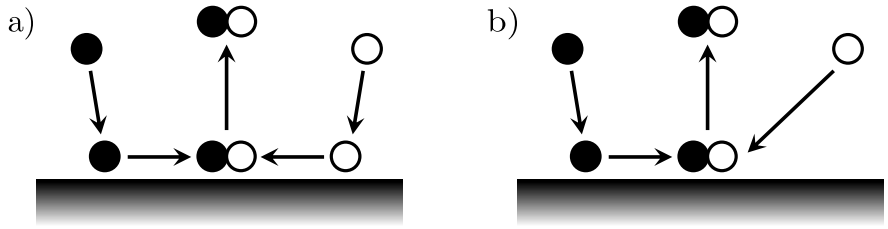

Figure 2.2: Illustration of the limiting surface mechanisms in heterogeneous catalysis. a) the Langmuir-Hinshelwood mechanism involves adsorption and surface diffusion of all reagents to the active surface site. b) The Eley-Rideal mechanisms involves adsorption and diffusion of a single reagent to the active surface site, where it is met by other reagents directly from the mobile phase.

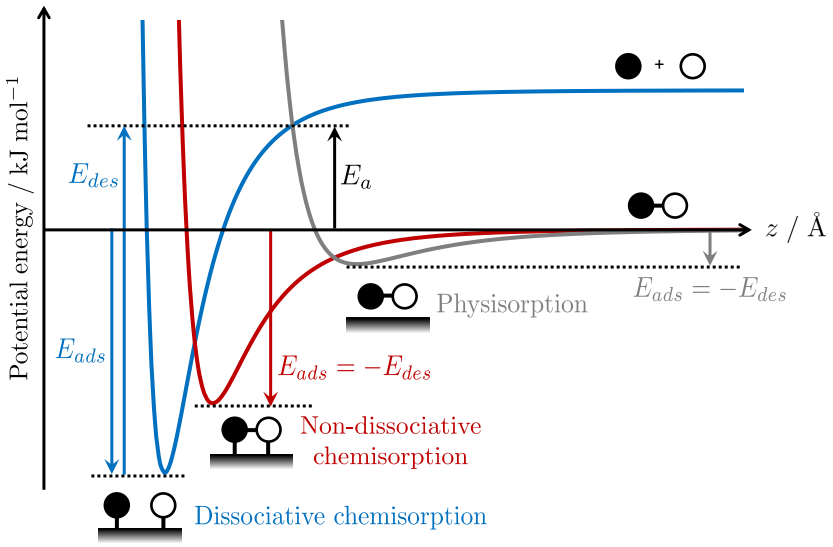

Figure 2.3: Lennard-Jones type adsorption energy curves for physisorption (grey), non-dissociative chemisorption (red) and dissociative chemisorption (blue) as a function of distance from the adsorbing surface z.

2.3.2 Adsorption interactions

It is appropriate here to consider and contrast the different forms of adsorption which may occur during such mechanisms. These adsorption interactions may be differentiated by the energetics involved, and by the nature of any electronic rearrangement which occurs upon interaction with the surface: [12]

- Physisorption (or physical adsorption) defines surface-adsorbate interactions dominated by van der Waals interactions. Adsorption energetics are weak – typically 10 - 50 kJ mol^{-1} – but may be further stabilised by lateral van der Waals interactions between adsorbed species. Such interactions are generally unspecific in terms of adsorption site, and the electronic – and often geometric – structure of the adsorbate remains largely unaltered. Typical examples of relevance to the present work include the interaction of alkanes with oxide surfaces. [13, 14] Physisorption is a non-activated process.

- Chemisorption (or chemical adsorption) involves strong surface-adsorbate interactions associated with electronic rearrangement of the adsorbing species and the solid surface. Such rearrangement arises from the overlap of electron density associated with the adsorbate and electronic states at the solid surface. Chemisorption interactions are more enthalpically favourable than those associated with physisorption (often comparable to the formation of covalent bonds), and are adsorption site specific, exhibiting a strong dependence on local surface chemistry. If the electronic redistribution within the adsorbate is small then its geometric structure may be retained upon adsorption; this process is termed non-dissociative chemisorption (or molecular chemisorption), and is typically a non-activated process. Alternatively, if the electronic redistribution is significant, the molecular structure of the adsorbate may be disrupted, resulting dissociation at the surface; this process is termed dissociative chemisorption. Adsorbate dissociation is clearly of fundamental importance to heterogeneous catalysis, and is an activated process.

The energetics of such interactions are illustrated in Figure 2.3. Here, the adsorption energy E_{ads} (a negative quantity) quantifies the potential energy change upon adsorption at the surface, while the desorption energy E_{des} (a positive quantity) quantifies the activation energy required for desorption to occur. For non-activated adsorption processes this is equal to E_{ads} apart from a change in sign. For activated adsorption, however, $E_{des} = -E_{ads} + E_a$, where E_a is the adsorption activation energy.

We may further consider E_{ads} in terms of the enthalpy changes which occur upon adsorption. Employing thermodynamic relations from the ideal gas, the molar enthalpy of the mobile phase H_m can be expressed as $H_m = U_m + RT_m$; here U_m and T_m are the internal energy and temperature of the mobile phase, respectively, and R is the gas constant. As the pressure of the adsorbed surface layer can be considered negligible in relation to the mobile phase, the molar enthalpy of the adsorbate is $H_{surf} = U_{surf}$. The enthalpy change upon adsorption is therefore [12]

$$\Delta H_{ads} = U_{surf} - U_m - RT, \tag{2.3}$$

where we may define $E_{ads} = U_{surf} - U_m$. [15] As E_{ads} is a negative quantity, this relationship implies that adsorption is an exothermic ($\Delta H_{ads} < 0$) process; we can confirm this interpretation through the consideration of the Gibbs free energy for adsorption,

$$\Delta G_{ads} = \Delta H_{ads} - T\Delta S_{ads}, \tag{2.4}$$

which must, of course, be negative for thermodynamically spontaneous adsorption processes. As the arrangement of adsorbates at solid surfaces is likely to cause a decrease in entropy upon adsorption ($\Delta S_{ads} < 0$), the $-T\Delta S_{ads}$ term will be positive. Adsorption is therefore usually exothermic in order to be thermodynamically favourable. Endothermic adsorption processes are, however, also possible; in particular, it is important to note that competitive adsorption interactions involve not only the adsorption of impinging adsorbates at the solid surface, but also the removal of species already occupying potential binding sites. The free energy change of such displacement processes therefore includes

both adsorption and desorption terms, as well as solvation and adsorbate-adsorbate interactions. It follows that competitive adsorption has the potential to be endothermic provided the overall displacement process is sufficiently thermodynamically favourable. [16]

2.3.3 Equilibrium adsorption dynamics

Elementary adsorption interactions of relevance to atomic and non-dissociative molecular adsorption processes may be considered in terms of the reversible surface-adsorbate reaction

$$\mathrm{A}_{(m)} + \mathrm{S} \underset{k_{des}}{\overset{k_{ads}}{\rightleftharpoons}} \mathrm{A}_{(ads)}. \tag{2.5}$$

Here $\mathrm{A}_{(m)}$ is the adsorbate is the mobile ($m = g$ or l) phase, S represents an unoccupied adsorption site at the solid surface and $\mathrm{A}_{(ads)}$ is A in an adsorbed state. The rate constants k_{ads} and k_{des} define the energetic contributions to the kinetics of such adsorption-desorption processes. As a typical first theoretical approach the Langmuir adsorption model provides a fundamental foundation to our understanding of such kinetics. [17] The model considers a homogeneous surface exhibiting a set of discrete and well-defined adsorption sites, each of which can accommodate a single adsorbate; it is further assumed that no inter-adsorbate or multilayer interactions occur. Let us briefly consider the Langmuirian kinetics associated with a solid surface of area A exhibiting N_{S} adsorption sites (mol) with an areal density $\sigma_0 = N_{\mathrm{S}}/A$ (mol m^{-2}). Upon adsorption of N_{ads} adsorbates this surface will exhibit an areal density $\sigma = N_{ads}/A$ of adsorbed species and $\sigma_0 - \sigma$ unoccupied sites. The coverage of a given adsorbate may then be defined in terms of a fractional coverage $\theta = \sigma/\sigma_0 = N_{ads}/N_{\mathrm{S}}$. The rate of adsorption R_{ads} (mol m^{-2} s^{-1}) resulting from the adsorption process in Equation 2.5 is often expressed as [18]

$$R_{ads} = \mathcal{F} s, \tag{2.6}$$

where $\mathcal{F}$ (mol m^{-2} s^{-1}) is the collision flux at the adsorbing surface; this quantity is given by [19]

$$\mathcal{F} = \frac{c_{\mathrm{A}} \overline{\nu}}{4}, \tag{2.7}$$

where c_{A} (mol m^{-3}) is the concentration of A in the mobile phase and $\overline{\nu} = (8RT/\pi M)^{1/2}$ is the mean velocity of an adsorbate of mass M perpendicular to the adsorbing surface. [20] The term

$$s = s_0(1-\theta_{\mathrm{A}})\exp\left(\frac{-E_a}{RT}\right) \tag{2.8}$$

is the sticking probability (or sticking coefficient). [12] Here s_0 denotes the sticking probability on a clean surface, E_a is the activation energy for adsorption (Figure 2.3) and the factor $(1-\theta)$ takes account of that fact that adsorption may only occur at unoccupied sites. The adsorption rate may also be expressed in the more typical form

$$R_{ads} = k_{ads}c_{\mathrm{A}}(1-\theta_{\mathrm{A}}), \tag{2.9}$$

where the units of R_{ads} are now s^{-1}. In this case the rate constant k_{ads} (m^3 mol^{-1} s^{-1}) is given by

$$k_{ads} = \frac{\overline{\nu}}{4\sigma_0}\exp\left(\frac{-E_a}{RT}\right). \tag{2.10}$$

The rate of desorption R_{des} (s^{-1}) is similarly defined as

$$R_{des} = k_{des}\theta_{\mathrm{A}}, \tag{2.11}$$

wherein the desorption rate constant k_{des} (s^{-1}) is determined by the activation energy for desorption E_{des} (Figure 2.3), readily defined with reference to the Eyring equation introduced previously,

$$k_{des} = \kappa_{des}\frac{k_B T_{surf}}{h}\exp\left(\frac{-\Delta^{\ddagger}G_{des}}{RT_{surf}}\right) \tag{2.12a}$$

$$= \kappa_{des}\frac{k_B T_{surf}}{h}\exp\left(\frac{\Delta^{\ddagger}S_{des}}{R}\right)\exp\left(\frac{-\Delta^{\ddagger}H_{des}}{RT_{surf}}\right). \tag{2.12b}$$

In this case κ_{des} is the transmission coefficient for desorption, $\Delta^{\ddagger}G_{des}$, $\Delta^{\ddagger}S_{des}$ and $\Delta^{\ddagger}H_{des}$ are the Gibbs free energy, entropy and enthalpy of activation for the desorption process, respectively, and T_{surf} is the absolute temperature of the solid

surface. Recognising that[1] $\Delta^{\ddagger}H_{des} = E_{des} - RT_{surf}$ this rate constant may be redefined as [21]

$$k_{ads} = \kappa_{des}\frac{k_B T_{surf}}{h}\exp\left(\frac{\Delta^{\ddagger}S_{des}}{R}\right)\exp\left(\frac{-(E_{des}-RT_{surf})}{RT_{surf}}\right) \tag{2.13a}$$

$$= e\kappa_{des}\frac{k_B T_{surf}}{h}\exp\left(\frac{\Delta^{\ddagger}S_{des}}{R}\right)\exp\left(\frac{-E_{des}}{RT_{surf}}\right), \tag{2.13b}$$

where $e = \exp(1) \approx 2.7$ is Euler's number. The mean surface lifetime of the adsorbate τ_s may then be expressed as [12]

$$\tau_s = \frac{1}{k_{des}} = \frac{1}{e}\frac{h}{\kappa_{des}k_B T_{surf}}\exp\left(\frac{-\Delta^{\ddagger}S_{des}}{R}\right)\exp\left(\frac{E_{des}}{RT_{surf}}\right), \tag{2.14}$$

while the number of adsorbates is [3]

$$N_{ads} = \mathcal{F}\tau_s = \frac{\mathcal{F}}{k_{des}}. \tag{2.15}$$

Under the conditions of thermal equilibrium between the solid surface, adsorbed surface layer and mobile phase, the rate of overall surface coverage change is

$$\frac{d\theta_{\mathrm{A}}}{dt} = k_{ads}c_{\mathrm{A}}(1-\theta_{\mathrm{A}}) - k_{des}\theta_{\mathrm{A}} = 0, \tag{2.16}$$

such that

$$k_{ads}c_{\mathrm{A}}(1-\theta_{\mathrm{A}}) = k_{des}\theta_{\mathrm{A}}. \tag{2.17}$$

Appropriate rearrangement of this expression yields the well-known Langmuir isotherm [17]

$$\theta_{\mathrm{A}} = \frac{bc_{\mathrm{A}}}{1+bc_{\mathrm{A}}}, \tag{2.18}$$

where $b = k_{ads}/k_{des}$ is the Langmuir equilibrium constant for Equation 2.5. Of particular relevance to this thesis is the realisation that when c_{A} is large then $bc_{\mathrm{A}} \gg 1$, such that $\theta_{\mathrm{A}} \sim 1$. This Langmuirian approach may also be extended to more complex adsorption dynamics; for instance, dissociation of an adsorbing molecule AB into the fragments $\mathrm{A}_{(ads)}$ and $\mathrm{B}_{(ads)}$ gives a Langmuir isotherm of the

[1] A full derivation of this relationship is provided in Appendix A.

form [3]

$$\theta_{\mathrm{A,B}} = \frac{\left(bc_{\mathrm{A,B}}\right)^{1/2}}{1 + \left(bc_{\mathrm{A,B}}\right)^{1/2}}. \tag{2.19}$$

Further corrections may also be made for the inclusion of non-negligible lateral interactions between adsorbates, [22] and for multilayer adsorption; indeed, the most notable and widely applied extension to the Langmuir theory is that of Brunauer, Emmett and Teller, known as BET theory. [23] In this approach, multilayer adsorption is assumed to follow the Langmuir adsorption model for each layer; as such, the adsorption energetics of the first layer are characterised by interactions with the adsorbing surface, while the adsorption of subsequent layers is determined by the energy of liquefaction. BET theory has gained particular note as a simplistic method for determining the surface areas of porous solids using probe gases. Utilising the above approach, a linear expression of the form [12]

$$\frac{p}{N_{abs}(p_0 - p)} = \frac{1}{N_{mon}c} + \frac{c - p}{N_{mon}c}\frac{p}{p_0} \tag{2.20}$$

may be derived. Here N_{abs} (mol g^{-1}) is the amount of absorbed probe gas at pressure p, while p_0 and N_{mon} (mol g^{-1}) are the saturation pressure and monolayer capacity of that same probe gas, respectively. The term c is known as the BET constant and contains contributions from the heats of adsorption and liquefaction. It follows that a plot of p/p_0 against $p/N_{abs}(p_0 - p)$ (typically in the range $0 < p/p_0 \leq 0.35$) should yield a straight line of gradient $(c - p)/N_{mon}c$ and intercept $1/N_{mon}c$; knowledge of N_{mon} for a probe gas of well-defined molecular cross-sectional area σ_{mol} (typically N_2) therefore yields the specific BET surface area S_{BET} (m^2 g^{-1}) according to

$$S_{BET} = N_{mon}N_A\sigma_{mol}, \tag{2.21}$$

where N_A is Avogadro's constant.

2.3.4 Surface diffusion

Adsorbates are rarely immobile. Indeed, while the collision of impinging adsorbates with the potential energy surface illustrated in Figure 2.3 reduces motion

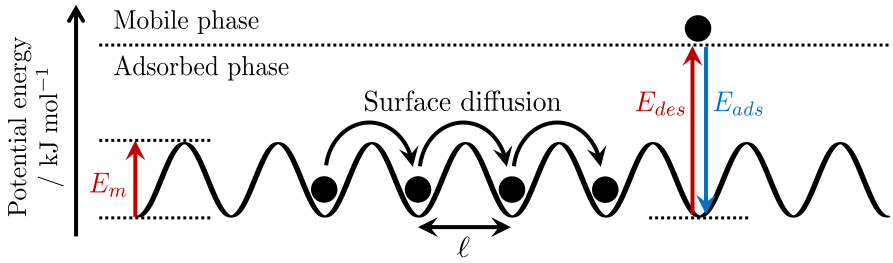

Figure 2.4: Illustration of the energetic properties of adsorbed species.

perpendicular to the adsorbing plane, translational motion in directions parallel to the surface often continues, facilitating the phenomenon of surface diffusion. Such motion is clearly of importance for the catalytic mechanisms illustrated in Figure 2.2 and can be considered to proceed *via* an activated hopping motion between adsorption sites. Figure 2.4 illustrates a simple potential energy surface across which such motion proceeds.

In the case of an isolated adsorbate the rate of migration R_m (units of s^{-1}) across the surface is [24, 25]

$$R_m = \kappa_m \frac{k_B T_{surf}}{h} \exp\left(\frac{\Delta^\ddagger F_m}{R T_{surf}}\right) \tag{2.22a}$$

$$= \kappa_m \frac{k_B T_{surf}}{h} \exp\left(\frac{\Delta^\ddagger S_m}{R}\right) \exp\left(\frac{-E_m}{R T_{surf}}\right). \tag{2.22b}$$

Here $\Delta^\ddagger F_m$, $\Delta^\ddagger S_m$ and E_m are the Helmholtz free energy of activation,[2] entropy of activation and internal energy of activation associated with the diffusion barrier, respectively, and κ_m is the relevant transmission coefficient. The average residence time at a given adsorption site τ_m is

$$\tau_m = \frac{1}{R_m} = \frac{h}{\kappa_m k_B T_{surf}} \exp\left(\frac{-\Delta^\ddagger S_m}{R}\right) \exp\left(\frac{E_m}{R T_{surf}}\right), \tag{2.23}$$

and the diffusion coefficient $\mathcal{D}_m$ ($\mathrm{m}^2\ \mathrm{s}^{-1}$) which quantifies the rate of this diffusive

[2]Here we have employed the common convention that the relevant free energy of activation for the surface diffusion of an isolated particle is the Helmholtz free energy $\Delta^\ddagger F_m = E_m - T\Delta^\ddagger S_m$ rather than the Gibbs free energy $\Delta^\ddagger G_m = \Delta^\ddagger H_m - T\Delta^\ddagger S_m$, where $E_m \equiv \Delta^\ddagger U_m$. This arises because it may be assumed that there is no change to the pressure or volume of the adsorbed surface layer during the translational motion of a single adsorbate. The enthalpy of activation $\Delta^\ddagger H_m$ is therefore equivalent to the internal energy $\Delta^\ddagger U_m$ such that $\Delta^\ddagger G_m \equiv \Delta^\ddagger F_m$. As a result there is no factor e in Equations 2.22b or 2.23.

motion may be expressed as [18, 25]

$$\mathcal{D}_m = \frac{\ell^2 R_m}{2n}, \tag{2.24}$$

where ℓ is the average jump length (Figure 2.4) and n is the dimensionality of the diffusion process ($n = 2$ in the usual description of surface diffusion).

Equation 2.24 is valid for low surface coverages, where adsorbate diffusion is unimpeded by the presence of other adsorbed species. [26] At high surface coverages, however, it is necessary that a hole forms at an adjacent adsorption site before migration may proceed. We must therefore take account not only of the rate of surface migration of the adsorbate, but also of the holes within the adsorbed surface layer. [27] To address this concept we may take inspiration from the hole theory of bulk liquid diffusion, [28] such that the self-diffusion coefficient may be written [29]

$$\mathcal{D} = \frac{\ell^2 R_m P_h}{2n}. \tag{2.25}$$

Here P_h is the probability that a hole is available to accommodate migration, [29]

$$P_h = \exp\left(\frac{-\Delta^{\ddagger} G_h}{RT}\right), \tag{2.26}$$

where $\Delta^{\ddagger} G_h$ is the free energy of activation for the hole making process. The self-diffusion coefficient for surface migration is then[3]

$$\mathcal{D}_m = \frac{\ell^2}{2n} \frac{\kappa_m k_B T_{surf}}{h} \exp\left(\frac{-\Delta^{\ddagger} G_h}{RT_{surf}}\right) \exp\left(\frac{-\Delta^{\ddagger} G_m}{RT_{surf}}\right), \tag{2.27}$$

which, after appropriate rearrangement yields [26]

$$\mathcal{D}_m = \mathcal{D}_{m,0} \exp\left(\frac{-(E_h + E_j)}{RT_{surf}}\right). \tag{2.28}$$

[3]Following the convention of Komiyama [29] we have restated the free energy of activation for the surface migration process in Equation 2.22b in terms of a Gibbs free energy, rather than a Helmholtz free energy. This arises from the need for a hole to form at an adjacent adsorption site for surface migration to occur under the conditions of liquid saturation. The hole may move in a transverse manner, but could also move from the mobile phase during desorption. It follows that there can be a change to the pressure and volume of the adsorbed surface layer under such conditions, such that the Gibbs and Helmholtz free energies of activation should not be considered equal.

Here E_h is an activation energy for the the hole-making processes, and we have combined the relevant entropy terms and pre-exponential factors into a convenient Arrhenius-type factor $\mathcal{D}_{m,0}$. In a macroscopic discussion of surface diffusion it is typical that the energy $E_h + E_j$ is combined into a single effective diffusion barrier E_m^*. [18]

2.4 Macrokinetics in heterogeneous catalysis

Let us return to the simple elementary reaction in Equation 2.1. When catalysed heterogeneously the rate of product formation may be written $k\theta_\mathrm{A}\theta_\mathrm{B}$ or $k\theta_\mathrm{B}c_\mathrm{A}$, depending on whether the Langmuir-Hinshelwood or Eley-Rideal mechanism prevails, respectively (Figure 2.2); [3] in either case $\theta_\mathrm{A,B}$ may be expanded further according to Equation 2.19. It is clear from these expressions that the absolute rate of product formation is a function of the surface area of the catalyst; industrial heterogeneous catalysts maximise the available surface area per unit volume through the use of highly porous support materials, such as oxides (for example Al_2O_3, SiO_2 and TiO_2) and carbons. The structure of such material means that macrokinetic phenomena associated with chemical transport are also of importance to heterogeneously catalysed reactions. Figure 2.5 summarises the physical reaction pathway which reagents and products must take during such a reaction. The relevant processes are: [2]

1. Diffusion of the reagents through the boundary layer at the catalyst pellet surface.
2. Diffusion of the reagents into the pore structure of the catalyst.
3. Adsorption onto the pore surface.
4. Surface-mediated reaction mechanisms.
5. Desorption of the products from the pore surface.
6. Diffusion of the products out of the pore structure.
7. Diffusion of the products across the boundary layer and into the bulk phase.

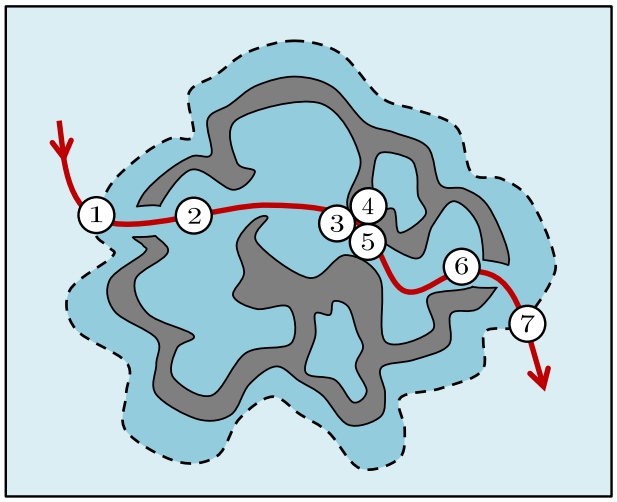

Figure 2.5: Illustration of basic transport and reaction steps in a heterogeneously catalysed chemical reaction occurring within a porous catalyst material. Numbered steps are defined in the main text.

Steps 3 - 5 clearly represent the surface-mediated reaction microkinetics introduced described previously. The remaining processes which occur pre- and post-surface interaction are also of importance to efficient catalytic processes; these steps are termed macrokinetics and depend on the mass transfer capabilities of the reaction system.

2.5 Liquid-phase heterogeneous reaction systems

As prominent international climate change agreements place considerable emphasis on the desire to reduce fossil fuel dependence, the establishment of a renewable chemical industry has become the subject of significant focus. [30] One of the most prominent areas of investigation is the effective utilisation of biomass; waste organic matter – typically from agricultural sources such as food refuse, animal waste and used vegetable oils – which may be processed to form value-added products such as platform chemicals and fuels. It is abundantly clear that the development and implementation of relevant catalytic processes is vital to facilitate these so-called green chemical reaction systems; [31–37] however, such transformations differ considerably from the gas-phase reaction systems commonly encountered in more traditional catalyst applications. [38] Foremost, biomass-derived compounds regularly possess multiple polar functional groups. [31] The

resulting intermolecular interactions lead such materials to exhibit notably low volatilities and vapour pressures. The effective transportation of such compounds therefore relies heavily on the use of solvents, such that the relevant chemistry is dominated by the dynamics of the liquid-phase. [16] The nature of such reaction conditions provides significant challenges for the rational design of porous catalyst materials. For instance, while the liquid-phase is favoured for effective macrokinetic transport processes, the high molecular density within such systems leads to complex – and often unfavourable – dynamics at the catalyst surface. Indeed, careful solvent selection is required not only to establish efficient macrokinetics, but is also necessary to facilitate the desired reaction variables at the solid surface. [39–41] The presence of solvent molecules has the potential to influence reactions through a variety of processes; reaction rates may be influenced through competitive adsorption interactions at active sites, and through the destabilisation of transition states. Reaction selectivities may be further influenced through competitive adsorption dynamics with surface-bound intermediates, the blocking (poisoning) of specific surface sites or adsorption configurations, and direct participation in side reactions. As a result, the development of robust approaches for the investigation of structure-activity relationships in the presence of the liquid-phase has become a significant goal in modern catalytic research. [16]

2.6 Probes of the catalyst-liquid interface

Obtaining insight from the buried interfaces responsible for liquid-phase heterogeneous catalysis is a formidable task, and is reliant on state-of-the-art surface science tools and techniques. Spectroscopic investigations of the solid-liquid interface are heavily impeded by the need to differentiate between adsorbed species and the mobile phase; relevant techniques must therefore exhibit an appropriate level of discrimination between the relatively small number of adsorbed species and the surrounding liquid. Traditional ultra-high vacuum methods which rely on the absence of a condensed mobile phase are therefore unsuitable for such investigations; nevertheless, there remains a variety of techniques which may be readily applied to

the study and understanding of adsorption and reaction phenomena occurring at the solid-liquid interface. A brief and strictly non-exhaustive overview of such techniques is given below.

2.6.1 Vibrational spectroscopy

Perhaps the most common class of techniques employed to study the solid-liquid interface are vibrational spectroscopies. Such methods subject the interfacial region to infra-red (IR) irradiation and assess the frequencies at which this radiation is absorbed through specific chemical bond vibrations. IR techniques are particularly well-suited to the elucidation of surface-adsorbate bonding phenomena as molecular vibrational characteristics are usually highly localised in nature (i.e. a particular absorption frequency will often pertain to single and well-defined chemical bonding interactions). However, as IR is absorbed by the majority of solids, and will also be absorbed by any free liquid molecules away from the solid surface, the discrimination of signals originating purely from bonding interactions at the interface can be challenging.

Perhaps the most suitable IR technique for studying buried interfaces is attenuated total reflectance (ATR). [42] ATR makes use of the phenomenon of total internal reflectance, wherein an IR beam impinging upon a surface at a certain angle results in an evanescent field, which penetrates a small distance ($\sim$ 1 μm) across the interface. A typical ATR experiment therefore involves the total internal reflection of an IR beam through a prism, the outer surface of which is utilised for the surface chemistry of interest through the deposition of thin solid films, which are then immersed within the mobile phase. IR absorption from the evanescent field is detected and the frequency response data may be analysed to probe adsorption mechanisms and geometries, which are of fundamental importance to the elucidation of surface reactions. Furthermore, as IR adsorption data is related to concentration, quantitative insights may be gained from ATR data through the estimation of adsorption isotherms.

Vibrational characteristics may also be observed from the direct reflection of an IR beam from reflective solid surfaces beneath a thin liquid film. Reflection-

absorption infra-red spectroscopy (RAIRS) experiments avoid excessive absorption of the IR beam by free liquid by sandwiching a thin film of the mobile phase between the solid surface of interest and the IR prism. [43]

Several non-IR-based vibrational techniques may also be applied to the study of the solid-liquid interface; such techniques typically employ visible or ultra violet (UV) radiation, which are better able to pass through liquids than IR. [44] Of particular note is the method of sum frequency generation (SFG), which involves the simultaneous impingement of two photons at the solid surface of interest. [45] In this technique one photon impinges with angular frequency ω_a within the IR region, while the second impinging photon has angular frequency ω_b within the visible spectrum; the two beams mix at the surface and reflect with frequency $\omega_c = \omega_a + \omega_b$. Typically ω_b remains fixed during such measurements while ω_a is scanned through a range of frequencies, providing insight into the vibrational characteristics of chemical bonding interactions occurring at the interface. Importantly, the intensity of the reflected beam is proportional not only to the intensities of the two impinging beams, but also to the second order electric susceptibility of the material under study, which is zero for centrosymmetric media such as isotropically tumbling liquid molecules. SFG may therefore be used to selectively probe the vibrational properties of anisotropically adsorbed species at the solid-liquid interface without interference from absorption by liquid molecules away from the solid surface.

The specific case of SFG analysis wherein $\omega_a = \omega_b$ is known as second harmonic generation (SHG). [46] Here both photons are provided by the same laser source, and combine to generate an outgoing beam of frequency $2\omega_a$. Much like SFG, SHG is highly sensitive to the solid-liquid interface due to its dependence on second order electric susceptibility. It should be noted, however, that as both impinging photons are typically within the visible light region of the electromagnetic spectrum, SHG is usually sensitive to the electronic structure of the interface, rather than its vibrational properties.

2.6.2 Scattering and diffraction techniques

Modern synchrotron facilities offer intense and highly tunable X-ray beams which can easily penetrate condensed phases to reach the solid-liquid interface. Unfortunately, the high intensity of the probe radiation means that such techniques do not exhibit intrinsic surface sensitivity, making the discrimination of signals arising purely from the interfacial region a challenge. The surface sensitivity of X-ray absorption spectroscopy (XAS) measurements may be increased through the use of high surface area samples such as porous solids. Herein, a high intensity X-ray source is applied to the sample and adsorption data acquired in transmission mode as a function of intensity. As the absorption of X-ray radiation increases substantially as the intensity of the incident beam approaches the binding energy of core electrons within the sample, XAS can provides intimate details on the electronic structure of species at the solid-liquid interface. [47] The acquisition and analysis of such data is referred to as X-ray absorption near edge spectroscopy (XANES), wherein the so-called edge is that of the core electron shell. Increasing the the intensity of the incident beam further produces oscillations in the observed X-ray absorption data which are sensitive to the local coordination environment of the probed species; the acquisition of this second data form is known as extended X-ray absorption fine structure (EXAFS).

Inherent surface sensitivity may be enforced through the use of reflection, scattering and diffraction methods. X-ray reflection (XRR) involves the evaluation of the intensity change of an X-ray beam following its reflection from a flat solid-liquid interface, typically from a single crystal system. [48] The acquired XRR data then provide details of the density profile of the interface normal to the reflecting surface. Grazing incidence small angle X-ray scattering (GISAXS) experiments may be applied to analyse scattered, out-of-plane X-rays, and provides density profile information in all directions. Both XRR and GISAXS may be employed to characterise the formation of self-assembled monolayer structures at the solid-liquid interface. [49] Complementary grazing incidence X-ray diffraction (GIXD) provides structural information on the interface such as enhanced degrees of ordering in the presences of adsorbed monolayers. GIXD utilised the same concepts as three-

dimensional X-ray diffraction processes; however, by employing a small incident angle near that of the critical angle of the solid, the associated Bragg reflections are known to emerge from the surface structure alone. [44]

Neutron reflection, scattering and diffraction experiments may also be employed to probe the solid-liquid interface. Unlike X-ray radiation which interacts with electronic structures, neutron scattering occurs due to interactions with atomic nuclei. It follows that a significant advantage of neutron-based techniques is that light atoms may be detected, and isotopic distributions analysed. The limited interaction of neutrons with matter also allows such techniques to be applied to *in situ* systems within complex experimental apparatus, such as those maintained at relevant high temperature and/or pressure-based reaction conditions. In analogy to the X-ray techniques briefly mentioned above, the relevant surface-sensitive neutron-based techniques are neutron reflectometry, [50] grazing incident small angle neutron scattering (GISANS), [51] and small angle neutron diffraction (SANS). [52]

2.6.3 Experimental methods for measuring sorption energetics

The adsorption and desorption energetics associated with liquid interactions at solid surfaces are clearly of importance in the characterisation of liquid-phase heterogeneous catalytic materials. Established techniques for the determination of such energetics include isoteric heat of adsorption measurements and thermal gravimetric analysis. By far the most prominent technique applied to the quantification of adsorption interactions on catalytic solids, however, is temperature programmed desorption (TPD). [12] TPD analysis involves the measurement of desorption as the temperature of the adsorbing surface is increased. Desorption events are observed through the use of a mass spectrometer allowing fragments associated with multiple surface components to be analysed simultaneously. The rate constant for desorption from a particular surface binding site is assumed to take an Arrhenius form, such that the desorption rate from that site is exponentially related to the activation energy for desorption E_{des}, which, when assuming first order desorption kinetics may be extracted by assessing the desorption rate process for a range of different heating rates, and fitting to the resulting data. [53]

2.6.4 The need for next-generation surface-sensitive techniques

While the above techniques can provide detailed molecular – and in some cases sub-molecular – level information on the nature of the solid-liquid interface, each have limitations regarding the evaluation of adsorption phenomena within industrially relevant catalyst surfaces. Notably, heterogeneous catalysts take the form of porous, optically opaque solids, and often exhibit highly heterogeneous pore surfaces and pore size distributions. Experimental probes requiring flat, highly accessible and reflective surfaces and thin liquid films are therefore inappropriate for the study of surface phenomena within such systems. Although transmission X-ray techniques are capable of probing optically opaque matter, high intensity synchrotron radiation is required, which entails complex and expensive experimental set-ups with limited *in situ* capabilities, and is often damaging to the materials under study. While neutron irradiation may be used to probe catalysts under industrially relevant conditions, quantitative data analysis often requires the use of modelling. The collimation of neutron beams is also difficult, and the flux low relative to X-ray sources, such that large samples are required. Furthermore, there exists only a few neutron sources in the world, such that beam time is expensive and competitive. Finally, in terms of adsorption energetics, isoteric heat of adsorption measurements are non-invasive, but are extremely time consuming to perform. TGA and TPD, however, are both destructive as they involve excessive sample heating, and may cause *in situ* reactions during analysis.

In short, it follows that the development and validation of a new generation of surface-sensitive techniques which might probe non-invasively surface dynamics and adsorption behaviour within industrially relevant catalyst material is highly desirable. The ideal methodology should be readily applicable to liquid-saturated porous media of relevance to heterogeneous catalysis, and provide significant surface sensitivity, so that bulk-like fluid towards the centre of the pore structure does not dominate the analysis. Implementation should be possible at the laboratory scale, and the apparatus should afford the possibility of *in situ* investigations under industrially relevant conditions. To this end, it is the aim of this thesis to detail one such possible technique – that of nuclear spin relaxation.

2.7 References

[1] K. J. Laidler and M. C. King, "Development of Transition-State Theory", *J. Phys. Chem.*, 1983, **87**, 2657–2664.

[2] J. Hagen, *Industrial Catalysis: A Practical Approach*, John Wiley & Sons, 2006.

[3] J. M. Thomas and W. J. Thomas, *Principles and Practice of Heterogeneous Catalysis*, Wiley VCH, Weinheim, 2nd Edition, 2014.

[4] A. Behr and P. Neubert, *Applied Homogeneous Catalysis*, John Wiley & Sons, 2012.

[5] B. List, "Introduction: Organocatalysis", *Chem. Rev.*, 2007, **107**, 5413–5415.

[6] M. T. Reetz, "Biocatalysis in Organic Chemistry and Biotechnology: Past, Present, and Future", *J. Am. Chem. Soc.*, 2013, **135**, 12480–12496.

[7] L. Liu and A. Corma, "Metal Catalysts for Heterogeneous Catalysis: From Single Atoms to Nanoclusters and Nanoparticles", *Chem. Rev.*, 2018, **118**, 4981–5079.

[8] J. M. Basset and R. Ugo, in *Modern Surface Organometallic Chemistry*, ed. J.-M. Basset, R. Psaro, D. Roberto and R. Ugo, Wiley-VCH Verlag GmbH & Co. KGaA, 2009, pp. 1–21.

[9] C. E. Barnes, in *Modern Surface Organometallic Chemistry*, ed. J.-M. Basset, R. Psaro, D. Roberto and R. Ugo, Wiley-VCH Verlag GmbH & Co. KGaA, 2009, pp. 137–165.

[10] M. M. Aboelhassan, A. F. Peixoto and C. Freire, "Sulfonic Acid Functionalized Silica Nanoparticles as Catalysts for the Esterification of Linoleic Acid", *New J. Chem.*, 2017, **41**, 3595–3605.

[11] T. Yokoi, Y. Kubota and T. Tatsumi, "Amino-Functionalized Mesoporous Silica as Base Catalyst and Adsorbent", *Appl. Catal., A*, 2012, **421-422**, 14–37.

[12] K. K. Kolasinski, *Surface Science: Foundations of Catalysis and Nanoscience*, Wiley-Blackwell, Chichester, West Sussex ; Hoboken, N.J, 3rd Edition, 2012.

[13] S. N. Lanin, E. V. Vlasenko, N. V. Kovaleva and F. T. Zung, "The Adsorption Properties of Titanium Dioxide", *Russ. J. Phys. Chem.*, 2008, **82**, 2152–2155.

[14] C. Li and P. Choi, "Molecular Dynamics Study of the Adsorption Behavior of Normal Alkanes on a Relaxed Alpha-Al2O3 (0001) Surface", *J. Phys. Chem. C*, 2007, **111**, 1747–1753.

[15] H. Y. Erbil, *Surface Chemistry of Solid and Liquid Interfaces*, Wiley, 2006.

[16] C. Sievers, Y. Noda, L. Qi, E. M. Albuquerque, R. M. Rioux and S. L. Scott, "Phenomena Affecting Catalytic Reactions at Solid–Liquid Interfaces", *ACS Catal.*, 2016, **6**, 8286–8307.

[17] I. Langmuir, "The Adsorption of Gases on Plane Surfaces of Glass, Mica and Platinum", *J. Am. Chem. Soc.*, 1918, **40**, 1361–1403.

[18] G. A. Somorjai and Y. Li, *Introduction to Surface Chemistry and Catalysis*, Wiley-Blackwell, Hoboken, N.J, 2nd edition, 2010.

[19] M. Boudart and D. G. Löffler, "Rate of Adsorption to and Desorption from a Langmuir Surface: The Case of Zero Activation Barrier to Adsorption without Dissociation", *Catal. Lett.*, 1990, **6**, 317–320.

[20] P. Atkins, J. de Paula and J. Keeler, *Atkins' Physical Chemistry*, OUP Oxford, Oxford, United Kingdom ; New York, NY, 11 edition, 2017.

[21] E. Roduner, "Understanding Catalysis", *Chem. Soc. Rev.*, 2014, **43**, 8226–8239.

[22] D. A. King and M. G. Wells, "Reaction Mechanism in Chemisorption Kinetics: Nitrogen on the {100} Plane of Tungsten", *Proc. R. Soc. Lond. A*, 1974, **339**, 245–269.

[23] S. Brunauer, P. H. Emmett and E. Teller, "Adsorption of Gases in Multimolecular Layers", *J. Am. Chem. Soc.*, 1938, **60**, 309–319.

[24] D. A. King, "Surface Diffusion of Adsorbed Species: A Review", *J. Vac. Sci. Technol.*, 1980, **17**, 241–247.

[25] S. J. Lombardo and A. T. Bell, "A Review of Theoretical Models of Adsorption, Diffusion, Desorption, and Reaction of Gases on Metal Surfaces", *Surf. Sci. Rep.*, 1991, **13**, 3–72.

[26] I. Medveď and R. Černý, "Surface Diffusion in Porous Media: A Critical Review", *Microporous Mesoporous Mater.*, 2011, **142**, 405–422.

[27] K. Miyabe and G. Guiochon, "Surface Diffusion in Reversed-Phase Liquid Chromatography", *J. Chromatogr. A*, 2010, **1217**, 1713–1734.

[28] E. McLaughlin, "Viscosity and Self-Diffusion in Liquids", *Trans. Faraday Soc.*, 1959, **55**, 28–38.

[29] H. Komiyama and J. M. Smith, "Surface Diffusion in Liquid-Filled Pores", *AIChE J.*, 1974, **20**, 1110–1117.

[30] C. H. Christensen, J. Rass-Hansen, C. C. Marsden, E. Taarning and K. Egeblad, "The Renewable Chemicals Industry", *ChemSusChem*, 2008, **1**, 283–289.

[31] A. Corma, S. Iborra and A. Velty, "Chemical Routes for the Transformation of Biomass into Chemicals", *Chem. Rev.*, 2007, **107**, 2411–2502.

[32] J. N. Chheda, G. W. Huber and J. A. Dumesic, "Liquid-Phase Catalytic Processing of Biomass-Derived Oxygenated Hydrocarbons to Fuels and Chemicals", *Angew. Chem. Int. Ed.*, 2007, **46**, 7164–7183.

[33] E. L. Kunkes, D. A. Simonetti, R. M. West, J. C. Serrano-Ruiz, C. A. Gärtner and J. A. Dumesic, "Catalytic Conversion of Biomass to Monofunctional Hydrocarbons and Targeted Liquid-Fuel Classes", *Science*, 2008, **322**, 417–421.

[34] C. M. Friend and B. Xu, "Heterogeneous Catalysis: A Central Science for a Sustainable Future", *Acc. Chem. Res.*, 2017, **50**, 517–521.

[35] P. Gallezot, "Conversion of Biomass to Selected Chemical Products", *Chem. Soc. Rev.*, 2012, **41**, 1538–1558.

[36] K. Wilson and A. F. Lee, "Catalyst Design for Biorefining", *Phil. Trans. R. Soc. A*, 2016, **374**, 20150081.

[37] D. E. Resasco, B. Wang and D. Sabatini, "Distributed Processes for Biomass Conversion Could Aid UN Sustainable Development Goals", *Nature Catalysis*, 2018, **1**, 731–735.

[38] B. M. Murphy and B. Xu, "Foundational Techniques for Catalyst Design in the Upgrading of Biomass-Derived Multifunctional Molecules", *Prog. Energy Combust. Sci.*, 2018, **67**, 1–30.

[39] U. K. Singh and M. A. Vannice, "Kinetics of Liquid-Phase Hydrogenation Reactions over Supported Metal Catalysts — a Review", *Appl. Catal., A*, 2001, **213**, 1–24.

[40] S. Mukherjee and M. A. Vannice, "Solvent Effects in Liquid-Phase Reactions: I. Activity and Selectivity during Citral Hydrogenation on Pt/SiO2 and Evaluation of Mass Transfer Effects", *J. Catal.*, 2006, **243**, 108–130.

[41] S. Mukherjee and M. A. Vannice, "Solvent Effects in Liquid-Phase Reactions II. Kinetic Modeling for Citral Hydrogenation", *J. Catal.*, 2006, **243**, 131–148.

[42] J.-M. Andanson and A. Baiker, "Exploring Catalytic Solid/Liquid Interfaces by in Situ Attenuated Total Reflection Infrared Spectroscopy", *Chem. Soc. Rev.*, 2010, **39**, 4571–4584.

[43] F. Zaera, "Infrared and Molecular Beam Studies of Chemical Reactions on Solid Surfaces", *Int. Rev. Phys. Chem.*, 2002, **21**, 433–471.

[44] F. Zaera, "Probing Liquid/Solid Interfaces at the Molecular Level", *Chem. Rev.*, 2012, **112**, 2920–2986.

[45] C. D. Bain, "Studies of Adsorption at Interfaces by Optical Techniques: Ellipsometry, Second Harmonic Generation and Sum-Frequency Generation", *Curr. Opin. Colloid Interface Sci.*, 1998, **3**, 287–292.

[46] C. T. Williams and D. A. Beattie, "Probing Buried Interfaces with Non-Linear Optical Spectroscopy", *Surf. Sci.*, 2002, **500**, 545–576.

[47] J.-D. Grunwaldt, M. Ramin, M. Rohr, A. Michailovski, G. R. Patzke and A. Baiker, "High Pressure in Situ X-Ray Absorption Spectroscopy Cell for Studying Simultaneously the Liquid Phase and the Solid/Liquid Interface", *Rev. Sci. Instrum.*, 2005, **76**, 054104.

[48] S. Erokhina, T. Berzina, L. Cristofolini, V. Erokhin, C. Folli, O. Konovalov, I.-G. Marino and M. P. Fontana, "X-Ray Reflectivity Measurements of Layer-by-Layer Films at the Solid/Liquid Interface", *Langmuir*, 2008, **24**, 12093–12096.

[49] W. A. Hamilton, "Conformation, Directed Self-Assembly and Engineered Modification: Some Recent near Surface Structure Determinations by Grazing Incidence Small Angle X-Ray and Neutron Scattering", *Curr. Opin. Colloid Interface Sci.*, 2005, **9**, 390–395.

[50] R. J. L. Welbourn and S. M. Clarke, "New Insights into the Solid–Liquid Interface Exploiting Neutron Reflectivity", *Curr. Opin. Colloid Interface Sci.*, 2019, **42**, 87–98.

[51] S. Nouhi, M. S. Hellsing, V. Kapaklis and A. R. Rennie, "Grazing-Incidence Small-Angle Neutron Scattering from Structures below an Interface", *J Appl Cryst*, 2017, **50**, 1066–1074.

[52] E. Hoinkis, "In Situ Small Angle Neutron Scattering Study of Benzene Adsorption in the Porous SiO2 Glass CPG-10-75", *Adv. Colloid Interface Sci.*, 1998, **76-77**, 39–55.

[53] D. A. King, "Thermal Desorption from Metal Surfaces: A Review", *Surf. Sci.*, 1975, **47**, 384–402.

Chapter 3

Principles and practice of nuclear magnetic resonance

3.1 Quantum mechanical origins of nuclear magnetism

The majority of nuclear isotopes possess an inherent form of angular momentum known as spin. The spin of a nucleus is defined by its internal structure; nuclei consist of protons and neutrons, which are themselves comprised from elementary particles called quarks and gluons. It is the spin-states of these elementary particles which define the angular momentum of protons and neutrons, [1] and in turn, the combination of these nucleons dictates the net spin angular momentum of a given nucleus. [2]

The magnitude of the nuclear spin angular momentum vector[1] $\mathbf{I} = (I_x, I_y, I_z)$ is quantised according to

$$|\mathbf{I}| = \hbar\sqrt{I(I+1)}, \tag{3.1}$$

where $\hbar = h/2\pi$ is the reduced form of Planck's constant and I is the nuclear spin quantum number, which may take integer or half-integer values. In analogy to classical electromagnetism the inherent sense of rotation associated with nuclear spin angular momentum results in the existence of a magnetic dipole moment $\boldsymbol{\mu}$ at the nucleus. Such a quantity is related to the spin angular momentum of the nucleus according to

$$\boldsymbol{\mu} = \gamma\mathbf{I}, \tag{3.2}$$

where γ is the gyromagnetic ratio.[2] Each nucleus with $I > 0$ has a characteristic value of γ, while $I = 0$ nuclei are magnetically inactive.

For a projection of $\mathbf{I}$ in an arbitrarily chosen direction (conventionally the z-direction), nuclear spin angular momentum may be described by

$$\mu_z = \gamma I_z, \tag{3.3}$$

[1] Throughout this thesis we will employ the mathematical convention that $(a, b, c) = a\hat{\mathbf{i}} + b\hat{\mathbf{j}} + c\hat{\mathbf{k}}$, where $\hat{\mathbf{i}}$, $\hat{\mathbf{j}}$ and $\hat{\mathbf{k}}$ are unit vectors in the x, y and z directions.

[2] More correctly, γ is the magnetogyric ratio, although the term gyromagnetic ratio is the common convention.

where

$$I_z = \hbar m_I. \tag{3.4}$$

Here, the quantity m_I is the magnetic quantum number and takes values $I, I-1, I-2, ..., -I$ such that the possible number of individual m_I values is $2I+1$. This thesis deals exclusively with the analysis of ^{1}H (proton) magnetic resonance experiments, for which $I = \frac{1}{2}$ and $\gamma = 267.522 \times 10^6$ rad s^{-1} T^{-1}. ^{1}H therefore has $|\mathbf{I}| = \frac{\sqrt{3}}{2}\hbar$ and two spin-states characterised by $m_I \pm \frac{1}{2}$, known conventionally as α and β states.

3.2 Nuclear spins in a magnetic field

3.2.1 The nuclear Zeeman interaction

In the absence of an external magnetic field the energies of the two ^{1}H spin-states are degenerate; however, the application of a static magnetic field $\mathbf{B}_0$ removes this degeneracy. The energy of a nucleus within such a field is primarily defined by its magnetic moment,

$$E_z = -\boldsymbol{\mu} \cdot \mathbf{B}_0, \tag{3.5}$$

where E_z is the energy for the nuclear Zeeman interaction. For a field of magnitude $|\mathbf{B}_0| = B_0$ it follows that

$$E_z = -\mu_z B_0 \cos(\theta) = -\hbar m_I \gamma B_0 \cos(\theta). \tag{3.6}$$

Here, θ defines the angle between μ_z and $\mathbf{B}_0$, such that if $\mathbf{B}_0 = (0, 0, B_z)$ the energy of the Zeeman interaction is

$$E_z = -\mu_z B_0 = -\hbar m_I \gamma B_0. \tag{3.7}$$

For $I = \frac{1}{2}$ spins this leads to the formation of $2I+1 = 2$ energy levels, as summarised in Figure 3.1a. These are the spin-up (α; $m_I = +\frac{1}{2}$) state, where μ_z is parallel to B_0,

$$E_z^{\alpha} = -\frac{1}{2}\hbar\gamma B_0, \tag{3.8}$$

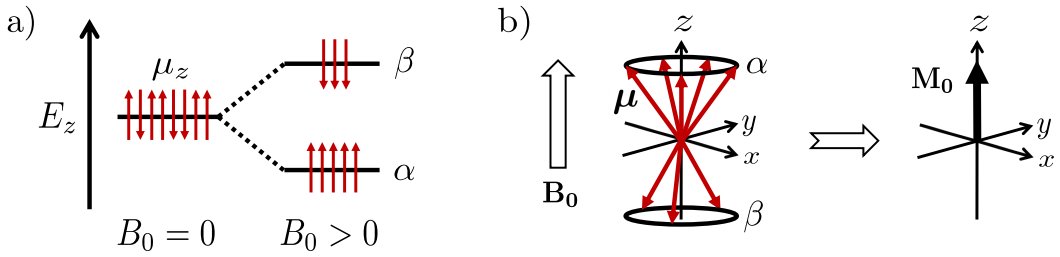

Figure 3.1: a) Nuclear Zeeman splitting of $I = \frac{1}{2}$ nuclei, such as ^{1}H. The application of a static magnetic field of magnitude $B_0 > 0$ removes the degeneracy of α and β states. The populations of the two states is described by a Boltzmann distribution and leads to an excess of α spins. b) Illustration of the Bloch vector model. The excess of magnetic moments $\boldsymbol{\mu}$ (red) with z-components parallel to $\mathbf{B_0}$ leads to a net polarisation of the spin ensemble, represented by the equilibrium magnetisation vector $\mathbf{M_0}$ (black).

and the spin-down (β; $m_I = -\frac{1}{2}$) state, where μ_z and B_0 are antiparallel,

$$E_z^{\beta} = \frac{1}{2}\hbar\gamma B_0. \tag{3.9}$$

Under thermal equilibrium the populations of the two spin states are described by a Boltzmann distribution of the form

$$\frac{N_\beta}{N_\alpha} = \exp\left(\frac{-\Delta E_z}{k_B T}\right). \tag{3.10}$$

Here N_α and N_β are the number of spins in α and β states, respectively, k_B is the Boltzmann constant and T is the absolute temperature. The difference in Zeeman energy ΔE_z between spin-up and spin-down states is

$$\Delta E_z = E_z^{\beta} - E_z^{\alpha} = \hbar\gamma B_0. \tag{3.11}$$

At typical experimental temperatures a small excess of spins is found in the low energy α state, leading to an overall polarisation of the sample along the direction of the static magnetic field. As a result, an ensemble of uncoupled $I = \frac{1}{2}$ nuclear spins may be described by a semi-classical vector model in which the bulk magnetisation vector $\mathbf{M} = (M_x, M_y, M_z)$ describes the macroscopic magnetisation of a spin ensemble, $\mathbf{M} = \int \boldsymbol{\mu}\, dV$. This vectoral representation is commonly described at the Bloch vector model. Under the conditions of thermal equilibrium $\mathbf{M}$ is equal to the equilibrium bulk magnetisation $\mathbf{M_0}$ (Figure 3.1b), which for N nuclear spins

is described by Curie's law, [3]

$$\mathbf{M_0} = \mathbf{B_0}\frac{N\gamma^2\hbar^2 I(I+1)}{3k_B T}. \tag{3.12}$$

3.2.2 Larmor precession

A fundamental property of the above spin system is the presence of a microscopic torque exerted onto each magnetic moment by the static magnetic field, resulting in the precession of $\boldsymbol{\mu}$ about $\mathbf{B_0}$. This process may be described by

$$\frac{d\boldsymbol{\mu}}{dt} = \boldsymbol{\mu} \times \gamma\mathbf{B_0}, \tag{3.13}$$

and is illustrated in Figure 3.2a. If the bulk magnetisation vector $\mathbf{M}$ is tipped away from equilibrium then a macroscopic precessional motion of the form

$$\frac{d\mathbf{M}}{dt} = \mathbf{M} \times \gamma\mathbf{B_0} \tag{3.14}$$

is also observed; this expression in known as the Bloch Equation. In both cases, the rate of precession is given by the angular frequency $\omega_0 = -\gamma B_0$ (units of $\mathrm{rad\,s^{-1}}$), known as the Larmor frequency.[3] Through use of the Planck-Einstein relation $E = \hbar\omega$, it is clear from examination of Equation 3.11 that ω_0 is the angular frequency of photons required to induce transitions between α and β Zeeman states. Indeed, irradiation of experimental samples with electromagnetic radiation of frequency[4] $\nu = \omega_0/(2\pi)$ (units of Hz or $\mathrm{s^{-1}}$) provides the fundamental basis of NMR experimentation.

3.3 Resonant excitation and the NMR experiment

3.3.1 Generation of the magnetic field

NMR experiments clearly require immersion of an experimental sample within a static magnetic field. In high-field experiments this field is generated by

[3]The negative sign defines the direction of precession about $\mathbf{B_0}$. For $\gamma > 0$ nuclei rotation is clockwise about $\mathbf{B_0}$ as illustrated in Figure 3.2. For $\gamma < 0$ nuclei rotation is anticlockwise.

[4]Linear and angular frequencies are used interchangeably in this thesis.

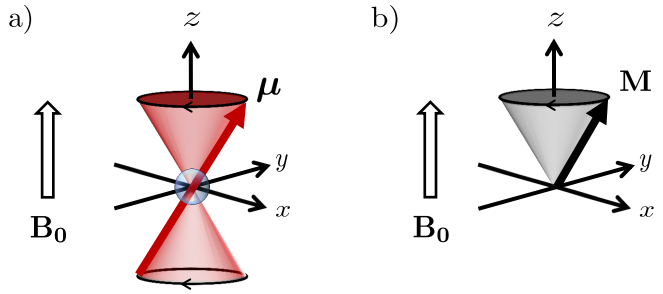

Figure 3.2: Illustration of Larmor precession as viewed from the laboratory frame of reference. a) Nuclear magnetic moments precess about $\mathbf{B_0}$ at the Larmor frequency $\omega_0 = -\gamma B_0$. In b) this same precession is shown for the macroscopic magnetisation vector $\mathbf{M}$, provided the bulk magnetisation has been tipped away from equilibrium through an external perturbation.

a superconducting solenoid coil maintained at a cryogenic temperatures using insulated baths of liquid N_2 and He (Figure 3.3a). [2] Such systems are ideal for high resolution NMR experiments where powerful, homogeneous magnetic fields are required. Experiments utilising lower magnetic field strengths – so-called low-field experiments – may be performed within an appropriately constructed array of permanent magnets, such as a cylindrical Halbach array; [4] an example of a simplified Halbach array is given in Figure 3.3b and involves the orientation of a series of permanent magnets so as to create a region of constant field, while the individual fields cancel outside of the active region. This concept is used in the 0.58 T benchtop imaging magnet shown in Figure 3.3c. The utilisation of low-field NMR apparatus can provide significant advantages over superconducting equipment, including compact and inexpensive magnet design, high portability, and removal of the requirement for expensive cryogenic liquids. [5]

3.3.2 Spin dynamics in the rotating frame of reference

At experimentally accessible magnetic field strengths ω_0 lies in the radio frequency (RF) part of the electromagnetic spectrum. RF irradiation is performed through a metallic coil which surrounds the sample. An electric current is passed through this coil and produces an oscillating magnetic field $\mathbf{B_1}$. This field is applied perpendicular to $\mathbf{B_0}$, and – although typically far weaker than the static field – may be used to manipulate the magnetisation vector away from equilibrium if set to oscillate near the Larmor frequency. [6]

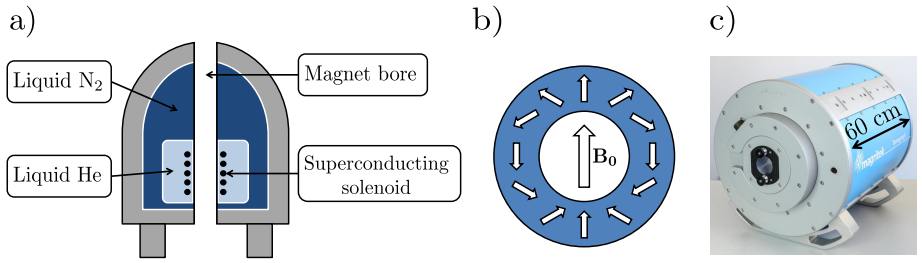

Figure 3.3: a) Illustration of a vertical-bore high-field magnet. A static magnetic field $\mathbf{B_0}$ is generated by a superconducting solenoid coil which is maintained at cryogenic temperatures through insulated baths of liquid N_2 and He. b) illustrates the concept of a cylindrical Halbach array involving a series of individual permanent magnets oriented in such a way as to cancel the magnetic field outside of the cylinder while maintaining a static magnetic field within the bore. The Magritek Tomograph imaging magnet shown in c) is a real-world example of a benchtop NMR magnet utilising a Halbach array of permanent magnets.

When considering the resonant behaviour of the magnetisation vector it is appropriate to move away from the laboratory (or stationary) frame of reference, and instead work from a rotating frame of reference in which the transverse axes rotate about z at some frequency ω_r. Axes rotating at this frequency are denoted by a prime.[5] An important concept in working from this frame of reference is to recognise that the application of a linearly oscillating magnetic field $\mathbf{B_1}$ applied along the x-axis may be interpreted as the vector-sum of two counter-rotating fields $\mathbf{B_{1+}}$ and $\mathbf{B_{1-}}$. If the rate of oscillation is ω_1 (the RF transmitter frequency) and we set $\omega_r = \omega_1$, then from the rotating frame of reference one counter-rotating component will be observed to be stationary while the other will rotate at $2\omega_1$; this second component is consider too rapid to be of significance in the following discussion and is no-longer considered. We will choose the directions of rotation such that $\mathbf{B_{1-}}$ is observed to be stationary and applied along x'.

As will be described below, the application of $\mathbf{B_1}$ has the effect of tipping the magnetisation vector away from equilibrium by some angle β, such that when observed in the laboratory frame of reference $\mathbf{M}$ precesses about the magnetic field at ω_0. This resonant behaviour is illustrated in Figure 3.2b. However, from the

[5]Although the z-axis must also precess at ω_r within the rotating frame of reference, as the rotation is about z it is clear that $z \equiv z'$. This axis therefore remains stationary as indicated in Figure 3.4.

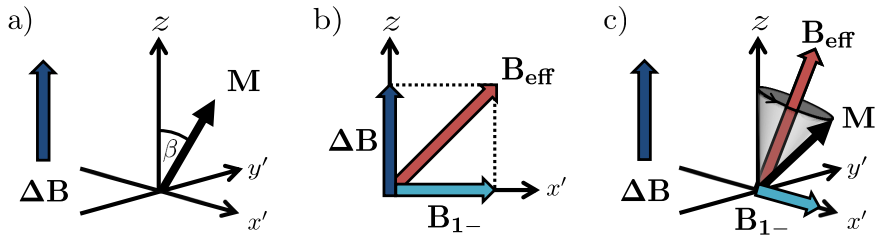

Figure 3.4: a) Precession of the bulk magnetisation vector $\mathbf{M}$ as viewed from the rotating frame of reference. b) Representation of the effective field $\mathbf{B_{eff}}$ which is the vector sum of the reduced and applied fields, $\mathbf{\Delta B}$ and $\mathbf{B_{1-}}$. These lie in the longitudinal and transverse planes, respectively, when observed from the rotating frame of reference. During the application of a RF pulse this results in precession of $\mathbf{M}$ about $\mathbf{B_{eff}}$, as illustrated in c).

rotating frame the resonant frequency will now appear as

$$\Omega = \omega_0 - \omega_r. \tag{3.15}$$

The reduced frequency Ω is called the offset and defines the magnitude of the reduced field,

$$\Delta B = -\frac{\Omega}{\gamma}, \tag{3.16}$$

which replaces the static magnetic field $\mathbf{B_0}$ in the rotating frame of reference; this concept is illustrated in Figure 3.4a.

During the application of $\mathbf{B_1}$ the bulk magnetisation vector experiences an effective field $\mathbf{B_{eff}}$, which is given by the vector sum of $\mathbf{\Delta B}$ and $\mathbf{B_{1-}}$ fields (Figure 3.4b). If ω_1 is then set to the Larmor frequency, such that $\omega_r = \omega_1 = \omega_0$, the so-called on-resonance condition is achieved and $\Omega = 0$. The effective field is therefore given by $\mathbf{B_{1-}}$ rather than $\mathbf{B_0}$. As a result, provided the transmitter frequency is resonant with the Larmor frequency, a small, oscillating $\mathbf{B_1}$ field may be used to dominate the precessional motion of the magnetisation vector, despite being very much weaker than the static magnetic field.

The bulk magnetisation vector precesses about the effective field at $\omega_{eff} = \gamma B_{eff}$. This concept is shown in Figure 3.4c and may be used to control the orientation of $\mathbf{M}$ with well-defined RF pulses. Starting from thermal equilibrium, the application of a RF pulse set to apply $\mathbf{B_{1-}}$ along x' results in rotation of the magnetisation vector through the zy' plane by a flip angle, β. The pulse length t_β

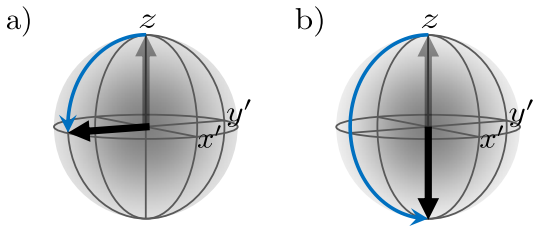

Figure 3.5: Magnetisation sphere representation of a) 90° and b) 180° flip angles, as induced through the application of RF pulses about the $+x$ axis, starting from equilibrium magnetisation. A 90°_x RF pulse rotates the sample magnetisation about x' and into the transverse plane, while a 180°_x RF pulse fully inverts the magnetisation, so that it aligns with $-z$.

relates to the flip angle according to

$$\beta = \omega_1 t_\beta. \tag{3.17}$$

Most common to NMR experiments are 90° (or $\pi/2$ rad) and 180° (or π rad) pulses, for which the pulse lengths t_{90} and t_{180} must be carefully calibrated. Typical t_{90} times are in the range of a few μs, with $t_{180} = 2t_{90}$. The influence of 90° and 180° RF pulses on the bulk magnetisation is described in Figure 3.5 using the magnetisation sphere representation. During a 90°_x pulse the magnetisation vector is rotated about the $+x'$ axis until it aligns with $-y'$. This has the effect of transferring the sample magnetisation from equilibrium into the transverse plane; as we will see below, the presence of transverse magnetisation is essential in order to detect a signal in NMR experiments. A 180°_x pulse applied under the same conditions will rotate the magnetisation vector through the transverse plane and onto the $-z$ axis; the magnetisation therefore remains in the longitudinal direction after such a pulse but is no-longer at equilibrium.

Rotations about other axes are made possible by altering the phase of the RF pulse ϕ_{rf}. This processes is performed by the NMR spectrometer circuitry and allows complete control of the magnetisation within a sample. If the RF transmitter wave evolves as $B_1 \cos(\omega_1 t + \phi_{rf})$, where $B_1 = |\mathbf{B_1}| = 2|\mathbf{B_{1\pm}}|$, then the axis about which rotation occurs follows Table 3.1. [2]

Table 3.1: Pulse phases ϕ_{rf} of the RF transmitter wave and the corresponding axes of rotation within the rotating frame of reference. Adapted from Levitt [2].

ϕ_{rf}	Axis of rotation
0	x'
$\pi/2$	y'
π	$-x'$
$3\pi/2$	$-y'$

3.3.3 Signal detection

Precession of the magnetisation vector is detected by surrounding the sample with a metallic coil. It is common to use the same coil as the one used to apply RF pulses, which is aligned in the transverse plane; for example, along the x axis. Following resonant excitation of the sample (for example, with a 90°_x RF pulse), $\mathbf{M}$ precesses in the transverse plane at ω_0. This transverse precession cuts the surrounding coil, imparting an electromotive force which causes a voltage. Following amplification, this voltage may be interpreted by the spectrometer, and when converted from its raw analogue form through analogue-to-digital processing, provides the digital NMR signal. It is pertinent to note, however, that typical values of ω_0 (up to several hundred MHz) are far too rapid to be processed by modern analogue-to-digital converters. The observed signal must therefore be down-converted to more manageable frequencies in order to be processed. This is performed by a mixing and filtering process which compares the observed Larmor frequency with that of the RF transmitter; this down-conversion process is therefore equivalent to observing the offset frequency from the rotating frame of reference. As the offset is typically set to far lower frequencies than ω_0 the resulting data may be readily interpreted by the spectrometer electronics and then up-converted back to the actual observed frequency.

The detected time domain signal $S(t)$, whose magnitude is directly proportional to that of the transverse magnetisation, therefore has the general form

$$S(t) \sim S_0 \cos(\Omega t) \exp(-\lambda t), \tag{3.18}$$

where $|S_0|$ defines the intensity of the acquired signal immediately following RF

excitation. The damping term $\exp(-\lambda t)$ represents relaxation of the nuclear spin magnetisation after excitation and will be discussed further in Section 3.5.

The final process we should note here is that of quadrature detection. Equation 3.18 cannot distinguish between positive and negative offsets. [6] We will see below in Section 3.4 that this is required to apply NMR as a structurally sensitive spectroscopy. To do this, the acquired signal must be split into two; during mixing with the transmitter frequency one component is then phase-shifted by 90°, such that two signals of the form

$$S_x(t) = S_0 \cos(\Omega t) \exp(-\lambda t), \tag{3.19}$$

$$S_y(t) = S_0 \sin(\Omega t) \exp(-\lambda t), \tag{3.20}$$

are generated. These are the real and imaginary parts of the complex NMR signal,

$$S(t) = S_x(t) + iS_y(t) \tag{3.21a}$$

$$= S_0 \cos(\Omega t) \exp(-\lambda t) + iS_0 \sin(\Omega t) \exp(-\lambda t) \tag{3.21b}$$

$$= S_0 \underbrace{\exp(i\Omega t)}_{\text{oscillation}} \underbrace{\exp(-\lambda t)}_{\text{decay}}, \tag{3.21c}$$

and allow direct interpretation of both positive and negative offsets. $S(t)$ is known as the free-induction decay (FID). Clearly from Equation 3.21c the FID for off-resonance Larmor precession ($\Omega \neq 0$) takes the form of a complex, exponentially-damped signal which oscillates at Ω. The FID for on-resonance Larmor precession ($\Omega = 0$) is an exponential decay which follows the envelope of this oscillation. For a system consisting of j signals of intensity $|S_{0j}|$, $S(t)$ takes the form

$$S(t) = \sum_j S_j(t), \tag{3.22}$$

where

$$S_j(t) = S_{0j} \exp(i\Omega_j t) \exp(\lambda_j t). \tag{3.23}$$

These signal forms are illustrated in Figure 3.6.

3.4 NMR spectroscopy

The phenomena of nuclear magnetic resonance is perhaps the most important spectroscopic tool avaliable for chemical structure determination. As we have seen above, magnetically active nuclear spins immersed in a static magnetic field can be forced to emit a resonant signal which oscillates in the time domain as $S(t) \sim \sum_j \exp(i\Omega_j t)$. While the resonant frequency of a particular nuclear spin environment is dominated by the Zeeman interaction, localised interactions which arise between the field and the molecular structure surrounding each nucleus result in structure-dependent resonances. We will see below that the different resonances Ω_j arising from these interactions provide detailed information on the population and connectivity of magnetically inequivalent chemical environments. To better access and interpret this information. however, it is important to move from the time domain to the frequency domain.

3.4.1 Data processing

Conversion of the time domain signal $S(t)$ to the frequency domain signal $S(\Omega)$ is performed through Fourier transformation of the FID according to

$$S(\Omega) = \int_{-\infty}^{\infty} S(t) \exp(-i\Omega t) dt. \tag{3.24}$$

The relationship between time and frequency response signals is illustrated in Figure 3.6. Following Equation 3.23 the frequency signals for the individual components j are

$$S_j(\Omega) = S_{0j} \int_{-\infty}^{\infty} S_j(t) \exp(-i\Omega t) \exp(i\Omega_j t) \exp(-\lambda_j t) dt, \tag{3.25}$$

with solutions $S_j(\Omega) = S_{0j}\mathcal{L}_j$. Here $\mathcal{L}_j = \mathrm{Re}\{\mathcal{L}_j\} + i\mathrm{Im}\{\mathcal{L}_j\}$ are complex Lorentzian functions with real and imaginary components [2]

$$\mathrm{Re}\{\mathcal{L}_j\} = \frac{\lambda_j}{\lambda_j^2 + (\Omega - \Omega_j)^2} \tag{3.26}$$

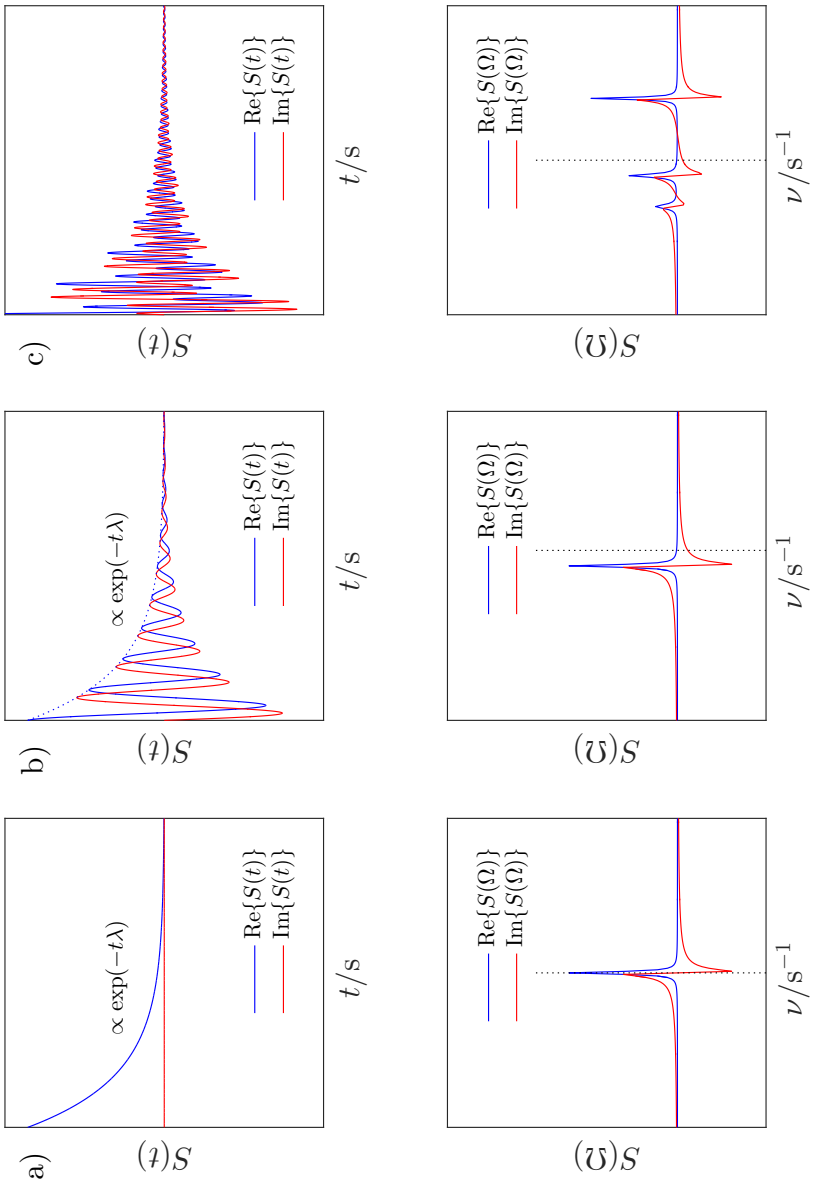

Figure 3.6: Simulated NMR signals. Top panels show the complex time domain response to a simple 90° RF excitation pulse; in each case the signal takes the form of a FID. Bottom panels show the frequency response signal obtained by the Fourier transform of each upper panel. Dotted vertical lines indicate the RF transmitter frequency. a) and b) therefore represent cases of on-resonance and off-resonance Larmor precession, respectively, while c) illustrates a multi-frequency response.

and

$$\mathrm{Im}\{\mathcal{L}_j\} = -\frac{\Omega - \Omega_j}{\lambda_j^2 + (\Omega - \Omega_j)^2}. \tag{3.27}$$

The lineshapes resulting from these components are known as the adsorption and dispersion Lorentzians, respectively.

Unfortunately we have no *a priori* knowledge of where the x- and y-axes lie within the spectrometer. It is therefore often the case that the acquired spectral data must be phase-corrected before it can be interpreted. This is equivalent to recognising that the signal amplitudes $S_{0j} = |S_{0j}| \exp(i\phi_{rec})$ are complex. The acquired frequency response data therefore has the typical form

$$S_j(\Omega) = |S_{0j}| \exp(i\phi_{rec})(\mathrm{Re}\{\mathcal{L}_j\} + i\mathrm{Im}\{\mathcal{L}_j\}), \tag{3.28}$$

where $\exp(i\phi_{rec})$ is the spectrometer receiver phase. If $\phi_{rec} \neq 0$ or 2π pure adsorption and dispersion lineshapes will not be obtained; rather, each will contain a combination of real and imaginary data. In general, the correct lineshapes may be recovered by multiplying $S_j(\Omega)$ by a correcting phase factor $\exp(i\phi_{corr})$, such that $\phi_{corr} = -\phi_{rec}$. The phase-corrected frequency data is therefore given by

$$S_j(\Omega)\exp(i\phi_{corr}) = |S_{0j}| \exp(i\{\phi_{rec} + \phi_{corr}\})(\mathrm{Re}\{\mathcal{L}_j\} + i\mathrm{Im}\{\mathcal{L}_j\}) \tag{3.29a}$$

$$= |S_{0j}|(\mathrm{Re}\{\mathcal{L}_j\} + i\mathrm{Im}\{\mathcal{L}_j\}). \tag{3.29b}$$

This is known as a zero-order phase correction. It is worth noting that a further frequency-dependent correction may also need to be applied in which the correcting phase varies linearly with frequency; this process is known as first-order phase correction.

Phase-corrected lineshapes are illustrated in Figure 3.6. It is the frequency domain adsorption lineshapes which are of interest in NMR spectroscopy; in particular, the positions of the peak maxima provide quantification of the resonance frequencies ν_j. Furthermore, lineshape integrals equal $\pi|S_{0j}|$ and are therefore proportional to the number of nuclei in the j^{th} environment. The full-width half-maximum of the j^{th} peak is λ_j/π.

3.4.2 Chemical shift

The term chemical shift describes the frequency shift experienced by magnetically active nuclei due to their surrounding electronic structure. This effect is slightly different for nuclei in different chemical environments; for example, ethanol presents three ^{1}H resonances indicative of the methyl ($-\mathrm{C}^1\mathrm{H}_3$), methylene ($-\mathrm{C}(^1\mathrm{H}_2)-$) and hydroxyl ($-\mathrm{O}^1\mathrm{H}$) environments of the molecule, with the ratio of the three adsorption lineshape integrals equal to 3:2:1. These differences in resonant frequency and peak area allow NMR spectroscopy to be applied as a powerful tool for structural analysis.

Specific chemical shift phenomena occur as a result of the interaction between the electron cloud of a molecule and the static magnetic field. This interaction causes circulating currents of electron density, which induces a small field $B_{induced}$ that opposes the static magnetic field. The magnitude of the local field B_{local} at the j^{th} nucleus is therefore

$$B_{local,j} = B_0 - B_{induced,j}. \tag{3.30}$$

Equation 3.30 provides the physical basis for the different resonant frequencies ν_j which might be observed in a given experiment. A fundamental property of the above effect is that the induced field is proportional to the magnitude of the static field, with the constant of proportionality known as the nuclear shielding constant σ,

$$B_{local,j} = B_0(1 - \sigma_j). \tag{3.31}$$

The ratio of the magnitudes of these fields and their corresponding resonant frequencies is therefore field-independent. A spectrometer-independent chemical shift δ describing the j^{th} nuclear environment in a given sample is typically expressed as

$$\delta_j = \frac{\nu_j - \nu_{ref}}{\nu_{ref}} \times 10^6, \tag{3.32}$$

where ν_{ref} is the resonant frequency of the same nuclear isotope within a reference compound, obtained at the same field strength as the chemically shifted frequency ν_j. In this thesis ν_{ref} is taken as the resonant signal obtained from an external

reference sample of neat tetramethyl silane (TMS). As δ_j values are typically very small, a 10^6 scaling is applied to make them more manageable. Although formally dimensionless, chemical shifts defined according to Equation 3.32 are therefore given in units of parts per million (ppm). Using the above formalism, typical chemical shifts obtained *via* ^{1}H NMR experimentation lie within the range $0 - 15$ ppm. [2]

3.4.3 J-coupling

As each magnetically active nucleus possesses a magnetic dipole moment $\boldsymbol{\mu}$, the local field at each nucleus is influenced by the presence of other nuclei nearby. Such interactions have the potential to affect the observed resonant frequencies obtained through NMR spectroscopy. J-coupling interactions occur as a result of the indirect dipole-dipole coupling of nuclei within the same molecule. Direct (or through-space) dipole-dipole interactions are orientationally dependent. In isotropically tumbling media such as liquids this interaction averages to zero and so has little affect on the resonant behaviour observed in NMR spectra. Indirect dipole-dipole interactions are also orientationally dependent, but do not average to zero in isotropically tumbling media. [2] The rotationally averaged interactions are known as scalar-couplings or J-couplings, and are mediated by the electronic structure of chemical bonds connecting magnetically inequivalent nuclei. For example, in the case of a scalar-coupled nuclear spin pair interacting *via* a filled molecular orbital, a slight polarisation of the electron spin density will occur in favour of parallel ^{1}H-electron spin pairing. [2] This energetic interaction – known as the Fermi contact mechanism – occurs due to the favourable antiparallel paring of electron and nuclear magnetic moments. As the gyromagnetic ratio of the electron is negative, this manifests itself as parallel spin pairing. The Fermi contact mechanism is illustrated in Figure 3.7.

In general form, the energy for weakly[6] scalar-coupled spins in a static magnetic field is given by [7]

$$E_{Z,J} = \underbrace{-h\sum_{j,k}\nu_j m_{I,j}}_{\text{Zeeman interaction}} \underbrace{+h\sum\sum_{j<k}J_{jk}m_{I,j}m_{I,k}}_{\text{scalar coupling}}, \tag{3.33}$$

where h is Planck's constant, ν_j and $m_{I,j}$ are the chemically-shifted frequency and magnetic quantum number of the j^{th} nucleus, respectively, and J_{jk} is the spin-spin coupling constant of the jk spin pair in s^{-1}, which may be positive or negative. As an example, for the simple system described in Figure 3.7 the observed resonances are given by transitions between the four possible $\alpha\beta$ spin combinations of the jk spin pair. Through the application of Equation 3.33 the four energy levels are

$$E_{Z,J}^{\alpha\alpha} = -\frac{1}{2}h\nu_j - \frac{1}{2}h\nu_k + \frac{1}{4}hJ_{jk} \tag{3.34}$$

$$E_{Z,J}^{\alpha\beta} = -\frac{1}{2}h\nu_j + \frac{1}{2}h\nu_k - \frac{1}{4}hJ_{jk} \tag{3.35}$$

$$E_{Z,J}^{\beta\alpha} = +\frac{1}{2}h\nu_j - \frac{1}{2}h\nu_k - \frac{1}{4}hJ_{jk} \tag{3.36}$$

$$E_{Z,J}^{\beta\beta} = +\frac{1}{2}h\nu_j + \frac{1}{2}h\nu_k + \frac{1}{4}hJ_{jk}. \tag{3.37}$$

The corresponding transition frequencies, which satisfy the single quantum spin-excitation selection rule $\sum m_I = \pm 1$, are shown in Figure 3.8. Clearly the observed resonant frequencies are split by $J \neq 0$ scalar coupling. In general, ^{1}H scalar coupling interactions between a given nuclear spin and N nuclei within a nearby magnetically inequivalent environment results in multiplet peak structures containing $N+1$ peaks.

[6]Weak scalar coupling is defined as $J \ll \Delta\nu_{jk}$, where $\Delta\nu_{jk}$ is the difference in the chemically-shifted frequencies exhibited by spins j and k.

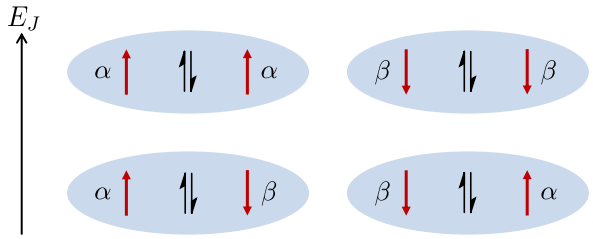

Figure 3.7: Illustration of the Fermi contact mechanism. Nuclear spins are represented by red doubled-headed arrows. Electron spins which populate the simple molecular orbital shown in blue are represented by black single-headed arrows and are paired according to the Pauli exclusion principle. The $\alpha\beta$ spin states of the nuclear spins are also indicated. Given that $\gamma > 0$ for ^{1}H but $\gamma < 0$ for the electron, parallel spin pairing leading to favourable antiparallel pairing of the nuclear and electronic magnetic moments. Adapted from Levitt [8].

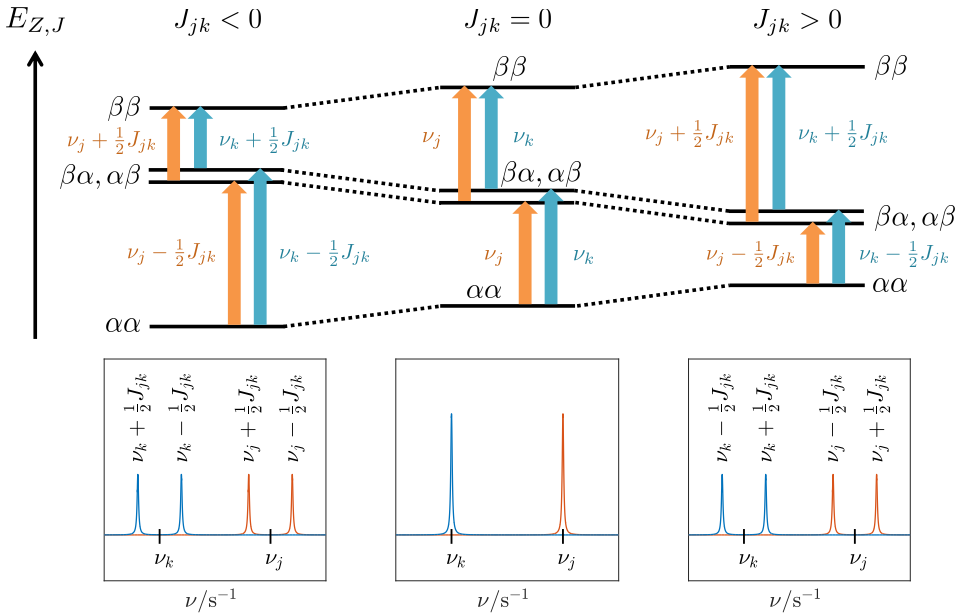

Figure 3.8: Energy level diagram for the magnetically inequivalent scalar-coupled ^{1}H spin pair jk. The resulting NMR spectra are shown below each set of transitions.

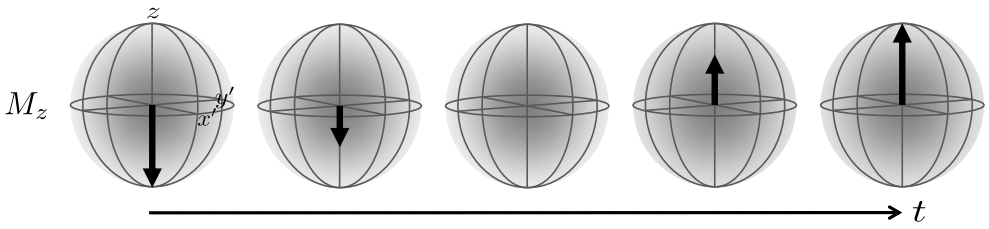

Figure 3.9: Magnetisation sphere illustration of longitudinal nuclear spin relaxation, which occurs on an exponential time frame according to Equation 3.39.

3.5 NMR relaxation

Following irradiation of a nuclear spin ensemble with a series of RF pulses, the magnetisation of the sample is no longer under the equilibrium conditions described in Figure 3.1. Return to this equilibrium occurs through a set of concurrent processes collectively known as nuclear spin relaxation. Importantly for our purposes, these relaxation processes are not instantaneous, and can provide important information on the microscopic dynamics occurring within the system under study. We may measure these processes through the application of relevant NMR pulse sequences designed to observe the sample magnetisation over time. The two dominant forms of nuclear spin relaxation are discussed below.

3.5.1 Longitudinal relaxation

Longitudinal (or spin-lattice) nuclear spin relaxation is the process by which the longitudinal component of the sample magnetisation M_z returns to thermal equilibrium with the surrounding molecular environment. [9] We will see below that this process is facilitated through the random thermal motion of the surrounding inter- and intramolecular environment, which results in locally fluctuating magnetic fields.

Within the Bloch vector model longitudinal relaxation processes occurs according to

$$\frac{dM_z}{dt} = -\frac{M_z - M_0}{T_1}, \tag{3.38}$$

where $M_0 = |\mathbf{M_0}|$ and T_1 is the spin-lattice relaxation time constant which characterises the rate of longitudinal relaxation $R_1 = 1/T_1$. Equation 3.38 has

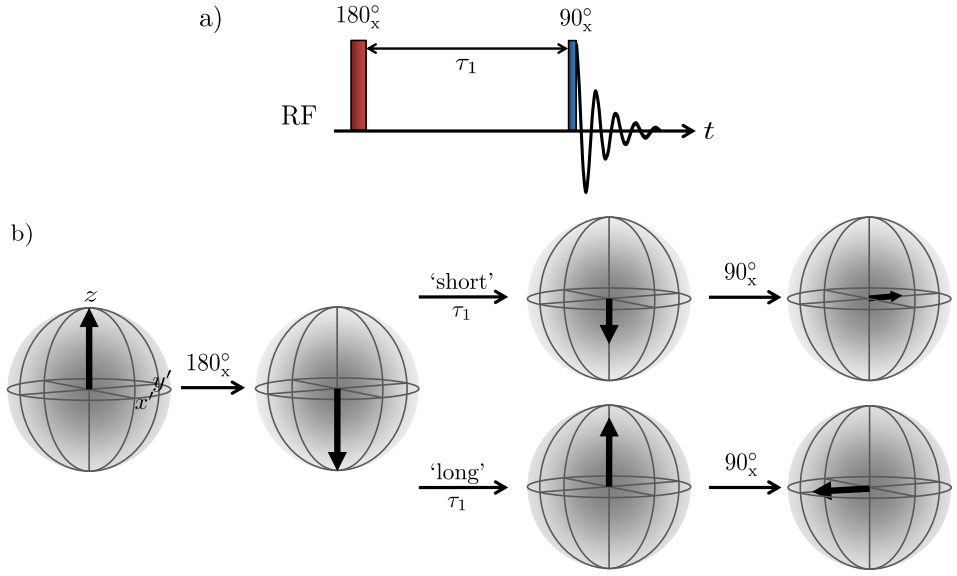

Figure 3.10: a) NMR pulse sequence for the inversion recovery method. Magnetisation sphere representations of the various stages in this sequence are depicted in b), where the specific cases of a 'short' and 'long' τ_1 time are emphasised. Clearly the phase of the resulting FID signals will differ by 180°.

the general solution

$$M_z(t) = M_z(0)\exp\left(\frac{-t}{T_1}\right) + M_0\left\{1 - \exp\left(\frac{-t}{T_1}\right)\right\}, \tag{3.39}$$

where $M_z(t)$ is the longitudinal magnetisation at time t.

The spin-lattice relaxation time constant T_1 is typically measured using the inversion recovery method.[10] The appropriate pulse sequence is illustrated in Figure 3.10a. Following initial polarisation of the spin ensemble by the static magnetic field a 180° pulse inverts the equilibrium of the spin system, placing the magnetisation vector onto the $-z$ axis. The system is then allowed to evolve for a time period τ_1, during which $\mathbf{M}$ relaxes longitudinally.[7] As no macroscopic precession occurs in the case of purely longitudinally bulk magnetisation a 90° pulse is then applied to flip $\mathbf{M}$ into the transverse plane. This allows transverse precession to occur which is detected as a FID.

The dynamics of the magnetisation vector during this pulse sequence are illustrated in Figure 3.10b. By repeating the pulse sequence for a number of τ_1 delays – typically varying in several orders of magnitude from $\sim$ 1 ms to $5T_1$ – a

[7]The subscript 1 will be used exclusively for time periods employed in the measurement of T_1.

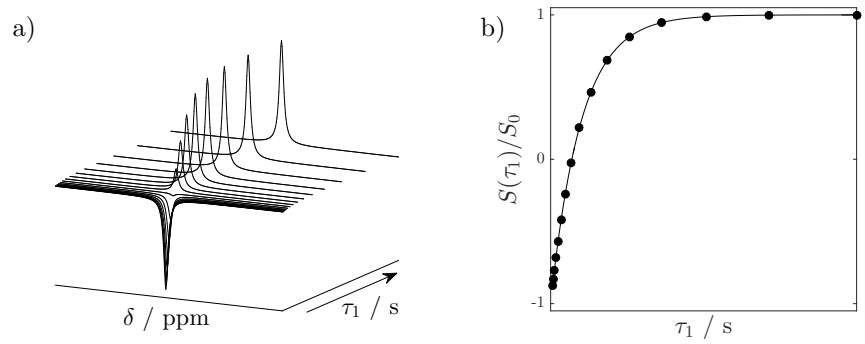

Figure 3.11: a) Simulated spectra obtained from a logarithmic range of τ_1 times during an inversion recovery experiment on a single resonant component. b) Illustration of the corresponding normalised signal intensities acquired through integration of the peaks shown in a). The solid line indicates a fit to the data according to Equation 3.40, which may be used to obtain the spin-lattice relaxation time constant T_1.

series of spectra are obtained as a function of τ_1 (Figure 3.11a). Recalling that the integral of a given peak is proportional to the signal intensity obtained from that spectral component, integration of the peaks of interest across the range of spectra obtained can be used to obtain their T_1 values. The 180° pulse which initiates longitudinal relaxation in the inversion recovery experiment sets the initial longitudinal magnetisation of the system to $M_z(0) = -M_0$. Evaluating Equation 3.39 with this initial condition means T_1 values may be obtained by fitting the acquired signal data to

$$\frac{S(\tau_1)}{S_0} = 1 - 2\exp\left(\frac{-\tau_1}{T_1}\right), \tag{3.40}$$

where $S_0 = S(\tau_1 \to \infty)$ is the signal obtained under thermal equilibrium. This value is approximated using the signal acquired from the longest τ_1 value employed, such that $S_0 = S(\tau_1 \sim 5T_1)$; the fitting process is illustrated in Figure 3.11b.

3.5.2 Transverse relaxation and the spin echo

Transverse or (or spin-spin) nuclear spin relaxation is the process by which the spins contained within a sample come into equilibrium between themselves. [9] While spin-lattice relaxation is an enthalpic process, requiring the redistribution of energy from the spin system into the surrounding environment, spin-spin relaxation is entropic in nature, and describes the irreversible loss of phase coherence exhibited by a spin ensemble over time. Figure 3.12 illustrates this dephasing process and the

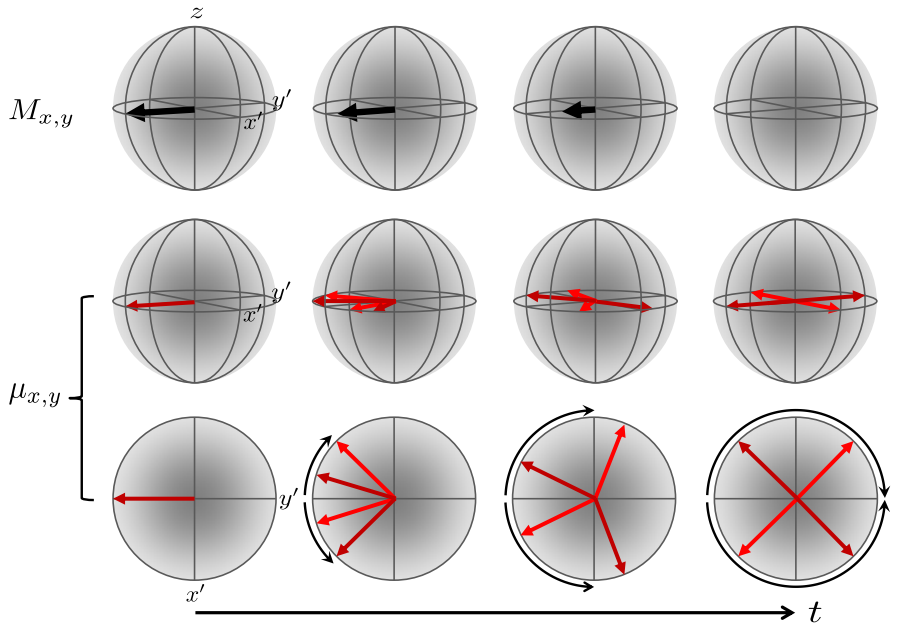

Figure 3.12: Illustration of transverse nuclear spin relaxation. As the transverse components of the individual spins dephase the transverse component of the bulk magnetisation is reduced. This process occurs on an exponential time frame according to Equation 3.42.

corresponding reduction of the transverse component of the magnetisation vector. Within the Bloch vector model this process occurs according to

$$\frac{dM_{x,y}}{dt} = -\frac{M_{x,y}}{T_2}, \tag{3.41}$$

where T_2 is the spin-spin relaxation time constant characterising the rate of transverse relaxation $R_2 = 1/T_2$. This time constant obeys the condition $T_2 \leq T_1$. Equation 3.41 has the general solution

$$M_{x,y}(t) = M_{x,y}(0) \exp\left(\frac{-t}{T_2}\right). \tag{3.42}$$

In analogy to spin-lattice relaxation, spin-spin relaxation rates are also sensitive to locally fluctuating fields which occur as a result of molecular motion. These time dependent fields alter the local field at each nucleus, in turn leading to a spread of Larmor frequencies across the sample. It is this range of precessional frequencies which causes this irreversible dephasing process illustrated in Figure 3.12, which is characterised by T_2.

In reality, the transverse magnetisation decays more rapidly than predicted by Equation 3.42. This occurs as a result of additional spin dephasing resulting from inhomogeneities in the static magnetic field ΔB_0. The observed relaxation rate $1/T_2^*$ is given by [11]

$$\frac{1}{T_2^*} = \frac{1}{T_2} + \frac{1}{T_2'}, \tag{3.43}$$

where $1/T_2' = \gamma \Delta B_0$. [12, 13] The transverse magnetisation therefore evolves as

$$M_{x,y}(t) = M_{x,y}(0) \exp\left(\frac{-t}{T_2^*}\right), \tag{3.44}$$

where $T_2^* \leq T_2$. It is important to note that this expression is equivalent to Equation 3.23. It follows that the damping constant λ used throughout Sections 3.3 and 3.4 is given by $1/T_2^*$. The envelope of the FID is then $\exp(-t/T_2^*)$, while the full-width half-maximum of the j^{th} spectral peak is $1/\pi T_{2,j}^*$. The presence of field inhomogeneities therefore results in additional peak broadening (inhomogeneous line broadening) which is separate to that caused by the inherent T_2 of the spin environment (homogeneous line broadening).

The spin-spin relaxation time constant T_2 is measured by utilising the concept of the spin-echo. [14] This approach is particularly useful as it allows us to separate T_2 dephasing from the observed T_2^* behaviour. Hahn first discovered the spin echo after observing that a pair of 90° pulses separated by a dephasing period led to a partial refocussing of the dephased magnetisation.[13] The resultant signal is known as an echo and takes the form of a *sinc* function $S(t) \sim \sin(t)/t$, the latter half of which may be Fourier transformed in analogy to a FID.

To fully appreciate the spin dynamics involved in the formation of a spin echo we must move from the semi-classical Bloch vector model to a quantum mechanical perspective known as the density operator formalism. [15] This approach considers the dynamics of the density operator $\sigma(t)$ through the course of given NMR pulse sequence. The density operator is simply an expression of the sample magnetisation over time; for an uncoupled $I = \frac{1}{2}$ nucleus such as ^{1}H it is given by [6]

$$\sigma(t) = a(t)I_x + b(t)I_y + c(t)I_z, \tag{3.45}$$

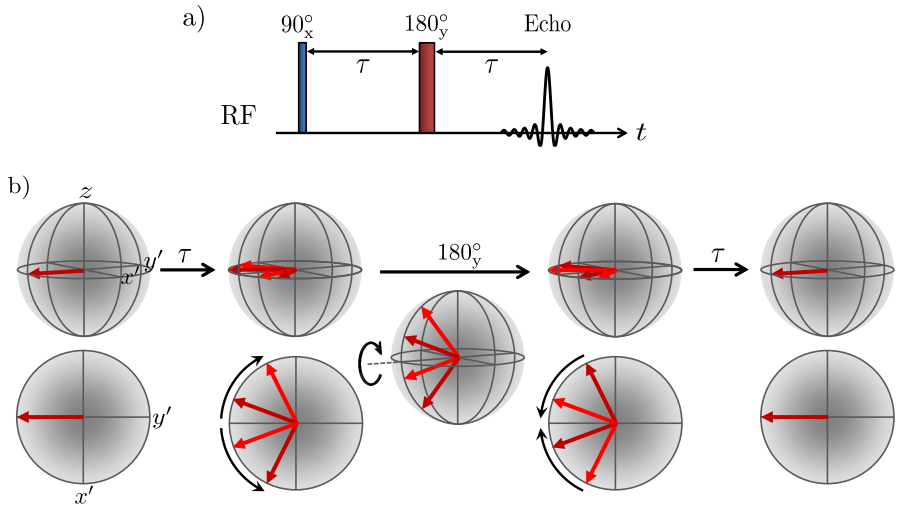

Figure 3.13: a) NMR pulse sequence for the spin echo. The 180° pulse refocusses the offset, forming an echo with maximum amplitude at time $t = 2\tau + t_{180}$ after RF excitation. b) Magnetisation sphere illustration of the formation of a spin echo.

where we recall I_x, I_y and I_z are operators representing the cartesian components of the spin angular momentum vector $\mathbf{I}$, and a, b and c are constants of proportionality which vary throughout a given pulse sequence. $\sigma(t)$ is calculated according to the Heisenberg equation of motion,

$$\sigma(t) = \exp(-i\mathcal{A}t)\sigma(0)\exp(i\mathcal{A}t), \tag{3.46}$$

where $\sigma(0)$ characterises the initial magnetisation and $\mathcal{A}$ is the relevant angular momentum operator representing the actions of the chosen pulse sequence: for a lone, uncoupled spin system $\mathcal{A} = \Omega I_z$ for free precession, while $\mathcal{A} = \omega_1 I_i$ represents a RF pulse set to perform a rotation about the axis i.

The modern spin echo follows the pulse sequence in Figure 3.13a. As the initial magnetisation is at thermal equilibrium we may set $\sigma(0) = I_z$. The first pulse is then

$$\sigma(t_{90}) = \exp(-i\omega_1 t I_x)I_z\exp(i\omega_1 t I_x), \tag{3.47}$$

which may be rewritten in terms of the flip angle $\beta = \omega_1 t_\beta$ as

$$\sigma(t_{90}) = \exp(-i\beta I_x)I_z\exp(i\beta I_x). \tag{3.48}$$

This expression is interpreted as a rotation from I_z about I_x by β, and may be solved with reference to well known trigonometric identities[8] such that

$$\sigma(t_{90}) = I_z \cos(\beta) - I_y \sin(\beta). \tag{3.49}$$

In the case of a 90° pulse $\beta = \pi/2$ and the expression simplifies to $\sigma(t) = -I_y$, which is exactly the result obtained from the Bloch vector model (see Figure 3.5a). The spin system is then allowed to precess for a dephasing period τ,

$$\sigma(t_{90} + \tau) = \exp(-i\Omega\tau I_z)\{-I_y\}\exp(i\Omega\tau I_z) \tag{3.50a}$$

$$= I_x \sin(\Omega\tau) - I_y \cos(\Omega\tau). \tag{3.50b}$$

This is followed by a 180°_y pulse,

$$\sigma(t_{90} + \tau + t_{180}) = \exp\big(-i\beta' I_y\big)\{I_x \sin(\Omega\tau) - I_y \cos(\Omega\tau)\}\exp\big(i\beta' I_y\big), \tag{3.51}$$

where $\beta' = \pi$. Here the sine and cosine components must be treated separately. As I_i is unaffected by rotations about I_i the cosine component $-I_y \cos(\Omega\tau)$ remains unaffected by this pulse,

$$\sigma(t_{90} + \tau + t_{180}) = \exp\big(-i\beta' I_y\big)\{-I_y \cos(\Omega\tau)\}\exp\big(i\beta' I_y\big) \tag{3.52a}$$

$$= -I_y \cos(\Omega\tau). \tag{3.52b}$$

Evolution of the sine component follows

$$\sigma(t_{90} + \tau + t_{180}) = \exp\big(-i\beta' I_y\big)\{I_x \sin(\Omega\tau)\}\exp\big(i\beta' I_y\big) \tag{3.53a}$$

$$= I_x \sin(\Omega\tau)\cos\big(\beta'\big) - I_z \sin(\Omega\tau)\sin\big(\beta'\big) \tag{3.53b}$$

$$= -I_x \sin(\Omega\tau), \tag{3.53c}$$

[8] The relevant identities are given in Appendix B and are taken from Keeler [6].

such that the overall evolution to this point is

$$\sigma(t_{90} + \tau + t_{180}) = -I_x \sin(\Omega\tau) - I_y \cos(\Omega\tau). \tag{3.54}$$

This is then followed by a second τ period,

$$\sigma(t_{90} + t_{180} + 2\tau) = \exp(-i\Omega\tau I_z)\{-I_y \cos(\Omega\tau) - I_x \sin(\Omega\tau)\} \exp(i\Omega\tau I_z). \tag{3.55}$$

The cosine component evolves as

$$\begin{aligned} \sigma(t_{90} + t_{180} + 2\tau) &= \exp(-i\Omega\tau I_z)\{-I_y \cos(\Omega\tau)\} \exp(-\Omega\tau I_z) && \text{(3.56a)} \\ &= I_x \cos(\Omega\tau) \sin(\Omega\tau) - I_y \cos(\Omega\tau) \cos(\Omega\tau), && \text{(3.56b)} \end{aligned}$$

while the sine component evolves as

$$\begin{aligned} \sigma(t_{90} + t_{180} + 2\tau) &= \exp(-i\Omega\tau I_z)\{-I_x \sin(\Omega\tau)\} \exp(-\Omega\tau I_z) && \text{(3.57a)} \\ &= -I_x \sin(\Omega\tau) \cos(\Omega\tau) - I_y \sin(\Omega\tau) \sin(\Omega\tau). && \text{(3.57b)} \end{aligned}$$

The overall evolution is therefore

$$\begin{aligned} \sigma(t_{90} + t_{180} + 2\tau) &= I_x\{\cos(\Omega\tau) \sin(\Omega\tau) - \cos(\Omega\tau) \sin(\Omega\tau)\} && \text{(3.58a)} \\ &\quad - I_y\{\cos(\Omega\tau) \cos(\Omega\tau) + \sin(\Omega\tau) \sin(\Omega\tau)\} && \text{(3.58b)} \\ &= -I_y, && \text{(3.58c)} \end{aligned}$$

which illustrates the ability of the spin echo to refocus the offset Ω at $-I_y$, irrespective of the length of the dephasing period τ. This process is illustrated classically in Figure 3.13b

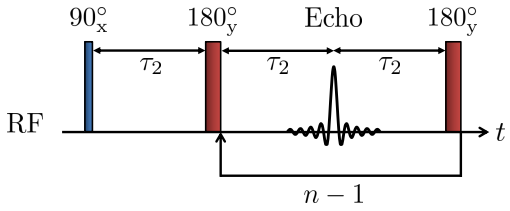

Figure 3.14: NMR pulse sequence for the CPMG experiment utilised to measure T_2. Following initial excitation of the spin system by a 90° RF pulse a train of n refocussing pulses leads to n echoes separated by a spin echo time of $t_e = 2\tau_2$

The above series of expressions may be written more succinctly using the standard density operator shorthand, [6, 14]

$$\begin{aligned} I_z &\xrightarrow{(\pi/2)I_x} -I_y \\ &\xrightarrow{\Omega\tau I_z} I_x \sin(\Omega\tau) - I_y \cos(\Omega\tau) \\ &\xrightarrow{\pi I_y} -I_x \sin(\Omega\tau) - I_y \cos(\Omega\tau) \\ &\xrightarrow{\Omega\tau I_z} -I_y. \end{aligned} \tag{3.59}$$

Here, the relevant operators, multiplied by the time for which they operate, are stated above the arrow representing each stage of the pulse sequence. Importantly, Equation 3.59 is also valid in the case of a distribution of offsets, such as that found in the presence of inhomogeneous line broadening. It follows that while T_2 relaxation is an irreversible process, $T_2^{'}$ dephasing is not, and may be reversed by the spin echo. This concept is regularly extended to the measurement of T_2 values through the application of the CPMG (Carr-Purcell-Meiboom-Gill) pulse sequence shown in Figure 3.14. [12, 16] Here the sample magnetisation is rotated into the transverse plane where it experiences T_2^* relaxation. The spin system is then subjected to a train of n 180° pulses which refocus any $T_2^{'}$ dephasing, resulting in n echoes which decay due to T_2 alone. The spin-spin relaxation time constant may be obtained by fitting the integrated signals obtained from these echoes according to

$$\frac{S(nt_e)}{S_0} = \exp\left(\frac{-nt_e}{T_2}\right), \tag{3.60}$$

where $t_e = t_{180} + 2\tau_2 \simeq 2\tau_2$[9,10] is the CPMG echo time (or echo spacing) and

[9]The subscript 2 will be used exclusively for time periods employed in the measurement of T_2.
[10]Note that as t_{180} is usually $\ll \tau_2$ it is typical to define the CPMG echo time as $t_e = 2\tau_2$. As

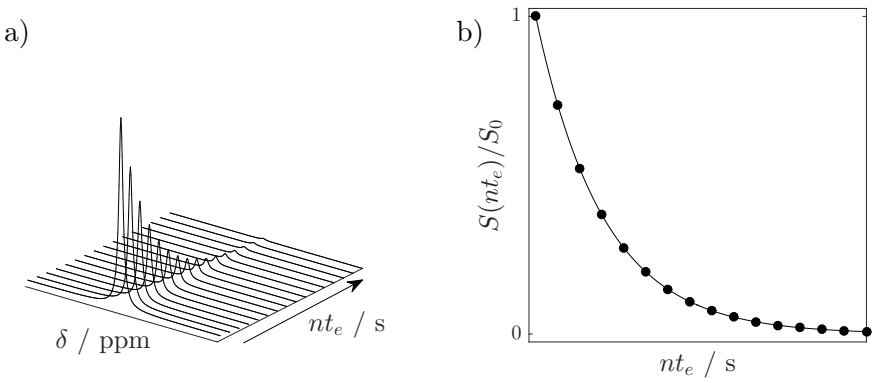

Figure 3.15: a) Spectra obtained from a simulated CPMG experiment on a single resonant component. b) Illustration of the corresponding normalised signal intensities acquired through integration of the peaks shown in a). The solid line indicates a fit to the data according to Equation 3.60, which may be used to obtain the spin-spin relaxation time constant T_2.

$S_0 = S(t \rightarrow 0)$ is the signal obtained in the absence of relaxation. This value is approximated from the signal obtained from the first echo acquired, such that $S_0 = S(t \sim t_e)$; the fitting process is illustrated in Figure 3.15.

The measurement of T_2 is more involved in the presence of J-coupling. For the uncoupled spin pair jk the magnetisation progression during the spin echo is

$$\begin{aligned} I_{jz} + I_{kz} &\xrightarrow{(\pi/2)I_{xj}} \xrightarrow{(\pi/2)I_{xk}} -\{I_{jy} + I_{ky}\} \\ &\xrightarrow{\Omega_j \tau I_{jz}} \xrightarrow{\Omega_k \tau I_{kz}} + I_{jx}\sin(\Omega_j\tau) - I_{jy}\cos(\Omega_j\tau) \\ &\qquad + I_{kx}\sin(\Omega_k\tau) - I_{ky}\cos(\Omega_k\tau) \\ &\xrightarrow{\pi I_{yj}} \xrightarrow{\pi I_{yk}} - I_{jx}\sin(\Omega_j\tau) - I_{jy}\cos(\Omega_j\tau) \\ &\qquad - I_{kx}\sin(\Omega_k\tau) - I_{ky}\cos(\Omega_k\tau) \\ &\xrightarrow{\Omega_j \tau_2 I_{jz}} \xrightarrow{\Omega_k \tau I_{kz}} -\{I_{jy} + I_{ky}\}, \end{aligned} \tag{3.61}$$

illustrating that both spin environments are refocussed, and that the spin echo is unaffected by the influence of multiple offsets. However, in the presence of weak scalar coupling such as that described in Section 3.4.3 the spin dynamics become more complex. For the scalar-coupled spin pair jk the operator for free precession is $\mathcal{A} = \Omega_j I_{jz} + \Omega_k I_{kz} + 2\pi J_{jk} I_{jz} I_{kz}$, where the factor of 2π transforms the scalar coupling constant J_{jk} from units of s^{-1} to rad s^{-1}. [6] The progression of the density

introduced in Section 3.3.2, t_{180} times are usually on the order of a few μs while τ_2 will typically vary from many hundreds of μs to several ms, depending on spectrometer hardware capabilities.

operator during the spin echo follows

$$
\begin{aligned}
I_{jz} + I_{kz} \xrightarrow{(\pi/2)I_{xj}} \xrightarrow{(\pi/2)I_{xk}} & -\{I_{jy} + I_{ky}\} \\
\xrightarrow{\Omega_j \tau I_{jz}} \xrightarrow{\Omega_k \tau I_{kz}} & \ldots \\
\ldots \xrightarrow{2\pi J_{jk} I_{jz} I_{kz} \tau} & + \{I_{jx}\sin(\Omega_j\tau) + I_{kx}\sin(\Omega_k\tau)\}\cos(\pi J_{jk}\tau) \\
& - \{I_{jy}\cos(\Omega_j\tau) + I_{ky}\cos(\Omega_k\tau)\}\cos(\pi J_{jk}\tau) \\
& + \{2I_{jx}I_{kz}\cos(\Omega_j\tau) + 2I_{kx}I_{jz}\cos(\Omega_k\tau)\}\sin(\pi J_{jk}\tau) \\
& + \{2I_{jy}I_{kz}\sin(\Omega_j\tau) + 2I_{ky}I_{jz}\sin(\Omega_k\tau)\}\sin(\pi J_{jk}\tau) \\
\xrightarrow{\pi I_{jy}} \xrightarrow{\pi I_{ky}} & - \{I_{jx}\sin(\Omega_j\tau) + I_{kx}\sin(\Omega_k\tau)\}\cos(\pi J_{jk}\tau) \\
& - \{I_{jy}\cos(\Omega_j\tau) + I_{ky}\cos(\Omega_k\tau)\}\cos(\pi J_{jk}\tau) \\
& + \{2I_{jx}I_{kz}\cos(\Omega_j\tau) + 2I_{kx}I_{jz}\cos(\Omega_k\tau)\}\sin(\pi J_{jk}\tau) \\
& - \{2I_{jy}I_{kz}\sin(\Omega_j\tau) + 2I_{ky}I_{jz}\sin(\Omega_k\tau)\}\sin(\pi J_{jk}\tau) \\
\xrightarrow{\Omega_j \tau I_{jz}} \xrightarrow{\Omega_k \tau I_{kz}} \xrightarrow{2\pi J_{jk} I_{jz} I_{kz} \tau} & - \{I_{jy} + I_{ky}\}\cos(2\pi J_{jk}\tau) \\
& + \{2I_{jx}I_{kz} + 2I_{kx}I_{jz}\}\sin(2\pi J_{jk}\tau).
\end{aligned}
\tag{3.62}
$$

Clearly the $-\{I_{jy} + I_{ky}\}$ term is not necessarily refocussed in the presence of scalar coupling; rather, this term is modulated by the scalar coupling constant. Further complications arise from the antiphase terms $2I_{jx}I_{kx}$ and $2I_{kx}I_{jx}$ which give multiplet peak structures both positive and negative components. [6] Clearly these components will alter our ability to accurately measure T_2 through the method described above. Theoretically these effects may be suppressed through the use of rapid refocussing pulses. Indeed, in the limit of $\tau_2 \to 0$ we find $\cos(2\pi J_{jk}\tau_2) \to 1$ and $\sin(2\pi J_{jk}\tau_2) \to 0$; however, hardware limitations often prevent such suppression. It is pertinent then to use more complex NMR pulse sequences in order to refocus the effects of scalar couplings. This may be performed through use of the so-called perfect echo, which is illustrated in Figure 3.16a. [17, 18] The perfect echo is similar in structure to the spin echo, but adds a 90°_y pulse at the midpoint between two 180°_y refocussing pulses. Through the use of the density operator formalism we can observe that this additional 90° pulse reverses the antiphase components generated by the initial spin echo. The second half of the double spin echo then reverses

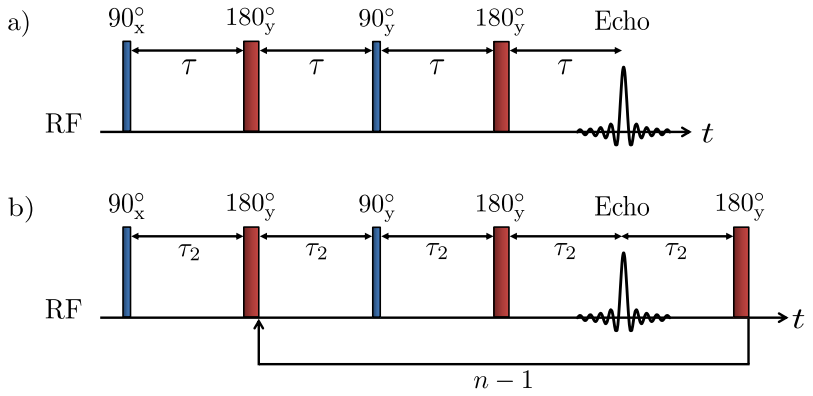

Figure 3.16: a) NMR pulse sequence for the perfect echo. b) The PROJECT pulse sequence used for measuring the spin-spin relaxation time constant T_2 in the presence of J-coupling. Following initial excitation of the spin system by a 90° RF pulse a train of n perfect echoes lead to n echoes separated by an echo time of $t_e = 4\tau_2$.

the influence of the first, leading to full refocussing of the jk spin pair at a time $t = 4\tau + t_{90} + 2t_{180} \simeq 4\tau$ after initial excitation. The evolution of the density operator following the spin echo component of the perfect echo is

$$
\begin{aligned}
&-\{I_{jy}+I_{ky}\}\cos(2\pi J_{jk}\tau)+\{2I_{jx}I_{kz}+2I_{kx}I_{jz}\}\sin(2\pi J_{jk}\tau)\ ...\\
&...\xrightarrow{(\pi/2)I_{jy}}\xrightarrow{(\pi/2)I_{ky}}-\{I_{jy}+I_{ky}\}\cos(2\pi J_{jk}\tau)-\{2I_{jx}I_{kz}+2I_{kx}I_{jz}\}\sin(2\pi J_{jk}\tau)\\
&\xrightarrow{\Omega_j\tau I_{jz}}\xrightarrow{\Omega_k\tau I_{kz}}\xrightarrow{2\pi J_{jk}I_{jz}I_{kz}}...\\
&...\{I_{jx}\sin(\Omega_j\tau)+I_{kx}\sin(\Omega_k\tau)-I_{jy}\sin(\Omega_j\tau)-I_{ky}\sin(\Omega_k\tau)\}\\
&\quad\times\{\cos(2\pi J_{jk}\tau)\cos(\pi J_{jk}\tau)+\sin(2\pi J_{jk}\tau)\sin(\pi J_{jk}\tau)\}\\
&+\{2I_{jx}I_{kz}\cos(\Omega_j\tau)+2I_{kx}I_{jz}\cos(\Omega_j\tau)+2I_{jy}I_{kz}\sin(\Omega_j\tau)+2I_{ky}I_{jz}\sin(\Omega_k\tau)\}\\
&\quad\times\{\cos(2\pi J_{jk}\tau)\sin(\pi J_{jk}\tau)-\sin(2\pi J_{jk}\tau)\cos(\pi J_{jk}\tau)\}\\
&\xrightarrow{\pi I_{jy}}\xrightarrow{\pi I_{ky}}...\\
&...\{-I_{jx}\sin(\Omega_j\tau)-I_{kx}\sin(\Omega_k\tau)-I_{jy}\sin(\Omega_j\tau)-I_{ky}\sin(\Omega_k\tau)\}\\
&\quad\times\{\cos(2\pi J_{jk}\tau)\cos(\pi J_{jk}\tau)+\sin(2\pi J_{jk}\tau)\sin(\pi J_{jk}\tau)\}\\
&+\{2I_{jx}I_{kz}\cos(\Omega_j\tau)+2I_{kx}I_{jz}\cos(\Omega_j\tau)-2I_{jy}I_{kz}\sin(\Omega_j\tau)-2I_{ky}I_{jz}\sin(\Omega_k\tau)\}\\
&\quad\times\{\cos(2\pi J_{jk}\tau)\sin(\pi J_{jk}\tau)-\sin(2\pi J_{jk}\tau)\cos(\pi J_{jk}\tau)\}\\
&\xrightarrow{\Omega_j\tau I_{jz}}\xrightarrow{\Omega_k\tau I_{kz}}\xrightarrow{2\pi J_{jk}I_{jz}I_{kz}}-\{I_{jy}+I_{ky}\}.
\end{aligned}
\tag{3.63}
$$

It follows that a cyclic analogue of the perfect echo may be employed to measure T_2 values in scalar-coupled systems. This is known as the PROJECT (Periodic

Refocussing of J Evolution by Coherence Transfer) sequence, and is illustrated in Figure 3.16b. [19] The removal of J-coupling interference through use of the PROJECT sequence comes at the cost of increasing the echo time from $t_e = 2\tau_2$ to $t_e = 4\tau_2$, which limits the ability of this sequence to measure very short T_2 values.

3.5.3 Distributions and correlation measurements

An inherent assumption in the above discussion of T_1 and T_2 measurements is that we expect the observed relaxation to exhibit single-exponential behaviour; while this is indeed commonplace for the most basic of spin systems there are several cases in which we may need to address multiexponential relaxation. For instance, nuclear spins in different magnetic environments within the same molecule will exhibit different relaxation time constants. If the chemical shift domain exhibits significant overlap of the resonances from these environments, then relaxation data obtained from peak integration cannot be expected to provide reasonable fits to Equations 3.40 and 3.60. This issue will be equally apparent for any spectral overlap encountered during the analysis of molecular mixtures. Furthermore, relaxation rates associated with liquids imbibed in porous media are dependent on the local pore geometry and the chemistry of the pore surface.[11] The observed relaxation will therefore depend on the rate of exchange of the spin-bearing species between physical environments exhibiting differing relaxation characteristics.

Relaxation time distributions

It is clear then that for a detailed analysis of complex relaxation phenomena we require a method of evaluating a distribution of relaxation time constants. This problem is of particular importance to the low magnetic field relaxation studies, which are commonly applied to porous systems of industrial interest, and in which chemical shift resolution is typically poor. [5] The normalised signal acquired from such systems is described by a Fredholm integral equation of the first kind, [20]

$$\frac{S(t)}{S_0} = \int_0^\infty p(T_i)\mathcal{K}_i(t, T_i)\, dT_i + \varepsilon(t). \tag{3.64}$$

[11] These phenomena are detailed in Chapter 4.

Here T_i $(i = 1, 2)$ is the relaxation time constant of interest, $p(T_i)$ is the probability density distribution of T_i and the kernel function $\mathcal{K}_i(t, T_i)$ describes the predicted, single-exponential form of the relevant relaxation process; it follows from our above discussion that $\mathcal{K}_1(\tau_1, T_1) = 1 - 2\exp(\tau_1/T_1)$ and $\mathcal{K}_2(nt_e, T_2) = \exp(nt_e/T_2)$ for T_1 and T_2 relaxation, respectively. The final term $\varepsilon(t)$ represents the experimental noise, which is typically assumed to be gaussian with zero mean.

In practice, nuclear spin relaxation time constants vary over a sufficiently wide range of decades that this expression is usually solved on a $\log_{10}$ scale, [21]

$$\frac{S(t)}{S_0} = \int_0^\infty f(T_i)\mathcal{K}_i \, d\log_{10}(T_i) + \varepsilon(t). \tag{3.65}$$

The desired distribution $f(T_i)$ is then obtained through inversion[12] of Equation 3.65. [20] However, unlike the Fourier relationship between time and frequency domains in NMR spectroscopy, $S(t) \leftrightarrow S(\Omega)$, there exists no mathematically well-defined method for determining $f(T_i)$ through the inversion of the exponentially decaying relaxation signal, $S(t) \rightarrow f(T_i)$. [22] Indeed, due to the contribution of random experimental noise $\varepsilon(t)$, the acquired NMR data is insufficient to determine a unique solution of $f(T_i)$; this is therefore an ill-poised problem. [23] A stable inversion result is obtained through the process of regularisation (or optimisation) by imposing the following constraints on the inverted distribution:

1. The distribution is non-negative.

2. The distribution has a well-define range.

3. The distribution is biased to be smooth.

[12] Also referred to as an inverse Laplace transform.

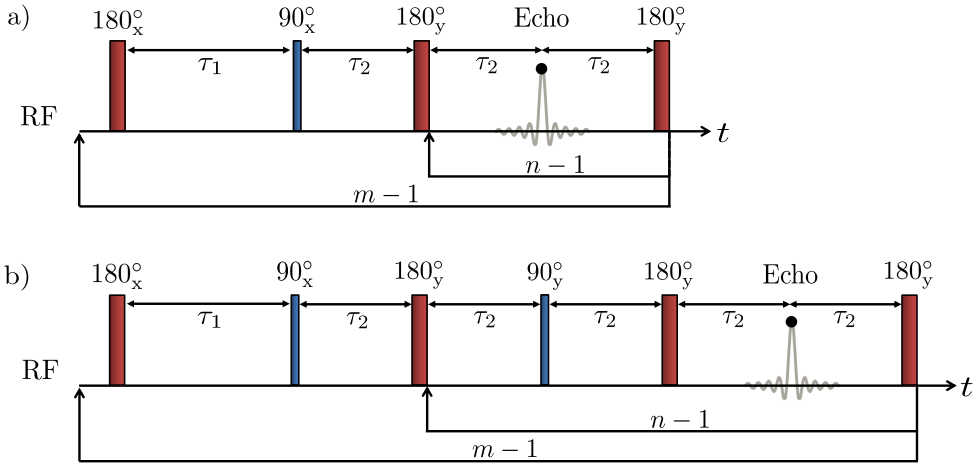

Figure 3.17: NMR pulse sequences for $T_1 - T_2$ correlation experiments. a) illustrates the inversion recovery-CPMG sequence while b) illustrates the inversion recovery-PROJECT sequence. The NMR data is typically acquired in a one-shot technique, which takes only the magnitude of the echo maximum as illustrated by the black data point.

$\mathbf{T_1 - T_2}$ correlation measurements

The concepts described above are readily extended to multidimensional correlation experiments. The application of NMR experiments designed to provide two or more dimensions of information (e.g. chemical shift, relaxation time constants, diffusion coefficients) is commonplace in the analysis of complex systems as they allow experimentalists to distinguish physical and/or chemical behaviour not readily apparent to more basic analyses.

In this thesis we will concentrate on the application of $T_1 - T_2$ correlation measurements to liquid-saturated porous media. The relevant NMR pulse sequences for such experiments are illustrated in Figure 3.17 and comprise a T_1 inversion recovery component ($180_x \xrightarrow{\tau_1} 90_x$) followed by either a CPMG [24] or PROJECT [25] echo train.[13] While the resultant echoes may be Fourier transformed to provide data in the chemical shift dimension it is more typical to employ a so-called one-shot acquisition technique in which a single data point is taken at each echo maximum. The pulse sequence is then cycled to evaluate m values of τ_1; in analogy to Equation

[13]The one-shot inversion recovery–PROJECT pulse sequence illustrated in Figure 3.17b was developed and implemented by Dr Christopher Robertson at the Magnetic Resonance Research Centre, University of Cambridge, in 2018,[25] concurrent to the experiments performed in this Thesis.

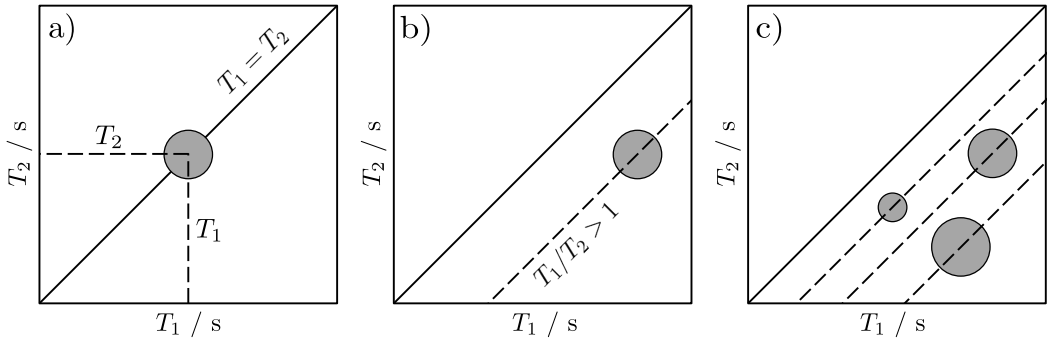

Figure 3.18: $T_1 - T_2$ relaxation correlation plots. Example correlation peaks are shown in grey. a) and b) illustrate a single relaxation distribution with $T_1 = T_2$ and $T_1 \neq T_2$, respectively. c) illustrates a multicomponent distribution. Relaxation environments in which $T_1 \neq T_2$ are often characterised by the ratio T_1/T_2.

3.65 the resulting two-dimensional data set takes the form [26]

$$\frac{S(nt_e, \tau_1)}{S_0} = \iint_0^\infty \mathcal{K}_1(\tau_1, T_1)\mathcal{K}_2(nt_e, T_2)\mathcal{F}(T_1, T_2)\, d\log_{10}(T_1)\, d\log_{10}(T_2). \quad (3.66)$$

These data are then inverted to provide a two-dimensional $T_1 - T_2$ distribution; a detailed review of the regularisation techniques required to implement 2D inversions is provided by Mitchell *et al.*. [21] Figure 3.18 illustrates typical $T_1 - T_2$ distributions which might be obtained from such correlation experiments. While the position of each correlation peak is dictated by the T_1 and T_2 values of the system, off-diagonal ($T_1 > T_2$) correlation peaks are often characterised by the dimensionless ratio T_1/T_2; we will see in later chapters that this ratio provides insight into the surface affinities exhibited by adsorbed species within liquid-saturated mesoporous solids. [27, 28]

3.5.4 Relaxation mechanisms

Both longitudinal and transverse nuclear spin relaxation processes are facilitated through the concurrent action of several relaxation mechanisms. These involve the interaction of time-dependent microscopic fields with the nuclear spins of interest; the time-dependence of these fields originates with the thermally driven molecular motion within the sample. These microscopic fields gain an oscillatory behaviour from this motion, facilitating interactions with the sample magnetisation in an analogous fashion to the resonant behaviour of RF pulses. It follows that the process of longitudinal relaxation is facilitated by fields oscillating transverse to

$\mathbf{B}_0$, while transverse relaxation processes are enabled by longitudinally oscillating fields. Relaxation mechanisms – i.e. the sources of these micropscopic fields – of importance to $I = \frac{1}{2}$ nuclei in the liquid phase are spin rotation, chemical shift anisotropy and dipole-dipole interactions. The general order of importance is: $\text{dipole} - \text{dipole} > \text{chemical shift anisotropy} > \text{spin rotation}$. [2] A brief description of these relaxation mechanisms is given below.

Spin rotation

The circulating electric charge associated with a rapidly rotating molecules or molecular functional groups is analogous to an electric current. Such motion therefore results in local magnetic fields which can interact with nearby nuclei. The spin rotation mechanism is often the dominant form of nuclear spin relaxation in the gas phase due to the rapid rates of molecular tumbling and large intermolecular separations; however, in the liquid phase spin rotation typically provides only a small contribution to the observed relaxation rates.

Chemical shift anisotropy

It was shown in Section 3.4.2 that the local field at each nucleus is determined by the nuclear shielding constant σ, which stems from B_0 driven currents of electron density in each magnetically inequivalent chemical environment. In all but the most symmetric of molecules these local fields are orientationally dependent, and are therefore anisotropic. The tumbling motion of molecules with anisotropic chemical shielding provides an additional source of nuclear spin relaxation. Note, however, that in isotropically tumbling liquids this anisotropy is not observed in the frequency spectrum. Instead, as molecules in the liquid phase may take any orientation, an isotropic average across the entire molecular ensemble is observed.

Dipole-dipole interactions

The through-space (or direct) dipole-dipole interaction is the most important source of nuclear spin relaxation for ^{1}H in the liquid-phase, [2, 9] and will be described in greater detail in Chapter 4. As previously introduced, magnetically active nuclei

posses a nuclear magnetic moment $\boldsymbol{\mu} = \gamma\mathbf{I}$, the magnitude of which is dictated by the gyromagnetic ratio γ. Each nuclear magnetic moment generates an associated magnetic field which may interact with surrounding nuclei. For the nuclear spin pair jk the rates of dipolar relaxation are proportional to the square of dipole-dipole coupling constant, [9]

$$b_{jk} = -\frac{\mu_0 \hbar}{4\pi} \frac{\gamma_j \gamma_k}{r_{jk}^3}, \tag{3.67}$$

where $\mu_0 = 4\pi \times 10^{-7} \text{J A}^{-2}$ is the permeability of free space and r_{jk} defines the internuclear distance. Relaxation rates are therefore clearly dependent on gyromagnetic ratios of the interacting nuclei. Both homonuclear (e.g. $^1\text{H}-^1\text{H}$) and heteronuclear (e.g. $^{13}\text{C}-^1\text{H}$) dipolar relaxation interactions may occur; however, given that the ^{1}H gyromagnetic ratio is large relative to the other $I > 0$ nuclei present in the following experiments, homonuclear $^1\text{H}-^1\text{H}$ interactions are considered to provide the dominant form of dipolar relaxation in the experiments discussed within this thesis. Relevant γ values are provided in Table 3.2.

Paramagnetic species

Finally we draw attention to a specific dipolar relaxation mechanism known as paramagnetic relaxation, which occurs in the presence of unpaired electrons. The $\text{e}-^1\text{H}$ interaction provides a significant relaxation contribution in the presence of paramagnetic species or ferromagnetic material due to the large gyromagnetic ratio of the electron.

Table 3.2: Gyromagnetic ratios for various magnetically active species which may partake in ^{1}H dipole-dipole relaxation interactions during the experiments described within the thesis. Nuclear values are taken from Levitt [2] while the electron value (e^-) is taken from the National Institute of Standards and Technology (NIST) [29, 30].

Species	Natural abundance / %	γ / rad s^{-1} T^{-1}
^{1}H	> 99	267.522×10^6
^{2}H	0.015	41.066×10^6
^{13}C	1.1	67.283×10^6
^{17}O	0.04	-36.281×10^6
^{29}Si	4.7	-53.190×10^6
e^-		-1.761×10^{11}

3.6 Pulsed field gradient NMR

3.6.1 Magnetic field gradients

The application of a spatially varying magnetic field $\mathbf{g} = (g_x, g_y, g_z)$ causes the Larmor frequency to change with position $\mathbf{r}$, [23]

$$\omega(\mathbf{r}) = -\gamma(B_0 + \mathbf{g} \cdot \mathbf{r}). \tag{3.68}$$

Such a field is known as a gradient. Let us consider a field gradient which varies in the z direction, such that $\mathbf{g} = (0, 0, g_z)$ where $g_z = \frac{\partial B_z}{\partial z}$. It follows that an effective precessional frequency is given by

$$\omega_{eff}(z) = -\gamma(B_0 + g_z z), \tag{3.69}$$

resulting in a spatially dependent offset

$$\Omega_{eff}(z) = \omega_0 - \omega_{eff}(z) = \gamma g_z z. \tag{3.70}$$

Magnetic field gradients are typically applied as a short pulse contained within a more complex NMR pulse sequence. Let us consider the usual case in which the sample magnetisation has been excited into the transverse plane following a 90° RF pulse prior to the application of any gradient. Working from the rotating frame of reference, the spatial dependence of $\Omega_{eff}(z)$ results in a rotation of the transverse magnetisation by a phase factor $\exp(i\phi_g)$. Assuming the gradient pulse to be rectangular the phase acquired by this rotation is

$$\phi_g = \gamma \int_0^{t_g} g_z z \, dt = \gamma g_z t_g z, \tag{3.71}$$

where the time t_g defines the length of the pulse. Neglecting relaxation effects, from the rotating frame of reference the complex transverse magnetisation may then be expressed as

$$M(z) = M_x(z) + iM_y(z) \tag{3.72a}$$

$$= M_0 \cos(\gamma g_z t_g z) + iM_0 \sin(\gamma g_z t_g z) \tag{3.72b}$$

$$= M_0 \exp(i\gamma g_z t_g z), \tag{3.72c}$$

and defines a spatially varying magnetisation helix generated by the gradient pulse; this concept is illustrated in Figure 3.19. The pitch of this helix is q^{-1} (units of m) where the wavenumber q (units of m^{-1}) is [23]

$$q = \frac{\gamma g_z t_g}{2\pi}. \tag{3.73}$$

This parameter clearly relates the dephasing power of a gradient pulse (typically thought of in terms of gradient area $g_z t_g$) to the phase of the transverse magnetisation, and illustrates that the sensitivity of a nuclear spin ensemble to pulsed field gradients is determined by the gyromagnetic ratio.

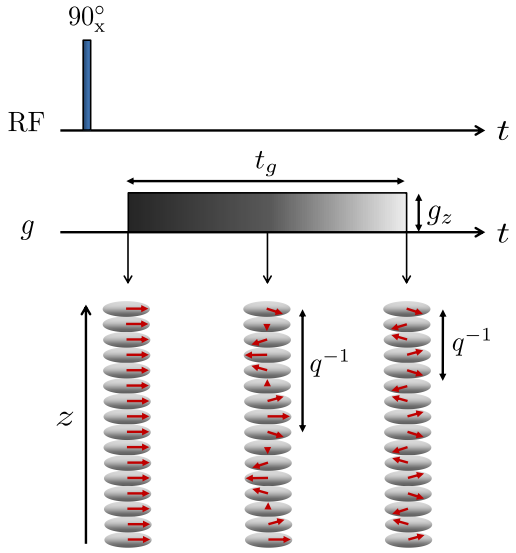

Figure 3.19: Illustration of the effects of a magnetic field gradient applied along the z-axis following RF excitation with a 90° pulse. The application of a gradient (g axis) of magnitude g_z applied for a time t_g leads to a spatially dependent phase shift. The pitch of the resulting magnetisation helix is $q^{-1} = 2\pi/(\gamma g_z t_g)$ and therefore reduces with increasing gradient area $g_z t_g$. Adapted from Callaghan [23].

3.6.2 Displacement and self-diffusion

The ability to encode the spatial position of nuclear spins is often extended to the measurement of molecular displacement. Indeed, pulsed field gradient (PFG) NMR may be applied to measure both coherent motion such a flow, and incoherent motion such as self-diffusion. Here we will concern ourselves with the observation of thermally driven self-diffusion. Such measurements may be performed by employing multiple field gradient pulses separated by an observation time t_Δ. Consider, for example, a displacement $\Delta z = z_1 - z_0$ in which the z-coordinate changes from z_0 at time $t = 0$ to z_1 at $t = t_\Delta$. Following RF excitation into the transverse plane a field gradient pulse encodes the position of a given nuclear spin by imparting a phase as defined in Equation 3.71. Displacement of the spin during t_Δ results in a phase shift $\Delta\phi_g$ of the form

$$\Delta\phi_g = \gamma g_z t_g \Delta z. \tag{3.74}$$

Following the observation time t_Δ the application of a second gradient of equal area $g_z t_g$ but opposite polarisation removes this spatial encoding. In the absence of displacement $\Delta z = 0$ and the transverse magnetisation returns to its original position. However, if molecular motion has occurred $\Delta z \neq 0$ and the original transverse magnetisation will not be fully recovered.

To consider such effects across an ensemble of nuclear spins we must make use of a parameter known as the diffusion propagator $P(z_1, t_\Delta|z_0)$. [31] This is simply the conditional probability of finding a spin at z_1 after a time $t = t_\Delta$ given that it started at z_0 at $t = 0$. The ensemble averaged probability of finding a spin at z_1 after t_Δ is

$$P(z_1, t_\Delta) = \int n(z_0) P(z_1, t_\Delta|z_0)\, dz_0, \tag{3.75}$$

where the spin density $n(z_0)$ gives the probability that a given spin starts at z_0. A closely related parameter is the average propagator $\langle P(\Delta z, t_\Delta)\rangle$ which defines the probability that a randomly selected spin will experience a displacement Δz during t_Δ,

$$\langle P(\Delta z, t_\Delta)\rangle = \int n(z_0) P(z_0 + \Delta z, t_\Delta|z_0)\, dz_0. \tag{3.76}$$

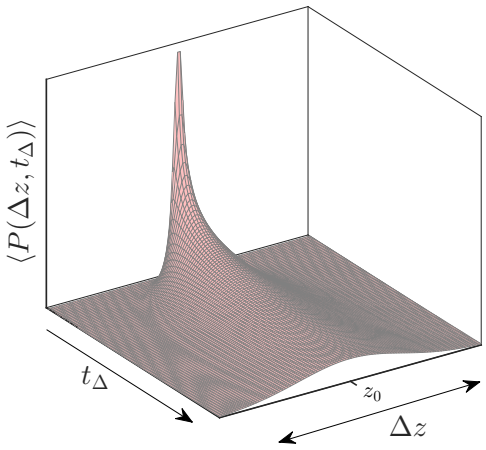

Figure 3.20: Average propagator $\langle P(\Delta z, t_\Delta)\rangle$ for unrestricted isotropic self-diffusion as a function of observation time t_Δ. The normal distribution described by Equation 3.77 is clearly evident, and illustrates an increase in displacement Δz with increasing t_Δ.

The average propagator for unrestricted diffusion takes the form a normal distribution about z_0, given by the Gaussian function [31]

$$\langle P(\Delta z, t_\Delta)\rangle = \frac{1}{\sqrt{4\pi\mathcal{D}t_\Delta}} \exp\left(\frac{-\Delta z^2}{4\mathcal{D}t_\Delta}\right), \tag{3.77}$$

where $\mathcal{D}$ is the self-diffusion coefficient (units of $\mathrm{m}^2\ \mathrm{s}^{-1}$) which quantifies the rate of displacement; this distribution is illustrated in Figure 3.20.

The mean displacement $\langle \Delta z\rangle = \langle z_1 - z_0\rangle$ resulting from self-diffusion is clearly zero; however, the mean square displacement (MSD) $\langle (\Delta z)^2\rangle = \langle (z_1 - z_0)^2\rangle$ is not, and is of significant interest in the measurement of molecular displacement. The MSD is related to the average propagator *via*

$$\langle (\Delta z)^2\rangle = \int \langle P(\Delta z, t_\Delta)\rangle (\Delta z)^2\, d\Delta z, \tag{3.78}$$

which gives the Einstein relation for one-dimensional (1D) displacement [31]

$$\langle (\Delta z)^2\rangle = 2\mathcal{D}t_\Delta. \tag{3.79}$$

Equation 3.79 provides a direct relationship between displacement and diffusion. As pulsed field gradient NMR is sensitive to displacement it follows that such

experiments may be extended to the measurement of self-diffusion coefficients. In particular, the signal detected following a pair of equal and opposite gradients separated by t_Δ is directly related to $\langle P(\Delta z, t_\Delta)\rangle$. When the gradients are set such that $\int_0^\tau g\ dt = 0$ an echo is generated at time τ following RF excitation; this concept is illustrated in Figure 3.21 and is known as a gradient echo. [23] The amplitude of this echo $S(q, t_\Delta)$ is given by

$$S(q, t_\Delta) = \int \langle P(\Delta z, t_\Delta)\rangle \exp(-i2\pi q \Delta z)\ d\Delta z, \tag{3.80}$$

which evaluates to[14]

$$S(q, t_\Delta) \sim \exp\big(-(2\pi q)^2 \mathcal{D} t_\Delta\big). \tag{3.81}$$

This expression illustrates a clear link between the PFG NMR signal and self-diffusion coefficient $\mathcal{D}$. If we include the effects of relaxation and finite gradient pulse lengths this signal becomes

$$S(q, \tau) = S_0 \exp\left(\frac{-\tau}{T_2^*}\right) \exp\big(-\gamma^2 g_z^2 t_g^2 \mathcal{D} t_{eff}\big). \tag{3.82}$$

Here, S_0 is the echo intensity acquired in the absence of diffusion or relaxation, τ is the time during which the magnetisation lies in the transverse plane before signal detection (Figure 3.21) and t_{eff} is an effective observation time which accounts for diffusion during the gradient pulses. [23, 31]

By normalising the acquired data relative to the echo intensity obtained when $g_z = 0$ the effects of relaxation can be mitigated,[15]

$$\frac{S(q)}{S(0)} = \frac{S_0 \exp(-\tau/T_2^*) \exp\big(-\gamma^2 g_z^2 t_g^2 \mathcal{D} t_{eff}\big)}{S_0 \exp(-\tau/T_2^*)} \tag{3.83a}$$

$$= \exp\big(-\gamma^2 g_z^2 t_g^2 \mathcal{D} t_{eff}\big). \tag{3.83b}$$

The only unknown in Equation 3.83b is the self-diffusion coefficient. It follows that by performing multiple PFG NMR experiments in which the gradient strength g_z is

[14] A full and detailed derivation is provided by Price in [31].

[15] Note that this does not remove the influence of relaxation when comparing data acquired at different observation times.

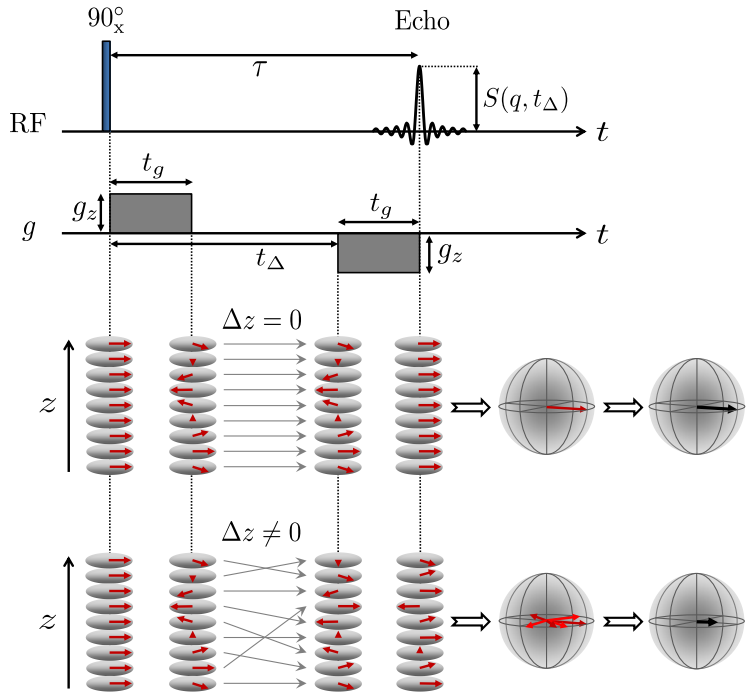

Figure 3.21: Illustration of the gradient echo. The nuclear spin ensemble is excited from thermal equilibrium with a 90° RF pulse. The transverse magnetisation is then subjected to a gradient of area $g_z t_g$ which encodes the spins with a spatially dependent phase. A second gradient of equal area but opposite polarisation is applied following an observation time t_Δ. This gradient decodes the phase information stored within the magnetisation helix, forming a gradient echo of amplitude $S(q, t_\Delta)$. In the absence of self-diffusion $\Delta z = 0$ and - neglecting any nuclear spin relaxation - the transverse magnetisation is fully refocussed by the second gradient. However, if diffusion motion occurs such that $\Delta z \neq 0$ then a loss of transverse phase coherence is observed. This is illustrated using magnetisation spheres and results in attenuation of the acquired NMR signal.

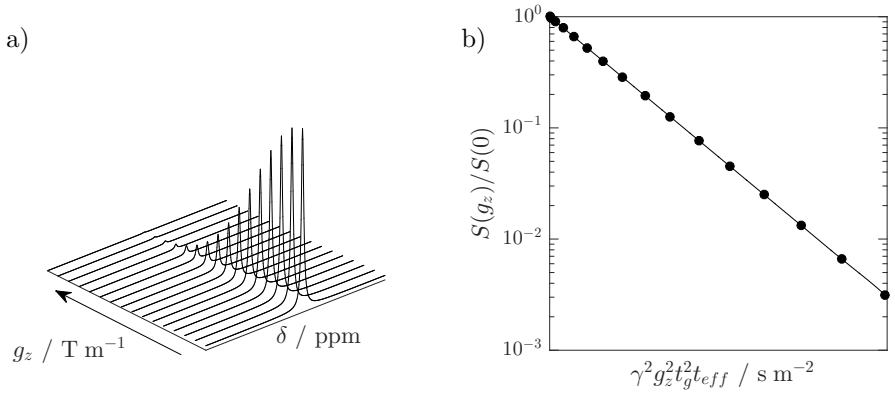

Figure 3.22: a) Spectra obtained from a simulated PFG NMR experiment on a single resonant component. b) Illustration of the corresponding normalised signal attenuation, acquired through integration of the peaks shown in a). The solid line indicates a fit to the attenuation data according to Equation 3.83b, which may be used to obtain the self-diffusion coefficient $\mathcal{D}$.

incremented through a range of values, the resulting attenuation data $S(g_z)/S(0)$ can be used to obtain $\mathcal{D}$. This fitting procedure is shown in Figure 3.22 and illustrates that a plot of $\ln(S(g_z)/S(0))$ against $(\gamma g_z t_g)^2 t_{eff}$ gives in a straight line with gradient $-\mathcal{D}$. Importantly, in analogy to relaxation experiments $S(g_z)$ is obtained *via* Fourier transformation and integration of the observed echo data. It therefore follows that integration of different spectral peaks can be used to quantify the diffusivities of different species within the same sample.

3.6.3 PFG NMR pulse sequences

While the simple gradient echo sequence illustrated in Figure 3.21 is a useful demonstration of PFG NMR, in practice it is rarely used to measure self-diffusion coefficients. This is largely due to the influence of T_2^* relaxation, which limits the length of the observation times which may be used. A brief description of the more complex pulse sequences typically employed is given below.

PGSE

The pulsed gradient spin echo (PGSE) sequence is the most basic PFG NMR experiment employed to quantify self-diffusion. [32] As illustrated in Figure 3.23 the sequence comprises a simple spin echo equipped with a field gradient pulse either side of the 180° RF pulse. As we have seen in Section 3.5.2, the spin echo refocusses T_2' relaxation such that the transverse magnetisation decays due to T_2 alone. This is particularly important when considering diffusion measurements as spins can easily have displaced throughout regions of different field homogeneity during the applied observation time. The signal attenuation for the PGSE sequence is

$$S(q, 2\tau) = S_0 \exp\left(\frac{-2\tau}{T_2}\right) \exp\left(-\gamma^2 g_z^2 t_g^2 \mathcal{D}\left(t_\Delta - \frac{t_g}{3}\right)\right), \tag{3.84}$$

where τ defines the delay between 90° and 180° RF pulses and $t_\Delta - \frac{t_g}{3}$ is the effective diffusion time. An important feature of the PGSE sequence is that both gradient pulses have the same polarisation. This is a consequence of the 180° RF pulse which inverts the magnetisation helix about the RF pulse axis (Figure 3.23). An effective

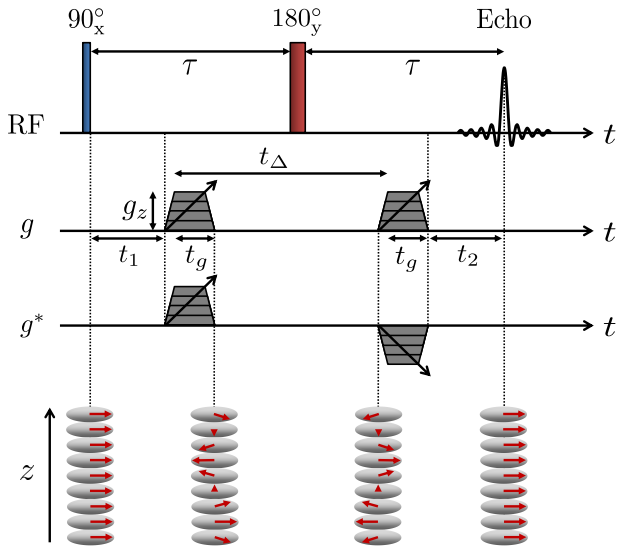

Figure 3.23: Illustration of the pulsed gradient spin echo (PGSE). This sequence comprises a basic spin echo equipped with two gradient pulses separated by an observation time t_Δ. Gradient amplitudes are ramped in successive repeat experiments such that the resulting attenuation data can be fit to Equation 3.83b. The progression of a magnetisation helix illustrates the ability of the 180° pulse to invert the phase-shifted transverse magnetisation; the effective gradient g^* takes account of this pulse as discussed in the main text.

gradient g^* is introduced to account for these effects; in analogy to the gradient echo we find that $\int_0^{2\tau} g^* \, dt = 0$. Trapezoidal – rather than rectangular – gradient lobes are also employed to maintain reproducible gradient shapes at all values of g_z. Self-diffusion coefficients may be obtained from the PGSE experiment by fitting the acquired attenuation data to

$$\frac{S(g_z)}{S(0)} = \exp\left(-\gamma^2 g_z^2 t_g^2 \mathcal{D}\left(t_\Delta - \frac{t_g}{3}\right)\right). \tag{3.85}$$

PGSTE

The pulsed gradient stimulated echo (PGSTE) sequence is illustrated in Figure 3.24. [33] This sequence is similar in structure to that used in the PGSE experiment; however, here the 180° pulse is split into two separate 90° pulses. These pulses facilitate the use of a longitudinal storage period $\mathrm{T} = \mathrm{t}_\Delta - \tau$ during which the sample magnetisation is stored along the z-direction rather than in the transverse plane. A homospoil gradient is applied to remove any remaining transverse phase coherence during the T storage period (Figure 3.24); $z-$storage has a number

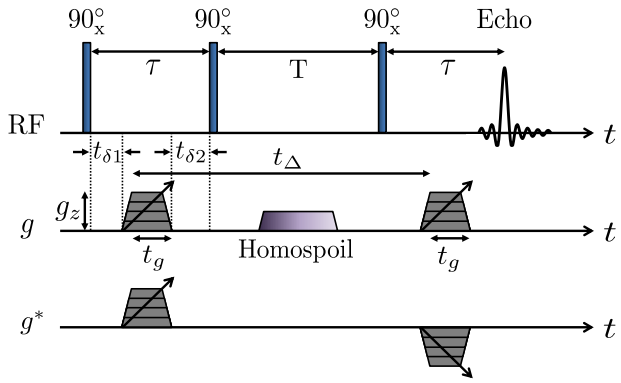

Figure 3.24: Illustration of the pulsed gradient stimulated echo (PGSTE) sequence. Following RF excitation and spatial encoding the sample magnetisation is stored longitudinally for a storage period T. This longitudinal storage minimises any J-coupling evolution within the spin ensemble, and allows long observation times t_Δ to be employed in systems where $T_1 > T_2$. A homospoil gradient is applied during T to remove any remaining coherent transverse magnetisation.

of advantages when compared to the transverse storage employed by the PGSE sequence. Longitudinal magnetisation is unaffected by J-coupling interactions; provided that $\mathrm{T} \gg \tau$ the PGSTE sequence is therefore far less susceptible to artefacts resulting for J-coupling evolution than the PGSE sequence. Moreover, given that $T_1 \geq T_2$, the PGSTE pulse sequence allows us to measure diffusive displacement in systems exhibiting shorter T_2 times than is possible using the PGSE sequence. The signal from the PGSTE experiment is [31]

$$S(q,\tau,\mathrm{T}) = \frac{S_0}{2}\exp\left(-\frac{2\tau}{T_2}-\frac{\mathrm{T}}{T_1}\right)\exp\left(-\gamma^2 g_z^2 t_g^2 \mathcal{D}\left(t_\Delta - \frac{t_g}{3}\right)\right). \tag{3.86}$$

The $S_0/2$ term arises because the second 90°_x pulse can only rotate the y-components of the sample magnetisation into longitudinal storage. As the x-components are lost in this transfer, only half of the original magnetisation can be detected upon formation of the echo. [13, 23] Self-diffusion coefficients may be obtained from the PGSE experiment by fitting the acquired attenuation data to Equation 3.85.

APGSTE

The alternating pulsed gradient stimulated echo (APGSTE) sequence – also known as the bipolar pulsed gradient stiumlated echo (BPPSTE) or the Cotts 13-interval Condition I sequence – is shown in Figure 3.25. [34] This variation of the PFG NMR

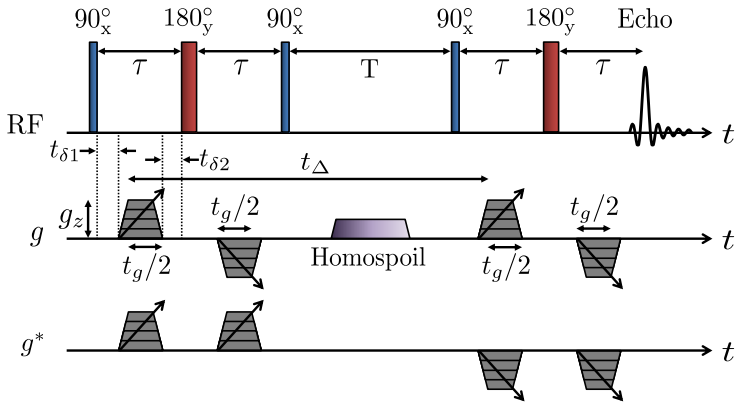

Figure 3.25: Illustration of alternating pulsed gradient stimulated echo (APGSTE) pulse sequence. This sequence is designed to minimise the influence of background field gradients on the observed echo attenuation.

experiment comprises a PGSTE sequence in which the gradient pulses are split into positive and negative lobes either side of an additional 180° RF pulse. The signal from the APGSTE experiment is

$$S(q,\tau,T) = \frac{S_0}{2}\exp\left(-\frac{4\tau}{T_2}-\frac{\mathrm{T}}{T_1}\right)\exp\left(-\gamma^2 g_z^2 t_g^2 \mathcal{D}\left(t_\Delta - \frac{t_g}{12} - \frac{\tau}{2}\right)\right), \qquad (3.87)$$

where $t_\Delta - \frac{t_g}{12} - \frac{\tau}{12}$ is the effective diffusion time.

The APGSTE sequence is designed to minimise the interference of background magnetic field gradients on the acquired echo attenuation data. [23] This is particularly important when assessing the diffusion of liquids imbibed within porous solids, where background field gradients often occur as a results of magnetic susceptibility differences across the solid-liquid interface. [35, 36] These background gradients can severely affect the NMR signal acquired using standard PFG pulse sequences. For instance, in the presence of a constant background field gradient of magnitude g_0 the PGSE attenuation will follow [36]

$$\begin{aligned}\frac{S(g_z,g_0)}{S(0,g_0)} = \exp\Bigg(-\gamma^2\mathcal{D}\Bigg\{ & \underbrace{g_z^2 t_g^2\left(t_\Delta - \frac{t_g}{3}\right)}_{\text{attenuation due to } g_z} \\ & + \underbrace{g_z g_0 t_g\left(2\tau^2 - t_1^2 - t_2^2 - t_g(t_1+t_2) - \frac{2}{3}t_g^2\right)}_{g_z g_0 \text{ cross-term}} + \underbrace{\frac{2}{3}\tau^3 g_0^2}_{g_0 \text{ term}}\Bigg\}\Bigg),\end{aligned} \qquad (3.88)$$

while attenuation of the PGSTE sequence is [36]

$$\begin{aligned}\frac{S(g_z,g_0)}{S(0,g_0)} = \exp\Bigg(-\gamma^2\mathcal{D}\Bigg\{ & \underbrace{g_z^2 t_g^2\left(t_\Delta - \frac{t_g}{3}\right)}_{\text{attenuation due to } g_z} \\ & + \underbrace{g_z g_0 t_g\left(2\tau^2 + 2\mathrm{T} - \frac{2}{3}t_g^2 - t_g(t_{\delta 1}+t_{\delta 2}) - (t_{\delta 1}^2 + t_{\delta 2}^2)\right)}_{g_z g_0 \text{ cross-term}} \\ & + \underbrace{g_0^2\tau^2\left(\frac{2}{3}\tau + \mathrm{T}\right)}_{g_0 \text{ term}}\Bigg\}\Bigg).\end{aligned} \tag{3.89}$$

The relevant time intervals are indicated within Figures 3.23 and 3.24. Clearly additional signal attenuation occurs due to the presence of g_0 (g_0 term); however, this contribution is typically negligible provided $g_0\tau \ll g_z t_g$. Further attenuation occurs due to the $g_z g_0$ cross-term. Given that g_z can be large this contribution has the potential to cause significant distortions of the acquired attenuation data, leading to erroneousness measurements of the self-diffusion coefficient. It is the $g_z g_0$ cross-term which the APGSTE pulse sequence aims to remove. [34] The attenuation of the APGSTE sequence in the presence of g_0 follows

$$\begin{aligned}\frac{S(g_z,g_0)}{S(0,g_0)} = \exp\Bigg(-\gamma^2\mathcal{D}\Bigg\{ & \underbrace{g_z^2 t_g^2\left(t_\Delta - \frac{t_g}{12} - \frac{\tau}{2}\right)}_{\text{attenuation due to } g_z} \\ & + \underbrace{g_z g_0 \tau t_g(t_{\delta 1} - t_{\delta 2})}_{g_z g_0 \text{ cross-term}} + \underbrace{\frac{4}{3}\tau^3 g_0^2}_{g_0 \text{ term}}\Bigg\}\Bigg),\end{aligned} \tag{3.90}$$

from which it is obvious that by setting $t_{\delta 1} = t_{\delta 2}$ the cross-term can be eliminated, such that the acquired signal attenuation is dominated by the application of g_z.

3.7 References

[1] S. D. Bass, "How Does the Proton Spin?", *Science*, 2007, **315**, 1672–1673.

[2] M. H. Levitt, *Spin Dynamics: Basics of Nuclear Magnetic Resonance*, Wiley-Blackwell, Chichester, England ; Hoboken, NJ, 2nd Edition, 2008.

[3] R. Kimmich, *Principles of Soft-Matter Dynamics: Basic Theories, Non-Invasive Methods, Mesoscopic Aspects*, Springer, Dordrecht ; New York, 2012 edition, 2012.

[4] P. Blümler, D. Holland, J. van Duynhoven, B. Balcom, E. Fukushima, M. Hurlimann, A. Legchenko, N. Sun, M. Espy, A. McDowell, M. Rosen and B. Blümich, *Mobile NMR and MRI: Developments and Applications*, ed. M. L. Johns, E. O. Fridjonsson, S. J. Vogt, A. Haber and W. Price, Royal Society of Chemistry, Cambridge, UK, 2015.

[5] J. Mitchell, L. F. Gladden, T. C. Chandrasekera and E. J. Fordham, "Low-Field Permanent Magnets for Industrial Process and Quality Control", *Prog. Nucl. Magn. Reson. Spectrosc.*, 2014, **76**, 1–60.

[6] J. Keeler, *Understanding NMR Spectroscopy*, Wiley-Blackwell, Chichester, U.K, 2nd Edition edition, 2010.

[7] H. Günther, *NMR Spectroscopy: Basic Principles, Concepts and Applications in Chemistry*, Wiley-VCH, Weinheim, 3 edition, 2013.

[8] M. H. Levitt, in *Spin Dynamics: Basics of Nuclear Magnetic Resonance*, Wiley-Blackwell, Chichester, England ; Hoboken, NJ, 2nd Edition, 2008, p. 221.

[9] J. Kowalewski and L. Maler, *Nuclear Spin Relaxation in Liquids: Theory, Experiments, and Applications*, CRC Press, 2006.

[10] R. L. Vold, J. S. Waugh, M. P. Klein and D. E. Phelps, "Measurement of Spin Relaxation in Complex Systems", *J. Chem. Phys.*, 1968, **48**, 3831–3832.

[11] L. F. Gladden, "Nuclear Magnetic Resonance in Chemical Engineering: Principles and Applications", *Chem. Eng. Sci.*, 1994, **49**, 3339–3408.

[12] H. Y. Carr and E. M. Purcell, "Effects of Diffusion on Free Precession in Nuclear Magnetic Resonance Experiments", *Phys. Rev.*, 1954, **94**, 630–638.

[13] E. L. Hahn, "Spin Echoes", *Phys. Rev.*, 1950, **80**, 580–594.

[14] P. T. Callaghan, *Principles of Nuclear Magnetic Resonance Microscopy*, Clarendon Press, New Ed edition, 1993.

[15] O. W. Sørensen, G. W. Eich, M. H. Levitt, G. Bodenhausen and R. R. Ernst, "Product Operator Formalism for the Description of NMR Pulse Experiments", *Prog. Nucl. Magn. Reson. Spectrosc.*, 1984, **16**, 163–192.

[16] S. Meiboom and D. Gill, "Modified Spin-Echo Method for Measuring Nuclear Relaxation Times", *Rev. Sci. Instrum.*, 1958, **29**, 688–691.

[17] K. Takegoshi, K. Ogura and K. Hikichi, "A Perfect Spin Echo in a Weakly Homonuclear J-Coupled Two Spin-1/2 System", *J. Magn. Reson.*, 1989, **84**, 611–615.

[18] P. C. M. van Zijl, C. T. W. Moonen and M. von Kienlin, "Homonuclear J Refocusing in Echo Spectroscopy", *J. Magn. Reson.*, 1990, **89**, 28–40.

[19] J. A. Aguilar, M. Nilsson, G. Bodenhausen and G. A. Morris, "Spin Echo NMR Spectra without J Modulation", *Chem. Commun.*, 2012, **48**, 811–813.

[20] J. D. Wilson, "Statistical Approach to the Solution of First-Kind Integral Equations Arising in the Study of Materials and Their Properties", *J. Mater. Sci.*, 1992, **27**, 3911–3924.

[21] J. Mitchell, T. C. Chandrasekera and L. F. Gladden, "Numerical Estimation of Relaxation and Diffusion Distributions in Two Dimensions", *Prog. Nucl. Magn. Reson. Spectrosc.*, 2012, **62**, 34–50.

[22] D. Bernin and D. Topgaard, "NMR Diffusion and Relaxation Correlation Methods: New Insights in Heterogeneous Materials", *Curr. Opin. Colloid Interface Sci.*, 2013, **18**, 166–172.

[23] P. T. Callaghan, *Translational Dynamics and Magnetic Resonance: Principles of Pulsed Gradient Spin Echo NMR*, OUP Oxford, Oxford ; New York, 2011.

[24] Y. Q. Song, L. Venkataramanan, M. D. Hürlimann, M. Flaum, P. Frulla and C. Straley, "T1–T2 Correlation Spectra Obtained Using a Fast Two-Dimensional Laplace Inversion", *J. Magn. Reson.*, 2002, **154**, 261–268.

[25] C. I. Robertson, Thesis, University of Cambridge, 2018.

[26] L. Venkataramanan, Y. Q. Song and M. D. Hurlimann, "Solving Fredholm Integrals of the First Kind with Tensor Product Structure in 2 and 2.5 Dimensions", *IEEE Trans. Signal Process.*, 2002, **50**, WOS:000174935200003, 1017–1026.

[27] D. Weber, J. Mitchell, J. McGregor and L. F. Gladden, "Comparing Strengths of Surface Interactions for Reactants and Solvents in Porous Catalysts Using Two-Dimensional NMR Relaxation Correlations", *J. Phys. Chem. C*, 2009, **113**, 6610–6615.

[28] C. D'Agostino, J. Mitchell, M. D. Mantle and L. F. Gladden, "Interpretation of NMR Relaxation as a Tool for Characterising the Adsorption Strength of Liquids inside Porous Materials", *Chem. Eur. J.*, 2014, **20**, 13009–13015.

[29] *NIST Chemistry WebBook*, `https://webbook.nist.gov/chemistry/` (visited on 07/07/2018).

[30] *CODATA Value: Electron Gyromagnetic Ratio*, `https://physics.nist.gov/cgi-bin/cuu/Value?gammae` (visited on 06/20/2018).

[31] W. S. Price, *NMR Studies of Translational Motion: Principles and Applications*, Cambridge University Press, Cambridge ; New York, 1 edition, 2009.

[32] E. O. Stejskal and J. E. Tanner, "Spin Diffusion Measurements: Spin Echoes in the Presence of a Time-Dependent Field Gradient", *J. Chem. Phys.*, 1965, **42**, 288–292.

[33] J. E. Tanner, "Use of the Stimulated Echo in NMR Diffusion Studies", *J. Chem. Phys.*, 1970, **52**, 2523–2526.

[34] R. M. Cotts, M. J. R. Hoch, T. Sun and J. T. Markert, "Pulsed Field Gradient Stimulated Echo Methods for Improved NMR Diffusion Measurements in Heterogeneous Systems", *J. Magn. Reson.*, 1989, **83**, 252–266.

[35] F. Stallmach and P. Galvosas, "Spin Echo NMR Diffusion Studies", *Annu. Rep. NMR Spectrosc.*, 2007, **61**, 51–131.

[36] G. Zheng and W. S. Price, "Suppression of Background Gradients in (B0 Gradient-Based) NMR Diffusion Experiments", *Concepts Magn. Reson.*, **30A**, 261–277.

Chapter 4

Spin dynamics in restricted and unrestricted liquids

4.1 Structural characteristics of porous solids

Porous solids are primarily characterised by their pore size, porosity, tortuosity and specific surface area. [1] The International Union of Pure and Applied Chemistry (IUPAC) categorise porous media according to their pore diameters, d_{pore}:

- Microporous materials: $0.2\,\text{nm} \leq d_{pore} < 2\,\text{nm}$ [2]
- Mesoporous materials: $2\,\text{nm} \leq d_{pore} < 50\,\text{nm}$ [3]
- Macroporous materials: $d_{pore} \geq 50\,\text{nm}$ [4]

The porosity of a material φ describes the void fraction present, and thus relates the total volume of a material V_t to that of its pores V_p according to

$$\varphi = \frac{V_p}{V_t}. \tag{4.1}$$

A more important quantity for our purpose is the effective porosity φ_{eff}, which describes the void fraction of open, interconnected pores within a structure,

$$\varphi_{eff} = \frac{V_{p,open}}{V_t}. \tag{4.2}$$

This parameter avoids characterisation of closed pores, which are inaccessible to molecular liquids; this concept is illustrated in Figure 4.1. The porous network is defined by a tortuosity $\hat{\tau}$ which defines the overall connectivity exhibited by the pore structures. More formally, the tortuosity of a given pathway is equal to the ratio

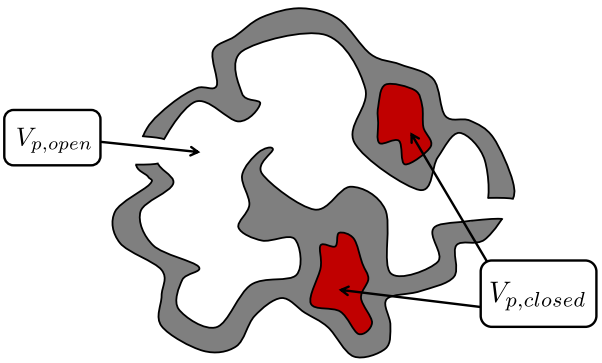

Figure 4.1: Illustration of open (white) and closed (red) pores.

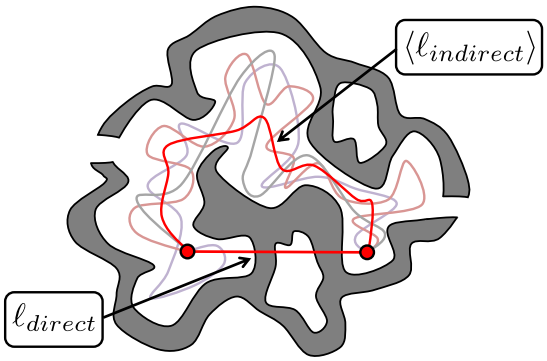

Figure 4.2: Illustration of the direct and indirect path lengths which define the tortuosity of a porous network.

between the lengths of a straight path connecting two arbitrary points within the structure ℓ_{direct}, and the average length of the indirect paths a particle may take to travel between these points $\langle \ell_{indirect} \rangle$,

$$\hat{\tau} = \frac{\langle \ell_{indirect} \rangle}{\ell_{direct}}. \tag{4.3}$$

An example of such a pathway is illustrated in Figure 4.2, from which we can see $\langle \ell_{indirect} \rangle \geq \ell_{direct}$ such that $\hat{\tau} \geq 1$. The tortuosity of a pore structure is defined by this relation, averaged over all possible start and end points within the material.

The specific surface area of a material is defined as the total surface area per unit mass ($m^2\ g^{-1}$). Together with the open pore volume, the specific surface area defines the surface-to-volume ratio S/V of a porous structure.

4.2 Nuclear spin relaxation

Through-space dipole-dipole interactions provide the primary contribution to $I = \frac{1}{2}$ nuclear spin relaxation in the liquid phase. [5, 6] For spin-lattice (longitudinal, $i = 1$) or spin-spin (transverse, $i = 2$) ^{1}H (proton) relaxation occurring with characteristic time constants T_i, the rates of nuclear spin relaxation $R_i = 1/T_i$ can be considered as a sum of intramolecular and intermolecular contributions,

$$R_i = \frac{1}{T_i} = \underbrace{\frac{1}{T_{i,intra}}}_{\text{rotation}} + \underbrace{\frac{1}{T_{i,inter}}}_{\text{translation}}. \tag{4.4}$$

Here intramolecular relaxation is facilitated by rotational dynamics, while intermolecular relaxation is dominated by translational motion. [6] The relative contributions of intra- and intermolecular relaxation are dependent on the exact system under study, as well as the spectrometer field strength employed. [7]

4.2.1 Intramolecular relaxation

Within unrestricted liquids it is typical to consider only intramolecular relaxation, which arises from rotational dynamics. Indeed, Abragam predicted in his seminal text that relaxation due to intramolecular interactions should contribute approximately 70 % of overall observed relaxation in the liquid phase. [8] Detailed molecular dynamics simulations have since confirmed this prediction; for example, Singer *et al.* showed that intramolecular spin-pair interactions contribute around 60 % of the overall spin relaxation in liquid water and *n*-pentane, with a significant increase in this contribution observed with increasing molecular size. [9] Work by Madhavi *et al.* suggests that by taking into account the discrete hydrogen bonding dynamics which dominate molecular rotational motion in liquid water that intramolecular $^{1}\mathrm{H}-^{1}\mathrm{H}$ relaxation actually constitutes 88 % of the observed relaxation at 298 K. [10]

The rates of intramolecular relaxation occurring between ^{1}H spin pairs in an unrestricted liquid are given by [5, 6]

$$\frac{1}{T_{1,intra}} = \frac{3}{10}\left(\frac{-\mu_0\hbar}{4\pi}\frac{\gamma^2}{r^3}\right)^2\left\{J_{intra}(\omega_0) + 4J_{intra}(2\omega_0)\right\}, \tag{4.5}$$

$$\frac{1}{T_{2,intra}} = \frac{3}{20}\left(\frac{-\mu_0\hbar}{4\pi}\frac{\gamma^2}{r^3}\right)^2\left\{3J_{intra}(0) + 5J_{intra}(\omega_0) + 2J_{intra}(2\omega_0)\right\}. \tag{4.6}$$

Here $\mu_0 = 4\pi \times 10^{-7}\,\mathrm{J\ A^{-2}}$ is the permeability of free space, γ is the gyromagnetic ratio of spin ^{1}H, $\hbar = h/2\pi$ where h is Plank's constant, and r is the internuclear distance. The dipole-dipole coupling constant introduced in Chapter 3 (Equation 3.67) is clearly apparent in parentheses. Perhaps the most important feature of Equations 4.5 and 4.6 are the intramolecular spectral density functions $J_{intra}(\omega)$, which describe the relationship between relaxation rates, molecular motion and

magnetic field strength. Most notably, these functions dictate the frequencies of molecular motion responsible for the random field nuclear spin relaxation introduced in Chapter 3. Various expressions exist throughout the literature for $J_{intra}(\omega)$; however, in order to define some of these we first need to consider the concept of random field relaxation in a little more detail.

Bloembergen-Purcell-Pound (BPP) theory

The random thermal motion of $I > 0$ spin-containing molecules in the liquid phase leads to the presence of time-dependent microscopic magnetic fields $\mathbf{B}_\mu(t)$, with amplitudes $B_\mu(t)$;[1] examples of such are provided in Figure 4.3a. The time-dependence of $B_\mu(t)$ is described by the intramolecular autocorrelation function $G_{intra}(\tau)$,

$$G_{intra}(\tau) = \langle B_\mu(t) B_\mu(t+\tau) \rangle. \tag{4.7}$$

This function describes the mean square field expressed by two points in time separated by an interval τ. Qualitatively, $G_{intra}(\tau)$ will be large ($\sim \langle B_\mu^2(t) \rangle$) when τ is much smaller than the characteristic time between fluctuations, but small if τ is much longer than this time; the autocorrelation function should therefore be considered as a smoothly decaying function which ranges from $G_{intra}(0) = \langle B_\mu^2(t) \rangle$ to $G_{intra}(\tau \to \infty) \sim 0$. Such a function is well described by the simple exponential

$$G_{intra}^{\mathrm{BPP}}(\tau) = \langle B_\mu^2(t) \rangle \exp\left(\frac{-\tau}{\tau_c}\right), \tag{4.8}$$

which is illustrated in Figure 4.3b. The BPP superscript indicates that this approximation of the autocorrelation function forms part of the so-called BPP theory of nuclear spin relaxation, named after the seminal contribution of Bloembergen, Purcell and Pound. [11] Equation 4.8 introduces the rotational correlation time τ_c, which is of unparalleled importance in the understanding of intramolecular nuclear spin relaxation; the rotational correlation time characterises the rate of the

[1] It is important here to notice a slight change in notation. Generally in this thesis the symbol B has been used to denote the magnitude of the field $\mathbf{B}$. Here, however, we are defining the amplitude of the field, rather than the magnitude, the difference being that the amplitude may take positive or negative values.

random fluctuations responsible for relaxation (Figure 4.3a) and dictates the rate of decay of $G_{intra}(\tau)$ with increasing τ (Figure 4.3b). Fast rotational fluctuations typical of small and unrestricted molecules are characterised by small τ_c and a rapid decay of $G^{\mathrm{BPP}}_{intra}(\tau)$ with increasing τ, while slow rotational fluctuations typical of macromolecules and restricted systems correspond with large τ_c, which leads to a slower decay of the autocorrelation function. More formally, τ_c is equal to the average time taken for a molecule to rotate by one radian through the influence of rotational diffusion[2], and may be estimated from [6]

$$\tau_c = \frac{4\pi\eta r_H^3}{3k_B T}, \tag{4.9}$$

where r_H is the hydrodynamic radius of the molecule in question, η is the viscosity, k_B is the Boltzmann constant and T is the absolute temperature.

Spectral density functions are directly related to the autocorrelation function. In particular, nuclear spin relaxation rates are sensitive to the rates of molecular rotation responsible for random field fluctuations. It follows that spectral density functions may be obtained through the Fourier transformation of $G(\tau)$ according to, [5]

$$J(\omega) = \mathrm{Re}\left\{ 2\int_0^\infty G(\tau)\exp(-i\omega\tau)\, d\tau \right\}, \tag{4.10}$$

of which we are interested in only the real (cosine) part. The factor of 2 takes account of the fact that we would typically choose to integrate over fluctuation frequencies ω between $\tau = 0$ and $\tau = \infty$, thus avoiding the curious concept of negative time steps; $J^{\mathrm{BPP}}_{intra}(\omega)$ is therefore given by twice the non-negative cosine transform of $G^{\mathrm{BPP}}_{intra}(\tau)$, which evaluates to

$$J^{\mathrm{BPP}}_{intra}(\omega) = \langle B^2_\mu(t)\rangle \frac{2\tau_c}{1+\omega^2\tau_c^2}. \tag{4.11}$$

Furthermore, the constant of proportionality $2\langle B^2_\mu(t)\rangle$ is often dropped when considering a qualitative description of random field relaxation, such that we may simply state

$$J^{\mathrm{BPP}}_{intra}(\omega) \propto \frac{\tau_c}{1+\omega^2\tau_c^2}. \tag{4.12}$$

[2]The term rotational diffusion refers to the process by which a particle rotates randomly due to diffusive collisions with surrounding particles.

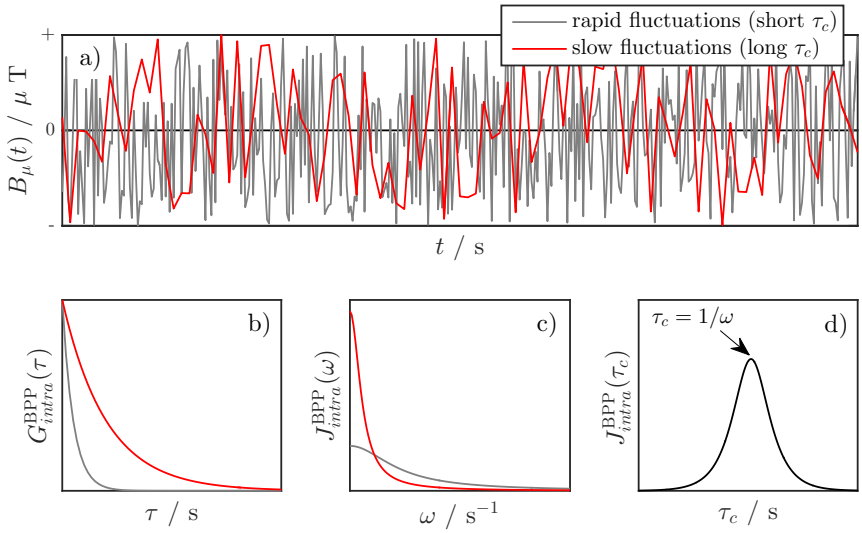

Figure 4.3: a) Illustration of a microscopically fluctuating field due to random rotational motional. The fluctuations are characterised by short (grey) and long (red) rotational correlation times τ_c, which correspond to rapid and slow fluctuations, respectively. b) shows the intramolecular BPP autocorrelation functions resulting from these fluctuations, as defined by Equation 4.8, while c) defines the corresponding spectral density functions. d) highlights that for a given frequency of motion, the maximum spectral density is obtained at the corresponding rotational correlation time.

This function describes the amount of random rotational motion occurring at a particular frequency ω. We can easily see from Figure 4.3c, and from the form of Equation 4.12, that $J^{\mathrm{BPP}}_{intra}(\omega)$ comprises a simple Lorentzian centred about zero frequency. The maximum amount of motion therefore occurs at $\omega = 0$, irrespective of τ_c. $J^{\mathrm{BPP}}_{intra}(\omega)$ then decreases with increasing ω; this decay is rapid for slowly fluctuating systems, illustrating that the majority of motion occurs at low frequency. The decay in J^{BPP}_{intra} is less abrupt for rapidly fluctuating systems, however, demonstrating that more high frequency motion is present. Indeed, the smaller τ_c, the greater the spread of J^{BPP}_{intra} across higher frequencies of motion.

It is of particular use to consider the spectral density function at a single frequency as a function of τ_c; an appropriate example function is shown in Figure 4.3d. Here a maximum in $J^{\mathrm{BPP}}_{intra}(\tau_c)$ is found at the corresponding correlation time. This concept is vital in realising that random field relaxation is dominated by molecular motion occurring at the Larmor frequency; indeed, utilising the above expression for intramolecular spectral density functions we may now express the nuclear spin relaxation time constants T_1 and T_2 as a function of the rotational

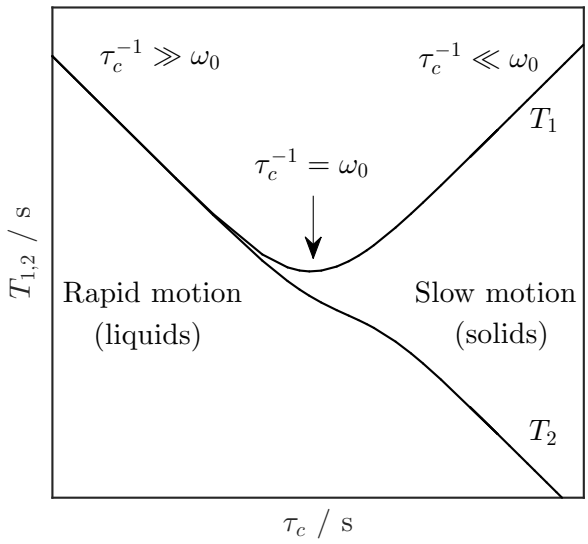

Figure 4.4: Illustration of T_1 and T_2 as a function of the rotational time constant τ_c.

correlation time. This is achieved through the simple combination of Equations 4.5, 4.6 and 4.12, and is illustrated in Figure 4.4. This figure provides a visual introduction to the important concept of motional regimes. For a given experimental Larmor frequency ω_0 there will exist some small τ_c values which dictate that the frequencies of molecular tumbling are greater than the Larmor frequency, $1/\tau_c \gg \omega_0$. This regime is characteristic of small, unrestricted, non-viscous liquids which experience rapid reorientational dynamics, and leads to a convergence of T_1 and T_2 values. Furthermore, as T_2 reaches a maximum for such systems, the full-width half-maximum of the corresponding spectral peaks ($1/\pi T_2^*$) is minimised; this regime is therefore commonly referred to as the motionally narrowed, extreme narrowing or extreme motional narrowing regime. [12] For systems exhibiting large τ_c the frequency of molecular tumbling will often be smaller than the Larmor frequency, $1/\tau_c \ll \omega_0$. This regime is characteristic of highly viscous and severely restricted systems, as well as the solid state, and leads to $T_1 \gg T_2$. These two motional regimes are separated by a minimum in T_1 which lies at $1/\tau_c = \omega_0$; here, the frequency of molecular tumbling exactly matches the experimental Larmor frequency. As T_1 is minimised the longitudinal relaxation rate $1/T_1$ is maximised. It therefore follows that the maximum rate of longitudinal relaxation occurs when molecular tumbling occurs at a comparable rate to the Larmor frequency. While T_2 is also reduced

relative to that observed in the motionally narrowed regime, it does not reach a minimum; rather, the $3J_{intra}(0)$ component of Equation 4.6 provides T_2 with sensitivity to extremely slow motions, such that $1/T_2$ continues to increase with large τ_c.

Lipari-Szabo theory

While the spectral density function provided in Equation 4.12 has been extensively applied in the description of NMR relaxation rates it is strictly only valid for spherical molecules, and is therefore limited in its ability to represent large, asymmetric (anisotropic) molecules, or those containing long, flexible chains. [13] The Lipari-Szabo (LS) spectral density function may be employed to consider these more complex systems. [14, 15] The LS theory of nuclear spin relaxation – also referred to as the LS model free approach – assumes that internal motions are uncorrelated from those of the whole molecule. The total intramolecular autocorrelation function of the system $G^{\mathrm{LS}}_{intra,t}(\tau)$ may therefore be considered a product of autocorrelation functions describing internal $G^{\mathrm{LS}}_{intra,int}(\tau)$ and overall molecular $G^{\mathrm{LS}}_{intra,mol}(\tau)$ motion,[14]

$$G^{\mathrm{LS}}_{intra,t}(\tau) = G^{\mathrm{LS}}_{intra,int}(\tau)G^{\mathrm{LS}}_{intra,mol}(\tau). \tag{4.13}$$

The behaviour of these components can be considered on the basis of BPP theory described above. For instance, the $G^{\mathrm{LS}}_{intra,mol}$ will exhibit very similar behaviour to G^{BPP}_{intra}, which describes the correlation of isotropic fluctuations in spherically symmetry liquids,

$$G^{\mathrm{LS}}_{intra,mol}(\tau) \propto \exp\left(\frac{-\tau}{\tau_{mol}}\right). \tag{4.14}$$

Here τ_{mol} is the correlation time for overall molecular motion and is equivalent to τ_c. The autocorrelation function defining internal motion will take a similar form, however, in the limit $\tau \to \infty$ the decay of this component may be limited by the anisotropy of the internal motions present. The limiting value $G^{\mathrm{LS}}_{intra,int}(\tau \to \infty) = S^2$ is known as the generalised order parameter and takes values between 0 and 1; $S^2 = 1$ indicates a total absence of internal motion, such that no decay

in $G^{\mathrm{LS}}_{intra,int}(\tau)$ is observed from $G^{\mathrm{LS}}_{intra,int}(0) = 1$, while $S^2 = 0$ is characteristic of totally unrestricted internal motion. This autocorrelation function therefore has the form [14]

$$G^{\mathrm{LS}}_{intra,int}(\tau) = S^2 + (1 - S^2)\exp\left(\frac{-\tau}{\tau_{int}}\right), \tag{4.15}$$

where τ_{int} is the correlation time defining the frequency of internal motions. The Fourier transformation of Equation 4.15 according to Equation 4.10 gives the LS spectral density function, [14]

$$J^{\mathrm{LS}}_{intra}(\omega) \propto \frac{S^2\tau_{mol}}{1 + \tau^2_{mol}\omega^2} + \frac{(1 - S^2)\tau_t}{1 + \tau^2_t\omega^2}, \tag{4.16}$$

where the time constant τ_t is defined according to

$$\frac{1}{\tau_t} = \frac{1}{\tau_{int}} + \frac{1}{\tau_{mol}}. \tag{4.17}$$

4.2.2 Intermolecular relaxation

Intermolecular relaxation in unrestricted liquids will not be treated in significant detail within this thesis, and is generally unimportant relative to intramolecular or surface-adsorbate interactions. The relaxation rates have a similar – albeit more approximate – form to the equations governing intramolecular relaxation, and may be expressed as [16–18]

$$\frac{1}{T_{1,inter}} \approx \frac{3}{10}\frac{N_H}{\lambda^3}\left(\frac{-\mu_0}{4\pi}\hbar\gamma^2\right)^2\left\{J_{inter}(\omega_0) + 4J_{inter}(2\omega_0)\right\} \tag{4.18}$$

$$\frac{1}{T_{2,inter}} \approx \frac{3}{20}\frac{N_H}{\lambda^3}\left(\frac{-\mu_0}{4\pi}\hbar\gamma^2\right)^2\left\{3J_{inter}(0) + 5J_{inter}(\omega_0) + 2J_{inter}(2\omega_0)\right\}. \tag{4.19}$$

Here, N_H is the number of ^{1}H spins *per* unit volume and λ defines the distance of closest approach between them.

Analytic expressions for the intermolecular spectral density functions $J_{inter}(\omega)$ are significantly more complex than those for intramolecular interactions, and are typically derived using a model known as the force-free hard sphere approach. [19] Polnaszek *et al.* suggest an appropriate expression for $J_{inter}(\omega)$ is [20]

$$J_{inter}(\omega) \propto \frac{1 + 5u/8 + u^2/8}{1 + u + u^2/2 + u^3/6 + 4u^4/81 + u^5/81 + u^6/648}, \tag{4.20}$$

where $u = \sqrt{2\omega\tau_d}$. Here τ_d is a translational correlation time defined as

$$\tau_d = \frac{\lambda^2}{\mathcal{D}_{12}}, \tag{4.21}$$

where $\mathcal{D}_{12} = \mathcal{D}_1 + \mathcal{D}_2$ is the mutual diffusion coefficient defining the relative motion of molecules with self-diffusion coefficients $\mathcal{D}_1$ and $\mathcal{D}_2$; for a single molecular species this is equal to twice the self-diffusion coefficient of the unrestricted liquid, $\mathcal{D}_{12} = 2\mathcal{D}_0$.

4.2.3 Relaxation in porous media

The nuclear spin relaxation characteristics of species confined to heterogeneous porous media can provide valuable information on the effects of pore structure and surface interactions on molecular dynamics. Here, of course, we are interested in the evolution of such effects within liquid-saturated mesoporous heterogeneous catalyst materials; however, much of the relevant theory required to analyse and interpret such characteristics can be borrowed from other fields. Prevalent areas of theoretical insight include rock wettability studies for the hydrocarbon recovery industry [21–24] and the characterisation of cement hydration kinetics. [25, 26] The relevant theories which emerge from such fields are introduced below.

The observed rates of nuclear spin relaxation $1/T_{i,obs}$ $(i = 1, 2)$ in liquid-saturated porous media are given by a linear combination of bulk (unrestricted liquid), surface and confinement effects, [22, 27]

$$\frac{1}{T_{i,obs}} \approx \frac{1}{T_{i,bulk}} + \frac{\alpha\rho_i}{\ell_s}\frac{1}{1 + \dfrac{\rho_i\ell_s}{2\mathcal{D}_o}} \tag{4.22a}$$

$$\approx \underbrace{\frac{1}{T_{i,bulk}}}_{\text{unrestricted}} + \underbrace{\frac{2\alpha\rho_i}{d_{pore}}}_{\text{surface}} + \underbrace{\frac{8\alpha\mathcal{D}_0}{d_{pore}^2}}_{\text{confinement}}. \tag{4.22b}$$

Here $\ell_s \sim d_{pore}/2$ is a characteristic length scale of the restricting pore geometry and α is a shape parameter which takes values of 1, 2 or 3 for planar, cylindrical of spherical pore geometries, respectively. [22] When saturated with a given molecular

liquid each of these pore geometries can be considered to form an adsorbed surface layer of thickness δ, in which the molecular dynamics will differ from that of the bulk-like liquid towards the centre of the pores. The surface relaxivities $\rho_i = \delta/T_{i,surf}$ exhibited by a particular pore surface are given by the rates of nuclear spin relaxation within this layer $1/T_{i,surf}$, multiplied by its thickness, and define the ability of the surface to facilitate enhanced rates relaxation. $\mathcal{D}_0$ is again the self-diffusion coefficient of the unrestricted liquid and d_{pore} is the modal pore diameter expressed by the porous material under study.

Equation 4.22a suggests two limiting cases for nuclear spin relaxation occurring within liquid-saturated mesoporous systems. These limiting cases may be characterised by the dimensionless variable known as the control parameter, [28, 29]

$$\kappa \equiv \frac{\rho_i \ell_s}{\mathcal{D}_0}, \tag{4.23}$$

which provides a simple comparison between the rates of relaxation within the adsorbed surface layer and the rate of diffusive displacement across the pore. A slow-exchange condition is characterised by $\kappa \gg 1$; in this case the rates of relaxation within the adsorbed surface layer are significantly more rapid than the rate of diffusive translation across the pore structure. The observed relaxation is therefore said to be diffusion-limited and Equation 4.22b reduces to

$$\frac{1}{T_{i,obs}} \approx \frac{1}{T_{i,bulk}} + \frac{8\alpha\mathcal{D}_0}{d_{pore}^2}. \tag{4.24}$$

Diffusion-limited relaxation is known to be dominant for systems exhibiting strong surface relaxivity (large ρ_i), slowly diffusing molecular species and/or large pores,[27] and is typically characterised by observing a linear correspondence between $T_{i,obs}$ and d_{pore}^2. [22]

A fast-exchange condition is characterisated by $\kappa \ll 1$; in this case the rates of diffusive displacement across the pore structures are far more rapid that the rates of nuclear spin relaxation occurring within the adsorbed surface layer. The observed relaxation is therefore said to be surface-limited and Equation 4.22b reduces to

$$\frac{1}{T_{i,obs}} \approx \frac{1}{T_{i,bulk}} + \frac{2\alpha\rho_i}{d_{pore}}. \tag{4.25}$$

In this case measured relaxation rates can provide information on molecular dynamics at the pores surface. Surface-limited relaxation is dominant for small pores, rapidly diffusing species and/or weak surface relaxivity, [27] and is typically characterised by observing a linear correspondence between $T_{i,obs}$ and d_{pore}.[22] Further, if we assume spherical pores ($\alpha = 3$) and recall that the surface-to-volume ratio of a sphere is $6/d_{sphere}$, then the surface-limited expression becomes

$$\frac{1}{T_{i,obs}} \approx \frac{1}{T_{i,bulk}} + \frac{S}{V}\rho_i, \tag{4.26}$$

illustrating sensitivity to the S/V ratio of the pore structure under investigation. If we then take account of the fact that there must exist a different fraction of molecules in the adsorbed surface layer P to within the bulk-like liquid towards the centre of the pores $1 - P$, and recognise that $P = \delta S/V$, we arrive at a complete expression for surface-limited nuclear spin relaxation within a liquid-saturated pore system undergoing biphasic fast exchange between adsorbed and unrestricted liquid,[3]

$$\frac{1}{T_{i,obs}} = \frac{1-P}{T_{i,bulk}} + \frac{P}{T_{i,surf}}. \tag{4.27}$$

The relevant components of this expression are illustrated in Figure 4.5.

Relaxation as a surface sensitive probe

The realisation of Equation 4.27 is vital in the application of nuclear relaxation as a surface sensitive tool. For systems within the fast exchange limit – which is often the case for liquid-saturated catalyst materials – it allows us to interpret the measured relaxation time characteristics as a non-invasive probe of pore structure and surface dynamics. Of particular importance in this interpretation is the concept of surface relaxivity ρ_i, and the idea that nuclear spin relaxation is typically more rapid within the adsorbed surface layer than away from the pore surface. Two clear mechanisms

[3] A short proof for this expression is provided in Appendix C .

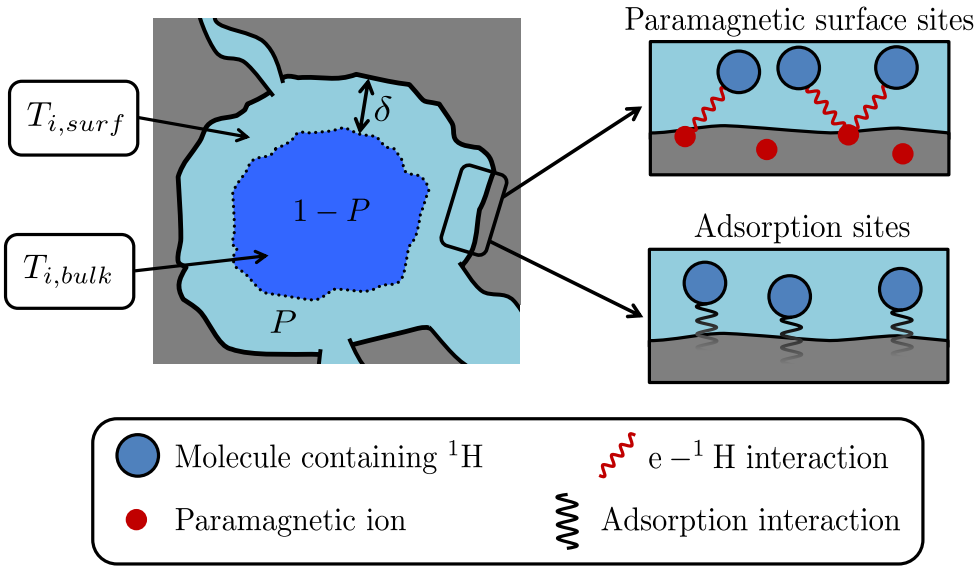

Figure 4.5: Illustration of a pseudo-spherical biphasic pore system according to Equation 4.27. An adsorbed surface layer of thickness δ and population P forms due to adsorption interactions at the solid-liquid interface, and exhibits relaxation rates $1/T_{i,surf}$ $(i = 1, 2)$. A bulk-like population $1 - P$ remains towards the centre of the pore and has relaxation rates $1/T_{i,bulk}$. Interactions with the pore surface facilitate enhanced nuclear spin relaxation within the adsorbed surface layer such that $1/T_{i,surf} \gg 1/T_{i,bulk}$. In the presence of paramagnetic impurities this enhanced surface relaxivity originates from encounters with paramagnetic relaxation sinks. In the absence of paramagnetic sites adsorption interactions may facilitate enhanced surface relaxation due to changes in molecular mobility.

facilitate these enhanced relaxation rates, both of which involve so-called relaxation sinks at the pore surface:

1. For liquids imbibed within porous media that contain paramagnetic ions within their solid matrix, relaxation rates within the adsorbed surface layer are enhanced due to encounters with paramagentic relaxation sinks. [30] Common examples include Fe^{3+} and Mn^{2+} species which have be observed within cement pastes and sedimentary rocks. [21, 24, 25, 31]

2. For liquids imbibed within porous media without significant paramagnetic contaminants, adsorption interactions occuring at the solid-liquid interface facilitate enhanced rates of nuclear spin relaxation through a reduction in rotational and translational mobility. [22, 32–34] This is generally taken to be the dominant source of surface relaxivity within liquid-saturated heterogeneous catalyst materials. [35–37]

These relaxation mechanisms are illustrated in Figure 4.5. An important result of the enhanced surface relaxation rates which result from these mechanisms is that $T_{i,surf} \ll T_{i,bulk}$ (or, alternatively $1/T_{i,surf} \gg 1/T_{i,bulk}$). Provided the S/V of the porous material under study is sufficiently large we find that $P/(T_{i,surf}) \gg (1-P)/T_{i,bulk}$, such that the relaxation of confined species experiencing relaxation within the fast exchange limit may be expressed as

$$\frac{1}{T_{i,obs}} \approx \frac{\delta S}{V}\frac{1}{T_{i,surf}}. \tag{4.28}$$

The observed relaxation characteristics may therefore be considered inherently surface sensitive. Equation 4.28 will be utilised in subsequent chapters to provide direct insight into the adsorption mechanisms and energetics which dictate molecular dynamics within the adsorbed surface layer.

Surface spectral density functions

To interpret nuclear spin relaxation phenomena in terms of molecular surface dynamics, careful consideration of the form of the dominant spectral density functions is required. Recalling the sensitivity of T_1 to molecular motion occurring at frequencies similar to the Larmor frequency, spin-lattice relaxation measurements performed at high magnetic field strength will exhibit sensitivity to rapid surface dynamics, typically associated with molecular tumbling. In this case the relevant spectral density functions might be considered equivalent to the intermolecular BPP or LS approaches introduced previously; D'Agostino *et al.* recently utilised this approach in the analysis of a wide range of liquid-phase adsorbates within several common mesoporous catalyst supports. [38] Alternatively, for T_1 measurements performed at low magnetic field strength, and T_2 measurements in general, surface relaxation measurements will exhibit sensitivity to the slow molecular dynamics associated with translational motion of adsorbed species. In this case we may consider surface relaxation rates on basis of the general expression [39, 40]

$$\frac{1}{T_{i,surf}} = \frac{1}{T_{i,b\ell}} + \frac{1}{T_{i,\ell\ell}} + \frac{1}{T_{i,S\ell}}, \tag{4.29}$$

which details the relevant intermolecular contributions to surface relaxation. Here $1/T_{i,b\ell}$ is the relaxation rate contribution from spin-pair interactions between the unrestricted bulk (b) and the adsorbed surface layer (ℓ); $1/T_{i,\ell\ell}$ is a similar contribution from spin-pair interactions within the adsorbed surface layer itself. These terms are therefore similar in nature to the intermolecular relaxation rates arising from molecular diffusion in unrestricted liquids. The primary source of enhanced surface relaxation comes from the term $1/T_{i,S\ell}$, which describes the relaxation contribution from interactions with static spins (S) on the solid surface. In analogy to Figure 4.5 this term may be further expanded such that

$$\frac{1}{T_{i,S\ell}} = \frac{1}{T_{i,e\ell}} + \frac{1}{T_{i,H\ell}}. \tag{4.30}$$

Here $1/T_{i,e\ell}$ describes the relaxation rate contribution from encounters with paramagnetic surface species while $1/T_{i,H\ell}$ indicates the contribution from homonuclear spin-pair encounters between the adsorbing species and surface-bound protons. Recalling the large gyromagnetic ratio of the electron and the correspondingly significant relaxation capabilities of paramagnetic ions, in the presence of paramagnetic species surface relaxation rates are $1/T_{i,surf} \sim 1/T_{i,e\ell}$. [40] Korb and co-workers have shown that an appropriate spectral density function for such relaxation is [22, 23, 41–43]

$$J_{surf}(\omega) = \tau_m \ln\left\{\frac{1+\omega^2\tau_m^2}{(\tau_m/\tau_s)^2+\omega^2\tau_m^2}\right\}, \tag{4.31}$$

where we may recall from Chapter 2 that τ_m and τ_s are the adsorption site residence time and surface lifetime of the adsorbate, respectively. Of more relevance to the present work is surface relaxation in the absence of significant paramagnetic impurities. In this case the dominant surface relaxation interaction comes from adsorption interactions with polar ^{1}H-containing surface groups which commonly terminate pore surfaces. [35–37] Importantly for our purposes, Mitchell *et al.* showed that the spectral density function in Equation 4.31 may also be applied to such systems. [36] By extending the relevant expressions for paramagnetic surface relaxation [6, 22] we find that the rates of homonuclear surface relaxation may be

given by [36]

$$\frac{1}{T_{1,surf}} \approx \frac{3}{10}\frac{\pi\sigma}{\lambda^4}\left(\frac{-\mu_0}{4\pi}\hbar\gamma^2\right)^2\left\{J_{surf}(\omega_0) + 4J_{surf}(2\omega_0)\right\} \tag{4.32}$$

$$\frac{1}{T_{2,surf}} \approx \frac{3}{20}\frac{\pi\sigma}{\lambda^4}\left(\frac{-\mu_0}{4\pi}\hbar\gamma^2\right)^2\left\{3J_{surf}(0) + 5J_{surf}(\omega_0) + 2J_{surf}(2\omega_0)\right\}, \tag{4.33}$$

where σ is the surface spin density. [22]

Internal gradients

A complete description of surface sensitive nuclear spin relaxation must also acknowledge the influence of magnetic susceptibility differences at the solid-liquid interface. The magnetic susceptibility of a material χ is a dimensionless parameter which expresses the response of that material to the presence of a magnetic field. [44] In particular, this parameter defines how readily a material develops a magnetic moment upon immersion within a magnetic field; it is important to note that such behaviour is usually dictated by the electronic structure of the material, rather than its nuclear magnetism. [5] Solid-liquid interfaces are of course common throughout liquid-saturated porous media, and exhibit susceptibility differences $\Delta\chi$ defined by the susceptibilities of the porous solid and the imbibed liquid. These susceptibility differences result in the formation of effective internal magnetic field gradients g_{eff} within the pore structure. In the presence of these internal gradients we must refine our understanding of T_2^* defined in Chapter 3 (Equation 3.43); in liquid-saturated porous media this time constant is defined according to [45]

$$\frac{1}{T_2^*} = \frac{1}{T_2} + \frac{1}{T_2^{'}} + \frac{1}{T_2^{''}}, \tag{4.34}$$

where we may recall from Chapter 3 that $1/T_2^{'} = \gamma\Delta B_0$ represents transverse nuclear spin dephasing to due inhomogeneity of the static magnetic field B_0. The additional term $1/T_2^{''} = \gamma\Delta\chi B_0$ represents additional dephasing resulting from internal gradients of strength $g_{eff} \sim \Delta\chi B_0$. [46] As $1/(\pi T_2^*)$ determines the full-width half-maximum of spectral peaks within the frequency domain, it follows that non-negligible $\Delta\chi$ values result in additional peak broadening beyond that

encountered in the analysis of unrestricted liquids; indeed it is well-acknowledged that liquids imbibed within porous media exhibit broadened NMR spectra, often resulting in a significant loss of chemical shift resolution.

The presence of internal gradients is of further importance when attempting to measure transverse nuclear spin relaxation within liquid-saturated mesoporous media. Recalling the measurement of T_2 *via* application of either the CPMG (Figure 3.14) or PROJECT (Figure 3.16b) NMR pulse sequences described in Chapter 3, the sample magnetisation is excited into the transverse plane by a 90° RF pulse; this is followed by the acquisition of a series of n echoes separated by an echo time t_e, the normalised signal from which attenuates according to

$$\frac{S(nt_e)}{S_0} = \exp\left(\frac{-nt_e}{T_2}\right). \tag{4.35}$$

The echo train of the chosen pulse sequence acts to refocus any $T_2^{'}$ relaxation, such that signal attenuation occurs due to T_2 alone. However, if self-diffusion through internal field gradients occurs during such measurements then additional transverse dephasing of the nuclear spin ensemble may occur between each echo. This diffusive attenuation follows [47]

$$\frac{S(nt_e)}{S_0} = \exp\big(-ant_e^k\big), \tag{4.36}$$

where the parameters a and k are related to the self-diffusive behaviour of the confined liquid as well as the structure of the confining porous solid. The overall signal attenuation is therefore [47]

$$\frac{S(nt_e)}{S_0} = \exp\left(\frac{-nt_e}{T_2} - ant_e^k\right), \tag{4.37}$$

and results in the measurement of an effective transverse relaxation time constant $T_{2,eff} \leq T_{2,obs}$. In extension to Equation 4.28 this effective time constant is given by [48]

$$\frac{1}{T_{2,eff}} \approx \frac{\delta S}{V}\frac{1}{T_{2,surf}} + at_e^{(k-1)}. \tag{4.38}$$

To define the parameters a and k we must first consider a series of appropriate length scales which result from self-diffusion during a given T_2 measurement. [12] In particular, we must define a diffusion path length $\ell_e \approx \sqrt{\mathcal{D}_0 t_e}$ which determines the root mean squared displacement during the echo time t_e of the CPMG ($t_e = 2\tau_2$) or PROJECT ($t_e = 4\tau_2$) pulse sequence, and a dephasing path length $\ell_g \approx \sqrt[3]{\mathcal{D}_0/(\gamma g_{eff})}$ which determines the distance molecules must diffuse through a gradient of strength g_{eff} for their spins to dephase by 2π radians. [49] Together with the structural length scale $\ell_s \sim d_{pore}/2$ defined previously, these length scales may be used to further our interpretation of Equation 4.38. Indeed the relative magnitudes of ℓ_s, ℓ_e and ℓ_g govern the influence of diffusion on $T_{2,eff}$. [45] When one of these length scales is less that the others by at least an order of magnitude then this diffusive behaviour is characterised by a defined regime: [50]

- The short time (ST) regime is observed when $\ell_e \ll \ell_s, \ell_g$. This regime corresponds to large pores and weak internal gradients, and is considered similar to diffusion through a constant gradient. Here $k = 3$ and $a = \mathcal{D}_0 \gamma^2 g_{eff}^2/12$. [51]

- The localisation (LOC) regime is observed when $\ell_g \ll \ell_e, \ell_s$. This regime corresponds to strong internal gradients which vary over the dephasing path length ℓ_g. Spin dephasing occurs rapidly within these localised regions resulting in non-uniform magnetisation across individual pores. Here $k = 1$ and $a \approx \sqrt{\gamma \Delta\chi B_0 \mathcal{D}_0}/\ell_s$. [52–54]

- The motional averaging (MAV) regime is observed when $\ell_s \ll \ell_g, \ell_e$. This regime corresponds to samples exhibiting small pores, such that each spin explores the pore multiple times during t_e. The magnetisation is insensitive to localised internal gradients and is instead sensitive to an average effective gradient $\overline{g}$ across the pore. Here $k = 1$ and $a \approx \gamma^2 \overline{g}^2 \ell_s^4/(120\mathcal{D}_0)$. [55]

These diffusive regimes are illustrated in Figure 4.6; however, it should be noted that the exact limits of these regimes are not well-defined. [48] Outside of these regimes $1 < k \leq 3$, but an analytical form of a is generally unknown, except that $\sqrt[k]{a}$ has units of s^{-1}. [47]

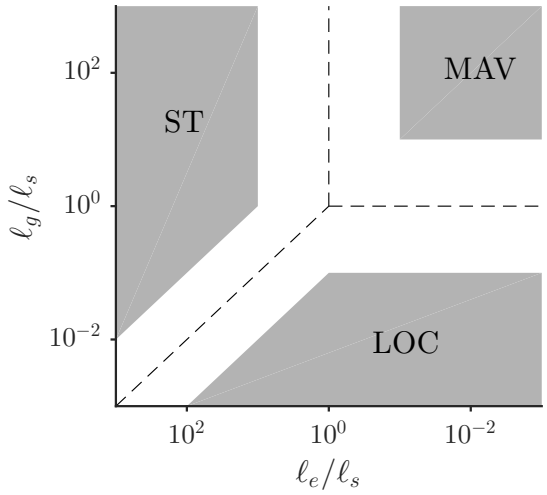

Figure 4.6: Illustration of the diffusion regimes MAV, ST and LOC, defined by the relative magnitudes of the length scales ℓ_s, ℓ_e and ℓ_g. Shaded areas define regions where these diffusive regimes are expected to apply; however, the limits of these regimes are poorly defined. Dashed lines indicate regions of equivalence between length scales. Adapted from Mitchell *et al.* [48].

Mitchell *et al.* showed that it may be possible to remove the influence of internal gradients on the measurement of T_2 through separation of the relaxation and diffusion contributions to the acquired signal described in Equation 4.37. [47, 48, 56] The proposed method explores the echo time dependence of the diffusive exponent (Equation 4.36) through the measurement of a series of CPMG or PROJECT echo trains with different values of t_e; when $k > 1$ this data may then be used to separate and remove the influence of diffusive attenuation on the acquired T_2 relaxation data. However, in the case that $k = 1$, corresponding to either the LOC or MAV regimes, Equation 4.37 reduces to

$$\frac{S(nt_e)}{S_0} = \exp\left(- nt_e \left\{ \frac{1}{T_2} + a \right\} \right), \tag{4.39}$$

and the contributions of relaxation and diffusion to the acquired data become indistinguishable.

An important realisation here is that the small pores associated with mesoporous materials means that liquid-saturated heterogeneous catalyst materials often fall close to, or within the MAV regime. [47] As a result, it is often the case that the influence of diffusion through internal gradients cannot be removed from the

acquired T_2 data when studying such systems. Recalling that $a \approx \gamma^2 \overline{g}^2 \ell_s^4/(120\mathcal{D}_0)$, the measured T_2 relaxation within the MAV regime follows

$$\frac{1}{T_{2,eff}} \approx \frac{\delta S}{V}\frac{1}{T_{2,surf}} + \frac{\gamma^2 \overline{g}^2 \ell_s^4}{120\mathcal{D}_0}. \tag{4.40}$$

As such, this influence of diffusive attenuation may be minimised by reducing the magnitude of $\overline{g}$. This can often be achieved by performing experiments at an appropriately low magnetic field strength; however, careful consideration of the possible effects of this additional transverse relaxation may be required at high field.

We note for completeness that the spin-lattice relaxation time constant T_1 is unaffected by the presence of internal gradients. [45, 46] It follows that T_1 provides an attractive option for performing relaxation studies on liquid saturated mesoporous catalyst materials at high field; the results described in Chapter 5 explore how such measurements can provide insight into molecular dynamics at the pore surface.

4.2.4 Limitations of surface relaxation measurements

It is appropriate at this stage to briefly summarise some of the limitations one may experience while performing nuclear spin relaxation measurements on heterogeneous catalyst materials. As detailed in the sections above, the relaxation characteristics of liquids confined to mesoporous media may be expressed as a function of pore structure and surface chemistry, as well as the diffusive and adsorptive characteristics of the imbibed liquid. Furthermore, both relaxation rates and the potential for significant magnetic susceptibility artefacts at the solid-liquid interface are dependent on the magnetic field strength used. It therefore follows that the comparison of relaxation measurements performed with varying temperature (as might readily be attempted during an *in situ* analysis) or magnetic field strength may be non-trivial.

Further complications may arise due to the deposition of active species at the pore surface. As several catalytically active metals exhibit ferromagnetism (e.g

Fe, Co and Ni), the analysis of relaxation data associated with liquids confined to supported metal catalysts can present a significant challenge. Indeed, in analogy to the influence of paramagnetic surface ions regularly observed with porous rock and cement samples, encounters with ferromagnetic metal nanoparticles will facilitate rapid relaxation due to the large gyromagnetic ratio of the electron. If such metal species are small and well dispersed across the pore surface then rapid surface diffusion processes will lead to surface relaxation behaviour described by Equation 4.30. As $T_{i,el}^{-1} >> T_{i,H}^{-1}$, the observed surface relaxation will simply be that associated with ferromagnetic species. If the deposited nanoparticles are large, however, then multiple different relaxation behaviours may be observed simultaneously, corresponding to liquids adsorbed at metal and oxide surfaces. Such effects have recently been demonstrated in the case of 1-octene imbibed within mesoporous alumina doped with varying concentrations of paramagnetic $CuSO_4$. [57] Using two-dimensional $T_1 - T_2$ correlation measurements, the authors showed that by increasing the quantity of paramagnetic species at the pore surface a second relaxation correlation peak associated with liquid interactions with the deposit could be identified. While this finding suggests a novel opportunity for relaxation measurements to be of use during catalyst preparation processes, it also demonstrates that such systems can present complex relaxation behaviour, leading to the erroneous interpretation of surface dynamics.

It should also be noted that materials exhibiting significant quantities of paramagnetic or ferromagnetic species may be unsuitable for surface relaxation analysis entirely. Indeed, it must be recalled that the elucidation of surface phenomena may only be obtained from surface-limited systems, such that the observed relaxation behaviour may be characterised by Equation 4.25. Significantly enhanced rates of surface relaxation have the potential to cause diffusion-limited relaxation, wherein the rates of surface relaxation are so rapid that sufficient mixing between the bulk and adsorbed surface layer cannot occur within the measured time constants. In this case the observed relaxation rates are described by Equation 4.24 and depend on the pore size of the confining solid and the diffusion characteristics of the imbibed liquid. This transition has previously been observed by Godefroy

et al.. [22] Here the authors illustrated using a packed bed of calibrated SiC grains reducing – but not eliminating entirely – the amount of paramagnetic species within the sample caused the variation in observed relaxation rates with pore size to change from quadratic from linear, in turn signifying a transition from Equation 4.24 ($T_{i,obs}^{-1} \propto d_{pore}^{-2}$) to Equation 4.25 ($T_{i,obs}^{-1} \propto d_{pore}^{-1}$).

4.3 Diffusion phenomena

4.3.1 Restricted diffusion

The significant physical boundary conditions implied by the presence of pore walls often leads to the observation of restricted diffusion phenomena within liquid-saturated porous media. [12, 58, 59] The information attainable from self-diffusion measurements of such systems is often dependent on the observation time t_Δ over which translational motion is measured. The influence of t_Δ is illustrated in Figure 4.7 for the simple case of an isolated spherical pore with a reflecting boundary. Recalling the Einstein relation for 1D displacement (Equation 3.79), we may characterise possible degrees of diffusive restriction by the dimensionless variable [12, 60]

$$\Xi = \frac{\mathcal{D}_0\, t_\Delta}{\ell_s^2}. \tag{4.41}$$

Equation 4.41 provides a simple comparison between the mean square displacement (MSD) of diffusing molecules with the pore radius $d_{pore}/2$, thereby defining a series of diffusive regimes:

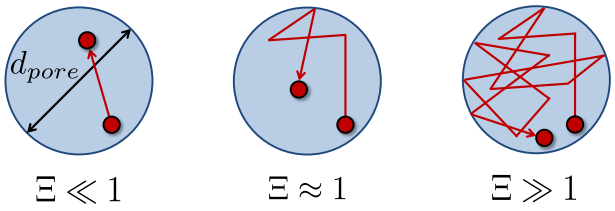

Figure 4.7: Illustration of the effects of time-scale on self-diffusion with an isolated spherical pore with a reflecting boundary. Adapted from Price [58].

- A short-time[4] diffusion limit ($\Xi \ll 1$) is characterised by small $\mathcal{D}_0$, short t_Δ or large d_{pore}. In this regime molecular displacements are not large enough to experience significant restriction through interactions with the pore walls; the observed self-diffusion coefficient is therefore equal to $\mathcal{D}_0$ and is independent of both t_Δ and d_{pore}.

- An intermediate regime ($\Xi \approx 1$) occurs when a significant portion of the molecules experience diffusive restriction due to interactions with the pore walls. The MSD is therefore reduced relative to that of unrestricted diffusion observed over the same t_Δ. This leads to the observation of an effective self-diffusion coefficient $\mathcal{D}_{eff} < \mathcal{D}_0$, which is dependent on both t_Δ and the S/V ratio of the pore according to [12]

$$\mathcal{D}_{eff}(t_\Delta) \approx \mathcal{D}_0\left(1 - \frac{4\sqrt{\mathcal{D}_0 t_\Delta}}{9\sqrt{\pi}}\frac{S}{V}\right). \tag{4.42}$$

- A long-time diffusion limit ($\Xi \gg 1$) is characterised by large $\mathcal{D}_0$, large t_Δ or small d_{pore}. In this regime all of the diffusing molecules are subjected to significant interactions with the pore walls. The MSD is limited to $(d_{pore})^2$ and $\mathcal{D}_{eff} = 0$. [12]

The observed diffusion behaviour is subtly different in the case of an interconnected pore network. Of particular interest is the observed self-diffusion coefficient in the long-time diffusion limit. While this regime is of limited use in the case of isolated pores, in an interconnected porous network the MSD is no-longer limited not by the structural characteristics of each isolated pore, but by the degree of interconnectivity between them. In particular, the effective self-diffusion coefficient $\mathcal{D}_{eff}(t_\Delta \to \infty) \equiv \mathcal{D}_\infty$ is given by [61]

$$\mathcal{D}_\infty = \frac{\mathcal{D}_0\,\varphi_{eff}}{\hat{\tau}}, \tag{4.43}$$

indicating a clear correlation between diffusivity and material structure. A summary of the relationship between MSD, observation time and self-diffusion coefficient is

[4]Note that this regime is different to the ST regime defined in Section 4.2.3.

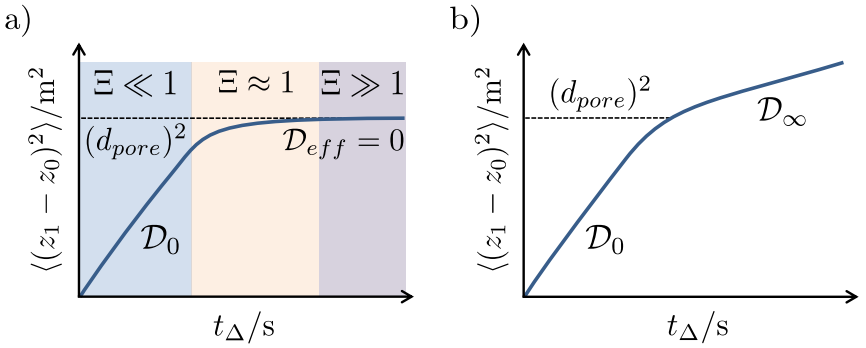

Figure 4.8: Illustration of the relationship between mean squared displacement $\langle (z_1 - z_0)^2 \rangle$, observation time t_Δ and self-diffusion in a) isolated and b) interconnected pore systems of pore diameter d_{pore}. In each case the relevant self-diffusion coefficient is given by the gradient of the blue line. Adapted from Callaghan [62].

illustrated in Figure 4.8 for both isolated and interconnected pore systems. [12]

4.3.2 PFG NMR of restricted diffusion

Equation 4.43 provides a direct link between the tortuosity of a porous network and the molecular self-diffusion coefficient observed in the long-time limit. Clearly molecular displacement – and hence $\mathcal{D}_\infty$ – is reduced by increasing $\hat{\tau}$, and is also dependent on the open void fraction of the interconnected pore system φ_{eff}. It is important to note, however, that $\mathcal{D}_\infty$ measured using PFG NMR will not follow this expression. To derive a more correct relationship we must consider $\mathcal{D}_\infty$ and $\hat{\tau}$ more carefully. First, we note that the void fraction is directly proportional to the nuclear spin density of the sample, $\varphi_{eff} \propto \rho(z_0)$, which we may recall from Equations 3.76 and 3.80 is already contained within the acquired NMR signal aquired during a given PFG NMR experiment. [61] It follows that the effective long-time diffusion coefficient as observed through PFG NMR is

$$\mathcal{D}_\infty^{\mathrm{PFG}} = \frac{\mathcal{D}_\infty}{\varphi_{eff}}. \tag{4.44}$$

Next we must consider the different length scales over which tortuosity may be considered. Rigby and Gladden showed that the tortuosity of a porous catalyst contains contributions from three distinct length scales. [63, 64] In particular, it was observed that $\hat{\tau}$ may be expressed as the product of the tortuosity of these

length scales,

$$\hat{\tau} = \hat{\tau}_m \hat{\tau}_n \hat{\tau}_\mu. \tag{4.45}$$

Here, $\hat{\tau}_m$ is a macroscopic contribution describing the tortuosity exhibited by pore structures ranging over the whole catalyst, and is sensitive to structural characteristics occurring on the mm length scale. [65] $\hat{\tau}_n$ is a mesoscopic contribution and describes structural connectivity over many pore diameters, exhibiting sensitivity to the μm length scale. $\hat{\tau}_\mu$ is a microscopic contribution to the overall tortuosity and is sensitive to the pore scale (nm). As typical PFG NMR experiments probe diffusive displacement on the μm length scale or below, such measurements are insensitive to macroscopic heterogeneity. The tortuosity relevant to PFG NMR experiments is therefore [63]

$$\hat{\tau}^{\mathrm{PFG}} = \hat{\tau}_n \hat{\tau}_\mu. \tag{4.46}$$

Combining these observations we find that [61]

$$\mathcal{D}_\infty^{\mathrm{PFG}} = \frac{\mathcal{D}_0^{\mathrm{PFG}}}{\hat{\tau}^{\mathrm{PFG}}}, \tag{4.47}$$

where $\mathcal{D}_0^{\mathrm{PFG}} \equiv \mathcal{D}_0$.[5] It follows that knowledge of $\mathcal{D}_0^{\mathrm{PFG}}$ and $\mathcal{D}_\infty^{\mathrm{PFG}}$ – as obtained through two separated PFG NMR experiments performed under identical conditions – can provide direct characterisation of $\hat{\tau}^{\mathrm{PFG}}$ *via* the ratio $\mathcal{D}_0^{\mathrm{PFG}}/\mathcal{D}_\infty^{\mathrm{PFG}}$.

Table 4.1 lists recent literature $\hat{\tau}^{\mathrm{PFG}}$ values obtained for a range of common catalysts and catalyst support materials. Small alkanes such as cyclohexane are the most common probe molecule of choice, and are selected as they provide near-negligible adsorption interactions with the porous matrix. Consistency in the extracted values of $\hat{\tau}^{\mathrm{PFG}}$ for a range of different alkanes (e.g. see the data from references [38] and [66] listed in Table 4.1) confirms that the obtained values $\mathcal{D}_0^{\mathrm{PFG}}/\mathcal{D}_\infty^{\mathrm{PFG}}$ are equal to the tortuosity. [38]

[5] In general we will drop the PFG superscripts in the following chapters.

Table 4.1: Literature tortuosity values obtained *via* PFG NMR experiments.

Porous material	Probe liquid	$\hat{\tau}^{\mathrm{PFG}}$	Ref.
TiO_2	cyclohexane	1.60 ± 0.04	[38]
	n-hexane	1.61 ± 0.04	
	n-octane	1.62 ± 0.04	
	n-decane	1.59 ± 0.04	
γ-Al_2O_3	cyclohexane	1.71 ± 0.04	[38]
	n-hexane	1.71 ± 0.04	
	n-octane	1.70 ± 0.04	
	n-decane	1.70 ± 0.04	
SiO_2	cyclohexane	1.60 ± 0.04	[38]
	n-hexane	1.58 ± 0.04	
	n-octane	1.60 ± 0.04	
	n-decane	1.50 ± 0.04	
γ-Al_2O_3	*n*-hexane	1.4 ± 0.1	[67]
γ-Al_2O_3	*n*-hexane	1.5 ± 0.3	[67]
γ-Al_2O_3	*n*-hexane	1.9 ± 0.3	[67]
KIT-6	cyclohexane	1.50 ± 0.05	[66]
	n-heptane	1.48 ± 0.03	
SBA-15	cyclohexane	1.23 ± 0.03	[66]
	n-heptane	1.20 ± 0.02	
0.7 *wt*% Au/SiO_2	*n*-octane	1.74 ± 0.03	[68]
5 *wt*% Au/TiO_2	*n*-octane	1.57 ± 0.03	[68]
5 *wt*% AuPd/TiO_2	*n*-octane	1.85 ± 0.04	[68]
1.5 *wt*% Au/TiO_2	cyclohexane	1.90 ± 0.05	[69]
1 *wt*% Au/TiO_2	cyclohexane	2.10 ± 0.06	[70]
1 *wt*% AuPt/C	*n*-octane	1.77 ± 0.08	[71]

4.3.3 PFG NMR of complex interactions

Equation 4.47 suggests that knowledge of $\mathcal{D}_0^{\mathrm{PFG}}$ and $\hat{\tau}^{\mathrm{PFG}}$ allows us to predict the long-time restricted diffusivity of any given probe liquid within a porous structure. In fact, this is far from the case. Deviations in the measured value of $\mathcal{D}_0^{\mathrm{PFG}}/\mathcal{D}_\infty^{\mathrm{PFG}}$ across a range of molecular liquids imbibed within the same porous solid are common, and imply the presence of complex interactions occurring between the probe liquid and the porous matrix. The results of such measurements are typically described using the so-called PFG interaction parameter ξ, [68]

$$\xi = \frac{\mathcal{D}_0^{\mathrm{PFG}}}{\mathcal{D}_\infty^{\mathrm{PFG}}}, \tag{4.48}$$

which, in the case of negligible interactions is identical to the tortuosity.

The observation that $\xi \neq \hat{\tau}^{\mathrm{PFG}}$ may be facilitated by hindered diffusion, adsorption interactions, and/or dynamic network disruption. Hindered diffusion occurs when regions of the porous material exhibit pore diameters of a similar size to the probe molecular employed, severely restricting molecular displacement. Common examples of relevance to heterogeneous catalysis include configurational diffusion through microporous zeolites, and the effects of coke deposition. [72, 73] Of more relevance to the present work are the influences of adsorption and dynamic network disruption, which are commonly observed when investigating the restricted diffusion of polar liquids or liquid mixtures within mesoporous catalyst materials. To discuss these interactions in more detail we may define ξ in terms of mesoscopic (ξ_n) and microscopic (ξ_μ) contributions,

$$\xi = \xi_n \xi_\mu, \tag{4.49}$$

which is of course analogous to Equation 4.46. We may further state that the condition $\xi \neq \hat{\tau}^{\mathrm{PFG}}$ is met when at least one of the following is true:

$$\xi_\mu \neq \hat{\tau}_\mu \tag{4.50}$$

$$\xi_n \neq \hat{\tau}_n. \tag{4.51}$$

These inequalities may be assigned to distinct physical processes occurring over different length scales. Condition 4.50 describes a change in the expected diffusivity due short-range processes, and is assigned to adsorption interactions occurring at the solid/liquid interface. Hydroxylated liquids such as alcohols, polyols and carboxylic acids diffusing through mesoporous oxide materials are particularly susceptible to such interactions due to the formation of hydrogen bonding interactions between liquid molecules and surface hydroxyl groups which typically terminate oxide structures at the pore surface. Non-negligible adsorption processes result in a reduction of the observed self-diffusion coefficient such that $\xi_\mu > \hat{\tau}_\mu$. Conversely, condition 4.51 describes complex diffusive behaviour due to long-range processes which occur over several pores, and is generally assigned to the disruption of

extensive dynamic hydrogen bonding networks present through hydroxylated liquids by the presence of the pore walls. [38, 66, 68–70] This dynamic network disruption results in an enhancement of the observed diffusivity, such that $\xi_n < \hat{\tau}_n$. Following these definitions we may state

$$\xi_\mu \geq \hat{\tau}_\mu \tag{4.52}$$

$$\xi_n \leq \hat{\tau}_n. \tag{4.53}$$

These two interactions clearly oppose one another; adsorption processes facilitate a reduction in $\mathcal{D}_\infty^{\mathrm{PFG}}$, while dynamic network disruption leads to an enhancement in diffusivity, relative to that expected from considering the tortuosity of the structure. The nature of the observed interaction parameter ξ is therefore largely empirical, and, recalling Equation 4.49, must depend on competition between these two opposing processes. We may, however, make a series of general observations by considering the wide range of literature data collated in Table 4.2. This table lists the relevant $\mathcal{D}_0^{\mathrm{PFG}}$ and $\mathcal{D}_\infty^{\mathrm{PFG}}$ values obtained through appropriate PFG NMR experiments, yielding the PFG interaction parameter ξ (Equation 4.48). The tortuosity of each material, as described in Table 4.1 is also given, and facilitates the calculation of an estimated diffusivity for each restricted liquid in the absence of any interactions with the porous solid, $\mathcal{D}_0^{\mathrm{PFG}}/\hat{\tau}^{\mathrm{PFG}}$. It is quite clear from Table 4.2 that $\mathcal{D}_\infty^{\mathrm{PFG}} < \mathcal{D}_0^{\mathrm{PFG}}/\hat{\tau}^{\mathrm{PFG}}$ indicates $\xi > \hat{\tau}^{\mathrm{PFG}}$, and $\mathcal{D}_\infty^{\mathrm{PFG}} > \mathcal{D}_0^{\mathrm{PFG}}/\hat{\tau}^{\mathrm{PFG}}$ indicates $\xi < \hat{\tau}^{\mathrm{PFG}}$, in turn revealing that ξ is dominated by adsorption interactions or by dynamic network disruption, respectively. A more compact comparison may be performed by considering the normalised PFG interaction parameter $\xi/\hat{\tau}^{\mathrm{PFG}}$. [38] Simply, $\xi/\hat{\tau}^{\mathrm{PFG}} > 1$ indicates dominance of the observed diffusivity by adsorption interactions, while $\xi/\hat{\tau}^{\mathrm{PFG}} < 1$ indicates dominance by dynamic network disruption. [38]

Let us briefly consider some of the diffusive behaviour detailed in Table 4.2. We will start with the wide range of organic liquids considered within the unfunctionalised mesoporous oxides TiO_2, γ-Al_2O_3 and SiO_2. [38] This data shows a clear trend, with polyols exhibiting $\xi/\hat{\tau}^{\mathrm{PFG}} < 1$, while all other liquids exhibit

$\xi/\hat{\tau}^{\mathrm{PFG}} > 1$. It appears then that adsorption interactions dominate the observed diffusive behaviour within these materials, apart from in the case of molecules possessing multiple hydroxyl groups. In turn, this observation suggests that the presence of hydrogen bonding networks dominate the diffusive behaviour of polyols. This phenomenon is also observed when considering the diffusion of octanols and butanediols in a 0.7 *wt*% Au/SiO_2 oxidation catalyst. [68] It is interesting to observe, however, that these same molecular liquids do not exhibit such behaviour within 5 *wt*% Au/TiO_2 or 5 *wt*% $AuPd/TiO_2$ catalysts. Rather, both octanols and butanediols are shown to exhibit $\xi/\hat{\tau}^{\mathrm{PFG}} < 1$ within these systems. This change in octanol behaviour is unexpected given the consistent $\xi/\hat{\tau}^{\mathrm{PFG}}$ trends exhibited by mono-hydroxylated alcohols within unfunctionalised SiO_2 and TiO_2. Unfortunately surface hydroxyl coverage data is not avaliable for these materials. We may, however, consider this change based on trends in tortuosity and metal coverage. Table 4.2 illustrates that while the 5 *wt*% $AuPd/TiO_2$ catalyst exhibits a larger $\hat{\tau}^{\mathrm{PFG}}$ than the 0.7 *wt*% Au/SiO_2 material, the tortuosity of the 5 *wt*% Au/TiO_2 catalyst is lower than the silica-based catalyst. It appears then that the change in octanol behaviour cannot be attributed to a change in $\hat{\tau}^{\mathrm{PFG}}$. It is pertinent, however, to consider the metal content of these catalysts; a distinctly higher metal coverage is present on the two titania-supported catalyst than is present on the silica material. Burgess *et al.* recently showed that rotationally mobile surface hydroxyl groups are of significant importance in the adsorption and nucleation of metal nanoparticles at the surface of catalyst support materials. [74] In particular, surface hydroxyl groups are known to anchor gold nanoparticles to the support surface through the formation of non-covalent $Au \cdots HO$ interactions. It follows that the significant difference in metal coverage between the 0.7 *wt*% Au/SiO_2 and the two 5 *wt*% titania-based catalysts may be responsible for the change in octanol behaviour; indeed, a reduction in the surface hydroxyl density available to partake in adsorption interactions, as reduced through their interactions with metal nanoparticles, may well result in a change in ξ_μ such that ξ_n effects begin to dominate the observed diffusivity of the octanols. This hypothesis is supported by the change in butanediol $\xi/\hat{\tau}^{\mathrm{PFG}}$ values, which are observed to decrease within the two titania catalysts, suggesting an increased

dominance of long-range network disruption.

The diffusivities of 1,2-propanediol and water have been explored in a 1 $wt\%$ AuPt/C oxidation catalyst. [71] We see that water shows polyol-like behaviour, exhibiting $\xi/\hat{\tau}^{\mathrm{PFG}} = 0.81 \pm 0.05$. It is particularly interesting to note, however, that 1,2-propanediol imbibed within this catalyst is observed to exhibit $\xi/\hat{\tau}^{\mathrm{PFG}} \approx 1$, suggesting that the ξ_μ and ξ_n interactions almost exactly cancel one-another out within this system.

Table 4.2 also lists the diffusive properties of polyols and carboxylic acids in solution. Polyols diluted in methanol and methanol/water solutions show similar diffusive properties to undiluted polyols, with $\xi/\hat{\tau}^{\mathrm{PFG}} < 0$ observed in all cases. [69, 70] Rottreau *et al.* investigated the diffusion of a homologous series of carboxylic acids in deuterated methanol within the ordered mesoporous silicas KIT-6 and SBA-15. [66] The results of this study show that small-chain acids experience enhanced self-diffusion similar to polyols and polyols in solution. Longer-chain acids ($\geq \mathrm{C}_6$), however, exhibit $\xi/\hat{\tau}^{\mathrm{PFG}} > 0$. The authors attribute these results to stronger hydrogen bonding networks within solutions containing the smaller acids. [66]

Table 4.2: Literature PFG NMR data illustrating complex solid-liquid interactions in a range of common porous catalyst and catalyst support materials. † indicates appropriate error bounds are not available from the original publication.

Porous material	Probe liquid	$\mathcal{D}_0^{\mathrm{PFG}} \times 10^{11}$ / m^2 s^{-1}	$\mathcal{D}_\infty^{\mathrm{PFG}} \times 10^{11}$ / m^2 s^{-1}	$\hat{\tau}^{\mathrm{PFG}}$	$\mathcal{D}_0^{\mathrm{PFG}}/\hat{\tau}^{\mathrm{PFG}}$ $\times 10^{11}$ / m^2 s^{-1}	ξ	$\xi/\hat{\tau}^{\mathrm{PFG}}$	Ref.
TiO_2	1-propanol	55.0 ± 1.4	29.4 ± 0.8	1.60 ± 0.04	34.4 ± 1.2	1.87 ± 0.07	1.17 ± 0.05	[38]
	2-propanol	47.2 ± 1.2	27.3 ± 0.7		29.5 ± 1.0	1.73 ± 0.06	1.08 ± 0.05	
	ethylene glycol	7.38 ± 0.18	4.97 ± 0.12		4.61 ± 0.16	1.48 ± 0.05	0.93 ± 0.04	
	1,2-propanediol	2.61 ± 0.07	1.75 ± 0.04		1.63 ± 0.06	1.49 ± 0.05	0.93 ± 0.04	
	1,3-propanediol	2.73 ± 0.07	1.83 ± 0.05		1.71 ± 0.06	1.49 ± 0.05	0.93 ± 0.04	
	glycerol	0.126 ± 0.003	0.112 ± 0.003		0.079 ± 0.003	1.13 ± 0.04	0.70 ± 0.03	
	acetone	430 ± 11	257 ± 6		269 ± 10	1.67 ± 0.06	1.05 ± 0.05	
	hydroxyacetone	45.0 ± 1.1	20.0 ± 0.5		28.1 ± 0.5	2.25 ± 0.08	1.41 ± 0.06	
	propanal	390 ± 10	182 ± 4.6		244 ± 5	2.14 ± 0.08	1.34 ± 0.06	
	propanoic acid	100 ± 3	54.1 ± 1.4		62.5 ± 1.4	1.85 ± 0.07	1.16 ± 0.05	
γ-Al_2O_3	1-propanol	55.0 ± 1.4	25.6 ± 0.6	1.71 ± 0.04	32.2 ± 1.1	2.15 ± 0.08	1.26 ± 0.05	[38]
	2-propanol	47.2 ± 1.2	26.3 ± 0.7		27.6 ± 1.0	1.79 ± 0.06	1.05 ± 0.04	
	ethylene glycol	7.38 ± 0.18	4.67 ± 0.12		4.32 ± 0.15	1.58 ± 0.06	0.92 ± 0.04	
	1,2-propanediol	2.61 ± 0.07	1.94 ± 0.05		1.53 ± 0.05	1.35 ± 0.05	0.79 ± 0.03	
	1,3-propanediol	2.73 ± 0.07	1.75 ± 0.04		1.60 ± 0.05	1.56 ± 0.06	0.91 ± 0.04	
	glycerol	0.126 ± 0.003	0.168 ± 0.004		0.074 ± 0.003	0.75 ± 0.03	0.44 ± 0.02	
	acetone	430 ± 11	214 ± 5		251 ± 9	2.01 ± 0.17	1.18 ± 0.05	

Continued on next page

Table 4.2 – *Continued from previous page*

Porous material	Probe liquid	$\mathcal{D}_0^{\mathrm{PFG}} \times 10^{11}$ / m^2 s^{-1}	$\mathcal{D}_\infty^{\mathrm{PFG}} \times 10^{11}$ / m^2 s^{-1}	$\hat{\tau}^{\mathrm{PFG}}$	$\mathcal{D}_0^{\mathrm{PFG}}/\hat{\tau}^{\mathrm{PFG}}$ $\times 10^{11}$ / m^2 s^{-1}	ξ	$\xi/\hat{\tau}^{\mathrm{PFG}}$	Ref.
	hydroxyacetone	45.0 ± 1.1	13.6 ± 0.3		26.3 ± 0.9	3.31 ± 0.11	1.93 ± 0.08	
	propanal	390 ± 10	142 ± 4		228 ± 8	2.75 ± 0.10	1.61 ± 0.07	
	propanoic acid	100 ± 3	37.4 ± 0.9		58.5 ± 2.0	2.67 ± 0.09	1.56 ± 0.07	
SiO_2	1-propanol	55.0 ± 1.4	28.4 ± 0.7	1.60 ± 0.04	34.4 ± 1.2	1.94 ± 0.07	1.21 ± 0.05	[38]
	2-propanol	47.2 ± 1.2	28.00 ± 0.70		29.5 ± 1.0	1.69 ± 0.06	1.05 ± 0.05	
	ethylene glycol	7.38 ± 0.18	5.16 ± 0.13		4.61 ± 0.16	1.43 ± 0.05	0.89 ± 0.04	
	1,2-propanediol	2.61 ± 0.07	1.75 ± 0.04		1.63 ± 0.06	1.49 ± 0.05	0.93 ± 0.04	
	1,3-propanediol	2.73 ± 0.07	1.81 ± 0.05		1.71 ± 0.06	1.51 ± 0.05	0.94 ± 0.04	
	glycerol	0.126 ± 0.003	0.118 ± 0.003		0.079 ± 0.003	1.07 ± 0.04	0.67 ± 0.03	
	acetone	430 ± 11	254.00 ± 6.53		269 ± 10	1.69 ± 0.06	1.06 ± 0.05	
	hydroxyacetone	45.0 ± 1.1	20.00 ± 0.50		28.13 ± 0.99	2.25 ± 0.08	1.41 ± 0.06	
	propanal	390 ± 10	190.00 ± 4.75		244 ± 9	2.05 ± 0.07	1.28 ± 0.06	
	propanoic acid	100 ± 4	50.00 ± 1.25		62.5 ± 2.2	2.00 ± 0.07	1.25 ± 0.05	
0.7 *wt*% Au/SiO_2	1-octanol	12.3 ± 0.3	6.60 ± 0.13	1.74 ± 0.03	7.07 ± 0.20	1.86 ± 0.05	1.07 ± 0.04	[68]
	2-octanol	14.3 ± 0.3	6.80 ± 0.14		8.22 ± 0.23	2.10 ± 0.06	1.21 ± 0.04	
	3-octanol	14.4 ± 0.3	6.60 ± 0.13		8.28 ± 0.23	2.18 ± 0.06	1.25 ± 0.04	
	1,2-butanediol	2.80 ± 0.06	2.00 ± 0.04		1.61 ± 0.05	1.40 ± 0.04	0.80 ± 0.03	
	1,3-butanediol	2.00 ± 0.04	1.40 ± 0.20		1.15 ± 0.03	1.43 ± 0.04	0.82 ± 0.03	

Continued on next page

Table 4.2 – *Continued from previous page*

Porous material	Probe liquid	$\mathcal{D}_0^{\mathrm{PFG}} \times 10^{11}$ / $\mathrm{m^2\ s^{-1}}$	$\mathcal{D}_\infty^{\mathrm{PFG}} \times 10^{11}$ / $\mathrm{m^2\ s^{-1}}$	$\hat{\tau}^{\mathrm{PFG}}$	$\mathcal{D}_0^{\mathrm{PFG}}/\hat{\tau}^{\mathrm{PFG}}$ $\times 10^{11}$ / $\mathrm{m^2\ s^{-1}}$	ξ	$\xi/\hat{\tau}^{\mathrm{PFG}}$	Ref.
5 *wt*% Au/TiO_2	1-octanol	12.3 ± 0.3	10.0 ± 0.2	1.57 ± 0.03	7.83 ± 0.22	1.23 ± 0.03	0.78 ± 0.03	[68]
	2-octanol	14.3 ± 0.3	10.3 ± 0.2		9.11 ± 0.26	1.39 ± 0.04	0.88 ± 0.03	
	3-octanol	14.4 ± 0.3	9.90 ± 0.20		9.17 ± 0.26	1.45 ± 0.04	0.93 ± 0.03	
	1,2-butanediol	2.80 ± 0.06	2.40 ± 0.05		1.78 ± 0.05	1.17 ± 0.03	0.74 ± 0.03	
	1,3-butanediol	2.00 ± 0.04	1.80 ± 0.04		1.27 ± 0.04	1.11 ± 0.03	0.71 ± 0.02	
5 *wt*% $AuPd/TiO_2$	1-octanol	12.3 ± 0.3	9.30 ± 0.19	1.85 ± 0.04	6.65 ± 0.19	1.32 ± 0.04	0.71 ± 0.02	[68]
	2-octanol	14.3 ± 0.3	10.2 ± 0.2		7.73 ± 0.22	1.40 ± 0.04	0.76 ± 0.03	
	3-octanol	14.4 ± 0.3	8.80 ± 0.18		7.78 ± 0.22	1.64 ± 0.05	0.88 ± 0.03	
	1,2-butanediol	2.80 ± 0.06	2.40 ± 0.05		1.51 ± 0.04	1.17 ± 0.03	0.63 ± 0.02	
	1,3-butanediol	2.00 ± 0.04	1.80 ± 0.04		1.08 ± 0.03	1.11 ± 0.03	0.60 ± 0.02	
1 *wt*% AuPt/C	water	205 ± 6	143 ± 4	1.77 ± 0.08	116 ± 6	1.43 ± 0.06	0.81 ± 0.05	[71]
	1,2-propanediol	2.60 ± 0.08	1.40 ± 0.04		1.47 ± 0.08	1.86 ± 0.08	1.05 ± 0.06	
1 *wt*% Au/TiO_2	10 % 1,3-propanediol in methanol	12.30 ± 0.25	9.30 ± 0.19	1.85 ± 0.04	6.65 ± 0.19	1.32 ± 0.04	0.71 ± 0.02	[70]
	10 % 2-methyl-1,3-propanediol in methanol	14.30 ± 0.29	10.20 ± 0.20		7.73 ± 0.22	1.40 ± 0.04	0.76 ± 0.03	
	10 % 2,2-dimethyl-1,3-propanediol in methanol	14.40 ± 0.29	8.80 ± 0.18		7.78 ± 0.22	1.64 ± 0.05	0.88 ± 0.03	

Continued on next page

Table 4.2 – *Continued from previous page*

Porous material	Probe liquid	$\mathcal{D}_0^{\mathrm{PFG}} \times 10^{11}$ / m^2 s^{-1}	$\mathcal{D}_\infty^{\mathrm{PFG}} \times 10^{11}$ / m^2 s^{-1}	$\hat{\tau}^{\mathrm{PFG}}$	$\mathcal{D}_0^{\mathrm{PFG}}/\hat{\tau}^{\mathrm{PFG}}$ $\times 10^{11}$ / m^2 s^{-1}	ξ	$\xi/\hat{\tau}^{\mathrm{PFG}}$	Ref.
	10 % 1,3-propanediol in 1:1 (*vol.*) water/methanol solution	2.80 ± 0.06	2.40 ± 0.05		1.51 ± 0.04	1.17 ± 0.03	0.63 ± 0.02	
	10 % 2-methyl-1,3-propanediol in 1:1 (*vol.*) water/methanol solution	2.00 ± 0.04	1.80 ± 0.04		1.08 ± 0.03	1.11 ± 0.03	0.60 ± 0.02	
	10 % 2,2-dimethyl-1,3-propanediol in 1:1 (*vol.*) water/methanol solution	2.00 ± 0.04	1.80 ± 0.04		1.08 ± 0.03	1.11 ± 0.03	0.60 ± 0.02	
1.5 *wt*% Au/TiO_2	5 % 1,4-butanediol in methanol	92 ± 1	54 ± 1	1.90 ± 0.05	48 ± 1	1.70 ± 0.04	0.90 ± 0.03	[69]
	5 % 1,4-butanediol in 1:1 (*mol.*) water/methanol solution	48 ± 1	28 ± 1		25 ± 1	1.71 ± 0.07	0.90 ± 0.04	
KIT-6	propanoic acid	$144^\dagger$	$109^\dagger$	1.48 ± 0.03	$97^\dagger$	1.33 ± 0.06	0.90 ± 0.04	[66]
	valeric acid	$137^\dagger$	$97^\dagger$		$93^\dagger$	1.41 ± 0.06	0.95 ± 0.04	
(all acids	hexanoic acid	$129^\dagger$	$87^\dagger$		$87^\dagger$	1.49 ± 0.05	1.01 ± 0.04	
20 mmol in	octanoic acid	$120^\dagger$	$78^\dagger$		$81^\dagger$	1.54 ± 0.05	1.04 ± 0.04	
methanol)	lauric acid	$102^\dagger$	$60^\dagger$		$67^\dagger$	1.72 ± 0.06	1.16 ± 0.05	
	myristic acid	$97^\dagger$	$58^\dagger$		$66^\dagger$	1.68 ± 0.05	1.14 ± 0.04	
	palmitic acid	$90^\dagger$	$58^\dagger$		$61^\dagger$	1.56 ± 0.05	1.05 ± 0.04	
SBA-15	propanoic acid	$144^\dagger$	$124^\dagger$	1.20 ± 0.02	$120^\dagger$	1.16 ± 0.04	0.97 ± 0.04	[66]

Continued on next page

Table 4.2 – *Continued from previous page*

Porous material	Probe liquid	$\mathcal{D}_0^{\mathrm{PFG}} \times 10^{11}$ / m^2 s^{-1}	$\mathcal{D}_\infty^{\mathrm{PFG}} \times 10^{11}$ / m^2 s^{-1}	$\hat{\tau}^{\mathrm{PFG}}$	$\mathcal{D}_0^{\mathrm{PFG}}/\hat{\tau}^{\mathrm{PFG}}$ $\times 10^{11}$ / m^2 s^{-1}	ξ	$\xi/\hat{\tau}^{\mathrm{PFG}}$	Ref.
	valeric acid	137†	116†		114†	1.18 ± 0.04	0.98 ± 0.04	
(all acids	hexanoic acid	129†	105†		108†	1.22 ± 0.04	1.02 ± 0.04	
20 mmol in	octanoic acid	120†	94†		100†	1.27 ± 0.03	1.06 ± 0.03	
methanol)	lauric acid	102†	71†		85†	1.43 ± 0.03	1.19 ± 0.03	
	myristic acid	97†	68.5†		81†	1.41 ± 0.03	1.18 ± 0.03	
	palmitic acid	90†	65†		75†	1.39 ± 0.04	1.16 ± 0.04	

4.4 References

[1] J. Rouquerol, F. Rouquerol, P. Llewellyn, G. Maurin and K. S. W. Sing, *Adsorption by Powders and Porous Solids, Second Edition: Principles, Methodology and Applications*, Academic Press, Amsterdam, 2 edition, 2013.

[2] *IUPAC Gold Book - Micropore in Catalysis*, `https://goldbook.iupac.org/html/M/M03906.html` (visited on 07/09/2018).

[3] *IUPAC Gold Book - Mesopore in Catalysis*, `https://goldbook.iupac.org/html/M/M03853.html` (visited on 07/09/2018).

[4] *IUPAC Gold Book - Macropore in Catalysis*, `https://goldbook.iupac.org/html/M/M03672.html` (visited on 07/09/2018).

[5] M. H. Levitt, *Spin Dynamics: Basics of Nuclear Magnetic Resonance*, Wiley-Blackwell, Chichester, England ; Hoboken, NJ, 2nd Edition, 2008.

[6] J. Kowalewski and L. Maler, *Nuclear Spin Relaxation in Liquids: Theory, Experiments, and Applications*, CRC Press, 2006.

[7] R. Kimmich, *NMR: Tomography, Diffusometry, Relaxometry*, Springer Science & Business Media, 2012.

[8] A. Abragam, *The Principles of Nuclear Magnetism*, Clarendon Press, 1961.

[9] P. M. Singer, D. Asthagiri, W. G. Chapman and G. J. Hirasaki, "Molecular Dynamics Simulations of NMR Relaxation and Diffusion of Bulk Hydrocarbons and Water", *J. Magn. Reson.*, 2017, **277**, 15–24.

[10] W. A. M. Madhavi, S. Weerasinghe and K. I. Momot, "Rotational-Diffusion Propagator of the Intramolecular Proton–Proton Vector in Liquid Water: A Molecular Dynamics Study", *J. Phys. Chem. B*, 2017, **121**, 10893–10905.

[11] N. Bloembergen, E. M. Purcell and R. V. Pound, "Relaxation Effects in Nuclear Magnetic Resonance Absorption", *Phys. Rev.*, 1948, **73**, 679–712.

[12] P. T. Callaghan, *Translational Dynamics and Magnetic Resonance: Principles of Pulsed Gradient Spin Echo NMR*, OUP Oxford, Oxford ; New York, 2011.

[13] P. M. Singer, D. Asthagiri, Z. Chen, A. Valiya Parambathu, G. J. Hirasaki and W. G. Chapman, "Role of Internal Motions and Molecular Geometry on the NMR Relaxation of Hydrocarbons", *J. Chem. Phys.*, 2018, **148**, 164507.

[14] G. Lipari and A. Szabo, "Model-Free Approach to the Interpretation of Nuclear Magnetic Resonance Relaxation in Macromolecules. 1. Theory and Range of Validity", *J. Am. Chem. Soc.*, 1982, **104**, 4546–4559.

[15] G. Lipari and A. Szabo, "Model-Free Approach to the Interpretation of Nuclear Magnetic Resonance Relaxation in Macromolecules. 2. Analysis of Experimental Results", *J. Am. Chem. Soc.*, 1982, **104**, 4559–4570.

[16] D. Kruk, R. Meier and E. A. Rössler, "Nuclear Magnetic Resonance Relaxometry as a Method of Measuring Translational Diffusion Coefficients in Liquids", *Phys. Rev. E*, 2012, **85**, 020201.

[17] D. Kruk, M. Wojciechowski, S. Brym and R. K. Singh, "Dynamics of Ionic Liquids in Bulk and in Confinement by Means of 1H NMR Relaxometry – BMIM-OcSO4 in an SiO2 Matrix as an Example", *Phys. Chem. Chem. Phys.*, 2016, **18**, 23184–23194.

[18] D. Kruk, M. Wojciechowski, Y. L. Verma, S. K. Chaurasia and R. K. Singh, "Dynamical Properties of EMIM-SCN Confined in a SiO2 Matrix by Means of 1H NMR Relaxometry", *Phys. Chem. Chem. Phys.*, 2017, **19**, 32605–32616.

[19] L. Hwang and J. H. Freed, "Dynamic Effects of Pair Correlation Functions on Spin Relaxation by Translational Diffusion in Liquids", *J. Chem. Phys.*, 1975, **63**, 4017–4025.

[20] C. F. Polnaszek and R. G. Bryant, "Nitroxide Radical Induced Solvent Proton Relaxation: Measurement of Localized Translational Diffusion", *J. Chem. Phys.*, 1984, **81**, 4038–4045.

[21] R. L. Kleinberg, W. E. Kenyon and P. P. Mitra, "Mechanism of NMR Relaxation of Fluids in Rock", *J. Magn. Reson.*, 1994, **108**, 206–214.

[22] S. Godefroy, J.-P. Korb, M. Fleury and R. G. Bryant, "Surface Nuclear Magnetic Relaxation and Dynamics of Water and Oil in Macroporous Media", *Phys. Rev. E*, 2001, **64**, 021605.

[23] S. Godefroy, M. Fleury, F. Deflandre and J.-P. Korb, "Temperature Effect on NMR Surface Relaxation in Rocks for Well Logging Applications", *J. Phys. Chem. B*, 2002, **106**, 11183–11190.

[24] K. E. Washburn, "Relaxation Mechanisms and Shales", *Concepts Magn. Reson.*, 2014, **43A**, 57–78.

[25] P. J. McDonald, J.-P. Korb, J. Mitchell and L. Monteilhet, "Surface Relaxation and Chemical Exchange in Hydrating Cement Pastes: A Two-Dimensional NMR Relaxation Study", *Phys. Rev. E*, 2005, **72**, 011409.

[26] P. J. McDonald, J. Mitchell, M. Mulheron, P. S. Aptaker, J.-P. Korb and L. Monteilhet, "Two-Dimensional Correlation Relaxometry Studies of Cement Pastes Performed Using a New One-Sided NMR Magnet", *Cem. Concr. Res.*, 2007, **37**, 303–309.

[27] J.-P. Korb, "Multiscale Nuclear Magnetic Relaxation Dispersion of Complex Liquids in Bulk and Confinement", *Prog. Nucl. Magn. Reson. Spectrosc.*, 2018, **104**, 12–55.

[28] K. R. Brownstein and C. E. Tarr, "Spin-Lattice Relaxation in a System Governed by Diffusion", *J. Magn. Reson.*, 1977, **26**, 17–24.

[29] K. R. Brownstein and C. E. Tarr, "Importance of Classical Diffusion in NMR Studies of Water in Biological Cells", *Phys. Rev. A*, 1979, **19**, 2446–2453.

[30] C. D'Agostino, P. Bräuer, P. Charoen-Rajapark, M. D. Crouch and L. F. Gladden, "Effect of Paramagnetic Species on T1, T2 and T1/T2 NMR Relaxation Times of Liquids in Porous CuSO4/Al2O3", 2017, **7**, 36163–36167.

[31] J.-P. Korb, B. Nicot, A. Louis-Joseph, S. Bubici and G. Ferrante, "Dynamics and Wettability of Oil and Water in Oil Shales", *J. Phys. Chem. C*, 2014, **118**, 23212–23218.

[32] G. Liu, Y. Li and J. Jonas, "Confined Geometry Effects on Reorientational Dynamics of Molecular Liquids in Porous Silica Glasses", *J. Chem. Phys.*, 1991, **95**, 6892–6901.

[33] A. Delville and M. Letellier, "Structure and Dynamics of Simple Liquids in Heterogeneous Condition: An NMR Study of the Clay-Water Interface", *Langmuir*, 1995, **11**, 1361–1367.

[34] J. S. Bhatt, P. J. McDonald, D. A. Faux, N. C. Howlett and S. V. Churakov, "NMR Relaxation Parameters from Molecular Simulations of Hydrated Inorganic Nanopores", *Int. J. Quantum Chem.*, 2014, **114**, 1220–1228.

[35] D. Weber, J. Mitchell, J. McGregor and L. F. Gladden, "Comparing Strengths of Surface Interactions for Reactants and Solvents in Porous Catalysts Using Two-Dimensional NMR Relaxation Correlations", *J. Phys. Chem. C*, 2009, **113**, 6610–6615.

[36] J. Mitchell, L. M. Broche, T. C. Chandrasekera, D. J. Lurie and L. F. Gladden, "Exploring Surface Interactions in Catalysts Using Low-Field Nuclear Magnetic Resonance", *J. Phys. Chem. C*, 2013, **117**, 17699–17706.

[37] C. D'Agostino, J. Mitchell, M. D. Mantle and L. F. Gladden, "Interpretation of NMR Relaxation as a Tool for Characterising the Adsorption Strength of Liquids inside Porous Materials", *Chem. Eur. J.*, 2014, **20**, 13009–13015.

[38] C. D'Agostino, J. Mitchell, L. F. Gladden and M. D. Mantle, "Hydrogen Bonding Network Disruption in Mesoporous Catalyst Supports Probed by PFG-NMR Diffusometry and NMR Relaxometry", *J. Phys. Chem. C*, 2012, **116**, 8975–8982.

[39] D. A. Faux, P. J. McDonald and N. C. Howlett, "Nuclear-Magnetic-Resonance Relaxation Due to the Translational Diffusion of Fluid Confined to Quasi-Two-Dimensional Pores", *Phys. Rev. E*, 2017, **95**, 033116.

[40] D. A. Faux and P. J. McDonald, "Explicit Calculation of Nuclear-Magnetic-Resonance Relaxation Rates in Small Pores to Elucidate Molecular-Scale Fluid Dynamics", *Phys. Rev. E*, 2017, **95**, 033117.

[41] P. J. McDonald, J.-P. Korb, J. Mitchell and L. Monteilhet, "Surface Relaxation and Chemical Exchange in Hydrating Cement Pastes: A Two-Dimensional NMR Relaxation Study", *Phys. Rev. E*, 2005, **72**, 011409.

[42] L. Monteilhet, J.-P. Korb, J. Mitchell and P. J. McDonald, "Observation of Exchange of Micropore Water in Cement Pastes by Two-Dimensional T2-T2 Nuclear Magnetic Resonance Relaxometry", *Phys. Rev. E*, 2006, **74**, 061404.

[43] J.-P. Korb, G. Freiman, B. Nicot and P. Ligneul, "Dynamical Surface Affinity of Diphasic Liquids as a Probe of Wettability of Multimodal Porous Media", *Phys. Rev. E*, 2009, **80**, 061601.

[44] S. Blundell, *Magnetism in Condensed Matter*, OUP Oxford, 2001.

[45] J. Mitchell, T. C. Chandrasekera, M. L. Johns, L. F. Gladden and E. J. Fordham, "Nuclear Magnetic Resonance Relaxation and Diffusion in the Presence of Internal Gradients: The Effect of Magnetic Field Strength", *Phys. Rev. E*, 2010, **81**, 026101.

[46] K. E. Washburn, C. D. Eccles and P. T. Callaghan, "The Dependence on Magnetic Field Strength of Correlated Internal Gradient Relaxation Time Distributions in Heterogeneous Materials", *J. Magn. Reson.*, 2008, **194**, 33–40.

[47] J. Mitchell, T. C. Chandrasekera and L. F. Gladden, "Measurement of the True Transverse Nuclear Magnetic Resonance Relaxation in the Presence of Field Gradients", *J. Chem. Phys.*, 2013, **139**, 074205.

[48] J. Mitchell and T. C. Chandrasekera, "Understanding Generalized Inversions of Nuclear Magnetic Resonance Transverse Relaxation Time in Porous Media", *J. Chem. Phys.*, 2014, **141**, 224201.

[49] M. D. Hürlimann, "Effective Gradients in Porous Media Due to Susceptibility Differences", *J. Magn. Reson.*, 1998, **131**, 232–240.

[50] E. J. Fordham and J. Mitchell, "Localization in a Single Pore", *Microporous Mesoporous Mater.*, 2018, **269**, 35–38.

[51] P. Le Doussal and P. N. Sen, "Decay of Nuclear Magnetization by Diffusion in a Parabolic Magnetic Field: An Exactly Solvable Model", *Phys. Rev. B*, 1992, **46**, 3465–3485.

[52] S. D. Stoller, W. Happer and F. J. Dyson, "Transverse Spin Relaxation in Inhomogeneous Magnetic Fields", *Phys. Rev. A*, 1991, **44**, 7459–7477.

[53] T. M. de Swiet and P. N. Sen, "Decay of Nuclear Magnetization by Bounded Diffusion in a Constant Field Gradient", *J. Chem. Phys.*, 1994, **100**, 5597–5604.

[54] L. J. Zielinski and P. N. Sen, "Relaxation of Nuclear Magnetization in a Nonuniform Magnetic Field Gradient and in a Restricted Geometry", *J. Magn. Reson.*, 2000, **147**, 95–103.

[55] M. D. Hurlimann, K. G. Helmer, T. M. Deswiet and P. N. Sen, "Spin Echoes in a Constant Gradient and in the Presence of Simple Restriction", *J. Magn. Reson.*, 1995, **113**, 260–264.

[56] J. Mitchell, T. C. Chandrasekera and L. F. Gladden, "Obtaining True Transverse Relaxation Time Distributions in High-Field NMR Measurements of Saturated Porous Media: Removing the Influence of Internal Gradients", *J. Chem. Phys.*, 2010, **132**, 244705.

[57] C. D'Agostino and P. Bräuer, "Exploiting Enhanced Paramagnetic NMR Relaxation for Monitoring Catalyst Preparation Using T1–T2 NMR Correlation Maps", *React. Chem. Eng.*, 2018, DOI: `10.1039/C8RE00173A`.

[58] W. S. Price, *NMR Studies of Translational Motion: Principles and Applications*, Cambridge University Press, Cambridge ; New York, 1 edition, 2009.

[59] R. Valiullin, *Diffusion NMR of Confined Systems: Fluid Transport in Porous Solids and Heterogeneous Materials*, Royal Society of Chemistry, 2016.

[60] W. S. Price, "Pulsed-Field Gradient Nuclear Magnetic Resonance as a Tool for Studying Translational Diffusion: Part 1. Basic Theory", *Concepts Magn. Reson.*, 1997, **9**, 299–336.

[61] M. P. Hollewand and L. F. Gladden, "Transport Heterogeneity in Porous Pellets—I. PGSE NMR Studies", *Chem. Eng. Sci.*, 1995, **50**, 309–326.

[62] P. T. Callaghan, in *Translational Dynamics and Magnetic Resonance: Principles of Pulsed Gradient Spin Echo NMR*, OUP Oxford, Oxford ; New York, 2011, p. 225.

[63] S. P. Rigby and L. F. Gladden, "The Use of Magnetic Resonance Images in the Simulation of Diffusion in Porous Catalyst Support Pellets", *J. Catal.*, 1998, **173**, 484–489.

[64] S. P. Rigby and L. F. Gladden, "The Prediction of Transport Properties of Porous Media Using Fractal Models and NMR Experimental Techniques", *Chem. Eng. Sci.*, 1999, **54**, 3503–3512.

[65] S. P. Rigby, "Macroscopic Diffusional Anisotropy in Porous Media", *Chaos, Solitons & Fractals*, 2000, **11**, 1297–1301.

[66] T. J. Rottreau, C. M. A. Parlett, A. F. Lee and R. Evans, "Diffusion NMR Characterization of Catalytic Silica Supports: A Tortuous Path", *J. Phys. Chem. C*, 2017, **121**, 16250–16256.

[67] E. Weiland, M.-A. Springuel-Huet, A. Nossov, F. Guenneau, A.-A. Quoineaud and A. Gédéon, "Transport Properties of Catalyst Supports Studied by Pulsed Field Gradient (PFG) and 2D Exchange (EXSY) NMR Spectroscopy", *New J. Chem.*, 2016, **40**, 4447–4454.

[68] M. D. Mantle, D. I. Enache, E. Nowicka, S. P. Davies, J. K. Edwards, C. D'Agostino, D. P. Mascarenhas, L. Durham, M. Sankar, D. W. Knight, L. F. Gladden, S. H. Taylor and G. J. Hutchings, "Pulsed-Field Gradient NMR Spectroscopic Studies of Alcohols in Supported Gold Catalysts", *J. Phys. Chem. C*, 2011, **115**, 1073–1079.

[69] C. D'Agostino, G. L. Brett, P. J. Miedziak, D. W. Knight, G. J. Hutchings, L. F. Gladden and M. D. Mantle, "Understanding the Solvent Effect on the Catalytic Oxidation of 1,4-Butanediol in Methanol over Au/TiO2 Catalyst: NMR Diffusion and Relaxation Studies", *Chem. Eur. J.*, 2012, **18**, 14426–14433.

[70] C. D'Agostino, T. Kotionova, J. Mitchell, P. J. Miedziak, D. W. Knight, S. H. Taylor, G. J. Hutchings, L. F. Gladden and M. D. Mantle, "Solvent Effect and Reactivity Trend in the Aerobic Oxidation of 1,3-Propanediols over Gold Supported on Titania: NMR Diffusion and Relaxation Studies", *Chem. Eur. J.*, 2013, **19**, 11725–11732.

[71] C. D'Agostino, Y. Ryabenkova, P. J. Miedziak, S. H. Taylor, G. J. Hutchings, L. F. Gladden and M. D. Mantle, "Deactivation Studies of a Carbon Supported AuPt Nanoparticulate Catalyst in the Liquid-Phase Aerobic Oxidation of 1,2-Propanediol", *Catal. Sci. Technol.*, 2014, **4**, 1313–1322.

[72] J. Wood and L. F. Gladden, "Effect of Coke Deposition upon Pore Structure and Self-Diffusion in Deactivated Industrial Hydroprocessing Catalysts", *Appl. Catal., A*, 2003, **249**, 241–253.

[73] B. Zhou, Z. Liao, C. Mattea, S. Stapf, H. Jiao, L. Wang, Z. Zhuang, B. Jiang, J. Wang and Y. Yang, "Solvents Molecular Mobility in Coked Catalyst ZSM-5 Studied by NMR Relaxation and Pulsed Field Gradient Techniques", *Ind. Eng. Chem. Res.*, 2018, **57**, 6647–6653.

[74] R. Burgess, C. Buono, P. R. Davies, R. J. Davies, T. Legge, A. Lai, R. Lewis, D. J. Morgan, N. Robinson and D. J. Willock, "The Functionalisation of Graphite Surfaces with Nitric Acid: Identification of Functional Groups and Their Effects on Gold Deposition", *J. Catal.*, 2015, **323**, 10–18.

Chapter 5

Exploring surface interactions with T_1 relaxation

5.1 Introduction

While many developments across the field of heterogeneous catalysis concern themselves with the performance of supported active species, [1–3] the nature of the support material itself can significantly influence catalytic processes. For example, supports may directly affect the performance of supported metal species through strong metal support interactions, [4–6] including metal cluster anchoring [7] and nanoparticle encapsulation, [8, 9] as well as direct participation in reaction pathways. [10] Away from the active regions of the catalyst surface the highly porous structures of typical catalyst supports also dictate mass transport properties through the existence of highly tortuous pore networks. [11] As introduced in Chapter 4, liquid-phase catalytic systems are also susceptible to enhanced mass transport effects arising from competition between adsorption processes at the pore surface and the disruption of dynamic networks throughout the liquid. [11, 12] Of these, adsorption interactions are typically the dominant effect and are primarily facilitated through the formation of hydrogen bonding interactions with the polar groups which regularly terminate oxide support materials at the pore surface. While such interactions have been observed to enhance catalyst performance by providing greater accessibility to the active surface, [13, 14] this effect is also highly dependent on the nature of competitive adsorption processes occurring between the reagent and any solvent molecules which may be present. [15] It seems therefore appropriate to consider how such effects might be reduced.

The most prominent approach to limit favourable interactions between the support and the mobile phase is to passivate the support *via* the covalent modification of surface hydroxyls groups. Indeed, the passivation of silica-based catalyst supports has been observed to enhance the performance of epoxidation, [16, 17] oxidation [18] and hydrogenation catalysts. [19–22] The influence of surface passivation also extends to other porous oxide materials; for example Ellis *et al.* reported that the partial passivation of γ-alumina leads to a 50 % increase in activity for the dehydration of 1,2-propanediol. [23]

The aim of this first results chapter is to introduce nuclear spin relaxation as a

versatile and surface sensitive tool with which adsorbate mobility within mesoporous oxide support materials may be explored. Given our particular focus here on the elucidation of surface dynamics related to the presence of surface-adsorbate hydrogen bonding interactions, by attempting to observe changes to adsorbate mobility upon surface passivation we hope to extend our understanding of the extent to which NMR relaxation measurements may be applied as a surface-sensitive probe within such systems.

Interestingly, we note that while the successful functionalisation of catalyst surfaces has been extensively quantified using magic angle spinning solid-state NMR, [16, 18, 21] changes to the dynamic behaviour (diffusion, rotation) of liquid molecules imbibed within the pore network of such materials has attracted far less attention. Pulsed-field gradient (PFG) NMR diffusometry has been used by Hansen [24] and Courivaud [25] to explore the influence of surface hydrophobicity on the self-diffusion of *n*-hexane imbibed within MCM-41. Elsewhere Weber *et al.* used PFG NMR analysis of a Pd/θ-alumina catalyst saturated with 1-octene to illustrate how molecular self-diffusion within the adsorbed surface layer is inhibited through passivation of the pore surface with long alkyl chains. [26] This investigation is therefore timely given the prominence of hydrogen bond mediated surface interactions in liquid-phase catalysis. In this chapter we detail the application of high field nuclear spin-lattice relaxation measurements to probe changes in surface dynamics experienced by methanol – used here to represent a prototypical polar molecule of relevance to solvated green chemical processes – within liquid-saturated catalyst supports that have been functionalised with alkyl groups.

5.2 Methods

5.2.1 Materials and surface passivation

Mesoporous γ-alumina (γ-Al_2O_3), θ-alumina (θ-alumina) and silica (SiO_2) were obtained from Johnson Matthey, while mesoporous anatase-titania (A-TiO_2) was obtained from Evonik-Degussa. Each material was functionalised with surface octyl groups through a simple liquid-phase treatment with triethoxyl(octyl)silane

(TEOS, Sigma Aldrich, $\geq$ 96 %).[27] This treatment generates a polymeric surface layer which passivates hydroxyl groups at the pore surface; the passivation mechanism is illustrated in Figure 5.1. To prevent excessive polymerisation of the liquid-phase TEOS before agregation at the surface the majority of physisorbed water was removed by first drying the oxide pellets for 2 hours at 105 °C. [28] The pellets were then soaked in excess TEOS for 12 hours under ambient conditions; remaining physisorbed water leads to hydrolysis of the ethoxy groups (Figure 5.1). The resulting hydroxysilane molecules then aggregate with the pore surface through hydrogen bonding interactions with surface hydroxyl groups, and condensation reactions between adjacent molecules form a polymeric surface layer which passivated the oxides. [28] Following this treatment the pellets were washed several times in cyclohexane to remove the evolved ethanol and unreacted TEOS, before being dried at 105 °C for a further 12 hours. The high TEOS concentration utilised here (excess, no solvent) suggests that a highly cross-linked polymeric surface layer is formed at the pore surface. [28] This approach is advantageous in the present study as it limits the ability of any remaining surface hydroxyl groups to interact with liquids imbibed within the passivated pore system.

5.2.2 Materials characterisation

DRIFTS

Diffuse reflectance infrared fourier transform spectroscopy (DRIFTS) measurements were performed to confirm successful passivation of the oxide supports. Measurements were performed on a ThermoFischer Nicolet iS50 FT-IR spectrometer equipped with a Praying Mantis diffuse reflectance cell and high temperature reaction chamber. Samples were ground by hand using a pestle and mortar, and were analysed without dilution. Approximately 50 mg of each catalyst support was loaded into the reaction cell supported by a small amount of quartz wool. To remove the influence of physisorbed water all samples were heated to 150 °C at a rate of 10 °C min^{-1} under a low flow of helium (10 ml min^{-1}); this temperature was maintained for 30 minutes, after which the samples were cooled to 25 °C at the same rate. Infrared absorption spectra were acquired with 64 repeat scans with a

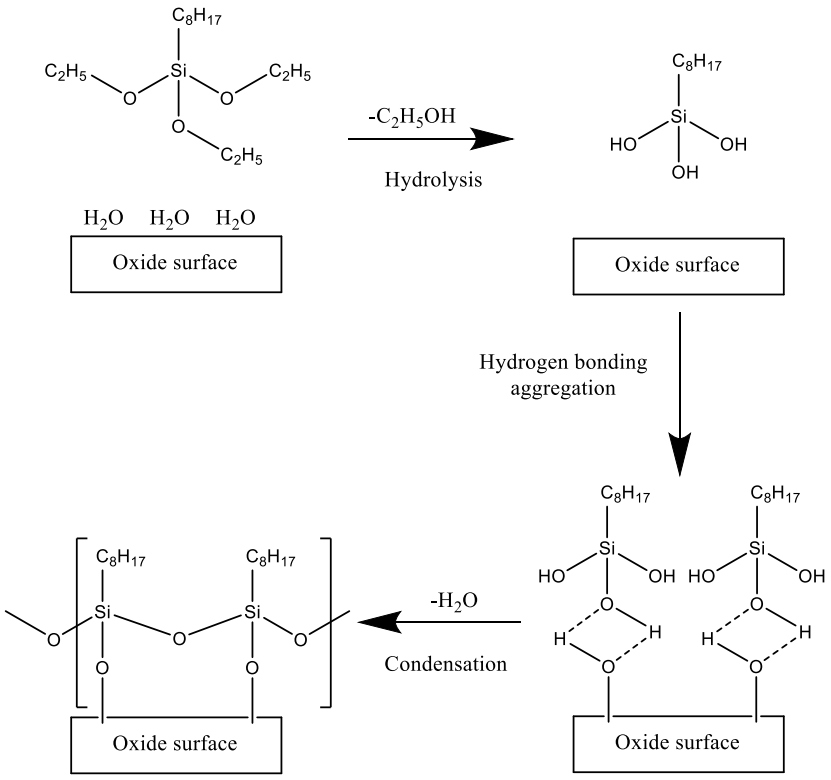

Figure 5.1: Illustration of the three-step mechanisms for the formation of polymeric surface layers at oxide surfaces by liquid-phase treatment with silanes, such as triethoxyl(octyl)silane (TEOS). Adapted from Pujari *et al.*.[28]

resolution of 4 cm^{-1}, relative to a KBr background measurement acquired under identical conditions.

Nitrogen porosimetry

N_2 isotherm measurements were carried out by technical support staff at the Department of Chemical Engineering and Biotechnology, University of Cambridge. Measurements were performed using a Micromeritics TriStar 3000 automated gas adsorption analyser. Specific surface areas S_{BET} were obtained using the Brunauer-Emmett-Teller (BET) method. Pore volumes V_{BJH} were calculated using the Barrett-Joyner-Halenda (BJH) method. All N_2 adsorption measurements were carried our at -196 °C.

5.2.3 NMR measurements

Sample preparation

Unfunctionalised oxides were dried for at least 12 hours at 105 °C before use. To ensure saturation, each material (both functionalised and unfunctionalised) was soaked in excess methanol (Sigma Aldrich, $\geq$ 99.8 %) for at least 24 hours; this allowed the pore structure to fill through the process of capillary imbibition. It has been shown elsewhere that soaking porous catalyst support materials in this way is sufficient to saturate the pore network. [29] Separately, each unfunctionalised material was also saturated with cyclohexane (Sigma Aldrich, $\geq$ 99.5 %) to provide a weakly-interacting reference. The saturated oxide materials were then removed from each liquid and rolled across a pre-soaked filter paper. This process removed any excess liquid on the outer surface of the pellets without extracting the imbibed liquid from the pore structure; it is necessary that this extrapellet excess be removed as it typically exhibits different nuclear spin relaxation characteristics to liquid within the porous network. Finally, the samples were transferred to sealed 5 mm NMR tubes for analysis; each sample consisted of between 5 and 10 saturated catalyst pellets so as to provide a well-averaged measurement of the surface-adsorbate interactions present between the imbibed liquids and the pore surfaces throughout each oxide support.

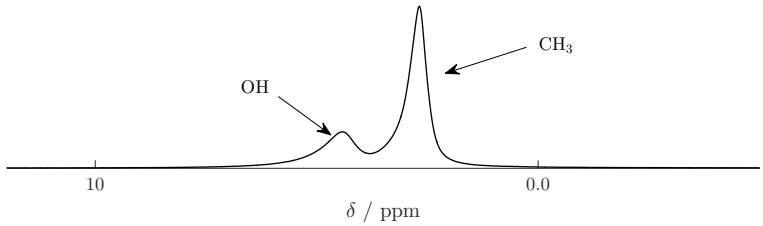

Figure 5.2: ^{1}H NMR spectrum obtained from methanol-saturated γ-Al_2O_3.

Nuclear spin-lattice relaxation

Nuclear spin relaxation measurements were performed using a Bruker DMX 300 NMR spectrometer equipped with a 7.1 T superconducting magnet, corresponding to a ^{1}H frequency of 300.13 MHz. Figure 5.2 illustrates a typical ^{1}H NMR spectrum obtained from the methanol-saturated catalyst materials under examination; no significant changes in peak shape or chemical shift were observed upon functionalisation. Separate resonance signals from the methyl and hydroxyl ^{1}H groups are clearly distinguishable; this allowed their relaxation properties to be evaluated individually without the use of complex correlation measurements. Values of the ^{1}H spin-lattice relaxation time constant T_1 were acquired using the inversion recovery method detailed in Chapter 3. [30] The appropriate pulse sequence is given in Figure 3.10a; here 16 τ_1 recovery delays were employed ranging logarithmically from 1 ms to $\sim 5T_1$. By selecting appropriate integration limits designed to minimise the effects of peak overlap the observed relaxation was found to exhibit near-single exponential behaviour; as such, T_1 values were obtained by fitting the acquired nuclear spin relaxation data to the simple expression

$$\frac{S(\tau_1)}{S_0} = 1 - 2\exp\left(\frac{-\tau_1}{T_1}\right). \tag{5.1}$$

Here $S(\tau_1)$ is the signal acquired from the time-dependent longitudinal magnetisation and S_0 is the signal acquired at thermal equilibrium. All NMR measurements were performed under ambient pressure and at 20 $\pm$ 0.2 °C.

5.3 Results and discussion

5.3.1 Surface chemistry and pore structure

Let us first examine the influence of our passivation treatment on the surface chemistry and pore structure of the mesoporous oxides under study. Figure 5.3 shows the results of the DRIFTS analysis performed on these materials; in particular, this figure illustrates the difference in infrared adsorption between passivated and unpassivated oxides.[1] It is clearly apparent that functionalisation of the pore surface with TEOS has resulted in a loss of surface hydroxyl groups, as characterised by the negative peaks present within each spectrum at wavenumbers above 3500 cm^{-1}. The frequencies and corresponding assignments for the peaks which appear upon passivation are indicated; four stretches are observed at around 2900 cm^{-1}, corresponding to $-CH_2$ (2926 cm^{-1} asymmetric and 2855 cm^{-1} symmetric) and $-CH_3$ (2961 cm^{-1} asymmetric and 2879 cm^{-1} symmetric) stretches. [31] An additional peak is observed at 1465 cm^{-1} which may be assigned to a $-CH_2$ bending mode. [31] The presence of these peaks, together with the negative peaks observed at high wavenumber, confirms qualitatively the successful passivation of surface hydroxyls with alkyl groups upon treatment of the oxide materials with TEOS.

To examine the effects of our passivation procedure on the pore structure of the four oxides, specific surface area and pore volume measurements were performed pre- and post-passivation through the measurement of nitrogen adsorption isotherms. The isotherm data obtained from these materials are illustrated in Figure 5.4; in each case the shape of the data indicates Type IV or V isotherms, indicative of mesoporous solids. From these data a clear reduction in the amount of nitrogen adsorbed *per* gram of adsorbent is evident upon functionalisation, indicating a reduction in pore size. This of course is expected following the introduction of such lengthy alkyl chains to the pore structure. A summary of the results of the BET and BJH pore size and surface area analysis is provided in Table 5.1 and confirms this observation, revealing a reduction of both surface area and pore volume upon passivation.

[1] Absorbance spectra obtained from each material is presented in Appendix D.

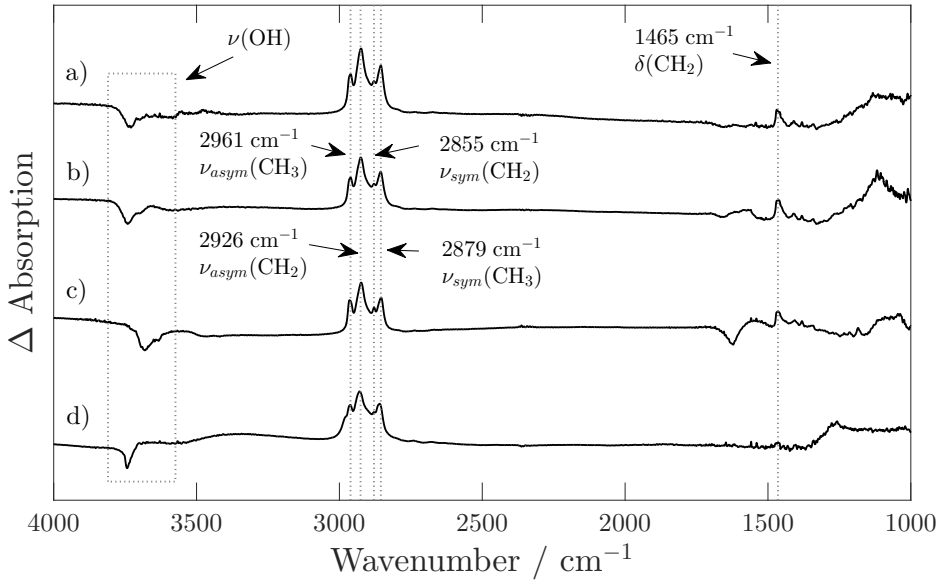

Figure 5.3: DRIFTS absorbance difference spectra for a) γ-Al_2O_3, b) θ-Al_2O_3, c) A-TiO_2 and d) SiO_2. Spectra are reported as the change in absorption upon passivation of each oxide with TEOS; negative peaks therefore represent a loss of signal upon surface passivation while positive peaks indicate a gain in signal upon passivation. Negative peaks associated with a loss of hydroxyl signal are indicated by a dashed box. Positive peaks which appear upon passivation are indicated with dashed lines.

Table 5.1: Pore textural properties.

Oxide support	BET surface area S_{BET} ($m^2\ g^{-1}$)	
	Oxide	Oxide + TEOS
γ-Al_2O_3	90	82
θ-Al_2O_3	108	99
A-TiO_2	40	37
SiO_2	272	236
Oxide support	BJH pore volume V_{BJH} ($cm^3\ g^{-1}$)	
	Oxide	Oxide + TEOS
γ-Al_2O_3	0.49	0.34
θ-Al_2O_3	0.57	0.52
A-TiO_2	0.28	0.19
SiO_2	1.29	1.01
Oxide support	BJH pore diameter d_{pore} (nm)	
	Oxide	Oxide + TEOS
γ-Al_2O_3	14.3	10.7
θ-Al_2O_3	14.8	13.4
A-TiO_2	20.4	15.0
SiO_2	13.3	11.2

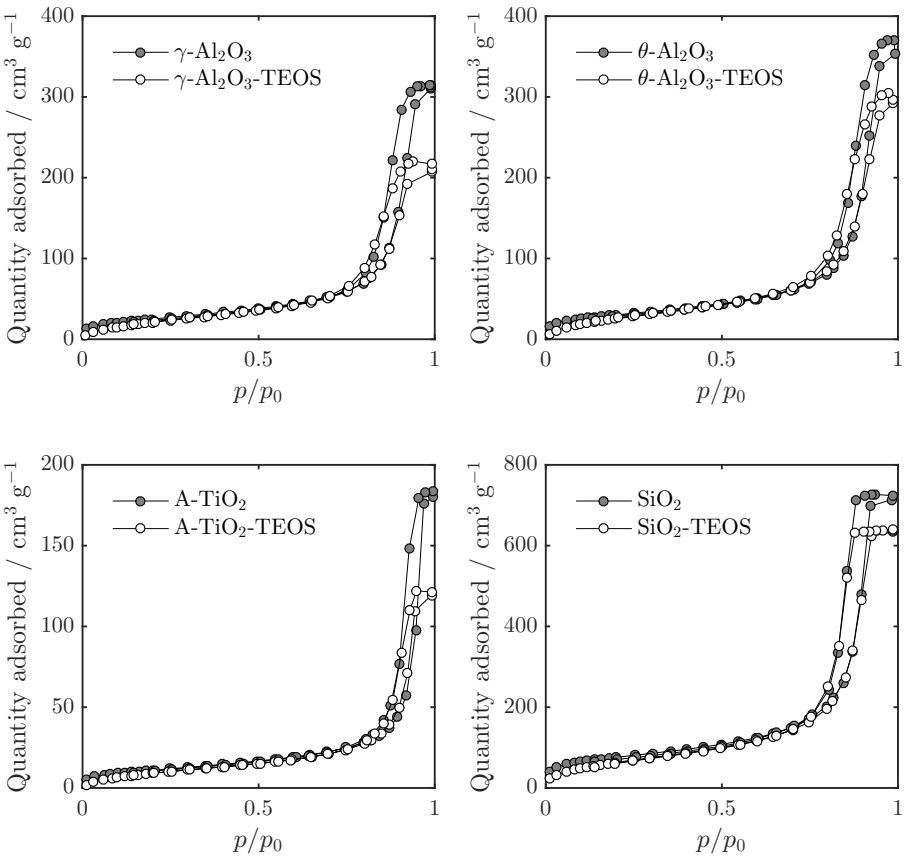

Figure 5.4: N_2 adsorption isotherms for each of the oxide materials investigated. Grey data points indicate the hysteresis of unfunctionalised oxides, while white data points dictate the isotherms of oxides functionalised with TEOS.

5.3.2 Nuclear spin-lattice relaxation

We now turn to our nuclear spin relaxation measurements. Given the highly non-viscous nature of the adsorbate under study, together with the small pore diameters investigated (Table 5.1), it is appropriate here to assume the conditions of biphasic fast exchange, as introduced at length in Chapter 4. The observed T_1 values $T_{1,obs}$ obtained from our liquid-saturated oxides are therefore considered to satisfy

$$\frac{1}{T_{1,obs}} = \frac{1-P}{T_{1,bulk}} + \frac{P}{T_{1,surf}}, \tag{5.2}$$

where $T_{1,bulk}$ and $T_{1,surf}$ are the T_1 values associated with the unrestricted bulk liquid, and with an adsorbed surface layer of population

$$P = \frac{\delta S}{V}. \tag{5.3}$$

Here δ is the thickness of the adsorbed surface layer and S/V is the modal surface-to-volume ratio of the pore network under study; given the general case that $1/T_{1,surf} \gg 1/T_{1,bulk}$ and that S/V is large then this expression simplifies to

$$\frac{1}{T_{1,obs}} \approx \frac{\delta S}{V}\frac{1}{T_{1,surf}}, \tag{5.4}$$

illustrating the sensitivity of $T_{1,obs}$ to the pore structure under study, and to nuclear spin relaxation occurring directly at the pore surface.

Figure 5.5 panels a-d show the T_1 inversion recovery data acquired from each methanol-saturated oxide investigated; the corresponding $T_{1,obs}$ values are illustrated in panels e and f of the same Figure. It is clearly evident from Figure 5.5e that the methanol methyl (CH_3) group presents a significantly longer ^{1}H T_1 relaxation time than exhibited by the methanol hydroxyl (OH) group within unpassivated oxides. This observation is consistent across the range of oxides investigated and is in agreement with investigations of methanol at Al_2O_3 surfaces by Stübner *et al.* [32] and Ward-Williams *et al.*. [33] Recalling the high magnetic field used for these relaxation experiments it is appropriate to interpret our results on the basis of molecular tumbling mobility; [34] a simple interpretation of this approach is given

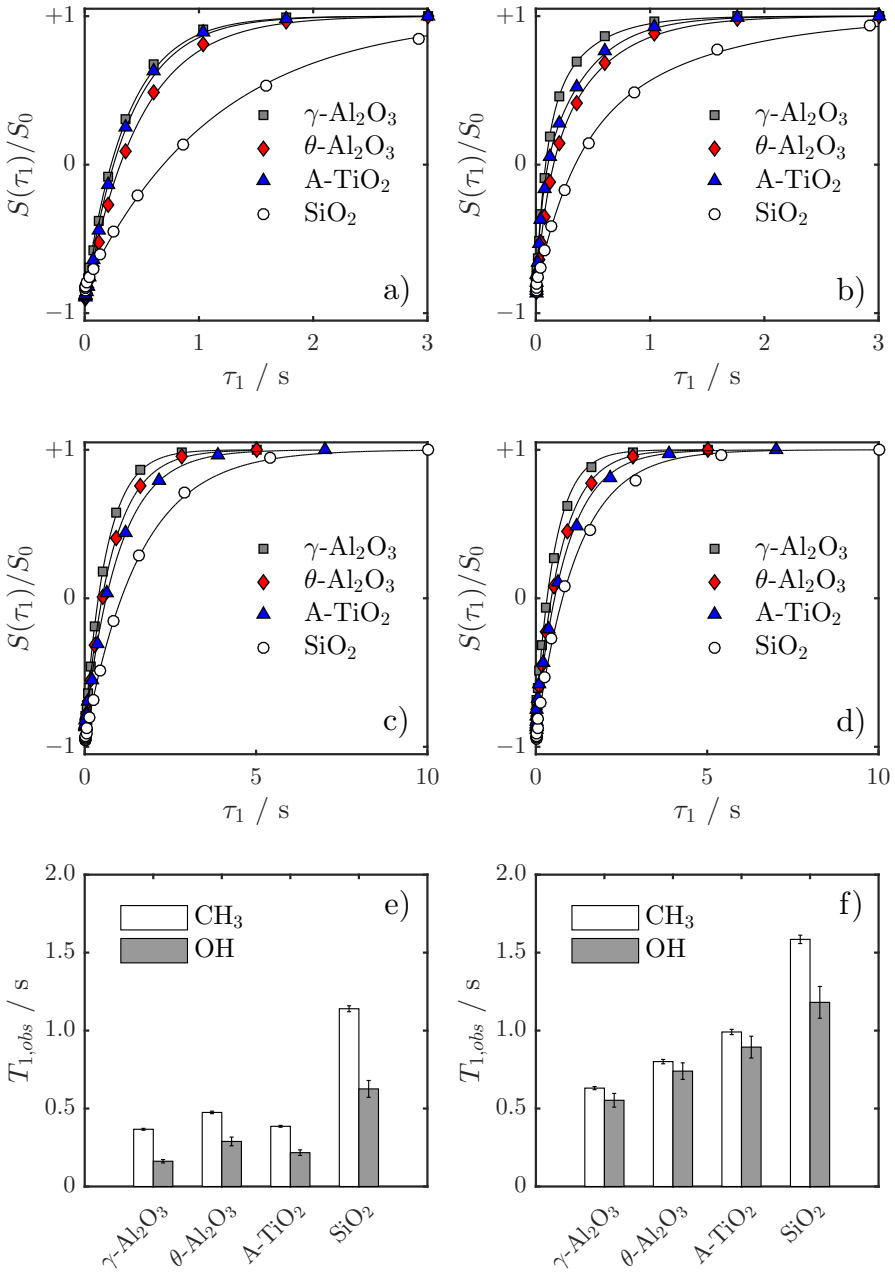

Figure 5.5: Nuclear spin-lattice relaxation characteristics of liquid methanol imbibed within mesoporous oxide materials. a) and b) illustrate T_1 inversion recovery curves obtained from the CH_3 and OH proton environments within unpassivated oxides, respectively, while c) and d) illustrate T_1 inversion recovery curves obtained from the CH_3 and OH proton environments within passivated oxides, respectively. Solid lines indicate fits to Equation 5.1; e) and f) show the T_1 values obtained from this fitting process. Data in panel e) illustrates T_1 values obtained from methanol imbibed within unpassivated oxides while panel f) illustrates T_1 values obtained from the same materials passivated with TEOS. Error bars were obtained from several repeat experiments on different samples. The relative errors in measured $T_{1,obs}$ values in unpassivated oxides are approximately 2 % and 20 % for CH_3 and OH relaxation, respectively; these errors are approximately 2 % and 10 % in passivated oxides, respectively.

by the theory of Bloembergen, Purcell and Pound (BPP), [35] where we recall

$$\frac{1}{T_1} \propto J(\omega_0) + 4J(2\omega_0). \tag{5.5}$$

Here ω_0 is the experimental Larmor frequency, and the spectral density function $J(\omega)$ is

$$J(\omega) \propto \frac{\tau_c}{1+\omega^2\tau_c^2}, \tag{5.6}$$

where τ_c is the rotational correlation time which characterises molecular mobility; τ_c is equal to the average time take for a molecule to rotate by 1 radian. Rapidly tumbling spin systems therefore express short τ_c values, while slow motion is characterised by longer correlation times. According to this simple interpretation of nuclear spin relaxation, as the rotational correlation time τ_c approaches 0, i.e. as molecular tumbling becomes more rapid, $T_1 \rightarrow \infty$. In consequence, longer relative T_1 values may be recognised as an indicator of the enhanced mobility of a particular proton environment. If we consider the difference in relaxation characteristics between methyl and hydroxyl protons within each mesoporous oxide material individually, Equation 5.4 tells us that the influence of pore structure or surface layer thickness are irrelevant; the observed difference may therefore be attributed to differences in mobility within the adsorbed surface layer. The reduced relative motional freedom exhibited by the methanol hydroxyl group is easily explained through their ability to form hydrogen bonds with other polar moieties, resulting in favourable adsorption interactions with the hydroxyl groups which decorate the pore surface within unpassivated oxides. Indeed it is well documented that the adsorption of alcohols at hydroxylated oxide surfaces is often dominated by the formation of surface-adsorbate hydrogen bonding interactions. [36–39] Hydroxyl protons therefore experience reduced mobility at the pore surface relative to the apolar methyl group, leading to more rapid spin-lattice relaxation and shorter $T_{1,obs}$ times. Other surface interactions may also cause a bias towards the reduced $T_{1,obs}$ of the hydroxyls group, such as the reversible dissociation of labile hydroxyl proton from adsorbed methanol molecules onto the pore surface, and interactions with metal sites. [39–42]

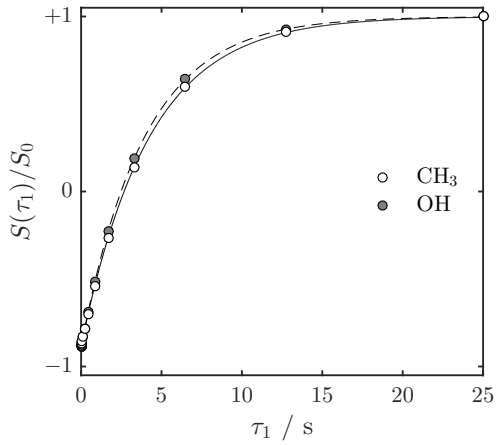

Figure 5.6: ^{1}H T_1 inversion recovery curve for unrestricted methanol. Solid and dashed lines indicate fits to Equation 5.1.

Figure 5.5f displays T_1 relaxation data from methanol-saturated oxides which have been subjected to our surface passivation treatment. We can observe through a comparison of Figures 5.5e and f that the difference in $T_{1,obs}$ experienced by the two proton environments is noticeably reduced upon passivation. We may quantify this change by taking the ratio of observed relaxation time constants $T_{1,obs}^{\mathrm{CH3}}/T_{1,obs}^{\mathrm{OH}}$. Importantly, this simple analysis may be performed without consideration of the changes to pore structure of surface chemistry upon passivation as the terms S/V and δ within Equation 5.4 cancel when considering identical molecules within the same pore structure,

$$\frac{T_{1,obs}^{\mathrm{CH_3}}}{T_{1,obs}^{\mathrm{OH}}} \approx \frac{(\delta S/V)T_{1,surf}^{\mathrm{CH_3}}}{(\delta S/V)T_{1,surf}^{\mathrm{OH}}} \approx \frac{T_{1,surf}^{\mathrm{CH_3}}}{T_{1,surf}^{\mathrm{OH}}}. \tag{5.7}$$

It is pertinent at this point to consider the differences in methyl and hydroxyl group relaxation characteristics within the unrestricted bulk. The corresponding inversion recovery curves for the two proton environments are illustrated in Figure 5.6; here the methyl group is found to exhibit $T_{1,bulk}^{\mathrm{CH_3}} = 4.22 \pm 0.01$ s while the hydroxyl group exhibits $T_{1,bulk}^{\mathrm{OH}} = 3.92 \pm 0.01$ s. The ratio of T_1 values for unrestricted methanol is therefore $T_{1,bulk}^{\mathrm{CH3}}/T_{1,bulk}^{\mathrm{OH}} \approx 1.08$; this ratio is indicated by a dashed line in Figure 5.7, together with the $T_{1,obs}^{\mathrm{CH_3}}/T_{1,obs}^{\mathrm{OH}}$ ratios obtained from the data in Figure 5.5. From consideration of these ratios we see that $T_{1,obs}^{\mathrm{CH_3}}/T_{1,obs}^{\mathrm{OH}}$ is large in the case of unpassivated oxides, while $T_{1,obs}^{\mathrm{CH_3}}/T_{1,obs}^{\mathrm{OH}} \approx 1$ in the case of passivated oxides. This

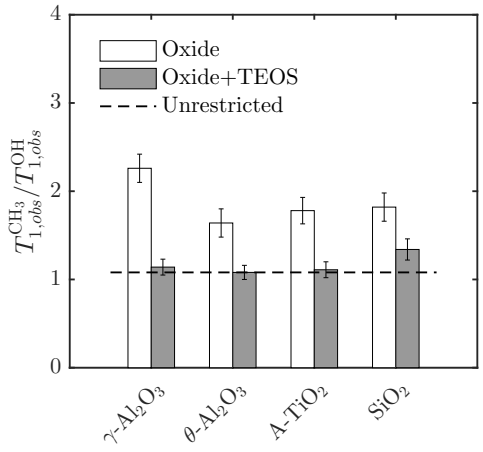

Figure 5.7: ^{1}H $T_{1,obs}^{CH_3}/T_{1,obs}^{OH}$ ratios for methanol imbibed within functionalised and unfunctionalised oxides, together with the corresponding ratio obtained from unrestricted methanol.

suggests that within these passivated materials the ratio of relaxation time constants tends towards that of the unrestricted bulk liquid, in turn, indicating that bulk-like dynamics occur near the surface of passivated pores. The significant increase in the ratio of relaxation time constants observed within upassivated oxides suggests a more significant difference in the mobility of the two methanol proton environments; such a difference is of course expected following the above discussion on hydrogen bonding interactions with hydroxylated surfaces.

5.3.3 Influence of passivation on relaxation time interpretation

A further observation from Figure 5.5 which we have neglected until this point is that $T_{1,obs}$ increases upon passivation regardless of the proton environment considered. From the above discussion we may be tempted to suggest that this is an obvious indication of enhanced molecular freedom within the adsorbed surface layer within passivated oxides. However, from Equation 5.4 it is clear that in order to perform a direct comparison of the dynamics of molecules within different materials we must also take into account any changes to the surface-to-volume ration S/V of the pores within each material, as well as the influence of passivation on the thickness of the adsorbed surface layer δ. In this section we therefore wish to explore an alternative method of analysing our relaxation data, in which the influence of our passivation procedure on pore structure and oxide surface chemistry are taken into account. It is

also of interest to provide a more general method of analysing changes to molecular mobility at pore surfaces in which the presence of multiple spin-bearing environments is not a prerequisite. We perform this analysis in two stages; first we establish an appropriate metric with which to work, and from which we may easily remove the influence of pore structure. Second we perform an empirical fitting to remove the influence of the adsorbed surface layer thickness δ.

Establishing a dimensionless interaction parameter

Let us define a dimensionless spin-lattice surface interaction parameter η_{surf}, given by the ratio of T_1 in the bulk to that of the same liquid at the pore surface,

$$\eta_{surf} = \frac{T_{1,bulk}}{T_{1,surf}}. \tag{5.8}$$

Figure 5.8 illustrates the utility of this parameter; this figure shows relaxation curves based on the simple BPP interpretation of nuclear spin relaxation. The circled area is considered indicative of spin-carrying molecules experiencing restricted mobility due to adsorption processes; [27] indeed, it is well established that T_1 and T_2 diverge under the conditions of adsorption. [43, 44]. As introduced in Chapter 4 it may be assumed that unrestricted liquids fall within the motionally narrowed regime, such that $1/\tau_c^{\text{bulk}} \gg \omega_0$. Adsorbed liquids clearly experience a reduction in mobility, such that $\tau_c^{\text{adsorbed}} > \tau_c^{\text{bulk}}$. Provided[2] $1/\tau_c^{\text{adsorbed}} \geq \omega_0$, which is a reasonable assumption for weak adsorption processes dominated by the formation of hydrogen bonding interactions, the reduction in molecular mobility upon adsorption results in a reduction in T_1. Our spin-lattice surface interaction parameter will therefore be sensitive to adsorption processes; η_{surf} defined according to Equation 5.8 provides a convenient limiting value of 1, in which case molecular mobility within the adsorbed surface layer can be considered identical to that within the unrestricted bulk. Adsorption interactions leading to a reduction in surface mobility will be expressed as an increase in η_{surf} from this limit.

[2]Here we should recall from Chapter 4 that T_1 is at a minimum when $1/\tau_c = \omega_0$.

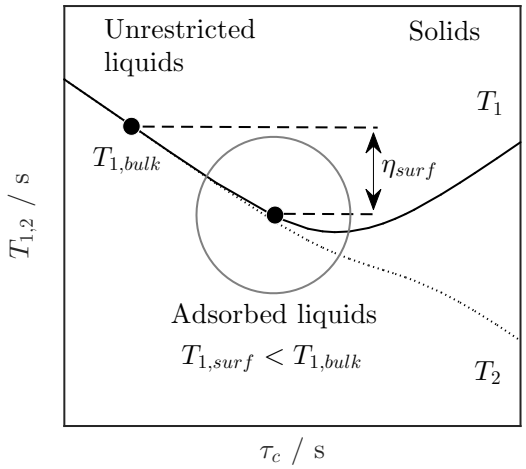

Figure 5.8: BPP theory-based illustration of the origin of the difference in relaxation time constants observed upon adsorption. T_1 and T_2 are illustrated by solid and dotted black lines, respectively. The relaxation of unrestricted liquids is assumed to fall with the motionally narrowed regime where $1/\tau_c \gg \omega_0$; an example is illustrated by the $T_{1,bulk}$ data point. The relaxation characteristics of adsorbed liquids is characterised by the grey circled area; here $T_{1,surf} > T_{2,surf}$ and $T_{1,surf} < T_{1,bulk}$. For weak adsorption processes it can be assumed that $1/\tau_c \geq \omega_0$. As illustrated by the example $T_{1,surf}$ data point, the resulting ratio $\eta_{surf} = T_{1,bulk}/T_{1,surf}$ increases as molecular motion becomes more restricted due to adsorption.

In previous work the application of a similar metric $T_{1,bulk}/T_{1,obs}$, or its inverse, has been reported. Staph *et al.* used the ratio $T_{1,obs}/T_{1,bulk}$ to investigate the surface dynamics of a range of polar and non-polar liquids imbibed within mesoporous silica glass. [45] It was observed through the use of field cycling NMR relaxometry that the value of $T_{1,obs}/T_{1,bulk}$ was significantly reduced in the case of polar liquids, relative to that exhibited by non-polar liquids, indicating stronger adsorption interactions. D'Agostino used the ratio $T_{1,bulk}/T_{1,obs}$ to explore the surface dynamics of various molecular liquids within a range of unfunctionalised catalyst support materials; again it was shown that polar liquids exhibit an enhanced affinity for the surface of mesoporous oxide materials. [11] Unfortunately however, we must note that these approaches are inappropriate for the comparsion of molecular dynamics here; this is because in order to compare the surface dynamics of adsorbed methanol molecules between unpassivatived and passivated oxides utilising the ratio

$$\frac{T_{1,bulk}}{T_{1,obs}} \approx \frac{\delta S}{V}\frac{T_{1,bulk}}{T_{1,surf}} \tag{5.9}$$

or its inverse, it must be assumed that no change occurs to either the thickness of the adsorbed surface layer δ or to the surface-to-volume ratio S/V upon passivation. In the present analysis we explicitly avoid this assumption by replacing the observed relaxation time constant with that associated with relaxation directly at the pore surface, $T_{1,bulk}/T_{1,surf}$.

A further study of note is that by Vecino *et al.*. [46] Here the authors used ^{13}C NMR relaxation measurements to investigate the adsorption configuration of several unsaturated linear and cyclic hydrocarbons at θ-Al_2O_3 and γ-Al_2O_3 surfaces. The ^{13}C ratio $T_{1,obs}/T_{1,bulk}$ was employed as a measure of reduced atomic mobility, which in analogy to the present work was then interpreted as an indication of surface affinity. Carbon atoms exhibiting the smallest relaxation time ratio were interpreted as adsorption centres, providing insight into favourable molecular configurations at the pore surface. Interestingly in this work, rather than fully saturating the pore structures with the chosen adsorbate, the authors evaporated only a monolayer coverage into the pore structures; the experimentally obtained values of $T_{1,obs}$ could then be considered directly comparable with $T_{1,surf}$, allowing the observed relaxation characteristics to be interpreted directly in terms of this monolayer. While this method is clearly an elegant approach to the problem of elucidating surface relaxation phenomena, a significant caveat is that it then falls to the experimentalist to dictate the surface coverage of the chosen adsorbate, and hence the thickness of the adsorbed surface layer under investigation; indeed, the authors of the aforementioned work illustrated that the ratio $T_{1,obs}/T_{1,bulk}$ exhibits sensitivity to the surface coverage employed. [46] In the present work we have chosen to explore the influence of passivation on adsorption dynamics under equilibrium adsorption conditions (dictated by fully saturated pore structures), which are of direct relevance to liquid-phase catalytic processes, and in which the exact nature of the adsorbed surface layer will typically be unknown *a priori*.

In this work $T_{1,surf}$ is obtained from our fully saturated samples through a simple rearrangement of Equation 5.2, such that

$$T_{1,surf}(\delta) = PT_{1,obs} - \frac{PT_{1,bulk}}{1-P}. \tag{5.10}$$

Table 5.2: Surface-to-volume ratios obtained from the BET and BJH textural properties listed in Table 5.1.

Oxide support	S_{BET}/V_{BJH} (m^{-1})	
	Oxide	Oxide + TEOS
γ-Al_2O_3	1.84×10^8	2.44×10^8
θ-Al_2O_3	1.88×10^8	1.89×10^8
A-TiO_2	1.42×10^8	1.96×10^8
SiO_2	2.11×10^8	2.35×10^8

A dependence on the unknown surface layer thickness δ arises from the presence of the surface population term $P = \delta S/V$; the surface-to-volume ratio S/V which is also present within this population term can be estimated from the results of our N_2 porosimetry described in Table 5.1, such that $S/V \cong S_{\mathrm{BET}}/V_{\mathrm{BJH}}$. Values of this ratio are provided in Table 5.2 from which it is clear that treatment of the oxide supports with TEOS has resulted in an increase in S/V across the range of oxide materials considered. From examination of the approximate relationship between $T_{1,obs}$ and S/V provided by Equation 5.4, and be assuming a constant surface layer thickness and $T_{1,surf}$ across both functionalised and unfunctionalised oxides, it is instructive to note that this increase in S/V should lead to a reduction in $T_{1,obs}$ upon passivation, rather than the observed increase illustrated in Figure 5.5. Our results, therefore, cannot be explained through the inclusion of S/V alone. Indeed, it is necessary that the change in surface relaxivity $\rho_1 = \delta/T_{1,surf}$ which occurs as a result of surface passivation outweighs the influence of increasing S/V.

Analysis of methyl group dynamics

The dependence of $T_{1,surf}(\delta)$ and of our spin-lattice surface interaction parameter on the surface layer thickness δ means our initial assessment must consider Equations 5.8 and 5.10 across a range of possible δ values; we choose here to investigate $T_{1,surf}(\delta)$ and $\eta_{surf}(\delta)$ across an adsorbed surface thickness range of $\delta = 1 - 5$ molecular layers. This is an appropriate range for the analysis of alcohols interacting with oxide surfaces; for example, molecular dynamics simulation of methanol at a model silica surface suggest that a surface layer thickness of 2 molecular layers is readily formed. [47] Experimental studies of the adsorption of ethanol at a silica

surface suggests a similar surface structure. [48] We define the thickness of a single adsorbed layer within a given liquid-saturated pore to be that of the kinetic diameter of the molecule under study d_{kin}; for methanol it is assumed that $d_{kin} \approx 0.36$ nm. [49]

To simplify the analysis of our observed methanol dynamics, and to generate a method dependent on the presence of only a single nuclear spin environment, we will consider only the T_1 of the methyl group, $T_1^{\mathrm{CH_3}}$. In comparison to the relaxation characteristics of the methanol hydroxyl group, relaxation of the methyl ^{1}H environment presents an attractive measure of molecular dynamics; not only does it contain a significantly higher fraction of the total ^{1}H spins present within a given methanol-saturated pore, but its relaxation dynamics are also independent of any proton hopping or other dissociative dynamics exhibited by the hydroxyl group. The sensitivity of $T_1^{\mathrm{CH_3}}$ to overall methanol dynamics may be considered on the basis of the Lipari-Szabo (LS) theory of nuclear spin relaxation as introduced in Chapter 4. [50, 51] LS theory gives the spectral density function $J(\omega)$ as

$$J(\omega) \propto \frac{S^2\tau_{mol}}{1+\tau_{mol}^2\omega^2} + \frac{(1-S^2)\tau_t}{1+\tau_t^2\omega^2}, \tag{5.11}$$

where

$$\frac{1}{\tau_t} = \frac{1}{\tau_{int}} + \frac{1}{\tau_{mol}}. \tag{5.12}$$

Here τ_{mol} is an isotropic rotational correlation time associated with the rate of overall molecular motion, while τ_{int} is an internal correlation time which defines the frequency of internal motions. S is known as the generalised order parameter and takes values between 0 and 1. This parameter defines the isotropy of the internal motions present; $S^2 = 0$ indicates perfectly isotropic internal motion while $S^2 = 1$ indicates totally restricted internal motion. In the present case τ_{int} characterises the mobility of the methyl group while τ_{mol} characterises the mobility of methanol molecules on the whole. As the hydrogen bonding dynamics of liquid methanol dictate that the internal methyl rotations will be rapid compared to overall molecular dynamics, the time constants τ_{int} and τ_{mol} satisfy the inequality $\tau_{int} \ll \tau_{mol}$ such that $\tau_t \sim \tau_{int}$. Provided $1/\tau_{int} \gg \omega_0$, i.e. the internal motion is rapid not only with

respect to the rates of molecular tumbling, but also with respect to the experimental Larmor frequency, Equation 5.11 reduces to [52]

$$J(\omega) \propto \frac{S^2\tau_{mol}}{1+\tau_{mol}^2\omega^2} + (1-S^2)\tau_{int}. \tag{5.13}$$

This expression is know as the truncated LS spectral density function. [52] Furthermore, in the presence of highly anisotropic internal motion S^2 will be large; recalling that τ_{int} is small this allows us to further simplify our LS approach to

$$J(\omega) \propto \frac{S^2\tau_{mol}}{1+\tau_{mol}^2\omega^2}, \tag{5.14}$$

which, in the limit of $S^2 \rightarrow 1$ is equivalent to the BPP interpretation of nuclear spin relaxation given by Equation 5.6. This interpretation therefore allows us to consider our acquired $T_{1,obs}^{\mathrm{CH_3}}$ data as a probe of overall methanol dynamics. It is worthwhile noting that this is an unusual application of the LS theory of nuclear spin relaxation. Indeed the LS spectral density function and its truncation to Equation 5.14 is typically only used in the analysis of protein NMR; however, a similar study to the present application has recently been put forward by Witherspoon *et al.* with regards to the elucidation of xylene dynamics within the metal-organic framework MOF-5. [53] In this work the authors make a similar series of approximations such that the rapid rotational motion of the xylene methyl groups provides access to overall molecular tumbling.

Calculated values of $T_{1,surf}(\delta)$ for the five δ values considered are illustrated in Figure 5.9a and b; the corresponding $\eta_{surf}(\delta)$ values for each of the methanol-saturated oxides investigated are presented in panels c and d of the same figure. There is significant variation in these values with increasing δ, hence these data are presented on a log-y scale. On examination of these results it is clear that functionalisation of the pore surface has a significant impact on $T_{1,surf}(\delta)$, and therefore on $\eta_{surf}(\delta)$. More specifically, passivation of the surface hydroxyl groups results in a notable decrease in $\eta_{surf}(\delta)$ irrespective of the oxide material considered. From Equation 5.8 it is clear that this is indicative of an increase in the molecular mobility of methanol molecules within the adsorbed surface layer. In particular,

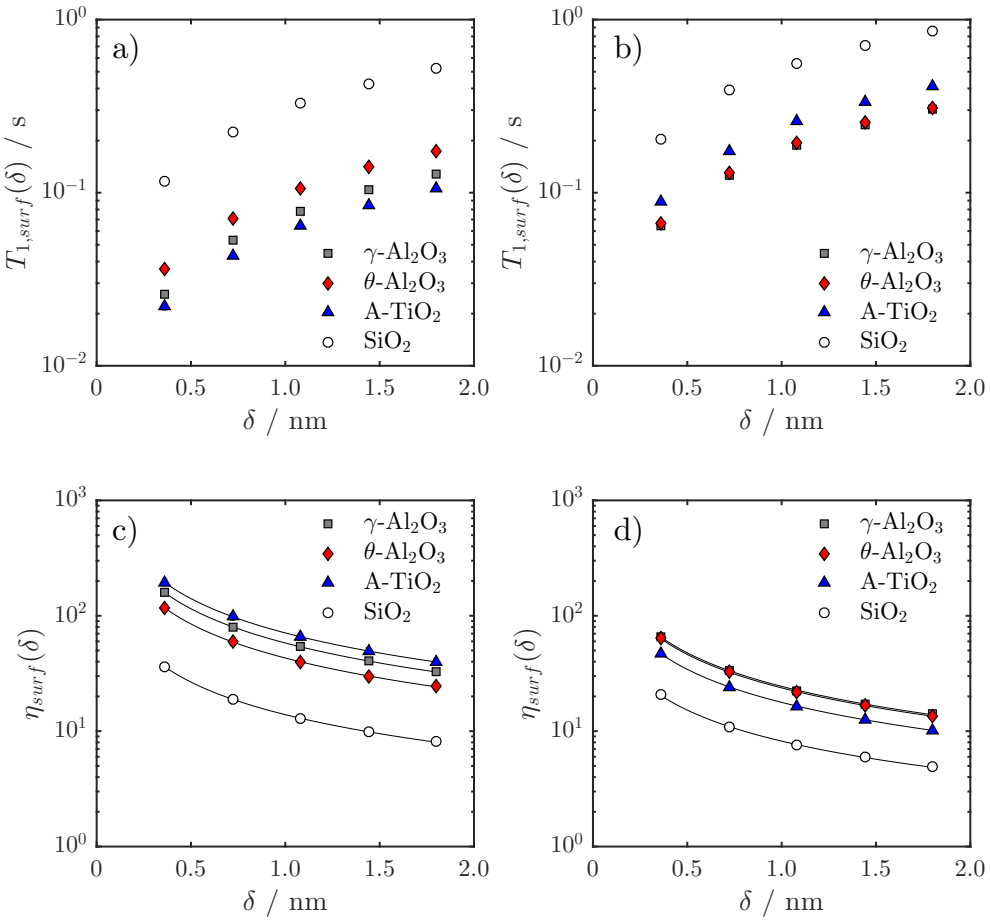

Figure 5.9: Calculated methanol $T_{1,surf}$ values and spin-lattice surface interaction parameters η_{surf} as a function of adsorbed surface layer thickness δ. a) and b) illustrate $T_{1,surf}(\delta)$ values for methanol within unpassivated and passivated oxides, respectively, as calculated according to Equation 5.10. Data points within panels c) and d) illustrate the corresponding $\eta_{surf}(\delta)$ values calculated from Equation 5.8, while solid lines represent a fit to Equation 5.15. Error bars are provided but it general are smaller than the data points in each panel.

our results suggest that as $\eta_{surf}(\delta)$ tends towards 1, the motional freedom of methanol molecules within the adsorbed surface layer tends towards that of the unrestricted bulk liquid upon interaction with passivated pore surfaces. As this change is accompanied by a decrease in surface hydroxyl density we may attribute this observation to a reduction in the hydrogen bonding ability of the oxide surfaces upon passivation. Importantly, this result is qualitatively identical to that proposed by the simple analysis described in Figure 5.7; however, here we have performed a far more extensive assessment, involving the analysis of only a single ^{1}H environment, and the evaluation and elimination of the effects of changing S/V values.

Derivation of a surface layer independent interaction parameter

While the $\eta_{surf}(\delta)$ results presented in Figure 5.9 provide a clear indication that passivation of the oxides in question leads to enhanced molecular mobility at the pore surface, a clear dependence on the surface layer thickness δ remains. As the assumption that δ remains constant upon passivation may not be valid, it is important to attempt to remove this dependence. It is interesting then to observe that the methanol $\eta_{surf}(\delta)$ data fit a power law of the form

$$\eta_{surf}(\delta) = \alpha_j \delta^{-\beta_j}. \tag{5.15}$$

Here α_j (units of length$^{\beta_j}$) and β_j (dimensionless) are constants and we use the index j to indicate the oxide under study. Fits of this form are indicated by solid lines within Figure 5.9c and d. Moreover, the simple relationship given in Equation 5.15 suggests an approximate method to remove the dependency of $\eta_{surf}(\delta)$ on δ. We attempt to achieve this here through the normalisation of η_{surf} by a weakly interacting reference liquid: cyclohexane. Cyclohexane ($d_{kin} \approx 0.62$ nm) [49] is often chosen as a weakly interacting reference species for NMR relaxation and diffusion studies involving heterogeneous catalysis due to its single proton environment, slow relaxation characteristics and low affinity for oxide surfaces. [11, 13–15, 54] To perform this normalisation we define a normalised spin-lattice surface interaction parameter η^N_{surf} as

$$\eta^{N}_{surf,j} = \frac{\eta^{\mathrm{CH_3}}_{surf,j}(\delta_k)}{\eta^{\mathrm{CHx}}_{surf,j}(\delta_k)}. \tag{5.16}$$

Here $\eta^{\mathrm{CH_3}}_{surf,j}$ and $\eta^{\mathrm{CHx}}_{surf,j}$ are the spin-lattice surface interaction parameters acquired from methanol- and cyclohexane-saturated oxides, respectively. The relevant spin-lattice relaxation data is presented in Figure 5.10; importantly, these data are found to exhibit the same power law relationship between $\eta_{surf}(\delta)$ and δ as observed for methanol (Figure 5.10e). We can then note from Equation 5.16 and from our empirical power law relationship in Equation 5.15 that for the dependency on δ to be removed, β values acquired from the fitting of methanol and cyclohexane interaction parameter data must satisfy the condition

$$\beta_j^{\mathrm{CH_3}} - \beta_j^{\mathrm{CHx}} \approx 0, \tag{5.17}$$

where the superscripts CH_3 and CHx again indicate the methanol methyl group and cyclohexane, respectively. In turn, the respective magnitudes of η^{N}_{surf} will be $\eta^{N}_{surf,j} \sim \alpha_j^{\mathrm{CH_3}}/\alpha_j^{\mathrm{CHx}}$. The power law constants α and β are listed in Table 5.3 for both methanol- and cyclohexane-saturated oxides. For the purposes of establishing a series of weakly-interacting reference measurements we restrict our cyclohexane investigation to unpassivated oxides. A physical interpretation of this normalisation process then becomes the comparison of methanol tumbling dynamics within the adsorbed surface layer of passivated or unpassivated mesoporous oxides with that of cyclohexane at the surface of unpassivated oxides; this is a favourable comparison given that the interaction of cyclohexane with hydroxylated oxide surfaces is known to be weak. [54] It follows that as $\eta^{N}_{surf} \rightarrow 1$ the tumbling dynamics under study can be considered to approach that of cyclohexane, while an increase from this limit indicates more restricted motion.

The index k within Equation 5.16 is provided to highlight the fact that the values of δ considered must be equal in units of length. Despite the differing values of d_{kin} for methanol and cyclohexane, the correct values of $\eta^{\mathrm{CHx}}_{surf,j}(\delta_k)$ are readily obtained by consulting the appropriate power law constants governing the behaviour of cyclohexane (Table 5.3) and solving from the corresponding methanol

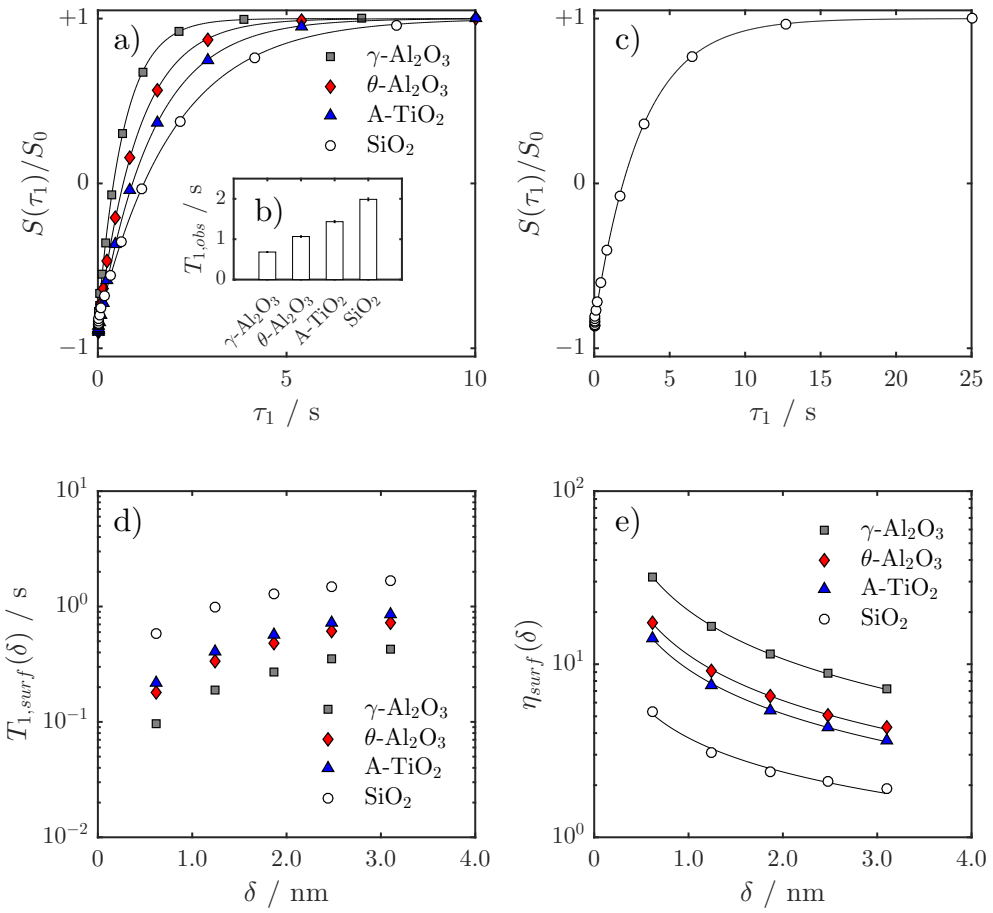

Figure 5.10: Nuclear spin-lattice relaxation characteristics of liquid cyclohexane. a) illustrates T_1 inversion recovery curves obtained from cyclohexane within unpassivated oxides. Solid lines indicate fits to Equation 5.1; the corresponding $T_{1,obs}$ values are given in panel b). The relative error in measured $T_{1,obs}$ values is approximately 1.5 % in all cases. c) illustrates the T_1 inversion recovery curve for unrestricted cyclohexane, from which a $T_{1,bulk}$ value of 3.102 ± 0.003 s is obtained. d) and e) illustrate the corresponding $T_{1,surf}$ and η_{surf} values calculated according to Equations 5.8 and 5.10, respectively; solid lines in panel e) represent fits to Equation 5.15

Table 5.3: α and β values obtained from fitting Equation 5.15 to the $\eta_{surf}(\delta)$ data in Figures 5.9 and 5.10.

Oxide support	Methanol				Cyclohexane	
	Oxide		Oxide+TEOS		Oxide	
	α / nm$^\beta$	β	α / nm$^\beta$	β	α / nm$^\beta$	β
γ-Al_2O_3	58.11	0.98	24.45	0.96	20.43	0.93
θ-Al_2O_3	43.06	0.98	23.72	0.96	11.30	0.87
A-TiO_2	71.03	0.99	17.76	0.95	9.31	0.85
SiO_2	13.91	0.94	8.20	0.89	3.75	0.65

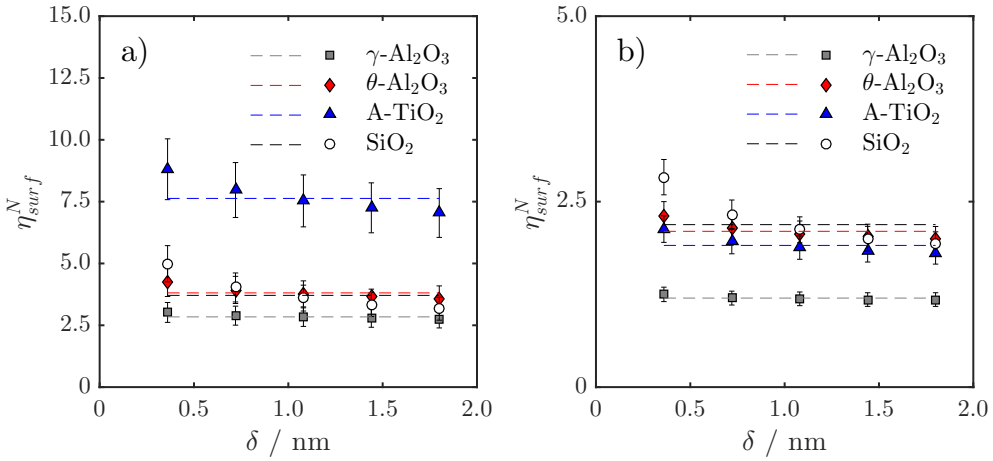

Figure 5.11: Normalised spin-lattice surface interaction parameter η^N_{surf} as obtained from Equation 5.16. a) illustrates normalised methanol surface dynamics within unpassivated oxides while b) illustrates normalised methanol surface dynamics within those same oxides passivated with TEOS. In each case the methanol dynamics in question are compared to that of cyclohexane at the surface of unfunctionalised oxides. The ratios $\alpha^{\mathrm{Me}}/\alpha^{\mathrm{CHx}}$ obtained from Table 5.3 are illustrated by dashed lines in each case, and provide good agreement with the calculated η^N_{surf} data.

δ values. The normalised spin-lattice surface interaction parameters η^N_{surf} for methanol imbibed within unpassivated and passivated oxides are shown in Figure 5.11a and b, respectively; this figure represents the culmination of the various data processing stages described within this chapter. From these data we can see that in the case of γ-Al_2O_3, θ-Al_2O_3 and A-TiO_2, any dependence of η^N_{surf} on δ has indeed been removed, to within the experimental error indicated for each oxide. The ratio $\alpha^{\mathrm{CH_3}}/\alpha^{\mathrm{CHx}}$ is also illustrated for each system by dashed lines; it is clear on comparison that this ratio provides a good estimate of η^N_{surf} in each case. The η^N_{surf} data for methanol-saturated SiO_2 illustrates less ideal behaviour and retains some curvature as a function of δ; this remaining δ-dependence can easily be traced back to the relevant β values in Table 5.3 and the nonconformity of this data to Equation 5.17. Notwithstanding the slight curvature[3] expressed by this SiO_2 data, the ratio $\alpha^{\mathrm{CH_3}}/\alpha^{\mathrm{CHx}}$ is still in reasonable agreement with calculated η^N_{surf} data points; we may therefore use these $\alpha^{\mathrm{CH_3}}/\alpha^{\mathrm{CHx}}$ values to perform a numerical comparison of our observed methanol dynamics at passivated and unpassivated surfaces. These

[3]It is important to note that Figure 5.11 expresses the calculated η^N_{surf} data on a linear-y scale, while the $\eta_{surf}(\delta)$ data detailed in Figure 5.9 is given on a log-y scale. The curvature of the SiO_2 η^N_{surf} data is therefore small compared to that of the $\eta_{surf}(\delta)$ data, and has been largely removed through our empirical normalisation process.

are approximately 2.8, 3.8, 7.6 and 3.7 for unpassivated γ-Al_2O_3, θ-Al_2O_3, A-TiO_2 and SiO_2, respectively. Upon passivation these reduce to approximately 1.2, 2.1, 1.9 and 2.2, respectively. Our empirical η^N_{surf} fitting therefore makes it apparent that the tumbling motion of methanol within the adsorbed surface layer tends towards that of our weakly-interacting reference – cyclohexane – upon passivation, again indicating a reduction in surface-adsorbate interactions upon removal of surface hydroxyl groups.

5.4 Conclusions

This chapter has demonstrated the application of simple, high-field nuclear spin-lattice relaxation measurements as a non-invasive probe of molecular dynamics within liquid-saturated mesoporous oxides of relevance to heterogeneous catalysis. A series of T_1 measurements have been performed to assess changes to methanol mobility near the pore surface of these oxides upon passivation of surface hydroxyl groups through a simple liquid-phase treatment with triethoxyl(octyl)silane; the results clearly indicate that passivation increases the dynamic freedom of methanol within the adsorbed surface layer. Indeed, by taking the ratio of observed spin-lattice relaxation time constants of the two ^{1}H environments present within this adsorbate, it is readily illustrated that passivation of the support surfaces causes methanol mobility within the adsorbed surface layer to tend towards that of the bulk unrestricted liquid. A more complex analysis based on the dynamics of the methyl group alone leads to the same conclusion. This second method is based on the calculation of a dimensionless spin-lattice surface interaction parameter and includes consideration of the influence of changing surface-to-volume ratio upon passivation. An empirical fitting of this interaction parameter data, and the subsequent comparison to results obtained from a weakly-interacting reference system has allowed the influence of surface layer thickness to be effectively removed. The results of this process suggest that methanol dynamics within the adsorbed surface layer tend towards that of our weakly-interacting reference (cyclohexane), again indicating enhanced molecular mobility upon the suppression of surface-

adsorbate hydrogen bonding interactions.

Overall these results illustrate a detailed example of how nuclear spin relaxation measurements may be utilised as a probe of adsorbate dynamics within mesoporous materials of relevance to liquid-phase catalysis. The calculation of relevant interaction parameters and their agreement with simpler methods of mobility analysis enhances our ability to interpret the results of spin-lattice relaxation measurements in terms of modified surface affinity within functionalised mesoporous materials exhibiting complex surface chemistry. With respect to the underlying themes of this thesis, the results presented here illustrate the significant potential of nuclear spin relaxation measurements for the investigation of adsorption phenomena at the catalyst-liquid interface; in particular, dynamics associated with surface-adsorbate hydrogen bonding interactions in saturated mesoporous oxides.

5.5 References

[1] C. H. Christensen, J. Rass-Hansen, C. C. Marsden, E. Taarning and K. Egeblad, "The Renewable Chemicals Industry", *ChemSusChem*, 2008, **1**, 283–289.

[2] F. Calle-Vallejo, J. Tymoczko, V. Colic, Q. H. Vu, M. D. Pohl, K. Morgenstern, D. Loffreda, P. Sautet, W. Schuhmann and A. S. Bandarenka, "Finding Optimal Surface Sites on Heterogeneous Catalysts by Counting Nearest Neighbors", *Science*, 2015, **350**, 185–189.

[3] A. A. Latimer, A. R. Kulkarni, H. Aljama, J. H. Montoya, J. S. Yoo, C. Tsai, F. Abild-Pedersen, F. Studt and J. K. Nørskov, "Understanding Trends in C-H Bond Activation in Heterogeneous Catalysis", *Nat. Mater.*, 2017, **16**, 225–229.

[4] J. C. Matsubu, S. Zhang, L. DeRita, N. S. Marinkovic, J. G. Chen, G. W. Graham, X. Pan and P. Christopher, "Adsorbate-Mediated Strong Metal–Support Interactions in Oxide-Supported Rh Catalysts", *Nat. Chem.*, 2017, **9**, 120–127.

[5] J. A. Farmer and C. T. Campbell, "Ceria Maintains Smaller Metal Catalyst Particles by Strong Metal-Support Bonding", *Science*, 2010, **329**, 933–936.

[6] S. J. Tauster, "Strong Metal-Support Interactions", *Acc. Chem. Res.*, 1987, **20**, 389–394.

[7] R. Burgess, C. Buono, P. R. Davies, R. J. Davies, T. Legge, A. Lai, R. Lewis, D. J. Morgan, N. Robinson and D. J. Willock, "The Functionalisation of Graphite Surfaces with Nitric Acid: Identification of Functional Groups and Their Effects on Gold Deposition", *J. Catal.*, 2015, **323**, 10–18.

[8] M. Bowker and R. Sharpe, "Pd Deposition on TiO2(110) and Nanoparticle Encapsulation", *Catal. Struct. React.*, 2015, **1**, 140–145.

[9] O. Dulub, W. Hebenstreit and U. Diebold, "Imaging Cluster Surfaces with Atomic Resolution: The Strong Metal-Support Interaction State of Pt Supported on TiO2 (110)", *Phys. Rev. Lett.*, 2000, **84**, 3646–3649.

[10] J. Graciani, K. Mudiyanselage, F. Xu, A. E. Baber, J. Evans, S. D. Senanayake, D. J. Stacchiola, P. Liu, J. Hrbek, J. F. Sanz and J. A. Rodriguez, "Highly Active Copper-Ceria and Copper-Ceria-Titania Catalysts for Methanol Synthesis from CO2", *Science*, 2014, **345**, 546–550.

[11] C. D'Agostino, J. Mitchell, L. F. Gladden and M. D. Mantle, "Hydrogen Bonding Network Disruption in Mesoporous Catalyst Supports Probed by PFG-NMR Diffusometry and NMR Relaxometry", *J. Phys. Chem. C*, 2012, **116**, 8975–8982.

[12] C. Sievers, Y. Noda, L. Qi, E. M. Albuquerque, R. M. Rioux and S. L. Scott, "Phenomena Affecting Catalytic Reactions at Solid–Liquid Interfaces", *ACS Catal.*, 2016, **6**, 8286–8307.

[13] C. D'Agostino, G. L. Brett, P. J. Miedziak, D. W. Knight, G. J. Hutchings, L. F. Gladden and M. D. Mantle, "Understanding the Solvent Effect on the Catalytic Oxidation of 1,4-Butanediol in Methanol over Au/TiO2 Catalyst: NMR Diffusion and Relaxation Studies", *Chem. Eur. J.*, 2012, **18**, 14426–14433.

[14] C. D'Agostino, T. Kotionova, J. Mitchell, P. J. Miedziak, D. W. Knight, S. H. Taylor, G. J. Hutchings, L. F. Gladden and M. D. Mantle, "Solvent Effect and Reactivity Trend in the Aerobic Oxidation of 1,3-Propanediols over Gold Supported on Titania: NMR Diffusion and Relaxation Studies", *Chem. Eur. J.*, 2013, **19**, 11725–11732.

[15] C. D'Agostino, M. R. Feaviour, G. L. Brett, J. Mitchell, A. P. E. York, G. J. Hutchings, M. D. Mantle and L. F. Gladden, "Solvent Inhibition in the Liquid-Phase Catalytic Oxidation of 1,4-Butanediol: Understanding the Catalyst Behaviour from NMR Relaxation Time Measurements", *Catal. Sci. Technol.*, 2016, **6**, 7896–7901.

[16] K. Lin, L. Wang, F. Meng, Z. Sun, Q. Yang, Y. Cui, D. Jiang and F.-S. Xiao, "Formation of Better Catalytically Active Titanium Species in Ti-MCM-41 by Vapor-Phase Silylation", *J. Catal.*, 2005, **235**, 423–427.

[17] M. Guidotti, I. Batonneau-Gener, E. Gianotti, L. Marchese, S. Mignard, R. Psaro, M. Sgobba and N. Ravasio, "The Effect of Silylation on Titanium-Containing Silica Catalysts for the Epoxidation of Functionalised Molecules", *Microporous Mesoporous Mater.*, 2008, **111**, 39–47.

[18] N. Igarashi, K. Hashimoto and T. Tatsumi, "Catalytical Studies on Trimethylsilylated Ti-MCM-41 and Ti-MCM-48 Materials", *Microporous Mesoporous Mater.*, 2007, **104**, 269–280.

[19] M. Ojeda, F. J. Pérez-Alonso, P. Terreros, S. Rojas, T. Herranz, M. López Granados and J. L. G. Fierro, "Silylation of a Co/SiO2 Catalyst. Characterization and Exploitation of the CO Hydrogenation Reaction", *Langmuir*, 2006, **22**, 3131–3137.

[20] L. Jia, L. Jia, D. Li, B. Hou, J. Wang and Y. Sun, "Silylated Co/SBA-15 Catalysts for Fischer–Tropsch Synthesis", *J. Solid State Chem.*, 2011, **184**, 488–493.

[21] A. S. Zola, L. S. da Silva, A. L. Moretti, A. d. C. Fraga, E. F. Sousa-Aguiar and P. A. Arroyo, "Effect of Silylation and Support Porosity of Co/MCM-41 and Co/SiO2 Catalysts in Fischer–Tropsch Synthesis", *Top. Catal.*, 2016, **59**, 219–229.

[22] N. A. Fellenz, J. F. Bengoa, M. V. Cagnoli and S. G. Marchetti, "Changes in the Surface Hydrophobicity Degree of a MCM-41 Used as Iron Support: A Pathway to Improve the Activity and the Olefins Production in the Fischer–Tropsch Synthesis", *J. Porous Mater.*, 2016, 1–12.

[23] L. D. Ellis, S. Pylypenko, S. R. Ayotte, D. K. Schwartz and J. W. Medlin, "Trimethylsilyl Functionalization of Alumina Increases Activity for 1,2-Propanediol Dehydration", 2016, **6**, 5721–5728.

[24] E. W. Hansen, F. Courivaud, A. Karlsson, S. Kolboe and M. Stöcker, "Effect of Pore Dimension and Pore Surface Hydrophobicity on the Diffusion of N-Hexane Confined in Mesoporous MCM-41 Probed by NMR—a Preliminary Investigation", *Microporous Mesoporous Mater.*, 1998, **22**, 309–320.

[25] F. Courivaud, E. W. Hansen, A. Karlsson, S. Kolboe and M. Stöcker, "Pulsed Field Gradient NMR Study of the Diffusion of N-Hexane Confined in Hydroxylated and Dehydroxylated MCM-41 of Various Pore Diameters", *Microporous Mesoporous Mater.*, 2000, **35–36**, 327–339.

[26] D. Weber, A. J. Sederman, M. D. Mantle, J. Mitchell and L. F. Gladden, "Surface Diffusion in Porous Catalysts", *Phys. Chem. Chem. Phys.*, 2010, **12**, 2619–2624.

[27] C. D'Agostino, Thesis, University of Cambridge, Cambridge, UK, 2011.

[28] S. P. Pujari, L. Scheres, A. T. M. Marcelis and H. Zuilhof, "Covalent Surface Modification of Oxide Surfaces", *Angew. Chem. Int. Ed.*, 2014, **53**, 6322–6356.

[29] M. P. Hollewand and L. F. Gladden, "Transport Heterogeneity in Porous Pellets—I. PGSE NMR Studies", *Chem. Eng. Sci.*, 1995, **50**, 309–326.

[30] R. L. Vold, J. S. Waugh, M. P. Klein and D. E. Phelps, "Measurement of Spin Relaxation in Complex Systems", *J. Chem. Phys.*, 1968, **48**, 3831–3832.

[31] F. Scheinmann, *An Introduction to Spectroscopic Methods for the Identification of Organic Compounds: Nuclear Magnetic Resonance and Infrared Spectroscopy*, Elsevier, 2013.

[32] B. Stuebner, H. Knoezinger, J. Conard and J. J. Fripiat, "Adsorption of Alcohols on Alumina. 2. Nuclear Magnetic Resonance Investigation", *J. Phys. Chem.*, 1978, **82**, 1811–1817.

[33] J. Ward-Williams, J.-P. Korb and L. F. Gladden, "Insights into Functionality-Specific Adsorption Dynamics and Stable Reaction Intermediates Using Fast Field Cycling NMR", *J. Phys. Chem. C*, 2018, **122**, 20271–20278.

[34] R. Kimmich and N. Fatkullin, "Self-Diffusion Studies by Intra- and Inter-Molecular Spin-Lattice Relaxometry Using Field-Cycling: Liquids, Plastic Crystals, Porous Media, and Polymer Segments", *Prog. Nucl. Magn. Reson. Spectrosc.*, 2017, **101**, 18–50.

[35] N. Bloembergen, E. M. Purcell and R. V. Pound, "Relaxation Effects in Nuclear Magnetic Resonance Absorption", *Phys. Rev.*, 1948, **73**, 679–712.

[36] D. Liu, G. Ma, M. Xu and H. C. Allen, "Adsorption of Ethylene Glycol Vapor on Alpha-Al2O3 (0001) and Amorphous SiO2 Surfaces: Observation of Molecular Orientation and Surface Hydroxyl Groups as Sorption Sites", *Environ. Sci. Technol.*, 2005, **39**, 206–212.

[37] S. K. Parida, S. Dash, S. Patel and B. K. Mishra, "Adsorption of Organic Molecules on Silica Surface", *Adv. Colloid Interface Sci.*, 2006, **121**, 77–110.

[38] J. R. Copeland, X.-R. Shi, D. S. Sholl and C. Sievers, "Surface Interactions of C2 and C3 Polyols with Gamma-Al2O3 and the Role of Coadsorbed Water", *Langmuir*, 2013, **29**, 581–593.

[39] S. Liu, A.-a. Liu, B. Wen, R. Zhang, C. Zhou, L.-M. Liu and Z. Ren, "Coverage Dependence of Methanol Dissociation on TiO2(110)", *J. Phys. Chem. Lett.*, 2015, **6**, 3327–3334.

[40] Z. Zhang, O. Bondarchuk, J. M. White, B. D. Kay and Z. Dohnálek, "Imaging Adsorbate O−H Bond Cleavage: Methanol on TiO2(110)", *J. Am. Chem. Soc.*, 2006, **128**, 4198–4199.

[41] R. S. de Armas, J. Oviedo, M. A. San Miguel and J. F. Sanz, "Methanol Adsorption and Dissociation on TiO2(110) from First Principles Calculations", *J. Phys. Chem. C*, 2007, **111**, 10023–10028.

[42] J. Oviedo, R. Sánchez-de-Armas, M. Á. San Miguel and J. F. Sanz, "Methanol and Water Dissociation on TiO2 (110): The Role of Surface Oxygen", *J. Phys. Chem. C*, 2008, **112**, 17737–17740.

[43] D. Weber, J. Mitchell, J. McGregor and L. F. Gladden, "Comparing Strengths of Surface Interactions for Reactants and Solvents in Porous Catalysts Using Two-Dimensional NMR Relaxation Correlations", *J. Phys. Chem. C*, 2009, **113**, 6610–6615.

[44] J. Mitchell, L. M. Broche, T. C. Chandrasekera, D. J. Lurie and L. F. Gladden, "Exploring Surface Interactions in Catalysts Using Low-Field Nuclear Magnetic Resonance", *J. Phys. Chem. C*, 2013, **117**, 17699–17706.

[45] S. Stapf, R. Kimmich and R.-O. Seitter, "Proton and Deuteron Field-Cycling NMR Relaxometry of Liquids in Porous Glasses: Evidence for Levy-Walk Statistics", *Phys. Rev. Lett.*, 1995, **75**, 2855–2858.

[46] P. A. Vecino, Z. Huang, J. Mitchell, J. McGregor, H. Daly, C. Hardacre, J. M. Thomson and L. F. Gladden, "Determining Adsorbate Configuration on Alumina Surfaces with 13C Nuclear Magnetic Resonance Relaxation Time Analysis", *Phys. Chem. Chem. Phys.*, 2015, **17**, 20830–20839.

[47] D. Roy, S. Liu, B. L. Woods, A. R. Siler, J. T. Fourkas, J. D. Weeks and R. A. Walker, "Nonpolar Adsorption at the Silica/Methanol Interface: Surface Mediated Polarity and Solvent Density across a Strongly Associating Solid/Liquid Boundary", *J. Phys. Chem. C*, 2013, **117**, 27052–27061.

[48] D. Wu, X. Guo, H. Sun and A. Navrotsky, "Energy Landscape of Water and Ethanol on Silica Surfaces", *J. Phys. Chem. C*, 2015, **119**, 15428–15433.

[49] H. Wu, Q. Gong, D. H. Olson and J. Li, "Commensurate Adsorption of Hydrocarbons and Alcohols in Microporous Metal Organic Frameworks", *Chem. Rev.*, 2012, **112**, 836–868.

[50] G. Lipari and A. Szabo, "Model-Free Approach to the Interpretation of Nuclear Magnetic Resonance Relaxation in Macromolecules. 1. Theory and Range of Validity", *J. Am. Chem. Soc.*, 1982, **104**, 4546–4559.

[51] G. Lipari and A. Szabo, "Model-Free Approach to the Interpretation of Nuclear Magnetic Resonance Relaxation in Macromolecules. 2. Analysis of Experimental Results", *J. Am. Chem. Soc.*, 1982, **104**, 4559–4570.

[52] J. Kowalewski and L. Maler, *Nuclear Spin Relaxation in Liquids: Theory, Experiments, and Applications*, CRC Press, 2006.

[53] V. J. Witherspoon, L. M. Yu, S. Jawahery, E. Braun, S. M. Moosavi, S. K. Schnell, B. Smit and J. A. Reimer, "Translational and Rotational Motion of C8 Aromatics Adsorbed in Isotropic Porous Media (MOF-5): NMR Studies and MD Simulations", *J. Phys. Chem. C*, 2017, **121**, 15456–15462.

[54] S. N. Lanin, E. V. Vlasenko, N. V. Kovaleva and F. T. Zung, "The Adsorption Properties of Titanium Dioxide", *Russ. J. Phys. Chem.*, 2008, **82**, 2152–2155.

Chapter 6

Correlating spin dynamics with adsorption energetics

6.1 Introduction

Thus far we have explored nuclear spin dynamics as a qualitative probe of surface dynamics. In this chapter we will explore whether such characteristics may be interpreted in a quantitative manner; specifically, we will compare and correlate a series of nuclear spin relaxation and diffusion measurements with adsorption energetics.

Low and intermediate field nuclear spin relaxation measurements have shown particular promise for the non-invasive evaluation of surface affinities within liquid-saturated porous media. [1] In particular, the ratio of longitudinal-to-transverse relaxation time constants T_1/T_2 has received considerable attention as an indicator of the relative surface affinities exhibited by adsorbed species. [2, 3] As introduced in Chapter 4, liquids imbibed within mesoporous solids can experience significant adsorption interactions with the pore walls, as well as bulk-like behaviour towards the centre of the pores. The rate of mixing between these environments will have notable effects on the observed NMR relaxation characteristics of the imbibed liquid. For small, non-viscous molecules it is typical for the exchange between surface and bulk-like environments to be significantly more rapid than the rates of nuclear spin relaxation being measured. The observed relaxation rates $1/T_{i,obs}$ are therefore a weighted average of bulk and surface contributions, described by

$$\frac{1}{T_{i,obs}} = \frac{1-P}{T_{i,bulk}} + \frac{P}{T_{i,surf}}. \tag{6.1}$$

Here $P = \delta S/V$ is the proportion of nuclear spins (molecules) within an adsorbed surface layer of thickness δ, where S/V is the surface-to-volume ratio. $T_{i,bulk}$ and $T_{i,surf}$ $(i = 1, 2)$ are the nuclear spin relaxation time constants within the bulk and adsorbed surface layer; as adsorbed species experience enhanced relaxation rates relative to the unrestricted bulk it is typical that $T_{i,surf} \ll T_{i,bulk}$. Provided the S/V of the material under study is sufficiently large we find that

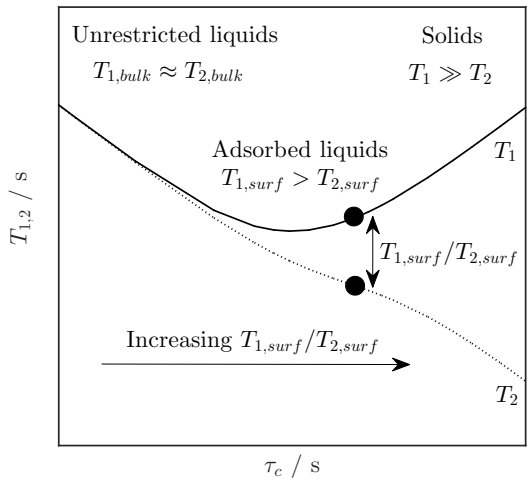

Figure 6.1: BPP theory-based illustration of the sensitivity of the ratio $T_{1,obs}/T_{2,obs}$ to surface mobility, and hence to surface interaction strength. T_1 and T_2 are illustrated by solid and dashed lines, respectively, and are shown as a function of the rotational correlation time τ_c. The relaxation of unrestricted liquids is assumed to fall within motionally narrowed regime where $1/\tau_c \gg \omega_0$ while the relaxation of adsorbed liquids is characterised by $T_{1,bulk} > T_{1,surf}$, $T_{2,bulk} > T_{2,surf}$ and $T_{1,surf} > T_{2,surf}$. As τ_c increases T_{surf} and $T_{2,surf}$ diverge, providing the ratio $T_{1,surf}/T_{2,surf}$ with sensitivity to the decrease in mobility associated with increased adsorption strength.

$$\frac{1}{T_{i,obs}} \approx \frac{\delta S}{V}\frac{1}{T_{i,surf}}, \tag{6.2}$$

such that the observed relaxation rates are inherently surface sensitive. The ratio $T_{1,obs}/T_{2,obs}$ is then

$$\frac{T_{1,obs}}{T_{2,obs}} \approx \frac{(\delta S/V)T_{1,surf}}{(\delta S/V)T_{2,surf}} \approx \frac{T_{1,surf}}{T_{2,surf}}, \tag{6.3}$$

and is considered largely independent of the S/V and δ components of Equation 6.2. It is the relaxation time ratio directly at the pore surface $T_{1,surf}/T_{2,surf}$ that is considered a measure of surface affinity. [4] A basic understanding of this relationship can be sought by consideration of the basic BPP curves shown in Figure 6.1. Here it is illustrated that a decrease in molecular mobility, as characterised by an increase in the rotational correlation time τ_c, leads to a divergence of T_1 and T_2, corresponding to an increase in their ratio. [5] It is assumed that for simple molecules that an increases in adsorption strength will correspond to an increase in molecular mobility at the pore surface, giving the ratio $T_{1,surf}/T_{2,surf}$ sensitivity to the strength of the

surface-adsorbate interaction. It is noteworthy that the approximation in Equation 6.3 then allows comparison of surface interaction strengths across porous media with different pore size characteristics, or as discussed in the present chapter, when saturated with different liquids.

While the ratio $T_{1,obs}/T_{2,obs}$ may be obtained through individual T_1 and T_2 measurements, it is more typically obtained through the use of $T_1 - T_2$ correlation pulses sequences, such as those described in Chapter 3. [6] Following appropriate processing of the acquired NMR data, [7] such an approach provides a robust method for the identification of T_1/T_2 values and relaxation time distributions associated with specific chemical groups. Figure 6.2 illustrates how such correlation plots may be interpreted in terms of the surface affinities of spin-bearing adsorbates. The first application of such analysis to liquid-saturated heterogeneous catalyst materials was presented by Weber *et al.*. [8] In this work, T_1/T_2 values were obtained to compare the surface affinities of solvents and reagents present during the liquid-phase hydrogenation of 2-butanone. The use of correlation measurements also allowed the time-dependent displacement of these adsorbates to be observed when present as a mixture; most notably, it was determined that the results of these displacement experiments correlated exactly with the relative magnitude of the T_1/T_2 values obtained from single-component experiments. In consequence, the acquisition of single component relaxation time ratios has subsequently become an established method for the prediction and evaluation of competitive adsorption and displacement behaviour, and for the comparison of surface affinities within liquid-saturated catalyst materials in general. [6, 9–17]

While such measurements are now widely accepted to provide valuable insight into the relative surface affinities of liquids confined to mesoporous catalysts, the vast majority of such studies have only considered the observed relaxation characteristics in a qualitative manner. However, a recent empirical investigation by D'Agostino *et al.* suggests that the ratio T_1/T_1 may be directly interpreted as a quantitative indication of adsorption energetics when obtained at intermediate magnetic field strength. [6] This work reported $T_1 - T_2$ correlation experiments performed on a range of water-saturated mesoporous oxides, regularly employed as catalysts or

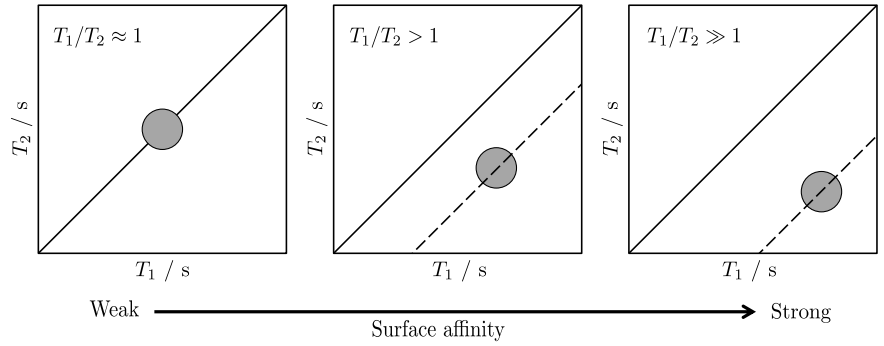

Figure 6.2: Example $T_1 - T_2$ correlation plots illustrating the appearance of changing T_1/T_2 ratio (dashed diagonal lines) and its interpretation in terms of surface affinity. Example correlation peaks are shown in grey and represent the probability that the spin system under study exhibits a particular combination of T_1 and T_2 values.

catalyst supports. A compact theoretical analysis based on the surface correlation times of adsorbed species showed that the ratio T_1/T_2 could be directly related to the energy of adsorption, as measured using temperature programmed desorption. Specifically, a clear correlation was shown to exist between the adsorption energy attributed to the strongest adsorption sites on the catalyst materials surface and the inverse relaxation time ratio $-T_2/T_1$; this result was rationalised on the basis that T_1/T_2 values are known to be dominated by the strongest relaxation sinks on the pore surface. [18]

In this Chapter we aim to provide significant supporting evidence in favour of this interpretation. Indeed, it is the purpose of the present investigation to validate and extend our understanding of spin dynamics as a quantitative probe of adsorption energetics. We approach this by performing a direct comparison of nuclear spin relaxation characteristics with *ab initio* adsorption energy calculations, utilising periodic density functional theory (DFT). Experimentally we investigate a homologous series of short chain ($C_1 - C_4$) primary alcohols within a mesoporous silica catalyst support material, together with cyclohexane, which is investigated as a weakly-interacting reference system. Additional experiments have also been performed to assess the influence of adsorption interactions on the diffusive characteristics of these adsorbates through the application of PFG NMR diffusion, and are discussed with reference to the PFG interaction parameter introduced in Chapter 4.

6.2 Methods

6.2.1 NMR measurements

Sample preparation

A commercial G57 silica support (BET surface area, $S_{BET} = 272$ m^2 g^{-1}, BJH average pore diameter, $d_{pore} = 15$ nm, BJH pore volume, $V_{BJH} = 1.3$ cm^3 g^{-1}) was obtained from Johnson Matthey and dried at 105 °C for at least 12 hours before use. Cyclohexane, methanol, ethanol, 1-propanol, and 1-butanol ($\geq$ 99 % purity, Sigma Aldrich) were used as received. Imbibed silica samples were prepared by soaking in excess liquid for at least 24 hours under ambient conditions. Samples were then separated from the liquids and rolled over a pre-soaked filter paper to remove any extrapore liquid on the outer surface of the material. For intermediate field analysis imbibed granules were transferred to sealed 7 ml glass vials; each sample consisted of $\sim$ 1 g imbibed silica corresponding to approximately 50 granules, which ranged from 2 – 5 mm in diameter. For high field analysis the imbibed granules were transferred to sealed 5 mm NMR tubes to a height of $\sim$ 15 mm.

$\mathbf{T_1 - T_2}$ correlation measurements

Intermediate field ^{1}H relaxation measurements were performed on a Bruker AV spectrometer equipped with a 2 T horizontal bore magnet with an operational ^{1}H frequency of $\omega_0/(2\pi) = 85.15$ MHz. Sample vials were placed at the centre of a 60 mm birdcage coil and left for at least 15 minutes prior to analysis in order to attain thermal equilibrium. $T_1 - T_2$ correlation plots were obtained by applying the 2D inversion recovery – PROJECT pulse sequence shown in Figure 3.17b; [19] here 16 τ_1 recovery delays were implemented ranging between 1 ms and $5T_1$ for each molecular liquid. The PROJECT echo train consisted of $n = 512$ echoes with $t_e = 4\tau_2 = 10$ ms; this value was limited by the duty cycle limitations of the spectrometer and by the $4\tau_2$ scaling of the PROJECT echo train. The limitations of this t_e value are discussed in Appendix F. The magnitude of each echo was recorded as a single data point using a one-shot technique, giving no spectral resolution. Experiments took approximately 40 minutes to complete and included 16 repeat scans to provide

adequate signal-to-noise averaging.

The acquired NMR data may be described by the 2D Fredholm integral equation of the first kind, [7]

$$\frac{S(nt_e,\tau_1)}{S_0} = \iint_0^\infty \left\{1 - 2\exp\left(\frac{-\tau_1}{T_1}\right)\right\} \exp\left(\frac{-nt_e}{T_2}\right) \times f(T_1,T_2)\, d\log_{10}(T_1)\, d\log_{10}(T_2) + \varepsilon. \tag{6.4}$$

Here the kernel function $\{1 - 2\exp(-\tau_1/T_1)\}\exp(-nt_e/T_2)$ describes the predicted form of the observed relaxation and ε represents the experimental noise, assumed to have a Gaussian distribution with zero mean. $f(T_1,T_2)$ is the desired 2D distribution of relaxation time constants and was obtained *via* a numerical inversion of the acquired NMR data. [20, 21] Stability of the inverted distribution in the presence of experimental noise was achieved through the use of Tikhonov regularisation [22] with the amplitude of the smoothing parameter chosen using the Generalised Cross Validation method. [7]

Bulk liquid T_1 measurements

Longitudinal bulk (unrestricted) liquid relaxation time constants $T_{1,bulk}$ were measured using an 85 MHz Bruker Biospin horizonal bore magnet as described above. The time-dependent recovery of longitudinal nuclear spin relaxation was measured using the inversion recovery method; [23] the appropriate NMR pulse sequence is given in Figure 3.10a. All experiments were performed at room temperature and under ambient pressure. 16 τ_1 recovery delays were employed ranging logarithmically from 1 ms to $\sim 5T_1$. The acquired data was found to exhibit single-exponential behaviour and were fit to

$$\frac{S(\tau_1)}{S_0} = 1 - 2\exp\left(\frac{-\tau_1}{T_1}\right) \tag{6.5}$$

to extract $T_{1,bulk}$ for each liquid. Here $S(\tau_1)$ is the time-dependent NMR signal associated with the longitudinal magnetisation of the spin system and S_0 is the signal acquired at equilibrium magnetisation. We consider the $T_{1,bulk}$ of only the alkyl peaks of each alcohol in the present analysis.

PFG NMR diffusion measurements

Pulsed field gradient (PFG) NMR diffusion measurements were performed using a Bruker DMX spectrometer equipped with a 7.1 T magnet ($\omega/(2\pi) = 300.13$ MHz for ^{1}H) and a Bruker Biospin Diff-30 diffusion probe capable of generating magnetic field gradient pulses of up to 11.76 T m^{-1}. The self-diffusion of unrestricted liquids was analysed using the pulsed gradient stimulated echo (PGSTE) method; [24] the relevant NMR pulse sequence is illustrated in Figure 3.24. Self-diffusion coefficients $\mathcal{D}_0$ were obtained by fitting the acquired experimental data to the Stejskal-Tanner equation, [25]

$$\frac{S(g)}{S(0)} = \exp(-b_{PGSTE}\mathcal{D}_0), \tag{6.6}$$

where

$$b_{PGSTE} = \gamma^2 g^2 t_g^2 \left(t_\Delta - \frac{t_g}{3} \right) \tag{6.7}$$

Here $S(0)$ is the NMR signal in the absence of any applied gradient, $S(g)$ is the signal is the presence of applied gradients of magnitude g and duration t_g, γ is the gyromagnetic ratio of ^{1}H, and t_Δ is the observation time during which molecules are allowed to diffuse. In the present work PGSTE measurements were carried out by holding $t_g = 1$ ms constant and varying the magnetic field gradient strength; 16 linearly spaced g values were used while observation time was set to $t_\Delta = 50$ ms. A homospoil gradient of magnitude $g_{max}/3$ and duration $t_H = 10$ ms was applied during the longitudinal storage interval to remove any remaining coherent transverse magnetisation, and the echo time was set to $\tau = 3.2$ ms.

The self-diffusion of liquids imbibed within the mesoporous silica was analysed using the alternating pulsed gradient stimulated echo (APGSTE) sequence shown in Figure 3.25. [26] Effective self-diffusion coefficients $\mathcal{D}_{eff}$ were obtained by fitting the acquired experimental data to [27]

$$\frac{S(g)}{S(0)} = \exp(-b_{APGSTE}\mathcal{D}_{eff}), \tag{6.8}$$

where

$$b_{APGSTE} = \gamma^2 g^2 t_g^2 \left(t_\Delta - \frac{t_g}{12} - \frac{\tau}{2} \right), \tag{6.9}$$

Table 6.1: Summary of the typical PFG NMR acquisition parameters employed here.

	Unrestricted liquids	Restricted liquids
Pulse sequence	PGSTE	APGSTE
Observation time, t_Δ / ms	50	100
Effective gradient pulse duration, t_g / ms	1	1
Maximum gradient pulse strength, g_{max} / T m^{-1}	$0.6 - 1.5$	$0.75 - 1.7$
Gradient rise & fall times / ms	0.2	0.2
Gradient stabilisation time, $t_{\delta 1,2}$ / ms	1	1
Echo time, τ / ms	3.2	2.7
Homospoil gradient duration, t_H / ms	5	10
Homospoil gradient strength / T m^{-1}	$g_{max}/3$	$g_{max}/3$
No. of gradient steps	16	16
No. of repeat scans	16	32

with the echo time set to $\tau = 2.7$ ms. In analogy to the PGSTE measurements described above, APGSTE measurements were carried out by holding $t_g = 1$ ms constants and varying the magnetic field gradient strength; 16 linearly spaced g values were used while the observation time was set to $t_\Delta = 100$ ms. A homospoil gradient of magnitude $g_{max}/3$ and duration $t_H = 10$ ms was again applied. A summary of the PFG NMR acquisition parameters employed is provided in Table 6.1. All diffusion measurements were performed at 20 ± 0.1 °C.

6.2.2 DFT calculations

Periodic DFT calculations were performed using the plane-wave code CASTEP (CAmbridge Serial Total Energy Package). [28] A introductory overview of periodic DFT calculations is provided in Appendix E. Structural optimisations were performed at the GGA (generalised gradient approximation) level of theory utilising the PBE (Perdew-Burke-Ernzerhof) exchange-correlation functional. [29] Dispersion (van der Waals) interactions, which are not explicitly contained within the PBE GGA, were added using the D2 semi-empirical dispersion correction by Grimme (PBE+D2). [30, 31] This correction lies on the first step of the chemical accuracy *vs* computational cost stairway as described by Klimes and Michaelides [32] and provides an excellent compromise between the chemical accuracy of the computed energies and the sizeable computational cost associated with the large number of calculations performed here. All calculations made use of ultrasoft pseudopotentials

to represent the core electrons. The plane-wave basis set was expanded using either a $3\times3\times3$ or $3\times3\times1$ Γ–centred Monkhorst-Pack grid for bulk unit cell or surface slabs, respectively, [33] and the cut-off energy was set to 350 eV. Molecular geometries were optimised within a 15 Å × 15 Å × 15 Å periodic box. Geometry optimisations were achieved through use of the BFGS (Broyden-Fletcher-Goldfarb-Shanno) energy minimiser, [34] during which energies and forces were converged to within 2×10^{-5} eV and 0.05 eV $Å^{-1}$

6.3 Results and discussion

6.3.1 $T_1 - T_2$ relaxation correlations

The ^{1}H $T_1 - T_2$ correlation plots obtained from our liquid-saturated silica samples are given in Figure 6.3. The relaxation distribution detailed by each correlation peak represents the relative probability of each system exhibiting a given probability of T_1 and T_2 relaxation time constants; however, the correlation peak shape is also influenced by the mathematics of the inversion procedure required to obtain the distribution from our acquired NMR data, which is susceptible to noise fluctuations. We therefore concentrate here on the modal relaxation times characterised by these correlation peaks, $\langle T_1 \rangle$ and $\langle T_2 \rangle$, as well as the modal T_1/T_2 relaxation time ratio $\langle T_1/T_2 \rangle$, and make no attempt to analyse differences in peak shape between samples.

Figure 6.3a illustrates the acquired relaxation correlation plot for methanol-saturated silica. Two distinct correlation peaks are clearly observed; in Chapter 5, simple T_1 relaxation measurements performed at high magnetic field allowed us to identify multiple relaxation environments within methanol-saturated mesoporous oxides. In particular, we observed that the methyl and hydroxyl ^{1}H environments exhibit significantly different relaxation rates, with the hydroxyl environment displaying more rapid rates of spin-lattice relaxation, leading to shorter T_1 times. Within Figure 6.3a we may therefore assign the peak at short $\langle T_1 \rangle$ ($\sim$ 0.22 s) to the ^{1}H relaxation of the methanol hydroxyl group, while the peak at longer T_1 ($\sim$ 0.56 s) is assigned to the methyl environment of the same molecules. This assignment is supported by the relative intensity of the two peaks, which we expect

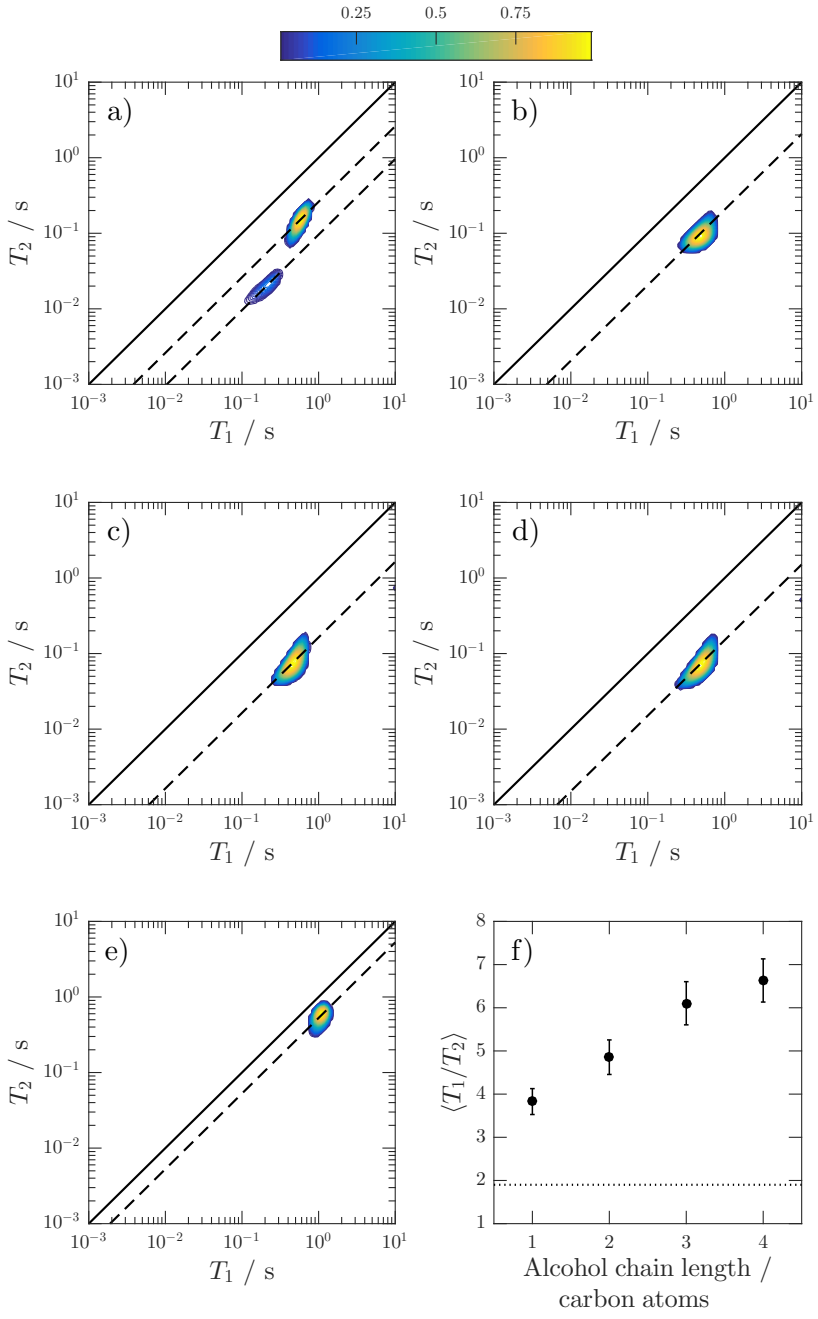

Figure 6.3: ^{1}H $T_1 - T_2$ correlation plots of a) methanol, b) ethanol, c) 1-propanol, d) 1-butanol and e) cyclohexane in mesoporous silica. All data was acquired at 85 Hz with $t_e = 10$ ms. Solid diagonal lines indicate the parity ratio $T_1 = T_2$. The observed $\langle T_1/T_2 \rangle$ values are indicated by dashed diagonal lines and are detailed in Table 6.2. Alkyl group relaxation ratios are presented as a function of carbon chain length in panel f), where error bar magnitudes have been determine through multiple repeat experiments; here the $\langle T_1/T_2 \rangle$ value for cyclohexane is indicated by a dashed line and represents a weakly-interacting reference measurement.

Table 6.2: Summary of the modal relaxation time constants and time ratios obtained from the $T_1 - T_2$ correlation plots in Figure 6.3.

Liquid	^{1}H assignment	$\langle T_1 \rangle$ / s	$\langle T_2 \rangle$ / s	$\langle T_1/T_2 \rangle$
Methanol	CH_3	0.56 ± 0.05	0.15 ± 0.02	3.8 ± 0.3
Methanol	OH	0.22 ± 0.01	0.018 ± 0.004	10.4 ± 0.8
Ethanol	C_2H_5	0.49 ± 0.05	0.08 ± 0.01	4.9 ± 0.4
1-Propanol	C_3H_7	0.51 ± 0.05	0.07 ± 0.01	6.1 ± 0.5
1-Butanol	C_4H_9	0.51 ± 0.05	0.06 ± 0.01	6.6 ± 0.5
Cyclohexane	C_6H_{12}	1.5 ± 0.1	0.56 ± 0.09	1.9 ± 0.1

to approximately correlate with the number of ^{1}H within each environment, weighted by any signal loss due to rapid T_2 relaxation at the pore surface.

The acquired relaxation data of ethanol–, 1-propanol– and 1-butanol–saturated silica are illustrated in Figures 6.3b – d. A single correlation peak is observed in each case, as is common for molecules imbibed within mesoporous catalyst materials. For instance, a single correlation peak has been observed in the analysis of 2-propanol within mesoporous Ru/SiO_2 and Pd/Al_2O_3, [8, 9] and for glycerol within mesoporous Au/TiO_2. [35] In the present work we assign these peaks to the alkyl ^{1}H environment of each alcohol. The lack of hydroxyl signal is attributed to dominance of the acquired relaxation data by alkyl ^{1}H within these larger alcohols, and the inadequacy of the PROJECT echo train to sample rapid T_2 decays; this assignment is discussed in detail in Appendix F. We further note that single relaxation peak corresponding to multiple alkyl protons has previously been observed in *n*-octane-saturated γ-Al_2O_3, [10] supporting the assignment of multiple similar alkyl ^{1}H environments to a single correlation peak.

The modal T_1/T_2 ratio $\langle T_1/T_2 \rangle$ is quantified by the diagonal positioning of each correlation peak maximum, and is indicated by dashed lines on each $T_1 - T_2$ correlation plot in Figure 6.3. A summary of these values, together with the corresponding $\langle T_1 \rangle$ and $\langle T_2 \rangle$ times is given in Table 6.2. Given the high alkyl-to-hydroxyl ^{1}H number ratio within each of the primary alcohols considered, and recalling from Chapter 5 that the alkyl relaxation of imbibed methanol exhibits sensitivity to overall molecular dynamics, we may interpret the observed alkyl relaxation characteristics as a probe of overall molecular dynamics. The alkyl $\langle T_1/T_2 \rangle$ values are given in Figure 6.3f as a function of carbon chain length.

As it is typical to interpret this ratio as an indicator of surface affinity, the positive correlation observed here suggests that short-chain primary alcohols exhibit a distinct increase in surface affinity with increasing carbon chain length; this observation is in agreement with adsorption energy measurements elsewhere. [36, 37] Cyclohexane, which is unable to hydrogen bond to polar groups at the pore surface, has also been examined. The relevant $T_1 - T_2$ correlation plot is given in Figure 6.3e. This system comprises a single correlation peak with low $\langle T_1/T_2 \rangle$, corroborating previous observations on the weakly-interacting nature of alkanes at oxide surfaces. [38]

We may further note from Figure 6.3a that the $\langle T_1/T_2 \rangle$ of the two methanol ^{1}H environments are not equivalent. This observation might be expected from the polar-protic nature of the adsorbate under observation, as previously explored in Chapter 5. In particular, the low intensity peak assigned to hydroxyl relaxation has an observed $\langle T_1/T_2 \rangle$ of more than double that of the corresponding alkyl environment (Table 6.2); this increase may be attributed to a combination of hydrogen bonding interactions with the pore surface – the existence of which will significantly hinder the motional freedom of the alcohol hydroxyl group relative to that of the apolar alkyl environment – and any proton exchange between labile hydroxyl protons and polar surface groups. It is shown in Appendix F that the hydroxyl correlation peaks of ethanol, 1-propanol and 1-butanol are observable using shorter echo times and also express large $\langle T_1/T_2 \rangle$ values.

6.3.2 Internal gradient considerations

It is appropriate here to consider the implications of any internal gradient effects present. Specifically, it is important, given that our relaxation correlations have been acquired at intermediate magnetic field, to evaluate whether the observed trend in $\langle T_1/T_2 \rangle$ values may be attributed to surface interaction phenomena alone, or whether differences in internal gradients across our range of alcohols has some influence.

We recall here from Chapter 4 that effective internal field gradients g_{eff} occur due to magnetic susceptibility differences $\Delta\chi$ at the solid–liquid interface, $g_{eff} \sim \Delta\chi B_0$. [39] The presence of such gradients may influence the observed T_2 (and therefore

T_1/T_2 ratio) of liquid-saturated porous systems by facilitating enhanced transverse relaxation during the diffusion of spin-bearing species across the pore structure. A qualitative assessment of Figure 6.3 suggests that any such effects here are unimportant. Indeed, it has been illustrated elsewhere that significant internal gradient effects cause $T_1 - T_2$ correlation plots to appear stretched over several orders of magnitude in the T_2 dimension; [40, 41] such behaviour is clearly not encountered in the systems discussed here. A more quantitative interpretation may be explored by investigating the diffusive regime within which our alcohols-saturated silica samples lie. To do this we note that the magnitude of any internal gradient is bound according to $g_{eff}\ell_g \leq \Delta\chi B_0$. [39] Here $\ell_g \approx (\mathcal{D}_0/(\gamma g_{eff}))^{1/3}$ is a dephasing length which describes the diffusion path over which the spin system will dephase by 2π radians, [42] where γ is the gyromagnetic ratio of the nuclear spin under study (^{1}H). It follows that we may consider the effects of a maximum possible effective internal field gradient [40]

$$g_{eff}^{max} = \frac{\Delta\chi B_0}{\ell_*}, \tag{6.10}$$

where ℓ_* is the so-called critical length scale which satisfies $g_{eff}^{max}\ell_* = \Delta\chi B_0$ and $\ell_* \approx (\mathcal{D}_0/(\gamma g_{eff}^{max}))^{1/3}$. It has been shown elsewhere that this critical length scale separates "small pores" which satisfy the motional averaging (MAV) regime and "large pores" which fall within the localisation (LOC) regime. [40] Appropriate rearrangement of these expressions yields [42]

$$g_{eff}^{max} \approx \left(\frac{\gamma}{\mathcal{D}_0}\right)^{1/2}\left(\Delta\chi B_0\right)^{3/2}, \tag{6.11}$$

such that an estimate of g_{eff}^{max} requires values of the unrestricted self-diffusion coefficient $\mathcal{D}_0$ and the magnetic susceptibility difference $\Delta\chi$.

Self-diffusion coefficients are readily obtained through appropraite PFG NMR experiments; Figure 6.4 displays the results of PGSTE experiments performed on the five liquids of interest. The magnetic susceptibility difference is more difficult to measure; however, recalling the relationship between Larmor frequency and static magnetic field strength $|\omega_0| = \gamma B_0$, an estimate may be made from the line broadening $\Delta\omega$ observed between restricted and unrestricted liquids. Indeed,

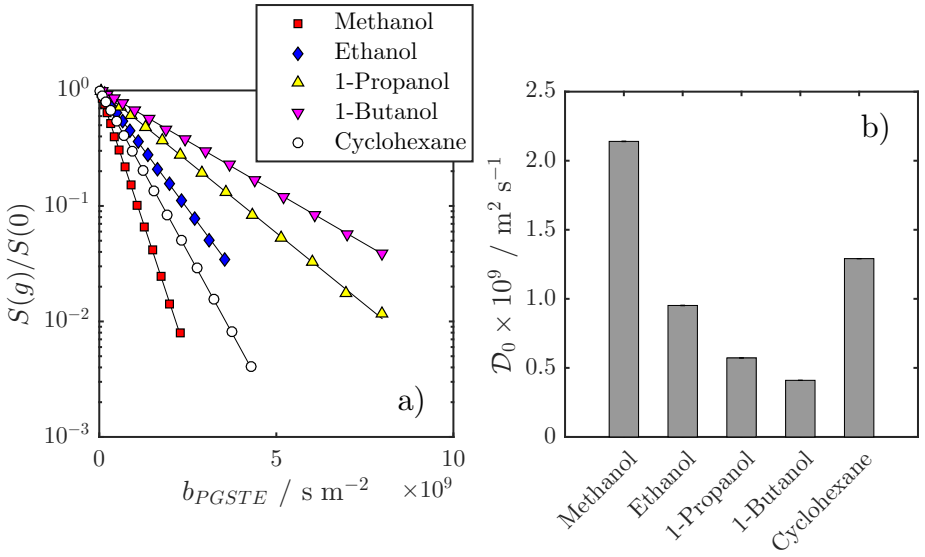

Figure 6.4: PGSTE diffusion analysis of unrestricted short-chain primary alcohols and cyclohexane at 20 ± 0.1°C. a) illustrates log-attenuation data obtained from each liquid. Solid lines indicate a fit to Equations 6.6 and 6.7. Self-diffusion coefficients $\mathcal{D}_0$ obtained from this fitting are shown in b). The relative error was found to be $< 1\%$ in each case, such that error bars are not visible.

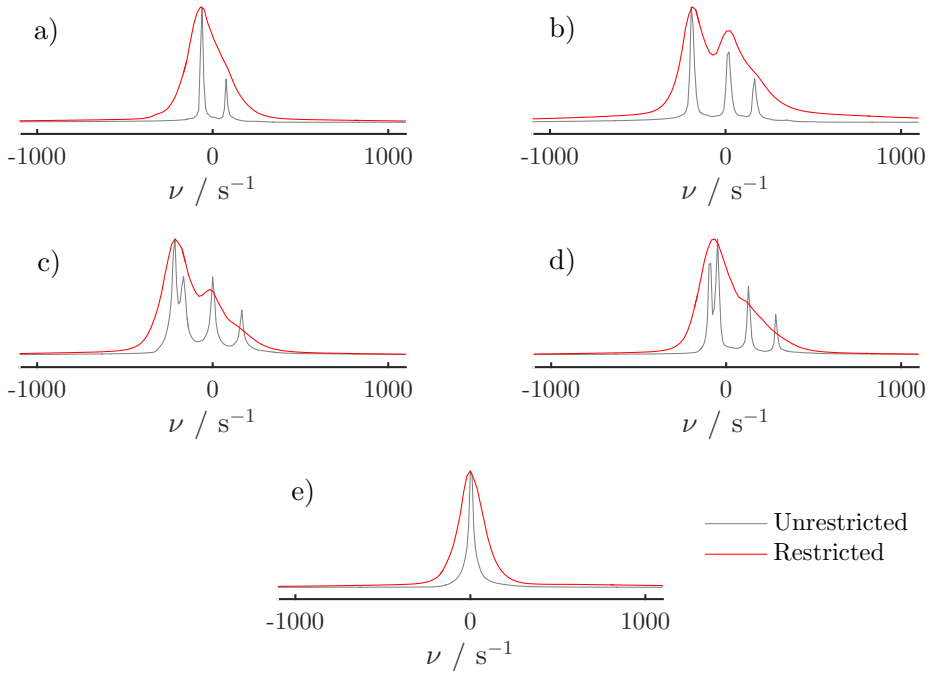

Figure 6.5: ^{1}H NMR spectral of a) methanol, b) ethanol c) 1-propanol, d) 1-butanol and e) cyclohexane, acquired at 85 MHz. Grey and red data sets represent unrestricted (bulk liquids) and liquids confined to mesoporous silica, respectively.

Table 6.3: Estimated maximum internal gradient parameters for short-chain primary alcohols and cylohexane in mesoporous silica at 2 T.

Liquid	$\Delta\chi$	$\Delta\chi B_0$ / T	g_{eff}^{max} / T m^{-1}	ℓ_* / μm
Methanol	1.15×10^{-5}	2.30×10^{-5}	15.6	1.48
Ethanol	5.01×10^{-6}	1.02×10^{-5}	6.7	1.49
1-Propanol	1.40×10^{-6}	2.80×10^{-6}	1.3	2.19
1-Butanol	7.37×10^{-7}	1.48×10^{-6}	0.6	2.55
Cyclohexane	1.13×10^{-5}	2.26×10^{-5}	19.5	1.16

provided any observed line broadening is dominated by susceptibility effects rather than inhomogeneity of the static magnetic field, the difference in peak width will be $\Delta\omega = \Delta\chi\gamma B_0$ such that $\Delta\chi$ may be estimated from [43]

$$\Delta\chi \approx \frac{\Delta\omega}{\gamma B_0}. \tag{6.12}$$

Figure 6.5 illustrates relevant NMR spectra obtained from our liquid-saturated silica samples, together with spectra from the unrestricted liquids. As the alcohol spectra contain peak contributions from multiple ^{1}H environments line broadening values $\Delta\omega$ have been estimated from the width of the peak base rather than the full width half maximum. The resultant approximate $\Delta\chi$ values are detailed in Table 6.3, together with the g_{eff}^{max} and ℓ_* values obtained from Equations 6.10 and 6.11; we note that values of $\Delta\chi B_0 \leq 10^{-5}$ T are typical of weak internal gradient effects found in the absence of paramagnetic species. [40] Given that $\ell_* \gg d_{pore}$, this series of results suggests that our liquid-saturated silica samples exist within the MAV regime. This interpretation is further confirmed in Figure 6.6 by considering the ratios $\ell_g/\ell_s \sim \ell_*/\ell_s$ and ℓ_e/ℓ_s, where we recall that $\ell_e \approx (\mathcal{D}_0 t_e)^{1/2}$ is a diffusion path length which quantifies diffusive displacement during the echo time t_e, and $\ell_s \approx d_{pore}/2$ is the structural length scale characterising the pores. [39]

We are now in a position to consider any influence of diffusive attenuation of our observed $\langle T_1/T_2 \rangle$ values. The observed rates of transverse nuclear spin relaxation within the MAV regime follow [39]

$$\frac{1}{T_{2,obs}} = \frac{1-P}{T_{2,bulk}} + \frac{P}{T_{2,surf}} + \underbrace{\frac{\gamma^2 \overline{g}^2 \ell_s^4}{120\mathcal{D}_0}}_{R_{diff}}. \tag{6.13}$$

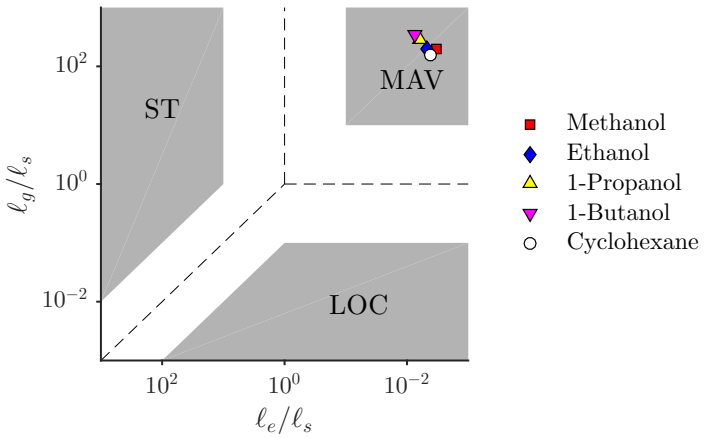

Figure 6.6: Illustration of the diffusive regime behaviour of mesoporous silica imbibed with short-chain primary alcohols and cyclohexane at 2 T. Shaded areas define regions where the motional averaging (MAV), short time (ST) and localisation (LOC) regimes are expected to apply, as defined by the relative magnitudes of the length scales ℓ_s, ℓ_e and ℓ_g. Dashed lines indicate regions of equivalence between length scales.

Here $\overline{g} \leq g_{eff}^{max}$ is an average effective gradient across the pore structure and R_{diff} is additional signal attenuation which occurs as a results of diffusion through internal gradients. By setting a limiting value of $\overline{g} = g_{eff}^{max}$ the maximum possible contribution of diffusive attenuation R_{diff}^{max} to our measured $\langle T_2 \rangle$ values may be quantified. Figure 6.7 provides a comparison of this R_{diff}^{max} contribution with the modal transverse relaxation rates obtained from our relaxation correlation plots (Table 6.2). We see from this figure that the proposed R_{diff}^{max} values of both cyclohexane and methanol are greater than that of the corresponding $\langle T_2 \rangle^{-1}$ rates, illustrating that such calculations have the potential to give unphysical results. This finding highlights the fact that our calculated values of g_{eff}^{max} (Table 6.3) are very much a worse case scenario; this maximal nature may also be further exacerbated by the assumption that the line broadening effects observed in Figure 6.5 contain zero contribution from static field inhomogeneities. As such, it is appropriate to shift our attention to the trends exhibited within Figure 6.7, rather than considering the absolute values. Figure 6.7a illustrates that a distinct increase in $\langle T_2 \rangle^{-1}$ occurs with increasing carbon chain length, leading to a the observation of a similar trend in the values of $\langle T_1/T_2 \rangle$. Conversely, we note that Figure 6.7b suggests that the potential contribution of diffusive attenuation to the observed transverse relaxation rates of our alcohol/silica systems decreases significantly with increasing carbon chain length.

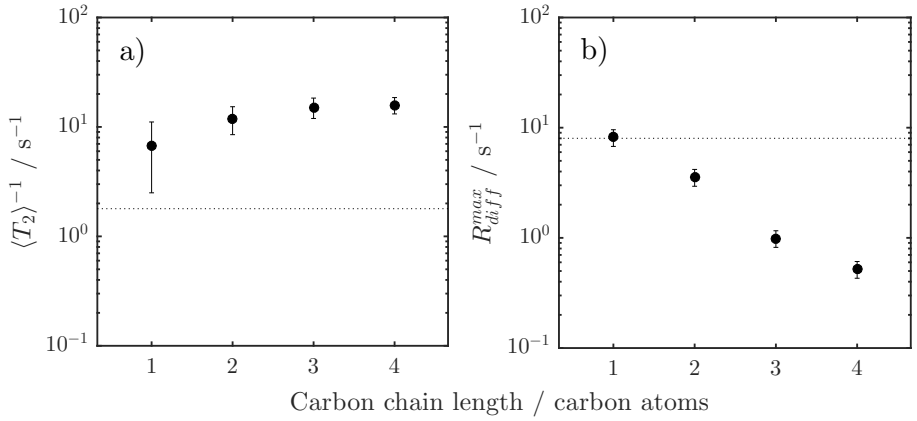

Figure 6.7: Transverse nuclear spin relaxation characteristics of short-chain primary alcohols in mesoporous silica. Additional cyclohexane data is indicated by dotted horizontal lines. a) illustrates the observed modal relaxation rates $\langle T_2 \rangle^{-1}$ obtained from our $T_1 - T_2$ correlation experiments. b) illustrates the maximum possible diffusive attenuation R_{diff}^{max}, as defined by the final term in Equation 6.13 with $\overline{g} = g_{eff}^{max}$. The error bars in a) corresponds to the uncertainty in the observed value of $\langle T_1 \rangle$ while error bars in b) have been calculated according to the uncertainty in $\mathcal{D}_0$ values and by assuming an error of $\pm 10\%$ in the estimation of the line broadening effects observed in Figure 6.5.

Given the reasonable assumption that R_{diff} will be approximately proportional to R_{diff}^{max} this comparison provides a strong indication that the observed trend in $\langle T_1/T_2 \rangle$ cannot be attributed to dominance of our acquired T_2 data by internal gradient effects.

6.3.3 Relaxation as a surface sensitive probe

Given that we can now have confidence that the trend observed in our relaxation correlation experiments is not dominated by the effects of diffusive attenuation, we may consider the surface sensitivity of the observed relaxation characteristics in more detail. The approximate expression provided in Equation 6.3 suggests that the ratio $\langle T_1/T_2 \rangle$ is dominated by relaxation within the adsorbed surface layer. A more complete expression is of course

$$\frac{T_{1,obs}}{T_{2,obs}} = \frac{(1-P)/T_{1,surf} + P/T_{1,surf}}{(1-P)/T_{2,surf} + P/T_{2,surf}}, \tag{6.14}$$

which maintains second-order sensitivity to pore geometry and surface layer structure. We may explore the surface sensitivity of our acquired $\langle T_1/T_2 \rangle$ values through a comparison with an estimate of the ratio $T_{1,surf}/T_{2,surf}$. As *per* our

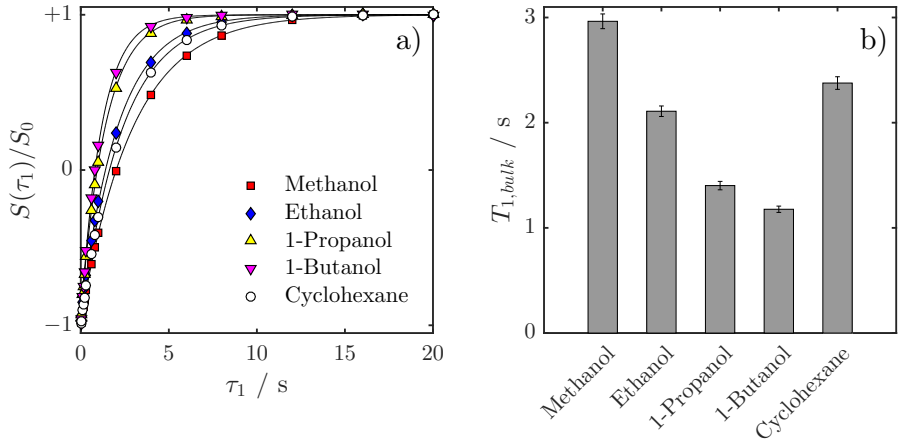

Figure 6.8: Nuclear spin lattice relaxation characteristics of unrestricted short-chain primary alcohols and cylohexane. a) illustrates T_1 inversion recovery curves for the alkyl ^{1}H environment of the five liquids investigated, acquired at 85 MHz. Solid lines indicate a fit to Equation 6.5; the corresponding $T_{1,bulk}$ values are given in panel b). The relative error in measured $T_{1,bulk}$ values is approximately 2.5 % in all cases.

approach in Chapter 5, the surface relaxation time constants $T_{i,surf}$ $(i = 1, 2)$ may be obtained through rearrangement of Equation 6.1,

$$T_{i,surf}(\delta) = PT_{i,obs} - \frac{PT_{i,bulk}}{1-P}. \tag{6.15}$$

Recalling that $T_1 = T_2$ in the unrestricted bulk we may set $T_{i,bulk} = T_{1,bulk}$, such that we need not concern ourselves with measuring $T_{2,bulk}$ relaxation; Figure 6.8 illustrates $T_{1,bulk}$ data for the liquids examined here. By setting $T_{i,obs} = \langle T_i \rangle$ (as obtained from Table 6.2) and observing that $S_{BET}/V_{BJH} \approx S/V \approx 2.1 \times 10^8$ m for the material in question, values of $T_{i,surf}$ are readily calculated for an appropriate choice of δ. For the purposes of solving Equations 6.15 we assume here that short-chain primary alcohols at hydroxylated silica surfaces form an adsorbed surface layer with a thickness equivalent to two molecular layers. This assumption is supported by molecular dynamics simulations of methanol at a model silica surface, [44] and experimental observations of ethanol adsorption. [45] We approximate the thickness of an adsorbed monolayer to be equivalent to the kinetic diameter of the molecule of interest d_k, such that $\delta = 2d_k$ for each of the primary alcohols investigated here. In the case of cylohexane we consider $\delta = d_k$.[1]

[1] Values of the kinetic diameter used here are 3.6 Å, 4.5 Å, 4.7 Å, 5.0 Å and 6.2 Å for methanol, ethanol, 1-propanol, 1-butanol and cyclohexane, respectively. [46]

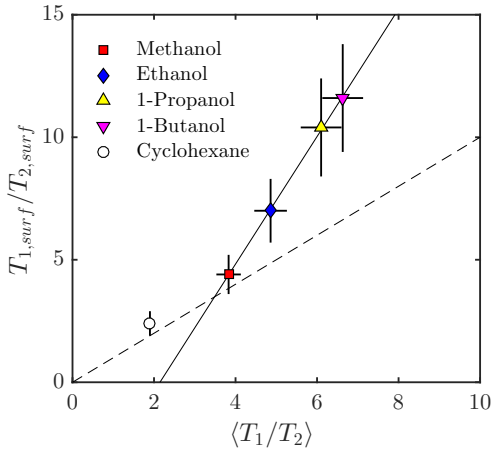

Figure 6.9: Plot of experimentally observed (alkyl) $\langle T_1/T_2 \rangle$ ratios against calculated $T_{1,surf}/T_{2,surf}$ values. $T_{1,surf}$ and $T_{2,surf}$ are defined by Equation 6.15. The solid diagonal line illustrates a linear fit to the alcohol data while the dashed diagonal line respresents $\langle T_1/T_2 \rangle = T_{1,surf}/T_{2,surf}$.

The sensitivity of our extracted modal relaxation time ratios to the adsorbed surface layer is illustrated in Figure 6.9; here our $\langle T_1/T_2 \rangle$ values are plotted against the ratio $T_{1,surf}/T_{2,surf}$, as calculated according to the above procedure. This figure reveals a strong, positive correlation between the two relaxation time ratios, such that we may state the general relation $\langle T_1/T_2 \rangle \propto T_{1,surf}/T_{2,surf}$. The dashed diagonal line indicates the perfect scenario of $\langle T_1/T_2 \rangle = T_{1,surf}/T_{2,surf}$. Clearly only cyclohexane and methanol conform to this relationship, illustrating the limitations of Equation 6.3. The solid diagonal line provides a linear fit to the alcohol data and provides a better description of the overall relationship between $\langle T_1/T_2 \rangle$ and $T_{1,surf}/T_{2,surf}$ within these systems; this fit takes the form $T_{1,surf}/T_{2,surf} = 2.6\langle T_1/T_2 \rangle - 5.6$.

6.3.4 ab initio adsorption energy calculations

The nature of silica surfaces has long been studied *via* computational techniques due to their relevance in a wide range of phenomena; these encompass both classical [47] and *ab initio* [48, 49] molecular dynamics simulations, Monte Carlo methods [50] and DFT models using both atomistic cluster models [51] and periodic surfaces. [52–54] A 2013 review covering the topic of biomolecules and their interactions with silica surfaces provides an excellent and in-depth summary of the modern plethora of

silica surface models, and the interested reader is directed here for a more complete overview of the field. [55]

In the present analysis we wish to develop a silica surface for static adsorption energy calculations performed at the dispersion-corrected DFT level of theory. Aperiodic cluster techniques are typically an inappropriate choice of system for adsorption modelling; however, we must note that the mesoporous silica employed experimentally in this work is untemplated, and therefore amorphous. The use of periodic DFT therefore requires the approximation that the experimental silica surfaces in question may be adequately represented by either a single, or combination of, periodic – i.e. crystalline – surfaces. Fortunately the surface chemistry of silicas are well characterised, and it is common knowledge that a small number of discrete and predictable surface silanol groups (surface hydroxyls anchored covalently to the solid surface *via* a silicon atom) comprise the vast majority of amorphous silica surfaces. [55] The more common of these are single silanols ($\equiv \mathrm{Si} - \mathrm{OH}$) and disilanols (also known as geminal silanols) ($= \mathrm{Si} - (\mathrm{OH})_2$), both of which may appear free (non-bonded to other surface groups) or hydrogen bonded to neighbouring silanols, and siloxane bridges ($\mathrm{Si} - \mathrm{O} - \mathrm{Si}$). The question of modelling amorphous silica surfaces *via* periodic means therefore becomes a question of whether crystalline silica polymorphs can be made to exhibit these relevant surface groups. Two crystalline structures are commonly used from which relevant surfaces may be formed: α-cristobalite and α-quartz. Surface expressing single silanols may be obtained through the hydroxylation of the $\{10\bar{1}1\}$ planes of either material, [52] while geminal silanol surfaces may be expressed by hydroxylation of either the $\{0001\}$ or $\{01\bar{1}0\}$ crystal planes of α-quartz, or the $\{0001\}$ and $\{11\bar{2}0\}$ planes of α-cristobalite. [52] Furthermore, the perfect reconstruction (no hydroxylation) of the $\{0001\}$ α-quartz plane leads to a crystal surface exhibiting siloxane bridge structures. [56, 57] A large periodic slab model of an amorphous silica surface has also been developed by Tielens *et al.*, [58] which has been shown to exhibit experimentally comparable NMR chemical shifts, dehydration energies and OH vibrational frequencies.

As previously introduced, empirical work by D'Agostino [6] suggests that the T_1/T_2 ratio obtained from liquid-saturated mesoporous media may be correlated

with the strongest adsorption sites present. Our aim in this section is to apply DFT calculations to directly probe such adsorption sites; this approach has been selected as DFT calculations provide unrivalled access to the adsorption energetics of well-defined surface interactions, and may be used to selectively probe the strongest adsorption sites at a particular surface. It is reasonable to assume that adsorption within our alcohol-saturated silica will be dominated by surface-adsorbate hydrogen bonding interactions between the imbibed primary alcohols and surface hydroxyl groups decorating the pore surface. Here, the strongest adsorption sites will be those capable of forming multiple bonding interactions with the same adsorbate molecule. [59] A high surface hydroxyl density is therefore required to model the relevant adsorption interactions using periodic methods. The fully hydroxylated {0001} surface of α-quartz presents a sensible choice for these calculations as it exhibits the highest surface hydroxyl density of common crystalline silica surfaces, [52] and has been employed throughout this chapter.

Unit cell optimisation

The structure of the α-quartz unit cell is illustrated in Figure 6.10, and consists of 6 oxygen and 3 silicon atoms. DFT-optimised unit cell parameters obtained at the PBE and PBE + D2 levels of theory are displayed in Table 6.4, and illustrate the superior performance of the calculations including a dispersion correlation. Indeed, in the case of our PBE + D2 calculations each parameter described exhibits a

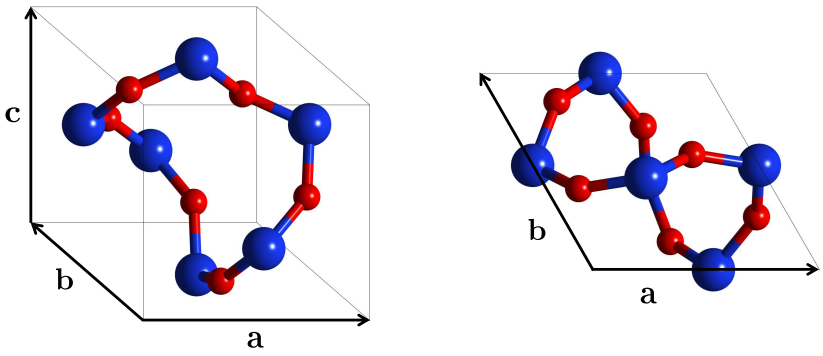

Figure 6.10: Illustration of the α-quartz unit cell. Silicon and oxygen atoms are coloured blue and red, respectively. The magnitude of the cell vectors **a**, **b** and **c** are given in Table 6.4.

Table 6.4: Summary of the DFT-optimised α-quartz unit cell lattice parameters at the PBE and PBE+D2 levels of theory, and their comparison to experimental values. Error values detail the % deviation from experiment. Cell vectors **a**, **b** and **c** are indicated on Figure 6.10.

Lattice parameter	Experiment [61]	PBE (% error)	PBE+D2 (% error)
Cell volume / Å	113.131	122.311 (8.1)	113.878 (0.7)
$\lvert\mathbf{a}\rvert = \lvert\mathbf{b}\rvert$ / Å	4.916	5.052 (2.8)	4.928 (0.2)
$\lvert\mathbf{c}\rvert$ / Å	5.405	5.533 (2.6)	5.414 (0.2)
Si − O (long) / Å	1.614	1.616 (0.1)	1.619 (0.3)
Si − O (short) / Å	1.605	1.614 (0.6)	1.614 (0.6)
∠ Si − O − Si / °	142.73	151.43 (5.4)	143.01 (0.2)

deviation from experiment of < 1 %, as might be expected considering the excellent performance of the D2 correction in capturing the geometry of bulk crystalline materials. [60]

Cleavage and hydroxylation of the {0001} α-quartz surface

Utilising the optimised PBE + D2 unit cell described above, symmetric slabs with a surface area of 1×1 units cells were cleaved to expose the {0001} α-quartz surface. As illustrated in Figure 6.11, the two symmetric surfaces were cleaved such that they exhibit highly reactive $=\mathrm{Si}=\mathrm{O}$ surface silanone groups, which protrude into the vacuum from surface silicon atoms. These surface silanones are known to be present upon cleavage of the {0001} surface, [62] and maintain the SiO_2 stoichiometry of the material.

Hydroxylated slabs were formed *via* a theoretical dissociative water reaction of the form [63]

$$n\mathrm{O}_{(surf)} + \square + n\mathrm{H_2O}_{(g)} \rightarrow 2n\mathrm{OH}_{(surf)}. \tag{6.16}$$

Here $\square$ represents the vacant fourth coordination site of a surface silicon atom and the subscript $(surf)$ indicates species covalently bound to the solid surface. For each surface unit cell this process requires the addition of a single water molecule. As shown in Figure 6.11 the resulting hydroxylated surfaces exhibit geminal silanol groups ($=\mathrm{Si}-(\mathrm{OH})_2$) with a surface silanol density of $\rho_{\mathrm{OH}} = 9.51$ nm^{-2}; this value is in perfect agreement with calculations by Musso *et al.*. [52]

Surface energy calculations

A series of surface energy calculations have been performed to establish the optimal surface slab thickness for our adsorption modelling. The surface energy of a solid γ (units of J m^{-2}) quantifies the energy input required to form a surface of known area; in general, the surface energy of a slab model of thickness j may be calculated according to [64]

$$\gamma = \frac{1}{2A}\big\{E_{slab}(j) - N(j)E_{bulk}\big\}, \tag{6.17}$$

where $E_{slab}(j)$ is the energy of the slab model under consideration, A is the surface energy of a single face of that slab structure and E_{bulk} is the energy of the bulk unit cell. The proportionality constant $N(j)$ relates the number of atoms (or groups of atoms) within the slab structure to that within the bulk unit cell. For sufficiently large values of j (or N), γ is expected to converge to the surface energy of the solid under investigation. [65]

It is important here to note that in the present work we have employed a method of fixing atoms such that the uppermost unit cell of each slab structure, along with the terminal surface hydroxyl groups were free to relax geometrically upon interaction with an adsorbate, but all other atoms were fixed in place. This method allows our slab structures to better represent a pseudo-infinite bulk structure and reduces the number of atoms required to relax during a given adsorption interaction. In the following discussion the upper surface which is allowed to relax will be referred to as the free surface, while the bottom surface which is geometrically constrained will be referred to as the fixed surface.

Evaluating the surface energies of either face of our slab models is more complex than suggested by Equation 6.17, and is instead given by

$$\gamma_{free} + \gamma_{fixed} = \frac{1}{A}\big\{E_{slab}(j) - \lambda(j)\big\}. \tag{6.18}$$

Here A and $E_{slab}(j)$ retain their definitions from above, while γ_{free} and γ_{fixed} are now the surface energies of the free and fixed surfaces, respectively. For hydroxylated surfaces $\lambda(j) = N(j)E_{bulk} + N_{\mathrm{H_2O}}E_{\mathrm{H_2O}}$, where E_{bulk} is again the energy of a single

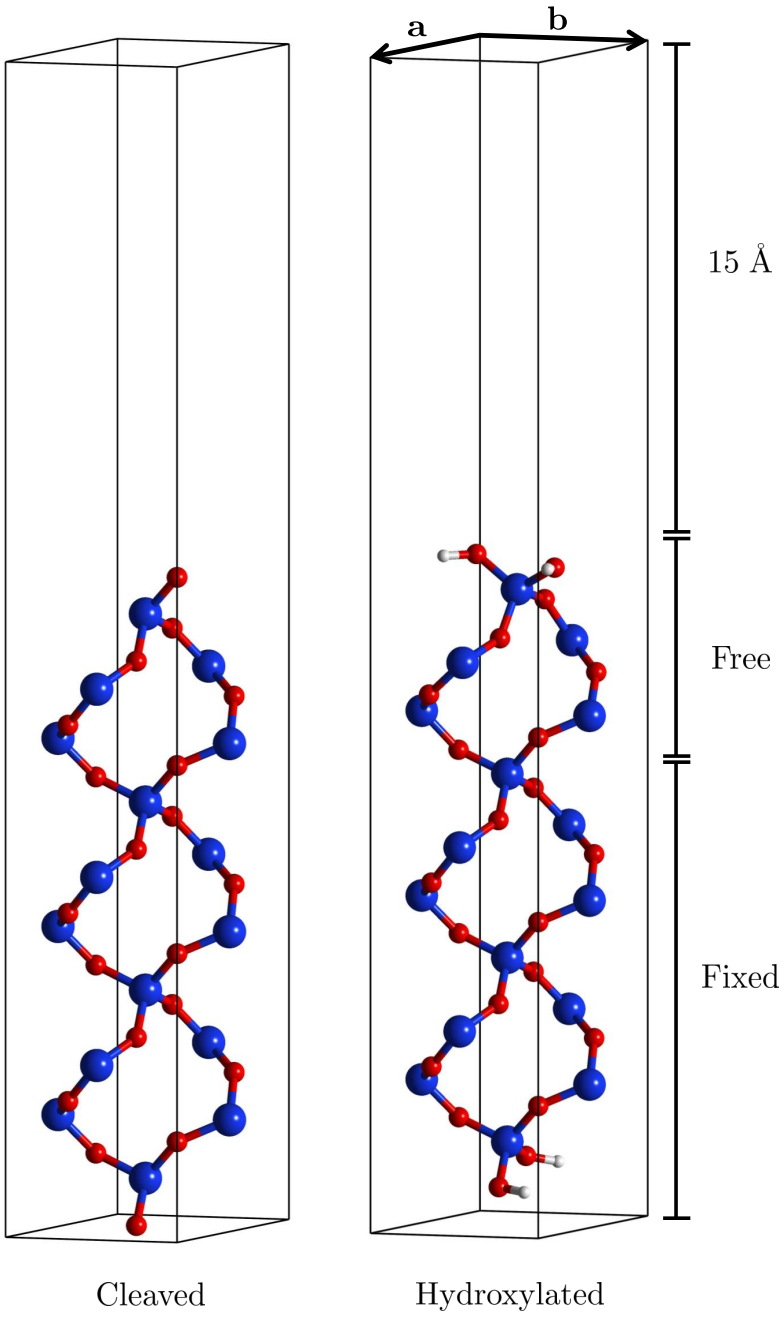

Figure 6.11: Illustration of the {0001} α-quartz surface slab models used in this chapter. In either case slabs were separated in the z–direction by a vacuum gap of 15 Å. Slabs consisted of an upper unit cell which was free to relax geometrically, below which there were between 1 and 4 fixed cells (2 are illustrated in this figure) which replicated a pseudo-infinite bulk structure. Silicon, oxygen and hydrogen atoms are coloured blue, red and white, respectively.

α-quartz unit cell, $N(j) = N_{slab}^{SiO_2}(j)/N_{bulk}^{SiO_2}$ is a stoichiometric factor which describes the ratio of SiO_2 units within each surface slab to that within the bulk unit cell, $N_{H_2O} = 2$ describes the number of water molecules added to hydroxylate each slab and E_{H_2O} is the calculated energy of a single gas–phase water molecule. Below we also detail the results of additional comparative surface energy calculations which have been performed on the cleaved $\{0001\}$ surface, for which $\lambda(j) = N(j)E_{bulk}$.

Our interest here of course lies in evaluating the slab thickness at which γ_{free} is well converged with respect to j; indeed, it is using the free surface of our slab model that we will later perform adsorption energy calculations. As such, Equation 6.18 may be rearranged to

$$\gamma_{free} = \frac{1}{A}\big\{E_{slab}(j) - \lambda(j)\big\} - \gamma_{fixed}, \tag{6.19}$$

where, in analogy to Equation 6.17,

$$\gamma_{fixed} = \frac{1}{2A}\big\{E'_{slab}(j) - \lambda\big\}. \tag{6.20}$$

Here E'_{slab} is the energy of each slab with fixed surfaces; for the cleaved slabs this corresponds to the energy of the slab having undergone no geometry optimisation after cleavage of the silanone surface, while for the hydroxylated slabs this corresponds to the results of separate geometry optimisation calculations (from the initial, unoptimised slab configuration) where only the surface hydroxyls were free to relax (i.e. no geometry optimisation on the upper-most unit cell).

Figure 6.12 illustrates γ_{free} values for cleaved and hydroxylated surface slabs with $2 \leq j \leq 5$ unit cells. Intriguingly, rather than converging, both sets of data show significant divergence in γ_{free} with increasing j; this divergence is a well-documented phenomenon, [66] and results not from a physically changing γ_{free} value with changing j, but from a small difference between the energy of the bulk unit cell E_{bulk} and the increase in slab energy E_{slab} upon an incremental increase in slab thickness by one bulk unit cell. A corrected value of the bulk unit cell energy E_{bulk}^{corr} is readily obtained by recognising that Equation 6.19 may be rearranged to give

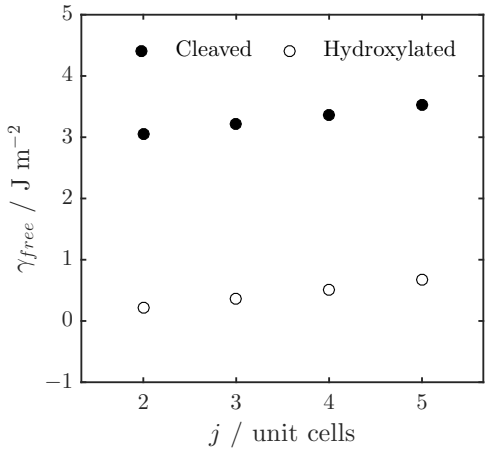

Figure 6.12: Illustration of the linear divergence of the surface energy γ_{free} with increasing slab thickness j.

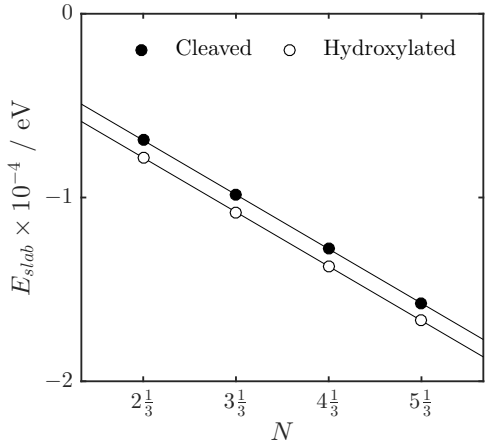

Figure 6.13: Illustration of the linear relationship between slab energy E_{slab} and the stoichiometric factor N, which defines the ratio between the number of SiO_2 groups within a slab and the number with the bulk unit cell illustrated in Figure 6.10. Solid lines indicate a linear fit to the data, the gradient of which provides the corrected bulk unit cell energy E_{bulk}^{corr}.

Table 6.5: Calculated surface energy values for cleaved and hydroxylated α-quartz surfaces.

j / unit cells	N	γ_{free} / J m^{-2}	
		Cleaved surface	Hydroxylated surface
2	$2\frac{1}{3}$	2.685	−0.156
3	$3\frac{1}{3}$	2.692	−0.173
4	$4\frac{1}{3}$	2.686	−0.183
5	$5\frac{1}{3}$	2.707	−0.175

$$E_{slab}(j) = A\{\gamma_{free} + \gamma_{fixed}\} + \lambda(j), \tag{6.21}$$

from which it follows that a plot of $E_{slab}(j)$ against N should yield a straight line of gradient E_{bulk}^{corr}. [67] This plot is given in Figure 6.13 and provides the small[2] corrections of $E_{bulk}^{corr} - E_{bulk} = 4.0653 \times 10^{-1}$ eV and $E_{bulk}^{corr} - E_{bulk} = 4.0545 \times 10^{-1}$ eV for cleaved and hydroxylated surfaces, respectively.

Table 6.5 details γ_{free} values calculated according to Equations 6.19 and 6.20, utilising E_{bulk}^{corr} in place of E_{bulk}. It is easily apparent from these data that the linear divergence in γ_{fixed} has been removed *via* the use of E_{bulk}^{corr}, and that the resulting values are similar across the range of surface slab thicknesses explored. For cleaved surfaces the surface energy is well converged to around 2.69 J m^{-2}. This large, positive value highlights the instability of the surface silanone termination and indicates rapid hydroxylation upon interaction of the surface with water, in agreement with previous work on the nature of this reaction. [68] Conversely the surface energy of the hydroxylated slabs is negative at around -0.17 J m^{-2}, suggesting a stable surface. Both sets of surface energies calculated here are found to compare well to those calculated by Goumans *et al.* on a similar α-quzrtz surface. [62]

For the purposes of establishing a hydroxylated surface slab for the adsorption modelling detailed below we choose the $j = 3$ structure as a reasonable compromise between γ_{free} convergence and the number of atoms required to model a relevant cell, which in turn influences the computational cost of our adsorption energy calculations; the structure of this $j = 3$ slab model is illustrated in Figure 6.11.

[2]We note that the original unit cell energy is $E_{bulk} = -2956.83397$ eV while the corrected values are $E_{bulk}^{corr} = -2956.42744$ eV and $E_{bulk}^{corr} = -2956.42852$ eV for the cleaved and hydroxylated surfaces, respectively. The corrections defined here are therefore on the order of 0.01 %.

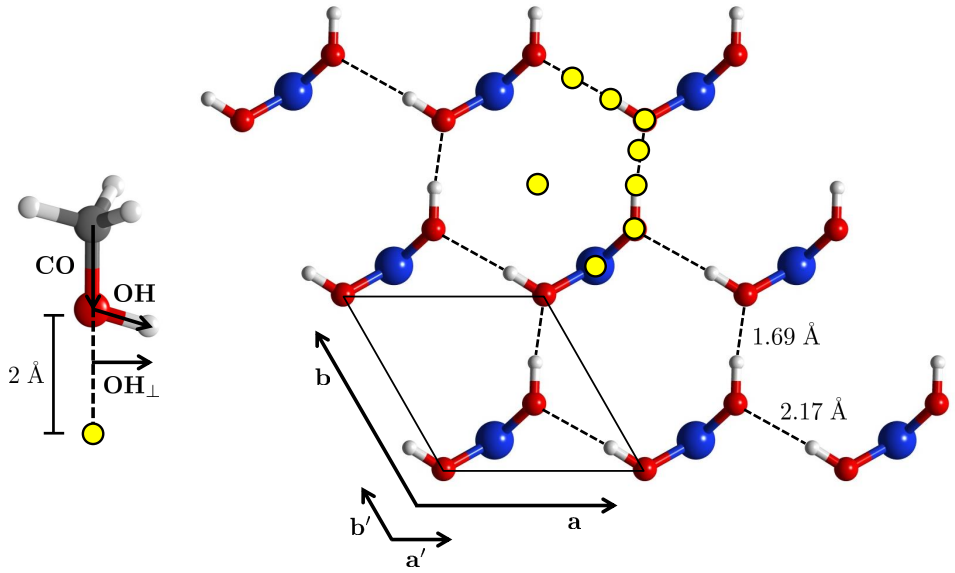

Figure 6.14: Top–down view of the hydroxylated α-quartz surface. For simplicity and clarity only surface silanol groups are shown; the hydrogen bonding network between these silanols are indicated by dashed lines. Solid black lines indicate the surface unit cell, as characterised by the cell vectors **a** and **b**. Yellow dots indicate the 8 initial adsorbate positions sampled; the **CO** bond vector of the adsorbing methanol was placed 2 Å above each start point and the transverse component of the methanol **OH** bond vector $\mathbf{OH}_{\perp}$ aligned with $\pm\mathbf{a}'$ and $\pm\mathbf{b}'$. The adsorption energy hypersurface of this structure was therefore sampled with $8 \times 4 = 32$ points in total, the energies of which are illustrated in Figure 6.15. Silicon, oxygen, hydrogen and carbon atoms are coloured blue, red, white and grey, respectively.

Methanol adsorption

We now turn to modelling the adsorption of relevant molecular species at free surface of our optimised slab structure. A methanol probe molecule has been employed to find the most optimal adsorption site for primary alcohols at the hydroxylated α-quartz {0001} surface; a top–down view of this surface is illustrated in Figure 6.14 and highlights the zigzagged hydrogen bonding network which exists between geminal surface silanols. To sample the adsorption energy surface of this structure a single methanol was placed approximately 2Å from the free surface of our optimised $j = 3$ hydroxylated slab in multiple locations and orientations, and adsorbed through structural relaxation. As illustrated in Figure 6.14, 8 adsorption locations[3] were sampled across the surface. It is useful for the purposes of defining the initial orientation of our methanol adsorbate at each of these locations to define the vectors $\mathbf{a}'$ and $\mathbf{b}'$ (Figure 6.14); these vectors point in the same directions as the vectors **a**

[3]More specifically these are the initial locations of the methanol adsorbate; in most of the geometry optimisation calculations performed here structural relaxation led to a small amount of transverse displacement.

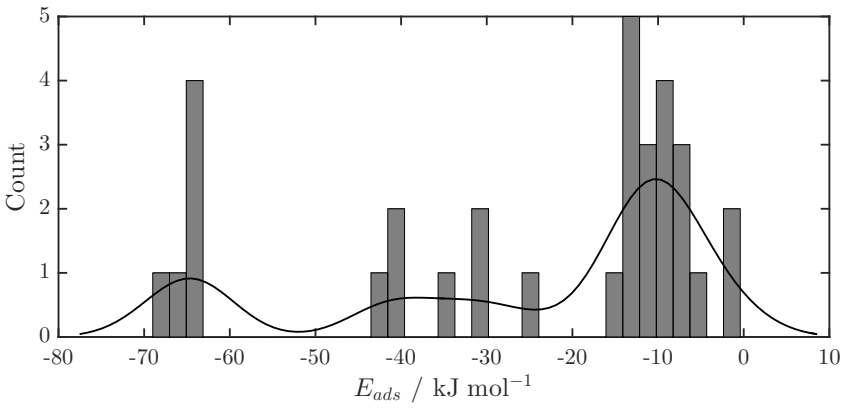

Figure 6.15: Adsorption energy distribution of methanol at the hydroxylated {0001} surface of α-quartz. In each case the adsorption energy E_{ads} was obtained according to Equation 6.22. The solid black line indicates a fit to the data bars and highlights the three binding modes characterised by van der Waals interactions (small $-E_{ads}$), single surface–adsorbate hydrogen bonding interactions (intermediate $-E_{ads}$) and polydentate surface–adsorbate hydrogen bonding interactions (large $-E_{ads}$).

and **b** which define the bulk unit cell (Figure 6.10 and Table 6.4) and surface unit cell of our surface structure (Figures 6.11 and 6.14), but are equal in magnitude to the transverse component of the **OH** bond vector of methanol, $\mathbf{OH}_{\perp}$ (Figure 6.14). To explore the adsorption energy hypersurface of methanol at our α-quartz surface the **CO** bond vector of the methanol adsorbate was positioned over each the 8 adsorption locations and the methanol molecule rotated about this vector such that $\mathbf{OH}_{\perp} = \pm\mathbf{a}', \pm\mathbf{b}'$; 4 initial adsorbate orientations were therefore sampled at each initial location.

Following DFT geometry optimisation the adsorption energy of each interaction E_{ads} was calculated according to

$$E_{ads} = E_{slab+mol} - E_{slab} - E_{mol}. \tag{6.22}$$

Here E_{slab} is the energy of the hydroxylated α-quartz slab, $E_{slab+mol}$ is the energy of the slab interacting with the adsorbate and E_{mol} is the energy of a single gas–phase adsorbate molecule. The distribution of adsorption energies obtained from our sampling is given in Figure 6.15; all alcohol adsorption energy calculations were performed at a surface coverage of one adsorbate *per* surface unit cell ($\theta = 1$ ML). These data clearly illustrates three different modes of surface interaction. Weak

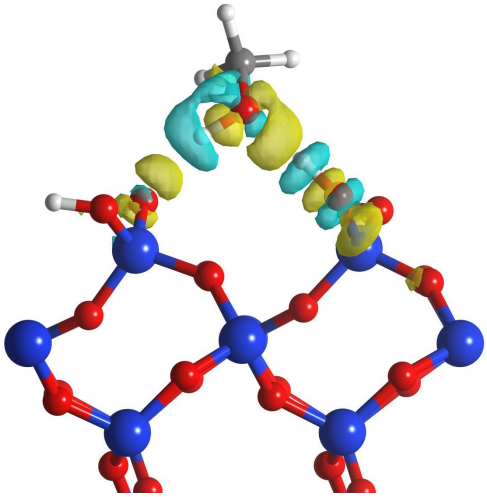

Figure 6.16: Illustration of the strongest surface–adsorbate interaction found *via* our manual sampling method. Methanol adsorption at this site involves two concurrent surface–adsorbate hydrogen bonding interactions between the hydroxyl groups of the adsorbing methanol and surface silanols on the α-quartz surface. The hydrogen bonding nature of this interaction is confirmed by overlaying an isosurface of the electron density change which occurs upon adsorption; coloured regions indicate a loss (blue) or gain (yellow) of electron density at a level of 6×10^{-4} electrons Å^{-3}. Silicon, oxygen, hydrogen and carbon atoms are coloured blue, red, white and grey, respectively.

adsorption interactions occur with $E_{ads} < 20$ kJ mol^{-1} and are dictated by dimple van der Waals interactions occurring between the adsorbate and the solid surface. Intermediate–strength interactions occur with 20 kJ mol^{-1} $< E_{ads} <$ 50 kJ mol^{-1} and are characterised by the formation of a single hydrogen bond between the adsorbing alcohol and hydroxylated surface. The strongest adsorption interactions occur with $E_{ads} > 60$ kJ mol^{-1} and are characterised by the formation of two surface–adsorbate hydrogen bonding interactions; for the purposes of exploring the hypothesis that nuclear spin relaxation measurements may be directly related to the strongest adsorption sites at a particular pore surface it is upon this strongest adsorption interaction that we will place our attention.

Figure 6.16 illustrates the most energetically favourable (most negative E_{ads} value) adsorption interaction between methanol and our hydroxylated {0001} α-quartz surface, associated with the left–most histogram bar in Figure 6.15 ($E_{ads} = -68$ kJ mol^{-1}). The geometric structure of this adsorption configuration is similar to that observed previously by Han *et al.*; [59] in particular, the adsorbing

methanol molecule has broken the longer of the two hydrogen bonds on the hydroxylated surface and formed two concurrent hydrogen bonds of reduced length with this adsorption site. As this interaction occurred spontaneously upon geometry optimisation of the system – i.e. it was not necessary to manually break the hydrogen bond at the surface for this interaction to occur – adsorption at this site may be considered non-activated. The hydrogen bonding nature of the surface–adsorbate interaction is confirmed through analysis of the electron charge density difference $\Delta\rho$ which occurs upon adsorption; this charge density difference is readily calculated according to

$$\Delta\rho = \rho_{mol+slab} - \rho_{slab} - \rho_{mol}, \tag{6.23}$$

where subscripts maintain their definitions from Equation 6.22. The electron density isosurfaces presented here clearly indicate a small redistribution of charge along the $H_3C - O - H \rightarrow O(H) - Si$ and $Si - O - H \rightarrow O(H) - CH_3$ directions, as might expected through the formation of $O^{\delta-} \cdots ^{\delta+}H$ hydrogen bonds.

Alcohol chain growth

Adsorbed primary alcohols containing longer carbon chains ($C_2 - C_4$) were subsequently developed from this optimal methanol adsorption configuration through that application of a novel carbon chain growth algorithm. This approach was necessitated by the complex structure of the adsorption energy landscape of our silica surface, which meant that simply attempting to replace the adsorbed methanol with larger molecules was found to be a poor method with which to ensure the binding of difference adsorbates at the same location. Indeed, due to subtle differences in the optimal surface–adsorbate hydrogen bond lengths between different primary alcohols, it was found during our calculations that this approach typically resulted in dissociation of the molecule away from the surface.

To mitigate the need to perform our manual adsorption sampling approach for each adsorbate considered, and to ensure the binding of each alcohol at the same location such that adsorption energies might be directly compared across a homologous series of adsorbate alcohols, a different approach utilising a simple chain

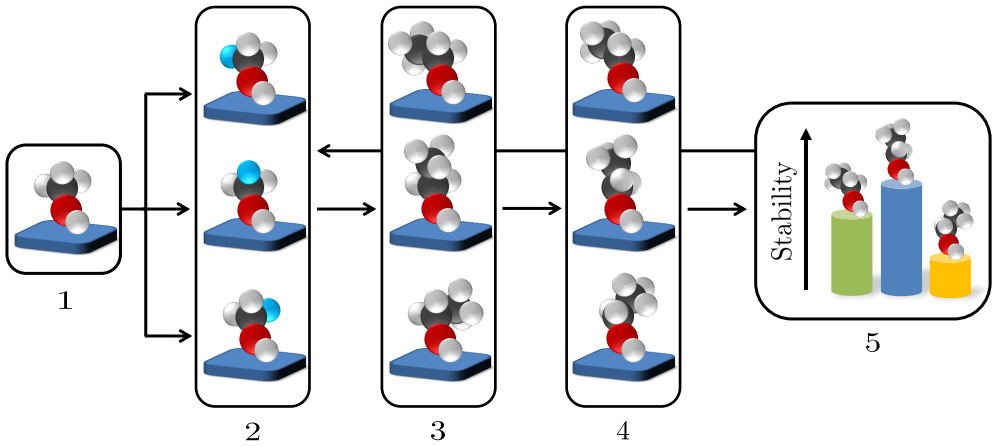

Figure 6.17: Illustration of the alcohol chain growth algorithm described in the main text. Oxygen, hydrogen and carbon atoms are coloured red, white and grey, respectively, while the silica surface is represented by a blue plane. Numbered boxes are referred to in the main text.

growth algorithm was developed. This method uses the initial binding configuration of the adsorbed methanol probe molecule as a 'seed' from which primary alcohols with longer carbon chains may be grown. The basic process is illustrated in Figure 6.17 and consists of the following stages: A seed site is selected through our manual adsorption energy hypersurface sampling processes describes above (Box 1, Figure 6.17). Each hydrogen atom within the methyl environment of the adsorbed methanol may be selected (Box 2) and separately replaced with an entire methyl group (Box 3). This approach yields three adsorbed ethanol molecules which differ only in the orientation of their carbon chain. Structural optimisation (geometric relaxation) of each adsorbate configuration (Box 4) is followed by an adsorption energy calculation of the form indicated by Equation 6.22, from which we take the most stable (most negative E_{ads}) configuration as our optimised adsorbate (Box 5). The above steps may then be repeated indefinitely to produce larger molecules bound to the same adsorption site.

The optimal configurations for each of the adsorbed alcohols considered here are shown in Figure 6.18, from which it is clear that all adsorbate molecules are bound to the surface in the same manner. Importantly, for the purposes of addressing a direct comparison between this adsorption modelling and the nuclear spin relaxation characteristics of liquid-saturated silica, we note that these adsorption interactions involve both hydroxyl groups at the pore surface, either as a hydrogen bond

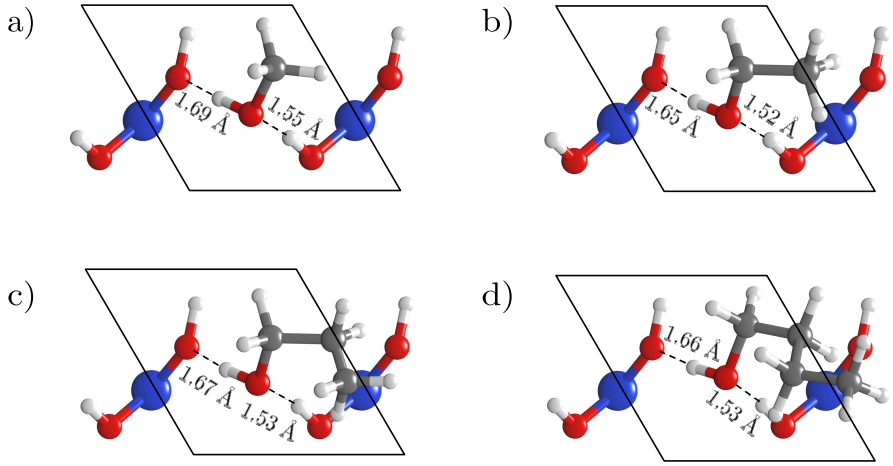

Figure 6.18: Top-down views of short-chain primary alcohols adsorbed at the strongest site on our hydroxylated {0001} α-quartz surface, as optimised using the novel alcohol chain growth algorithm detailed in Figure 6.17. For simplicity and clarity only surface atoms and adsorbates are shown. a), b) c) and d) display the DFT–optimised geometry of methanol, ethanol, 1-propanol and 1-butanol at this adsorption site, respectively. Dashed black lines indicate surface–adsorbate hydrogen bonds while solid black lines illustrate the 1×1 surface unit cell. Silicon, oxygen, hydrogen and carbon atoms are coloured blue, red, white and grey, respectively.

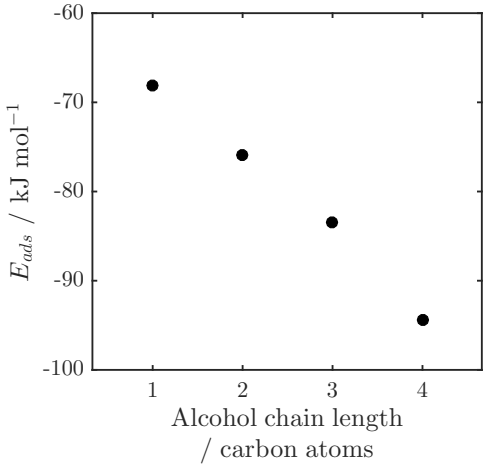

Figure 6.19: Adsorption energies E_{ads} of short-chain primary alcohols at the strongest adsorption site of the hydroxylated {0001} α-quartz surface, displayed as a function of carbon chain length. The corresponding adsorption configurations are illustrated in Figure 6.18.

donor ($Si-O-H \rightarrow O(H)-CH_3$) or acceptor ($H_3C-O-H \rightarrow O(H)-Si$). The surface–adsorbate hydrogen bond lengths indicated on this figure are all shorter than the intersilanol hydrogen bond which is broken upon adsorption, likely providing a significant driving force for polydentate hydrogen bond-mediated adsorption at this site. The adsorption energetics of these alcohols – as calculated according to Equation 6.22 – is explored in Figure 6.19, which illustrates a near-linear increase in adsorption strength with increasing carbon chain length. Although comparable experimental studies are – perhaps surprisingly – sparse, this trend is in agreement with that observed for these same alcohols on silicatene (two-dimensional SiO_2). [69]

Cyclohexane adsorption

Recalling that we have also investigated the nuclear spin dynamics of cyclohexane within our mesoporous silica support material, additional DFT calculations have been performed to quantify the adsorption energetics of this weakly–interacting reference molecule. Unfortunately cyclohexane does not readily fit within the simple 1×1 α-quartz $\{0001\}$ surface unit cell used for our alcohol adsorption (Figures 6.14 and 6.18). Saturation coverage was instead approximated at a coverage of 2 cyclohexane adsorbates *per* 4 surface unit cells ($\theta = 0.5$ ML). The optimal geometry of this system is illustrated in Figure 6.20 and was found through a manual search of the adsorption energy surface similar to that performed with methanol; however, given prior knowledge that cyclohexane is unable to form hydrogen bonds with the silica surface far fewer initial locations and orientations were sampled than during our consideration of alcohol adsorption. The corresponding adsorption energy was calculated according to

$$E_{ads} = E_{slab+mol} - 4E_{slab} - 2E_{mol}, \tag{6.24}$$

from which we obtain $E_{ads} = -31.2$ kJ mol^{-1}. This small adsorption energy confirms the weakly-interacting nature of alkanes at hydroxylated oxide surfaces. [70]

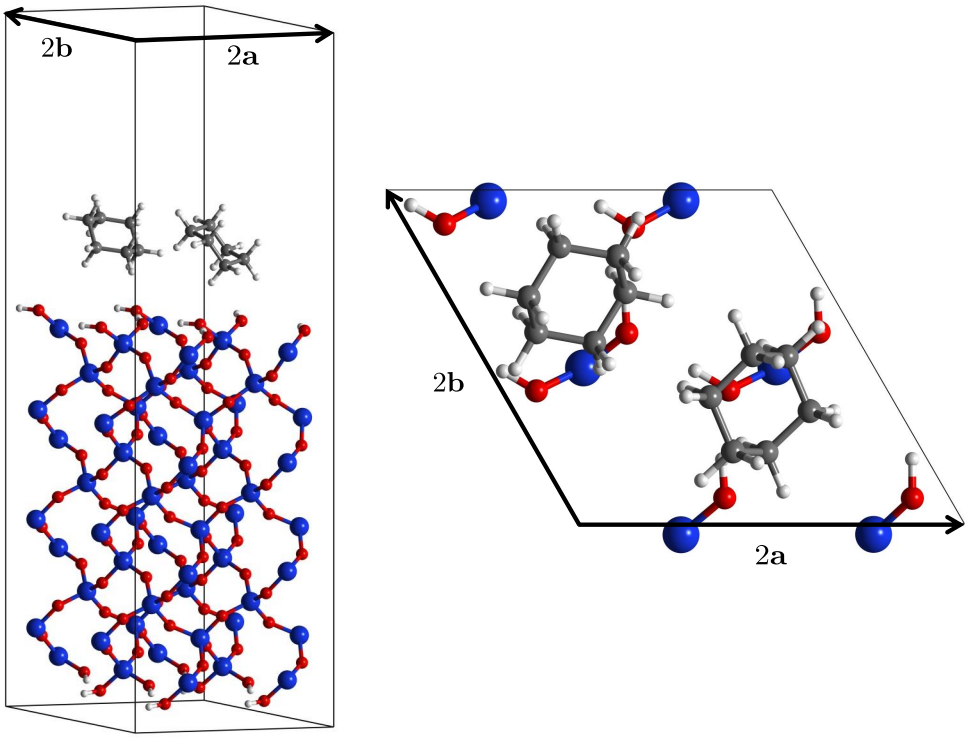

Figure 6.20: Side-on and top-down views of cyclohexane adsorbed at the hydroxylated {0001} α-quartz surface; for simplicity and clarity only surface atoms and adsorbates are shown within the top-down view. Saturation coverage is approximated *via* the optimisation of 2 cyclohexane molecules within a 2×2 supercell; this cell is indicated by black lines and characterised by the vectors **a** and **b** from Table 6.4. Silicon, oxygen, hydrogen and carbon atoms are coloured blue, red, white and grey, respectively.

6.3.5 Comparing NMR relaxation with adsorption energetics

We are now in a position to consider the best approach to compare our observed nuclear spin relaxation characteristics with our calculated adsorption energetics. An important consideration here is determining which spectral density function best applies to our experimental measurements. Given that our relaxation correlation measurements have been performed at intermediate magnetic field strength it is perhaps most appropriate to interpret our results based on the sensitivity of such measurements to the slow dynamics associated with molecular translation across the pore surface. Accordingly, we interpret our according to the translational self-diffusion model of Mitchell *et al.*; [9] here the ratio of surface relaxation time constants is

$$\frac{T_{1,surf}}{T_{2,surf}} = \frac{3J(0) + 5J(\omega_0) + 2J(2\omega_0)}{2J(\omega_0) + 8J(2\omega_0)}, \tag{6.25}$$

where the spectral density function for relaxation due to surface translation is [4]

$$J(\omega) = \tau_m \ln\left(\frac{1+\omega^2\tau_m^2}{(\tau_m/\tau_s)^2 + \omega^2\tau_m^2}\right). \tag{6.26}$$

Here ω_0 is the Larmor frequency and we recall from Chapter 2 that τ_m and τ_s are the average adsorption site residence time and the mean surface lifetime of the adsorbate, respectively. [71] These surface correlation times are illustrated in Figure 6.21 for the case of methanol interacting with a hydroxylated oxide surface. Recalling from Figure 6.9 that $\langle T_1/T_2 \rangle \propto T_{1,surf}/T_{2,surf}$ Equations 6.25 and 6.26 provide a clear connection between our observed relaxation characteristics and the adsorption phenomena captured by our DFT adsorption calculations.

As previously introduced, an empirical theory describing a relationship between the ratio T_1/T_2 and adsorption energetics has been put forward by D'Agostino *et al.* [6] and is of direct relevance to this work. Here we present a detailed derivation of this theory. As introduced in Chapter 2 the diffusion coefficient associated with the translation of species across the surface of a liquid-saturated porous structure takes the form [72]

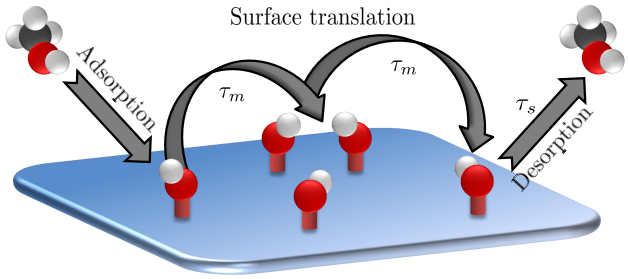

Figure 6.21: Illustration of the surface dynamics of alcohols across a hydroxylated pore surface, as captured by the spectral density function describing relaxation due to surface translation (Equation 6.26). Molecules first adsorb through the formation of surface-adsorbate hydrogen bonding interactions with polar surface groups. Translational motion then occurs with a characteristic correlation time τ_m, which describes the frequency of surface hopping across the pore surface. Desorption from the surface then occurs after an average surface residence time τ_s. Carbon, oxygen and hydrogen atoms are coloured grey, red and white, respectively.

$$\mathcal{D}_m = \mathcal{D}_{m,0} \exp\left(\frac{-E_m^*}{RT}\right), \tag{6.27}$$

where $\mathcal{D}_{m,0}$ is a relevant pre-exponential factor which contains contributions from molecular vibrations at the solid surface, R is the gas constant and T is the absolute temperature. The effective diffusion barrier $E_m^* = E_h + E_j$ contains energetic contributions from the jumping process (or bond-breaking process) E_j associated with the partial desorption required for surface mobility (which is considered some fraction α_1 of the relevant desorption energy E_{des}, $0 < \alpha_1 \leq 1$), and the hole-formation process E_h required to generate a hole at the next adsorption site. [73] For such a hole to form at an adjacent adsorption site we note that a molecule must either desorb from the surface ($E_h \sim E_{des}$) or hop to another vacant site ($E_h \sim E_j$), such that $E_h = \alpha_2 E_{des}$ ($0 < \alpha_2 \leq 1$). It follows that both E_j and E_h may be considered functions of the desorption energy, such that we may state the general surface diffusion expression [74]

$$\begin{aligned} \mathcal{D}_m &\propto \exp\left(\frac{-(\alpha_1 E_{des} + \alpha_2 E_{des})}{RT}\right) \\ &\propto \exp\left(\frac{-\alpha E_{des}}{RT}\right), \end{aligned} \tag{6.28}$$

where the proportionality constant α conforms to $0 < \alpha \leq 1$.

Returning to our consideration of nuclear spin relaxation at the pore surface,

we recall from Chapter 2 (Equation 2.25) that the diffusion coefficient for surface motion is directly related to τ_m according to [75]

$$\mathcal{D}_m \propto \frac{\ell^2}{4\tau_m}, \tag{6.29}$$

where ℓ is the mean distance between adsorption sites. It follows from Equations 6.28 and 6.29 that the frequency of surface hopping may be described as

$$\frac{1}{\tau_m} \propto \exp\left(\frac{-\alpha E_{des}}{RT}\right). \tag{6.30}$$

Mitchell *et al.* used fast field cycling relaxometry to explore the surface dynamics of various liquids at the pore surface of a 1 wt% Pd/Al_2O_3 catalyst. [9] This method measures relaxation rates (typically $1/T_1$) as a function of magnetic field strength; the resulting data can then be fit using relevant spectral density functions to obtain an estimate of the surface correlation times τ_m and τ_s. In this work the correlation times for 2-propanol were observed to be $\tau_m = 2.0 \times 10^{-10}$ s and $\tau_s = 1.1 \times 10^{-5}$ s, confirming that such adsorbates undergo extensive surface translation before desorption ($\tau_s \gg \tau_m$). Given the relative magnitude of these values we may refine the spectral density function given in Equation 6.26; in particular, we may assume that[4] $(\tau_m/\tau_s)^2 \ll (\omega_0\tau_m)^2 \ll 1$ such that Equation 6.26 reduces to

$$\begin{aligned} J(\omega > 0) &\approx \tau_m \ln\left(\frac{1}{\omega^2\tau_m^2}\right) \\ &\approx -2\tau_m \ln\big(\omega\tau_m\big). \end{aligned} \tag{6.31}$$

Following some basic algebraic manipulation Equation 6.25 then becomes

$$\frac{T_{1,surf}}{T_{2,surf}} \approx \frac{3\ln(\tau_s/\tau_m) - 5\ln(\omega_0\tau_m) - 2\ln(2\omega_0\tau_m)}{-2\ln(\omega_0\tau_m) - 8\ln(2\omega_0\tau_m)}. \tag{6.32}$$

Furthermore, given that[5,6] $\ln(\tau_s/\tau_m) \gg -\ln(\omega_0\tau_m) > -\ln(2\omega_0\tau_m)$ we may state a

[4] Utilising these 2-propanol τ_m and τ_s values and recalling that our nuclear spin correlation measurements have been performed at a Larmor frequency of $\omega_0/(2\pi) = 85$ MHz we obtain $(\tau_m/\tau_s)^2 \approx 3 \times 10^{-10}$ and $(\omega_0\tau_m)^2 \approx 1 \times 10^{-2}$.

[5] Again taking τ_m and τ_s from literature 2-propanol data and $\omega/(2\pi) = 85$ MHz we obtain $\ln(\tau_s/\tau_m) \approx 11$, $\ln(\omega_0\tau_m) \approx -1$ and $\ln(2\omega_0\tau_m) \approx -1/2$.

[6] Here we have also made use of the standard logarithmic transform $-\log(xy) = -\log(x) - \log(y)$ such that $-\ln(\omega_0\tau_m) - \ln(2\omega_0\tau_m) \propto -\ln(\omega_0\tau_m)$.

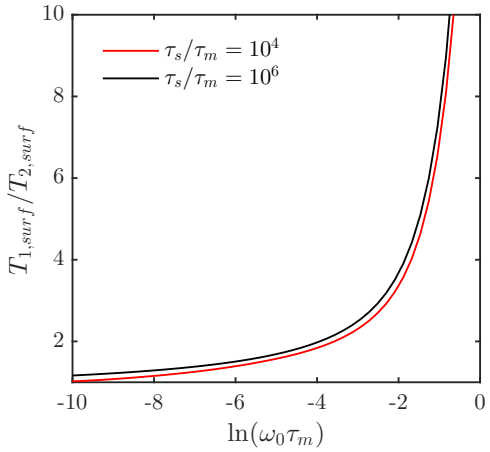

Figure 6.22: Illustration of the frequency and τ_m dependence of the ratio $T_{1,surf}/T_{2,surf}$ as a function of τ_s/τ_m, as calculated according to Equations 6.25 and 6.26. The τ_s/τ_m values explored are expected to cover a relevant range for primary alcohol dynamics at hydroxylated pore surfaces. [9] The sensitivity of $T_{1,surf}/T_{2,surf}$ to changing τ_s/τ_m ratio is observed to be negligible.

general equation of proportionality [6]

$$\frac{T_{1,surf}}{T_{2,surf}} \propto -\frac{\ln(\tau_m/\tau_s)}{\ln(\omega_0\tau_m)}, \tag{6.33}$$

which significantly simplifies the dependence of T_1/T_2 values on the surface correlation times τ_m and τ_s.

McDonald *et al.* have previously suggested that for water-saturated cement pastes the ratio T_1/T_2 is approximately independent of $\ln(\tau_m/\tau_s)$, while maintaining sensitivity to $\ln(\omega_0\tau_m)$. [76] Here, however, surface relaxation was found to be dominated by the presence of paramagnetic relaxation sinks, requiring a heteronuclear description of $J(\omega)$. As this is not considered to be the case for the liquid-saturated silica investigated here, the theoretical calculations performed in the aforementioned work have been repeated using the homonuclear description of surface relaxation given by Equations 6.25 and 6.26. The results of these calculations are illustrated in Figure 6.22, where in keeping with our model literature value of $\tau_m/\tau_s \approx 10^{-5}$ [9] we have considered $\tau_m/\tau_s = 10^{-4}$ and $\tau_m/\tau_s = 10^{-6}$. It is clear from this figure that the ratio T_1/T_2 is indeed largely insensitive to changes to τ_m/τ_s over this range, while presenting a strong dependence on $\ln(\omega_0\tau_m)$.

As our nuclear spin relaxation correlation measurements were performed at fixed magnetic field we may separate the ω_0 and τ_m contributions within the term $\ln(\omega_0\tau_m)$ such that[7], $T_{1,surf}/T_{2,surf} \propto -1/\ln(\tau_m)$. Importantly, by combining this expression with Equation 6.30 it follows that [6]

$$\frac{T_{1,surf}}{T_{2,surf}} \propto \frac{-1}{\ln(\tau_m)} \propto \frac{-1}{E_{des}}, \tag{6.34}$$

so that the ratio $-T_{2,surf}/T_{1,surf}$ might be directly compared with a formal measure of adsorption (or desorption) energetics.

Recalling that $\langle T_1/T_2 \rangle \propto T_{1,surf}/T_{2,surf}$ (Figure 6.9), if the highly empirical theory outlined above is robust we might expect to observe a linear correlation between $-1/\langle T_1/T_2 \rangle$ and E_{des}. It is therefore appropriate to recall from Chapter 2 that for the non-activated adsorption explored through our DFT modelling this energy is simply $E_{des} = -E_{ads}$. To explore the sensitivity of our nuclear spin relaxation measurements to the adsorption energetics of strongly adsorbing surface sites we therefore illustrate in Figure 6.23 a plot of our experimentally observed $-1/\langle T_1/T_2 \rangle$ data against $-E_{ads}$ values, as acquired *via* our extensive DFT adsorption energy calculations. An excellent correlation between these two very difference measurements is clearly apparent. Of particular note is the solid diagonal line which represents a linear fit to the data points; this fit takes the form $-1/\langle T_1/T_2 \rangle \approx -6.3 \times 10^{-3} \times E_{ads} - 0.7$, and predicts that at $E_{ads} = 0$ the observed modal relaxation time ratio will be $\langle T_1/T_2 \rangle \approx 1.4$. Remarkably, this apparent limiting $\langle T_1/T_2 \rangle$ value is in excellent agreement with the $T_1/T_2 \approx 1$ value predicted for unrestricted (and therefore totally non-interacting) liquids. [77] Overall this correlation appears to provide strong evidence that the nuclear spin characteristics of liquid-saturated catalyst material acquired at intermediate magnetic field provide a quantitative indication of adsorption energetics associated with the strongest adsorption sites present. A summary of the $\langle T_1/T_2 \rangle$ values and adsorption energetics illustrated within Figure 6.23 is provided in Table 6.6.

[7]Here we have again made use of the standard logarithmic transform $-\log(xy) = -\log(x) - \log(y)$ such that $-\ln(\omega_0\tau_m) = -\ln(\omega_0) - \ln(\tau_m)$. As ω_0 is constant for our experiments the term $-\ln(\omega_0)$ is simply enveloped by the proportionality sign.

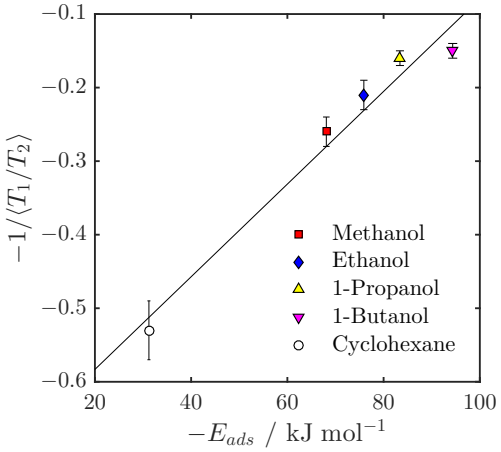

Figure 6.23: Comparison of the inverse relaxation time ratio $-1/\langle T_1/T_2\rangle$ with adsorption energy values E_{ads}, as obtained from our DFT calculations. Error bars indicate the uncertainty in obtaining $\langle T_1/T_2\rangle$ for each liquid-saturated silica system, as calculated through multiple repeat experiments on multiple samples. The solid diagonal line represents a linear fit to the data.

Table 6.6: Numerical summary of the data illustrated in Figure 6.23. Nuclear spin relaxation values correspond to the alkyl ^{1}H environment of each liquid at 85 MHz. Error bounds indicate the uncertainty in obtaining $\langle T_1/T_2\rangle$ for each liquid-saturated silica system, as calculated through multiple repeat experiments on multiple samples.

Liquid	$\langle T_1/T_2\rangle$	$-1/\langle T_1/T_2\rangle$	$-E_{ads}$ / kJ mol^{-1}
Methanol	3.8 ± 0.3	-0.26 ± 0.02	68.10
Ethanol	4.9 ± 0.4	-0.21 ± 0.02	75.89
1-Propanol	6.1 ± 0.5	-0.16 ± 0.01	83.40
1-Butanol	6.6 ± 0.5	-0.15 ± 0.01	94.36
Cyclohexane	1.9 ± 0.1	-0.49 ± 0.04	31.22

6.3.6 Comparing PFG NMR diffusion with adsorption phenomena

In this final results section we wish to provide a brief comparative exploration of the sensitivity of pulsed field gradient (PFG) self-diffusion measurements to surface interactions. As introduced in Chapter 4, the ratio of the unrestricted self-diffusion coefficient $\mathcal{D}_0$ to the effective diffusion coefficient $\mathcal{D}_{eff}(t_\Delta \rightarrow \infty) \equiv \mathcal{D}_\infty$ which characterises restricted motion in liquid-saturated mesoporous media in the long-time ($t_\Delta \rightarrow \infty$) diffusion limit gives a dimensionless parameter ξ known as the PFG interaction parameter, [78]

$$\xi = \frac{\mathcal{D}_0}{\mathcal{D}_\infty}. \tag{6.35}$$

In the case of weakly interacting, non-viscous liquids (typically short-chain alkanes) this ratio is equal to the tortuosity of the pore network, $\xi = \hat{\tau}$. [38] However, in the presence of non-negligible intermolecular or surface-adsorbate interactions this relationship does not hold.

Of interest to the present study is the influence of adsorption interactions on Equation 6.35. Although self-diffusion measurements performed on liquid-saturated porous structures are primarly sensitive to liquid towards the centre of the pores, such measurements can still be expected to exhibit some surface-sensitivity due to the multiple encounters these diffusing molecule will have with the pore walls during a given PFG NMR experiment. [79] If such collisions result in significant adsorption interactions then the observed effective self-diffusion coefficient will be reduced from that expected purely from the tortuosity of the structure, leading to an increase in ξ. To explore whether such effects present a quantitative relationship with the surface-adsorbate interactions explored in previous sections we have performed a series of PFG NMR experiments to quantify the diffusive behaviour of our alcohol- and cyclohexane-saturated silica support material. Figure 6.24 presents the results of APGSTE experiments performed on these systems; the resulting effective self-diffusion coefficients together with the $\mathcal{D}_0$ values described previously in Figure 6.4 are detailed in Table 6.7. In all cases the diffusion observation time for our APGSTE analysis was set to $t_\Delta = 100$ ms; given the self-diffusion coefficients obtained from these experiments (Table 6.7) we may readily calculate that the relevant root mean

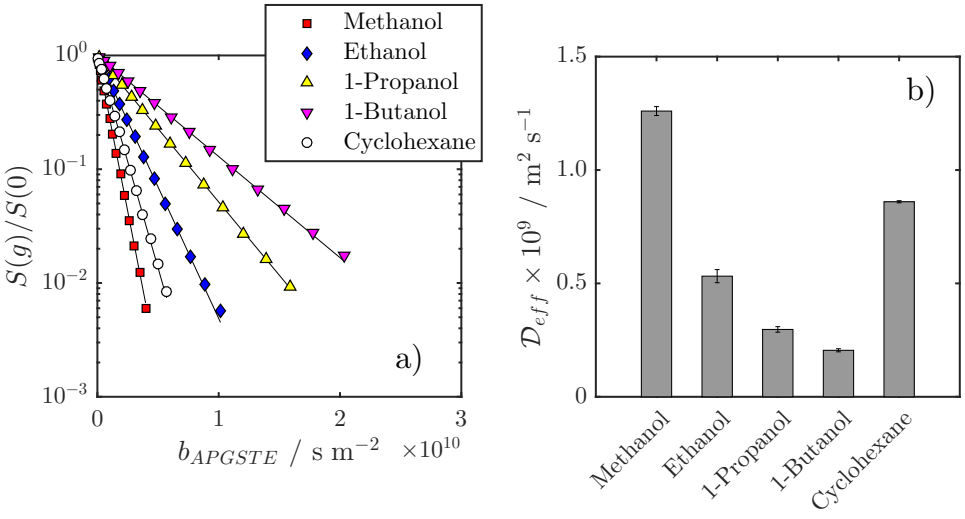

Figure 6.24: APGSTE diffusion analysis of restricted short-chain primary alcohols and cyclohexane in mesoporous silica at 20 ± 0.1°C. a) illustrates log-attenuation data obtained from each liquid. Solid lines indicate a fit to Equations 6.8 and 6.9. In all cases the observation time was set to $t_\Delta = 100$ ms. Self-diffusion coefficients $\mathcal{D}_{eff}$ obtained from this fitting are shown in b). The relative error was found to be approximately 2.5% in each case.

squared displacements (RMSD $= \sqrt{2t_\Delta D_{eff}}$) fall within the range $0.64 - 1.59$ μm. As these displacements are significantly greater than the modal pore diameter of the material under study ($d_{pore} = 15$ nm) it is appropriate to make the approximation $\mathcal{D}_{eff}(t_\Delta = 100 \text{ ms}) \approx \mathcal{D}_\infty$, in turn allowing us to calculate the PFG interaction parameter according to Equation 6.35; these values are also provided in Table 6.7.

It is clear from our calculated ξ data that primary alcohols exhibit significantly larger $\mathcal{D}_0/\mathcal{D}_{eff}$ values than expected from the tortuosity of our silica support material, which may be approximated from our cyclohexane diffusion data, $\hat{\tau} \approx \xi \approx 1.5$. This value is in agreement with previous analyses of the tortuosity of similar materials. [38] The observed increase in ξ away from this value suggests that adsorption interactions at the solid-liquid interface have a non-negligible effect on the self-diffusion of our primary alcohols within this material, and dominate any dynamics network disruption interactions which may cause an apparent increase in the effective self-diffusivity relative to the pore network tortuosity.[8] Furthermore, there is a distinct increase in ξ with increasing carbon chain length. This trend is similar to that previously observed when considering our nuclear spin relaxation correlation experiments; as such, we provide in Figure 6.25 a comparison of these

[8] Such effects are discussed in Chapter 4.

Table 6.7: Summary of the PFG NMR diffusion characteristics of short-chain primary alcohols at 20 ± 0.1 °C. $\mathcal{D}_{eff}$ values correspond to the effective self-diffusion of these liquids is mesoporous silica ($d_{pore} = 15$ nm) with the observation time set to $t_\Delta = 100$ ms. The PFG interaction parameter ξ has been calculated from these data according to Equation 6.35 assuming $\mathcal{D}_{eff} \equiv \mathcal{D}_\infty$; the ξ value for cyclohexane is expected to be a good approximation of the tortuosity of this material.

Liquid	$\mathcal{D}_0 \times 10^{10}$ / m^2 s^{-1}	$\mathcal{D}_{eff} \times 10^{10}$ / m^2 s^{-1}	$\sqrt{2t_\Delta D_{eff}}$ / μm	$\sqrt{2t_\Delta D_{eff}}/d_{pore}$ / pores	ξ
Methanol	21.40 ± 0.03	12.6 ± 0.3	1.59 ± 0.04	106 ± 2	1.70 ± 0.04
Ethanol	9.52 ± 0.01	5.3 ± 0.1	1.03 ± 0.02	69 ± 2	1.79 ± 0.04
1-Propanol	5.72 ± 0.01	2.0 ± 0.1	0.77 ± 0.02	51 ± 1	1.93 ± 0.04
1-Butanol	4.10 ± 0.01	2.1 ± 0.1	0.64 ± 0.01	43 ± 1	2.00 ± 0.05
Cyclohexane	12.91 ± 0.02	8.6 ± 0.2	1.31 ± 0.03	87 ± 2	1.50 ± 0.03

ξ values with the T_1/T_2 ratios obtained in Section 6.3.1, together with the results of our DFT adsorption energy calculations in Section 6.3.4. We find that there is a remarkably clear trend between these measurements. Figure 6.25a illustrates a comparison between ξ and our intermediate-field $\langle T_1/T_2 \rangle$ ratios, and reveals an excellent positive correlation between these dimensionless ratios; the solid diagonal line in this figure represents a linear fit to the data points and suggests that $\mathcal{D}_0/\mathcal{D}_\infty \approx \langle T_1/T_2 \rangle/10 + 1.3$. Given our knowledge of the surface sensitivity of this relaxation time ratio the significant agreement observed here between our diffusion and relaxation measurements highlights the influence that surface interactions must have on $\mathcal{D}_\infty$. To further establish whether there may be a more quantitative relationship between the diffusive characteristics of our imbibed liquids and their interactions with the pore surface Figure 6.25b provides a comparison of our observed ξ values with the results our DFT adsorption energy calculations. In analogy to Figure 6.23 this figure provides an excellent correlation between these very different measurements. The solid diagonal line again illustrates a linear fit to the data and suggests that $\mathcal{D}_0/\mathcal{D}_\infty \approx -8 \times 10^{-3} \times E_{ads} + 1.2$.

Exploring the influence of adsorption on $\mathcal{D}_\infty$

It is appropriate here to briefly consider how self-diffusion measurements performed in the long-time diffusion limit might exhibit sensitivity to adsorption energetics. We may recall from our discussion of nuclear spin relaxation that a given liquid-

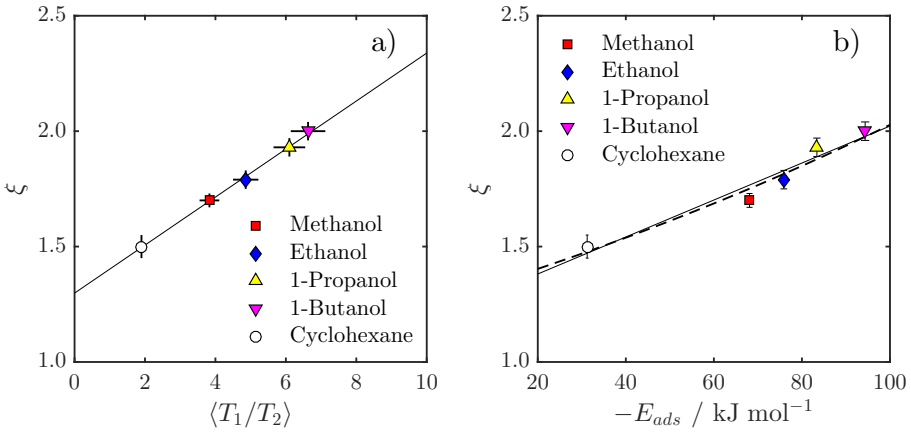

Figure 6.25: Comparison of the PFG interaction parameter ξ with a) the modal relaxation time ratios $\langle T_1/T_2 \rangle$, and b) the DFT-calculated adsorption energies associated with the strongest surface-adsorbate interaction. An excellent correlation is observed in each case, illustrating the sensitivity of restricted diffusion to adsorption interactions at the pore surface. Solid diagonal lines indicate a linear fit to the data in each case, while the dashed line in b) indicates a fit to Equation 6.41.

saturated pore consists of bulk-like liquid towards the centre of the pore and an adsorbed surface layer at the solid-liquid interface. If molecular exchange between these two environment is rapid with respect to the relaxation time constant measured then we observe an average value which is weighted by the molecular populations of these two environments. However, if the mixing of these populations is slow on the time scale of the relaxation characteristic being measured then the resulting data will contain contributions from both environments. The same concepts may be applied to diffusion measurements. [80] If the diffusion observation time is short with respect to this exchange (biphasic slow-exchange) then the resulting PFG data will attenuate as

$$\frac{S(g)}{S(0)} = (1-P)\exp(-b\mathcal{D}_0) + P\exp(-b\mathcal{D}_m). \tag{6.36}$$

Here $S(g)/S(0)$ is the normalised signal attenuation, P is the fraction of molecules within the adsorbed surface layer, $\mathcal{D}_0$ and $\mathcal{D}_m$ are the self-diffusion coefficients for unrestricted and surface motion and b is the relevant b-factor for the pulse sequence employed. This data form will be apparent in the resulting log-attenuation plot as a curve with limiting gradients $-\mathcal{D}_0$ and $-\mathcal{D}_m$ at low and high b, respectively. [81] It follows from the prominent $\mathcal{D}_m$ term in Equation 6.36 that PFG NMR analyses

of surface diffusion coefficients are typically undertaken at very small observations times. [81–84] We note, however, that direct evaluation of surface diffusion using PFG NMR techniques is often significantly impeded by the inherently slow diffusion coefficients, small molecular populations and enhanced nuclear spin relaxation rates associated with the adsorbed surface layer. The evaluation of possible surface effects discernible from the bulk-pore population observed in the long-time diffusion limit is therefore interest for pragmatic reasons.

If the diffusion observation time is long with respect to this exchange process (biphasic fast-exchange) then the resulting PFG attenuation data for diffusion through an isolated pore will follow [80]

$$\frac{S(g)}{S(0)} = \exp(-b\langle\mathcal{D}\rangle), \tag{6.37}$$

where

$$\langle\mathcal{D}\rangle = (1-P)\mathcal{D}_0 + P\mathcal{D}_m. \tag{6.38}$$

Given the large diffusion observation time employed in our APGSTE experiments ($t_\Delta = 100$ ms) it is reasonable to assume that this biphasic fast-exchange expression is applicable to the self-diffusion processes explored here; this interpretation is supported by the log-attenuation plots in Figure 6.24a which present a single diffusion coefficient, as characterised by a straight line on the log-scale.

We introduce the concept of an isolated pore in Equations 6.37 and 6.38 as the diffusion within such a structure is independent of any tortuosity factor. In the present experiments, however, our silica has been found to exhibit a tortuosity of $\hat{\tau} \approx 1.5$, which influences the bulk-like fluid towards to the centre of the pores. Likewise a separate 'surface tortuosity' $\hat{\tau}_{surf}$ will influence diffusion through the adsorbed surface layer [85] and relates to the topology of the pore surface over the length scale $\ell_m \sim \sqrt{\mathcal{D}_m\tau_s}$, [79] where we recall from Figure 6.21 that the surface correlation time τ_s describes the mean surface residence time of the adsorbate. As such, we may state our observed long-time self-diffusion coefficient as

$$\mathcal{D}_\infty = \frac{(1-P)\mathcal{D}_0}{\hat{\tau}} + \frac{P\mathcal{D}_m}{\hat{\tau}_{surf}}. \tag{6.39}$$

From this expression it follows that for $(1-P)\mathcal{D}_0/\hat{\tau} \gg P\mathcal{D}_m/\hat{\tau}_{surf}$ we have the usual condition of $\mathcal{D}_0/\mathcal{D}_\infty \approx \hat{\tau}$. However, if the surface term $P\mathcal{D}_m/\hat{\tau}_{surf}$ is non-negligible then $\mathcal{D}_0/\mathcal{D}_\infty > \hat{\tau}$, leading to Equation 6.35.

For the purposes of attempting to derive a relationship between E_{ads} and our observed diffusion characteristics we may express the PFG interaction parameter as,

$$\xi = \frac{\mathcal{D}_0}{\mathcal{D}_\infty} = \frac{\mathcal{D}_0}{\hat{\tau}^{-1}(1-P)\mathcal{D}_0 + \hat{\tau}_{surf}^{-1} P\mathcal{D}_m} \tag{6.40a}$$

$$= \frac{\mathcal{D}_{0,0}\exp(-E_0/RT)}{\hat{\tau}^{-1}(1-P)\mathcal{D}_{0,0}\exp(-E_0/RT) + \hat{\tau}_{surf}^{-1} P\mathcal{D}_{m,0}\exp(-E_m/RT)}. \tag{6.40b}$$

Here we have combined Equations 6.28, 6.35 and 6.39 and make the common assumption that the diffusion coefficient for unrestricted liquids may be expressed as $\mathcal{D}_0 = \mathcal{D}_{0,0}\exp(-E_0/RT)$, where E_0 is an activation energy for the unrestricted transport process. By assuming typical literature values[9] for E_0, E_m and the pre-exponential terms $\mathcal{D}_{0,0}$ and $\mathcal{D}_{m,0}$ [73, 86] we find that $1/\mathcal{D}_m \gg 1/\mathcal{D}_0 \gg \mathcal{D}_0$. This allows us to define the empirical relationship

$$\frac{\mathcal{D}_0}{\mathcal{D}_\infty} \propto \exp\left(\frac{-\alpha E_{ads}}{RT}\right), \tag{6.41}$$

where we have made use of the relations $E_m \propto E_{des}$, $1/\exp(-\alpha E_{des}) = \exp(\alpha E_{des})$ and $E_{des} = -E_{ads}$. The dashed line in Figure 6.25b illustrates a fit of this form. While it is noted that this fit provides no significant improvement over the basic linear relationship illustrated between ξ and E_{ads}, the fact that this line gives reasonable agreement with our data provides confidence in the above empirical derivation. It is, however, evident from this figure that a larger set of data points covering a wider range of both ξ and E_{ads} values is necessary to evaluate whether the relationship described in Equation 6.41 is robust.

[9]For example, taking $\mathcal{D}_{0,0} \approx \mathcal{D}_{m,0} \approx 10^{-7}$ m^2 s^{-1}, [73] $E_0 \approx 15$ kJ mol^{-1} [86], $E_m \approx 30$ kJ mol^{-1} [73] and $T = 300$ K we obtain $\mathcal{D}_0 = \mathcal{D}_{0,0}\exp(-E_0/RT) \approx 1.8\times10^{-9}$ m^2 s^{-1}, $1/\mathcal{D}_0 = 1/(\mathcal{D}_{0,0}\exp(-E_0/RT)) \approx 5.5\times10^{8}$ m^2 s^{-1}, $\mathcal{D}_m = \mathcal{D}_{m,0}\exp(-E_m/RT) \approx 4.5\times10^{-12}$ m^2 s^{-1} and $1/\mathcal{D}_m = 1/(\mathcal{D}_{m,0}\exp(-E_m/RT)) \approx 2.2\times10^{11}$ m^2 s^{-1}. It follows that $1/\mathcal{D}_m \gg 1/\mathcal{D}_0 \gg \mathcal{D}_0$ such that $\xi \sim 1/\mathcal{D}_m$. Alternatively the same reasoning can be made through the direct comparison of unrestricted and surface diffusion coefficients. For example Weber *et al.* observed that 1-octene in a mesoporous 1 wt% Pd/Al_2O_3 catalyst exhibits $\mathcal{D}_0 = 2.9\times10^{-9}$ m^2 s^{-1} and $D_m = 1.7\times10^{-11}$ m^2 s-1, [81] from which $1/\mathcal{D}_0 = 3.4\times10^{8}$ m^2 s^{-1} and $1/\mathcal{D}_m = 5.9\times10^{10}$ m^2 s^{-1}.

6.4 Conclusions

In this chapter we have explored the ability of nuclear spin relaxation and diffusion measurements to probe surface-adsorbate interactions in a quantitative manner. The nuclear spin relaxation time ratios T_1/T_2 obtained from a homologous series of short-chain primary alcohols imbibed within an industrial silica catalyst support material have been found to exhibit a distinct, positive trend with increasing carbon chain length. T_1/T_2 ratios are well-known to provide a non-destructive indication of the relative surface affinities exhibited by adsorbates within liquid-saturated mesoporous media, and as such indicate a corresponding increase in adsorption energy across this range of molecules. Through a direct comparison with *ab initio* adsorption energy calculations we have provided clear evidence for the existence of a quantitative relationship between this ratio and hydrogen bond-mediated adsorption interactions occurring at the pore surface; basic T_1 measurements were shown to exhibit a qualitative degree of sensitivity to such interactions in Chapter 5. In this chapter we have extended this interpretation to shown that a clear correlation exists between T_1/T_2 values and the adsorption energetics associated with the strongest adsorption sites present. Cyclohexane has also been investigated as a weakly-interacting reference molecule and provides excellent agreement with this correlation, in turn suggesting that insight gained here is applicable during the comparison of adsorbates with differing chemical functionalities. Overall the results detailed here provide substantial validation to previous theoretical insight into the relationship between adsorption energetics and nuclear spin relaxation phenomena occurring at simple, hydroxylated pore surfaces under saturation conditions.

The self-diffusion behaviour of our liquid/silica systems has also been investigated through the application of pulsed field gradient diffusometry measurements. An extensive discussion on how surface interactions cause the self-diffusion characteristics of our imbibed alcohols to differer from that expected from the tortuosity has been given. In particular, the calculation of a relevant surface interaction parameter has illustrated significant agreement between our diffusion, relaxation and adsorption energy results, suggesting that such measurements may

be a potential source of additional insight in terms providing rational connections between adsorption phenomena and mass transfer characteristics.

6.5 References

[1] J. Mitchell, L. F. Gladden, T. C. Chandrasekera and E. J. Fordham, "Low-Field Permanent Magnets for Industrial Process and Quality Control", *Prog. Nucl. Magn. Reson. Spectrosc.*, 2014, **76**, 1–60.

[2] L. F. Gladden and J. Mitchell, "Measuring Adsorption, Diffusion and Flow in Chemical Engineering: Applications of Magnetic Resonance to Porous Media", *New J. Phys.*, 2011, **13**, 035001.

[3] L. F. Gladden, "Magnetic Resonance in Reaction Engineering: Beyond Spectroscopy", *Curr. Opin. Chem. Eng.*, 2013, **2**, 331–337.

[4] S. Godefroy, J.-P. Korb, M. Fleury and R. G. Bryant, "Surface Nuclear Magnetic Relaxation and Dynamics of Water and Oil in Macroporous Media", *Phys. Rev. E*, 2001, **64**, 021605.

[5] C. D'Agostino, Thesis, University of Cambridge, Cambridge, UK, 2011.

[6] C. D'Agostino, J. Mitchell, M. D. Mantle and L. F. Gladden, "Interpretation of NMR Relaxation as a Tool for Characterising the Adsorption Strength of Liquids inside Porous Materials", *Chem. Eur. J.*, 2014, **20**, 13009–13015.

[7] J. Mitchell, T. C. Chandrasekera and L. F. Gladden, "Numerical Estimation of Relaxation and Diffusion Distributions in Two Dimensions", *Prog. Nucl. Magn. Reson. Spectrosc.*, 2012, **62**, 34–50.

[8] D. Weber, J. Mitchell, J. McGregor and L. F. Gladden, "Comparing Strengths of Surface Interactions for Reactants and Solvents in Porous Catalysts Using Two-Dimensional NMR Relaxation Correlations", *J. Phys. Chem. C*, 2009, **113**, 6610–6615.

[9] J. Mitchell, L. M. Broche, T. C. Chandrasekera, D. J. Lurie and L. F. Gladden, "Exploring Surface Interactions in Catalysts Using Low-Field Nuclear Magnetic Resonance", *J. Phys. Chem. C*, 2013, **117**, 17699–17706.

[10] K. Ralphs, C. D'Agostino, R. Burch, S. Chansai, L. F. Gladden, C. Hardacre, S. L. James, J. Mitchell and S. F. R. Taylor, "Assessing the Surface Modifications Following the Mechanochemical Preparation of a Ag/Al2O3 Selective Catalytic Reduction Catalyst", *Catal. Sci. Technol.*, 2014, **4**, 531–539.

[11] A. T. Krzyżak and I. Habina, "Low Field 1H NMR Characterization of Mesoporous Silica MCM-41 and SBA-15 Filled with Different Amount of Water", *Microporous Mesoporous Mater.*, 2016, **231**, 230–239.

[12] C. D'Agostino, S. Chansai, I. Bush, C. Gao, M. D. Mantle, C. Hardacre, S. L. James and L. F. Gladden, "Assessing the Effect of Reducing Agents on the Selective Catalytic Reduction of NOx over Ag/Al2O3 Catalysts", *Catal. Sci. Technol.*, 2016, **6**, 1661–1666.

[13] C. D'Agostino, M. R. Feaviour, G. L. Brett, J. Mitchell, A. P. E. York, G. J. Hutchings, M. D. Mantle and L. F. Gladden, "Solvent Inhibition in the Liquid-Phase Catalytic Oxidation of 1,4-Butanediol: Understanding the Catalyst Behaviour from NMR Relaxation Time Measurements", *Catal. Sci. Technol.*, 2016, **6**, 7896–7901.

[14] C. D'Agostino, G. Brett, G. Divitini, C. Ducati, G. J. Hutchings, M. D. Mantle and L. F. Gladden, "Increased Affinity of Small Gold Particles for Glycerol Oxidation over Au/TiO2 Probed by NMR Relaxation Methods", *ACS Catal.*, 2017, 4235–4241.

[15] D. Espinat, F. Gaulier, F. Norrant, J. Barbier, B. Guichard, M. Rivallan and P. Levitz, "Characterization of Asphaltenes in Solution and Inside the Pores of Catalysts by 1H NMR Relaxometry", *Energy Fuels*, 2017, **31**, 7382–7395.

[16] J. J. Varghese, L. Cao, C. Robertson, Y. Yang, L. F. Gladden, A. A. Lapkin and S. H. Mushrif, "Synergistic Contribution of the Acidic Metal Oxide-Metal Couple and Solvent Environment in the Selective Hydrogenolysis of Glycerol: A Combined Experimental and Computational Study Using ReOx-Ir as the Catalyst", *ACS Catal.*, 2018, DOI: `10.1021/acscatal.8b03079`.

[17] M. Leutzsch, A. J. Sederman, L. F. Gladden and M. D. Mantle, "In Situ Reaction Monitoring in Heterogeneous Catalysts by a Benchtop NMR Spectrometer", *Magn. Reson. Imaging*, 2018, DOI: `10.1016/j.mri.2018.09.006`.

[18] J.-P. Korb, M. W. Hodges, T. Gobron and R. G. Bryant, "Anomalous Surface Diffusion of Water Compared to Aprotic Liquids in Nanopores", *Phys. Rev. E*, 1999, **60**, 3097–3106.

[19] C. I. Robertson, Thesis, University of Cambridge, 2018.

[20] L. Venkataramanan, Y.-Q. Song and M. D. Hurlimann, "Solving Fredholm Integrals of the First Kind with Tensor Product Structure in 2 and 2.5 Dimensions", *IEEE Trans. Signal Process.*, 2002, **50**, 1017–1026.

[21] Y. Q. Song, L. Venkataramanan, M. D. Hürlimann, M. Flaum, P. Frulla and C. Straley, "T1–T2 Correlation Spectra Obtained Using a Fast Two-Dimensional Laplace Inversion", *J. Magn. Reson.*, 2002, **154**, 261–268.

[22] A. N. Tikhonov and V. Y. Arsenin, *Solutions of Ill-Posed Problems*, Winston, 1977.

[23] R. L. Vold, J. S. Waugh, M. P. Klein and D. E. Phelps, "Measurement of Spin Relaxation in Complex Systems", *J. Chem. Phys.*, 1968, **48**, 3831–3832.

[24] J. E. Tanner, "Use of the Stimulated Echo in NMR Diffusion Studies", *J. Chem. Phys.*, 1970, **52**, 2523–2526.

[25] E. O. Stejskal and J. E. Tanner, "Spin Diffusion Measurements: Spin Echoes in the Presence of a Time-Dependent Field Gradient", *J. Chem. Phys.*, 1965, **42**, 288–292.

[26] R. M. Cotts, M. J. R. Hoch, T. Sun and J. T. Markert, "Pulsed Field Gradient Stimulated Echo Methods for Improved NMR Diffusion Measurements in Heterogeneous Systems", *J. Magn. Reson.*, 1989, **83**, 252–266.

[27] F. Stallmach and P. Galvosas, "Spin Echo NMR Diffusion Studies", *Annu. Rep. NMR Spectrosc.*, 2007, **61**, 51–131.

[28] S. J. Clark, M. D. Segall, C. J. Pickard, P. J. Hasnip, M. I. J. Probert, K. Refson and M. C. Payne, "First Principles Methods Using CASTEP", *Zeitschrift für Kristallographie*, 2005, **220**, 567–570.

[29] J. P. Perdew, K. Burke and M. Ernzerhof, "Generalized Gradient Approximation Made Simple", *Phys. Rev. Lett.*, 1996, **77**, 3865–3868.

[30] S. Grimme, "Semiempirical GGA-Type Density Functional Constructed with a Long-Range Dispersion Correction", *J. Comput. Chem.*, 2006, **27**, 1787–1799.

[31] S. Grimme, "Density Functional Theory with London Dispersion Corrections", *WIREs Comput. Mol. Sci.*, 2011, **1**, 211–228.

[32] J. Klimeš and A. Michaelides, "Perspective: Advances and Challenges in Treating van Der Waals Dispersion Forces in Density Functional Theory", *J. Chem. Phys.*, 2012, **137**, 120901.

[33] H. J. Monkhorst and J. D. Pack, "Special Points for Brillouin-Zone Integrations", *Phys. Rev. B*, 1976, **13**, 5188–5192.

[34] B. G. Pfrommer, M. Côté, S. G. Louie and M. L. Cohen, "Relaxation of Crystals with the Quasi-Newton Method", *J. Comput. Phys.*, 1997, **131**, 233–240.

[35] C. D'Agostino, R. D. Armstrong, G. J. Hutchings and L. F. Gladden, "Product Inhibition in Glycerol Oxidation over Au/TiO2 Catalysts Quantified by NMR Relaxation", *ACS Catal.*, 2018, **8**, 7334–7339.

[36] B. J. Stanley and G. Guiochon, "Calculation of Adsorption Energy Distributions of Silica Samples Using Nonlinear Chromatography", *Langmuir*, 1995, **11**, 1735–1743.

[37] M. A. Natal-Santiago and J. A. Dumesic, "Microcalorimetric, FTIR, and DFT Studies of the Adsorption of Methanol, Ethanol, and 2,2,2-Trifluoroethanol on Silica", *J. Catal.*, 1998, **175**, 252–268.

[38] C. D'Agostino, J. Mitchell, L. F. Gladden and M. D. Mantle, "Hydrogen Bonding Network Disruption in Mesoporous Catalyst Supports Probed by PFG-NMR Diffusometry and NMR Relaxometry", *J. Phys. Chem. C*, 2012, **116**, 8975–8982.

[39] J. Mitchell, T. C. Chandrasekera, M. L. Johns, L. F. Gladden and E. J. Fordham, "Nuclear Magnetic Resonance Relaxation and Diffusion in the Presence of Internal Gradients: The Effect of Magnetic Field Strength", *Phys. Rev. E*, 2010, **81**, 026101.

[40] J. Mitchell, T. C. Chandrasekera and L. F. Gladden, "Obtaining True Transverse Relaxation Time Distributions in High-Field NMR Measurements of Saturated Porous Media: Removing the Influence of Internal Gradients", *J. Chem. Phys.*, 2010, **132**, 244705.

[41] J. Mitchell, T. C. Chandrasekera and L. F. Gladden, "Measurement of the True Transverse Nuclear Magnetic Resonance Relaxation in the Presence of Field Gradients", *J. Chem. Phys.*, 2013, **139**, 074205.

[42] M. D. Hürlimann, "Effective Gradients in Porous Media Due to Susceptibility Differences", *J. Magn. Reson.*, 1998, **131**, 232–240.

[43] K. E. Washburn, C. D. Eccles and P. T. Callaghan, "The Dependence on Magnetic Field Strength of Correlated Internal Gradient Relaxation Time Distributions in Heterogeneous Materials", *J. Magn. Reson.*, 2008, **194**, 33–40.

[44] D. Roy, S. Liu, B. L. Woods, A. R. Siler, J. T. Fourkas, J. D. Weeks and R. A. Walker, "Nonpolar Adsorption at the Silica/Methanol Interface: Surface Mediated Polarity and Solvent Density across a Strongly Associating Solid/Liquid Boundary", *J. Phys. Chem. C*, 2013, **117**, 27052–27061.

[45] D. Wu, X. Guo, H. Sun and A. Navrotsky, "Energy Landscape of Water and Ethanol on Silica Surfaces", *J. Phys. Chem. C*, 2015, **119**, 15428–15433.

[46] H. Wu, Q. Gong, D. H. Olson and J. Li, "Commensurate Adsorption of Hydrocarbons and Alcohols in Microporous Metal Organic Frameworks", *Chem. Rev.*, 2012, **112**, 836–868.

[47] M. Schaible, "Empirical Molecular Dynamics Modeling of Silicon and Silicon Dioxide: A Review", *Crit. Rev. Solid State Mater. Sci.*, 1999, **24**, 265–323.

[48] B. M. Lowe, C.-K. Skylaris and N. G. Green, "Acid-Base Dissociation Mechanisms and Energetics at the Silica–Water Interface: An Activationless Process", *J. Colloid Interface Sci.*, 2015, **451**, 231–244.

[49] P. E. M. Lopes, E. Demchuk and A. D. Mackerell, "Reconstruction of the (011) Surface on Alpha-Quartz: A Semiclassical Ab Initio Molecular Dynamics Study", *Int. J. Quantum Chem.*, 2009, **109**, 50–64.

[50] T. Bakos, S. N. Rashkeev and S. T. Pantelides, "Reactions and Diffusion of Water and Oxygen Molecules in Amorphous SiO2", *Phys. Rev. Lett.*, 2002, **88**, 055508.

[51] A. Butenuth, G. Moras, J. Schneider, M. Koleini, S. Köppen, R. Meißner, L. B. Wright, T. R. Walsh and L. C. Ciacchi, "Ab Initio Derived Force-Field Parameters for Molecular Dynamics Simulations of Deprotonated Amorphous-SiO2/Water Interfaces", *Phys. Status Solidi B*, 2012, **249**, 292–305.

[52] F. Musso, M. Sodupe, M. Corno and P. Ugliengo, "H-Bond Features of Fully Hydroxylated Surfaces of Crystalline Silica Polymorphs: A Periodic B3LYP Study", *J. Phys. Chem. C*, 2009, **113**, 17876–17884.

[53] F. Musso, P. Ugliengo, X. Solans-Monfort and M. Sodupe, "Periodic DFT Study of Radical Species on Crystalline Silica Surfaces", *J. Phys. Chem. C*, 2010, **114**, 16430–16438.

[54] F. Musso, P. Mignon, P. Ugliengo and M. Sodupe, "Cooperative Effects at Water–Crystalline Silica Interfaces Strengthen Surface Silanol Hydrogen Bonding. An Ab Initio Molecular Dynamics Study", *Phys. Chem. Chem. Phys.*, 2012, **14**, 10507–10514.

[55] A. Rimola, D. Costa, M. Sodupe, J.-F. Lambert and P. Ugliengo, "Silica Surface Features and Their Role in the Adsorption of Biomolecules: Computational Modeling and Experiments", *Chem. Rev.*, 2013, **113**, 4216–4313.

[56] J. Yang, S. Meng, L. Xu and E. G. Wang, "Water Adsorption on Hydroxylated Silica Surfaces Studied Using the Density Functional Theory", *Phys. Rev. B*, 2005, **71**, 035413.

[57] M. V. Koudriachova, J. V. L. Beckers and S. W. de Leeuw, "Computer Simulation of the Quartz Surface: A Combined Ab Initio and Empirical Potential Approach", *Computational Materials Science*, 2001, **20**, 381–386.

[58] F. Tielens, C. Gervais, J. F. Lambert, F. Mauri and D. Costa, "Ab Initio Study of the Hydroxylated Surface of Amorphous Silica: A Representative Model", *Chem. Mater.*, 2008, **20**, 3336–3344.

[59] J. W. Han, J. N. James and D. S. Sholl, "First Principles Calculations of Methylamine and Methanol Adsorption on Hydroxylated Quartz (0 0 0 1)", *Surf. Sci.*, 2008, **602**, 2478–2485.

[60] T. Björkman, A. Gulans, A. V. Krasheninnikov and R. M. Nieminen, "Are We van Der Waals Ready?", *J. Phys.: Condens. Matter*, 2012, **24**, 424218.

[61] L. Levien, C. T. Prewitt and D. J. Weidner, "Structure and Elastic Properties of Quartz at Pressure", *Am. Mineral.*, 1980, **65**, 920–930.

[62] T. P. M. Goumans, A. Wander, W. A. Brown and C. R. A. Catlow, "Structure and Stability of the (001) Alpha-Quartz Surface", *Phys. Chem. Chem. Phys.*, 2007, **9**, 2146–2152.

[63] N. H. de Leeuw, F. M. Higgins and S. C. Parker, "Modeling the Surface Structure and Stability of Alpha-Quartz", *J. Phys. Chem. B*, 1999, **103**, 1270–1277.

[64] D. Sholl and J. A. Steckel, *Density Functional Theory: A Practical Introduction*, John Wiley & Sons, 2011.

[65] J. C. Boettger, "Nonconvergence of Surface Energies Obtained from Thin-Film Calculations", *Phys. Rev. B*, 1994, **49**, 16798–16800.

[66] W. Sun and G. Ceder, "Efficient Creation and Convergence of Surface Slabs", *Surf. Sci.*, 2013, **617**, 53–59.

[67] A. Kiejna, T. Pabisiak and S. W. Gao, "The Energetics and Structure of Rutile TiO2(110)", *J. Phys.: Condens. Matter*, 2006, **18**, 4207.

[68] G.-M. Rignanese, J.-C. Charlier and X. Gonze, "First-Principles Molecular-Dynamics Investigation of the Hydration Mechanisms of the (0001) Alpha-Quartz Surface", *Phys. Chem. Chem. Phys.*, 2004, **6**, 1920–1925.

[69] M. T. Nayakasinghe, N. Sivapragasam and U. Burghaus, "Adsorption of Alcohols on a Two-Dimensional SiO2 Single Crystal – Alcohol Adsorption on Silicatene", *Chem. Phys. Lett.*, 2017, **689**, 105–110.

[70] S. N. Lanin, E. V. Vlasenko, N. V. Kovaleva and F. T. Zung, "The Adsorption Properties of Titanium Dioxide", *Russ. J. Phys. Chem.*, 2008, **82**, 2152–2155.

[71] K. K. Kolasinski, *Surface Science: Foundations of Catalysis and Nanoscience*, Wiley-Blackwell, Chichester, West Sussex ; Hoboken, N.J, 3rd Edition, 2012.

[72] G. A. Somorjai and Y. Li, *Introduction to Surface Chemistry and Catalysis*, Wiley-Blackwell, Hoboken, N.J, 2nd edition, 2010.

[73] K. Miyabe and G. Guiochon, "Surface Diffusion in Reversed-Phase Liquid Chromatography", *J. Chromatogr. A*, 2010, **1217**, 1713–1734.

[74] I. Medveď and R. Černý, "Surface Diffusion in Porous Media: A Critical Review", *Microporous Mesoporous Mater.*, 2011, **142**, 405–422.

[75] D. A. King, "Surface Diffusion of Adsorbed Species: A Review", *J. Vac. Sci. Technol.*, 1980, **17**, 241–247.

[76] P. J. McDonald, J.-P. Korb, J. Mitchell and L. Monteilhet, "Surface Relaxation and Chemical Exchange in Hydrating Cement Pastes: A Two-Dimensional NMR Relaxation Study", *Phys. Rev. E*, 2005, **72**, 011409.

[77] N. Bloembergen, E. M. Purcell and R. V. Pound, "Relaxation Effects in Nuclear Magnetic Resonance Absorption", *Phys. Rev.*, 1948, **73**, 679–712.

[78] M. D. Mantle, D. I. Enache, E. Nowicka, S. P. Davies, J. K. Edwards, C. D'Agostino, D. P. Mascarenhas, L. Durham, M. Sankar, D. W. Knight, L. F. Gladden, S. H. Taylor and G. J. Hutchings, "Pulsed-Field Gradient NMR Spectroscopic Studies of Alcohols in Supported Gold Catalysts", *J. Phys. Chem. C*, 2011, **115**, 1073–1079.

[79] R. Valiullin, *Diffusion NMR of Confined Systems: Fluid Transport in Porous Solids and Heterogeneous Materials*, Royal Society of Chemistry, 2016.

[80] W. S. Price, *NMR Studies of Translational Motion: Principles and Applications*, Cambridge University Press, Cambridge ; New York, 1 edition, 2009.

[81] D. Weber, A. J. Sederman, M. D. Mantle, J. Mitchell and L. F. Gladden, "Surface Diffusion in Porous Catalysts", *Phys. Chem. Chem. Phys.*, 2010, **12**, 2619–2624.

[82] M. Schönhoff and O. Söderman, "PFG-NMR Diffusion as a Method To Investigate the Equilibrium Adsorption Dynamics of Surfactants at the Solid/Liquid Interface", *J. Phys. Chem. B*, 1997, **101**, 8237–8242.

[83] R. Valiullin, P. Kortunov, J. Kärger and V. Timoshenko, "Surface Self-Diffusion of Organic Molecules Adsorbed in Porous Silicon", *J. Phys. Chem. B*, 2005, **109**, 5746–5752.

[84] T. G. A. Youngs, D. Weber, L. F. Gladden and C. Hardacre, "Liquid Structure and Dynamics of Aqueous Isopropanol over Gamma-Alumina", *J. Phys. Chem. C*, 2009, **113**, 21342–21352.

[85] H. Komiyama and J. M. Smith, "Surface Diffusion in Liquid-Filled Pores", *AIChE J.*, 1974, **20**, 1110–1117.

[86] M. Holz, S. R. Heil and A. Sacco, "Temperature-Dependent Self-Diffusion Coefficients of Water and Six Selected Molecular Liquids for Calibration in Accurate 1H NMR PFG Measurements", *Phys. Chem. Chem. Phys.*, 2000, **2**, 4740–4742.

Chapter 7

Summary and outlook

7.1 Summary

By combining a thorough and wide-ranging theoretical foundation with a series of novel experiments and simulations, this thesis has provided an extensive exploration of the utility of NMR for probing molecular dynamics and adsorption phenomena occurring at the catalyst-liquid interface. The following summarises the main achievements of Chapters 2 – 6 of this Thesis:

Chapter 2 provided a basic introduction to heterogeneous catalysis and detailed a series of important energetic phenomena and molecular transport processes which dictate the nature of chemical transformations at solid surfaces. The need for improved surface-sensitive analysis techniques for the study of buried interfaces ubiquitous with optically opaque porous media was introduced, facilitating the question of how the measurement of nuclear spin dynamics might provide useful insight.

Chapter 3 provided extensive theoretical background to the phenomena of nuclear magnetic resonance, and illustrated a range of experimental pulse sequences for the determination of chemical structure, nuclear spin relaxation characteristics and molecular self-diffusion coefficients.

Chapter 4 provided a detailed and in-depth review of the relevant theories and approximations required to understand how the nuclear spin relaxation and diffusion characteristics of liquids imbibed within mesoporous solids can exhibit significant sensitivity to surface phenomena.

Chapter 5 detailed the application of longitudinal nuclear spin relaxation (T_1) measurements as a simple probe of adsorbate mobility within a range of mesoporous oxides regularly employed as catalysts and catalyst support materials. The experimental results detailed within this chapter compared the spin dynamics of methanol – investigated here as a prototypical polar molecule of relevance to liquid-phase catalysis – within hydroxylated pores systems to within materials in which a simple surface passivation treatment had been applied to reduce the surface hydroxyl density. The observed T_1 characteristics illustrate that the mobility of methanol within the adsorbed surface layer is clearly sensitive to this surface modification,

and tends towards the dynamics of the unrestricted bulk liquids upon suppression of surface-adsorbate hydrogen bonding interactions. Overall, the results and discussion described within this chapter demonstrate the significant potential of nuclear spin relaxation measurements for the non-invasive evaluation of molecular dynamics associated with surface-adsorbate interactions. This chapter provides the first direct experimental validation that surface relaxation observed within hydroxylated oxide materials is determined by hydrogen bonding interactions with the pore surface.

Chapter 6 provided a novel exploration of the relationship between nuclear spin dynamics and the energetics associated with adsorption interactions at the solid-liquid interface. The majority of this chapter focused on a discussion of the ratio of nuclear spin relaxation time constants T_1/T_2, which is widely considered a probe of surface affinity. Using a recently developed two-dimensional pulse sequence designed to suppress any effects of J-coupling on our measurements, values of the ratio T_1/T_2 were obtained for a homologous series of primary alcohols within an industrial silica catalyst support; cyclohexane was also investigated to provide weakly-interacting reference data. The results of these relaxation experiments suggest that the surface interaction strength of short-chain primary alcohols increases with increasing carbon chain length. Extensive *ab initio* molecular modelling was found to agree with this finding. The results presented in this chapter provide strong evidence that the ratio T_1/T_2 provides a quantitative indication of adsorption energetics associated with the strongest adsorption sites at the pore surface. Importantly, this finding provides significant validation to previous theoretical predictions on the relationship between T_1/T_2 and adsorption energetics. It should be highlighted that the results and discussion within this chapter represent the first instance in which nuclear spin relaxation and *ab initio* adsorption energy measurements have been compared and contrasted. Further investigation then considered the nature of molecular self-diffusion within these systems; it was found that the ratio of unrestricted-to-restricted self-diffusion coefficients exhibits notable sensitivity to adsorption phenomena, implying the future potential of such measurements to yield discernible insight into the relationship between adsorption processes and mass transport characteristics.

7.2 Future work

Insight obtained during the completion of this thesis leads the author to consider the following as potential areas of future investigation:

Surface relaxation trends of complex molecules

The adsorbates considered in this work took the form of simple, short-chain primary alcohols and cyclohexane. This was of course intentional and facilitated the comparison of our experimental results with state-of-the-art *ab initio* adsorption energy calculations (Chapter 6), as well as allowing us to perform analysis of molecular tumbling based on the simple BPP interpretation of nuclear spin relaxation (Chapter 5). While these liquids are of direct relevance to solvated heterogeneous reaction systems, further investigations should consider the robustness of the trends observed here when investigating the nuclear spin characteristics of more complex adsorbates. For instance, it is known from our discussion of the Lipari-Szabo spectral density function that internal motion can influence the relaxation characteristics of molecular species. This has recently been confirmed through extensive molecular dynamics simulations of long-chain hydrocarbons. [1] It follows that the T_1/T_2 ratio of large, flexible adsorbates may not simply be a function of adsorption interaction strength; rather, counter-intuitive relationships may be observed due to competition between surface-adsorbate relaxation phenomena and complex intramolecular spin dynamics. It is suspected that the partial non-conformity of our 1-butanol data in Figure 6.23 to the strong linear correlation presented by smaller alcohols may emerge from such effects, although this has not been investigated in detail. It is likely that any such effects will be more prominent in the measurement of T_1 than in T_2 given the sensitivity of the spin-lattice relaxation time constant to rapid motion; as such, it may be the case that such effects can be suppressed by performing relaxation measurements at appropriately low magnetic field strengths.

Characterisation of nuclear spin dynamics at complex pore surfaces.

While significant pore surface modifications were performed in Chapter 5, the functionality-mobility relationship of our methanol adsorbate within these structures was studied in only a qualitative manner. While this was sufficient to establish that the nuclear spin relaxation characteristics of polar hydroxylated adsorbates exhibit significant sensitivity to the presence – or lack – of surface-adsorbate hydrogen bonding interactions, it would be interesting to perform a more quantitative series of experiments on systems exhibiting well-defined functionalised pore surfaces. While the experiments detailed in Chapter 5 were performed at high magnetic field strength, future investigations performed at low or intermediate field would be advantageous given the sensitivity of surface relaxation dynamics to the surface spin density (see Equations 4.32 and 4.33). Such insight would be highly applicable to the evaluation and development of surface-functionalised templated silica catalysts, which are favourable due to highly tunable pore morphology and surface activity. [2–5] This also leads us to the consideration of how $T_1 - T_2$ relaxation correlation measurements might be used for the interpretation of adsorption phenomena occurring within such materials. Indeed, it is of significant interest to investigate whether our empirically-derived relationship between adsorption energetics and the ratio T_1/T is robust in the presence of significant covalent modifications of the pore surface. Care would also need to be taken that any changes to pore size and structure which occur as a result of the surface functionalisation process do not lead to notable changes in internal gradient effects, leading to misinterpretation of trends between pore functionality and apparent surface dynamics.

Adsorbate fingerprinting

From the point of view of developing multidimensional relaxation correlation techniques as a formal surface science the observation in Chapter 6 (and Appendix F) that $T_1 - T_2$ correlation plots of liquid-saturated mesoporous media can exhibit discrete correlation peaks associated with different ^{1}H environments within the same molecule highlights the potential application of such measurements for adsorbate fingerprinting. Recent developments in pulse sequence design – i.e. the

implementation of the inversion recovery - PROJECT sequence for the suppression of J-coupling artefacts [6] – mean that an extensive range of adsorbates exhibiting different chemical moieties might by considered and an investigation undertaken as to whether predicable characteristics are found to appear across a range of relevant correlation measurements. While we note that the observation of high T_1/T_2 peaks can be impeded by hardware limitations, modern bench-top NMR spectrometers are often capable implementing extremely short $\leq 500\mu$s echo times for the quantification of rapid T_2 relaxation.

Advanced molecular simulations

Recent advances have illustrated the significant potential of molecular dynamics simulations for the assessment of nuclear spin relaxation phenomena. Such techniques involve explicit calculation of the autocorrelation function; as such, the need to assume a particular spectral density for the interpretation of T_1 and T_2 characteristics is removed. Development of relevant molecular dynamics simulations of fluids within porous structures is currently led by Faux *et al.*. [7–12] While these simulations have thus far centred on the understanding of the relaxation characteristics of water, there is significant potential for the extension of such studies to the evaluation of organic liquids. Such simulations also provide insight into the diffusion characteristics of confined species, and as such might provide insight into the strong correlation observed between our self-diffusion results and surface phenomena in Chapter 6.

7.3 References

[1] P. M. Singer, D. Asthagiri, Z. Chen, A. Valiya Parambathu, G. J. Hirasaki and W. G. Chapman, "Role of Internal Motions and Molecular Geometry on the NMR Relaxation of Hydrocarbons", *J. Chem. Phys.*, 2018, **148**, 164507.

[2] M. M. Aboelhassan, A. F. Peixoto and C. Freire, "Sulfonic Acid Functionalized Silica Nanoparticles as Catalysts for the Esterification of Linoleic Acid", *New J. Chem.*, 2017, **41**, 3595–3605.

[3] T. Yokoi, Y. Kubota and T. Tatsumi, "Amino-Functionalized Mesoporous Silica as Base Catalyst and Adsorbent", *Appl. Catal., A*, 2012, **421-422**, 14–37.

[4] J. C. Manayil, V. C. dos Santos, F. C. Jentoft, M. Granollers Mesa, A. F. Lee and K. Wilson, "Octyl Co-Grafted PrSO3H/SBA-15: Tunable Hydrophobic Solid Acid Catalysts for Acetic Acid Esterification", *ChemCatChem*, 2017, **9**, 2231–2238.

[5] I. Ogino, Y. Suzuki and S. R. Mukai, "Esterification of Levulinic Acid with Ethanol Catalyzed by Sulfonated Carbon Catalysts: Promotional Effects of Additional Functional Groups", *Catal. Today*, 2018, **314**, 62–69.

[6] C. I. Robertson, Thesis, University of Cambridge, 2018.

[7] D. A. Faux, P. J. McDonald, N. C. Howlett, J. S. Bhatt and S. V. Churakov, "Nuclear Magnetic Resonance Relaxometry of Water in Two and Quasi-Two Dimensions", *Phys. Rev. E*, 2013, **87**, 062309.

[8] J. S. Bhatt, P. J. McDonald, D. A. Faux, N. C. Howlett and S. V. Churakov, "NMR Relaxation Parameters from Molecular Simulations of Hydrated Inorganic Nanopores", *Int. J. Quantum Chem.*, 2014, **114**, 1220–1228.

[9] D. A. Faux, S.-H. P. Cachia, P. J. McDonald, J. S. Bhatt, N. C. Howlett and S. V. Churakov, "Model for the Interpretation of Nuclear Magnetic Resonance Relaxometry of Hydrated Porous Silicate Materials", *Phys. Rev. E*, 2015, **91**, 032311.

[10] D. A. Faux and P. J. McDonald, "Explicit Calculation of Nuclear-Magnetic-Resonance Relaxation Rates in Small Pores to Elucidate Molecular-Scale Fluid Dynamics", *Phys. Rev. E*, 2017, **95**, 033117.

[11] D. A. Faux, P. J. McDonald and N. C. Howlett, "Nuclear-Magnetic-Resonance Relaxation Due to the Translational Diffusion of Fluid Confined to Quasi-Two-Dimensional Pores", *Phys. Rev. E*, 2017, **95**, 033116.

[12] D. A. Faux and P. J. McDonald, "Nuclear-Magnetic-Resonance Relaxation Rates for Fluid Confined to Closed, Channel, or Planar Pores", *Phys. Rev. E*, 2018, **98**, 063110.

Appendix A

The thermodynamics of activation energies

It is of significant utility to perform a direct comparison between empirical activation energies and thermodynamic expressions. Let us consider the process

$$\mathrm{A} + \mathrm{B} \underset{k_-}{\overset{k_+}{\rightleftharpoons}} [\mathrm{A} \cdots \mathrm{B}]^{\ddagger} \rightarrow \mathrm{AB}. \tag{A.1}$$

Equilibrium between reagents and the transition state $[\mathrm{A} \cdots \mathrm{B}]^{\ddagger}$ is quantified by the equilibrium constant $K^{\ddagger}$, which relates to the concentrations of A, B and $[\mathrm{A} \cdots \mathrm{B}]^{\ddagger}$ as

$$K^{\ddagger} = \frac{c_{\ddagger}}{c_{\mathrm{A}} c_{\mathrm{B}}}, \tag{A.2}$$

where c_j indicates concentration terms, and the Gibbs free energy of activation $\Delta^{\ddagger}G$ according to the van t'Hoff Equation

$$\Delta^{\ddagger}G = -RT \ln\left(K^{\ddagger}\right), \tag{A.3}$$

where R is the gas constant and T is the absolute temperature. The rate constant for the forward reaction k_+ may be expressed by either Arrhenius-type or Erying-type

expressions. The Eyring Equation for this rate constant is

$$k_+ = \kappa \frac{k_B T}{h} \exp\left(\frac{-\Delta^\ddagger G}{RT}\right) \tag{A.4a}$$

$$= \kappa \frac{k_B T}{h} \exp\left(\frac{\Delta^\ddagger S}{R}\right) \exp\left(\frac{-\Delta^\ddagger H}{RT}\right), \tag{A.4b}$$

where κ is the transmission coefficient, k_B is the Boltzmann constant, and $\Delta^\ddagger S$ and $\Delta^\ddagger H$ are the entropy and enthalpy of activation, respectively. The Arrhenius Equation takes the form

$$k_+ = \mathcal{A} \exp\left(\frac{-E_a}{RT}\right), \tag{A.5}$$

where $\mathcal{A}$ is a pre-exponential factor and E_a is an empirically observed activation energy.

To compare E_a with the thermodynamic quantities within the Eyring Equation we must consider the natural log forms of these expressions,

$$\ln(k_+) = \ln\left(\frac{\kappa k_B T}{h}\right) + \frac{\Delta^\ddagger S}{R} - \frac{\Delta^\ddagger H}{RT}, \tag{A.6}$$

$$\ln(k_+) = \ln(\mathcal{A}) - \frac{E_a}{RT}. \tag{A.7}$$

Differentiation of Equation A.6 with respect to $1/T$ gives

$$\frac{d\ \ln(k_+)}{d\ T^{-1}} = \frac{1}{T} + \frac{\Delta^\ddagger H}{RT^2}, \tag{A.8}$$

while differentiation of Equation A.7 with respect to $1/T$ gives

$$\frac{d\ \ln(k_+)}{d\ T^{-1}} = \frac{E_a}{RT^2}. \tag{A.9}$$

Combining these expressions we obtain

$$\frac{E_a}{RT^2} = \frac{1}{T} + \frac{\Delta^\ddagger H}{RT^2}, \tag{A.10}$$

and simple rearrangement yields

$$\boxed{E_a = \Delta^{\ddagger}H + RT.} \tag{A.11}$$

This expression provides a direct relationship between the enthalpy of activation and activation energy. If we then input this result into Equation A.7 and equate it with Equation A.6 we obtain

$$\ln(\mathcal{A}) - \frac{\Delta^{\ddagger}H + RT}{RT} = \ln\left(\frac{\kappa k_B T}{h}\right) + \frac{\Delta^{\ddagger}S}{R} - \frac{\Delta^{\ddagger}H}{RT}, \tag{A.12}$$

from which rearrangement yields

$$\boxed{\mathcal{A} = e\kappa\frac{k_B T}{h}\exp\left(\frac{\Delta^{\ddagger}S}{R}\right).} \tag{A.13}$$

Appendix B

Density operator identities

Table B.1: This table shows the identities required to solve the density operator expressions in Chapter 3

Initial state	Rotation axis	Equation of motion	Solution
I_x	I_y	$\exp(-i\theta I_y)I_x \exp(i\theta I_y)$	$I_x \cos(\theta) - I_z \sin(\theta)$
I_x	I_z	$\exp(-i\theta I_y)I_x \exp(i\theta I_y)$	$I_x \cos(\theta) + I_y \sin(\theta)$
I_y	I_x	$\exp(-i\theta I_y)I_y \exp(i\theta I_y)$	$I_y \cos(\theta) + I_z \sin(\theta)$
I_y	I_z	$\exp(-i\theta I_y)I_y \exp(i\theta I_y)$	$I_y \cos(\theta) - I_x \sin(\theta)$
I_z	I_x	$\exp(-i\theta I_y)I_z \exp(i\theta I_y)$	$I_z \cos(\theta) - I_y \sin(\theta)$
I_z	I_y	$\exp(-i\theta I_y)I_z \exp(i\theta I_y)$	$I_z \cos(\theta) + I_x \sin(\theta)$
I_{jx}	$I_{jz}I_{kz}$	$\exp(-i\theta I_{jz}I_{kz})I_{jx} \exp(i\theta I_{jz}I_{kz})$	$I_{jx} \cos\left(\frac{1}{2}\theta\right) + 2I_{jy}I_{kz} \sin\left(\frac{1}{2}\theta\right)$
I_{jy}	$I_{jz}I_{kz}$	$\exp(-i\theta I_{jz}I_{kz})I_{jy} \exp(i\theta I_{jz}I_{kz})$	$I_{jy} \cos\left(\frac{1}{2}\theta\right) - 2I_{jx}I_{kz} \sin\left(\frac{1}{2}\theta\right)$
$2I_{jx}I_{kz}$	$I_{jz}I_{kz}$	$\exp(-i\theta I_{jz}I_{kz})\{2I_{jx}I_{kz}\} \exp(i\theta I_{jz}I_{kz})$	$2I_{jx}I_{kz} \cos\left(\frac{1}{2}\theta\right) + I_{jy} \sin\left(\frac{1}{2}\theta\right)$
$2I_{jy}I_{kz}$	$I_{jz}I_{kz}$	$\exp(-i\theta I_{jz}I_{kz})\{2I_{jy}I_{kz}\} \exp(i\theta I_{jz}I_{kz})$	$2I_{jy}I_{kz} \cos\left(\frac{1}{2}\theta\right) - I_{jx} \sin\left(\frac{1}{2}\theta\right)$
$2I_{jz}I_{kx}$	$I_{jz}I_{kz}$	$\exp(-i\theta I_{jz}I_{kz})\{2I_{jz}I_{kx}\} \exp(i\theta I_{jz}I_{kz})$	$2I_{jz}I_{kx} \cos\left(\frac{1}{2}\theta\right) + I_{ky} \sin\left(\frac{1}{2}\theta\right)$
$2I_{jz}I_{ky}$	$I_{jz}I_{kz}$	$\exp(-i\theta I_{jz}I_{kz})\{2I_{jz}I_{ky}\} \exp(i\theta I_{jz}I_{kz})$	$2I_{jz}I_{ky} \cos\left(\frac{1}{2}\theta\right) - I_{kx} \sin\left(\frac{1}{2}\theta\right)$

Appendix C

A biphasic fast-exchange expression for nuclear spin relaxation

Let a given liquid-saturated pore structure have the following characteristic properties:

- Surface area, S (m^2 g^{-1})
- Modal Pore volume, V_p (m^3 g^{-1})
- Mean surface layer thickness, δ (m)
- Molecular volume, V_m (m^3 $molecule^{-1}$)

Under the conditions of biphasic fast exchange, the observed relaxation rates R_{obs} are proposed to be a weighted average of bulk (non-adsorbed) and surface contributions,

$$R_{obs} = P_{bulk}R_{bulk} + P_{surf}R_{surf}. \tag{C.1}$$

Here, P_{bulk} and P_{surf} describe the fractions of molecules in the bulk and within the adsorbed surface layer, respectively, in which the relaxation rates proceed at R_{bulk} and R_{surf}, respectively. We make the assumption that no other spin populations are present, such that $P_{bulk} + P_{surf} = 1$.

Here we attempt to establish an analytical expression for P_{surf}, and therefore for R_{obs}. For a given pore system saturated with $N = N_{surf} + N_{bulk}$ molecules (molecules g^{-1}), N_{surf} molecules will be adsorbed leaving N_{bulk} away from the pore walls. P_{surf} therefore takes the initial form

$$P_{surf} = \frac{N_{surf}}{N} = \frac{N_{surf}}{N_{surf} + N_{bulk}}, \tag{C.2}$$

where the number of adsorbed molecules per unit volume may be evaluated as

$$\frac{N_{surf}}{V_p} = \frac{S\delta}{V_p}\frac{1}{V_m}. \tag{C.3}$$

It is therefore clear that

$$N_{surf} = \frac{S\delta}{V_m}. \tag{C.4}$$

The evaluation of N is simply

$$N = \frac{V_p}{V_m}, \tag{C.5}$$

such that

$$P_{surf} = \frac{S\delta V_m}{V_p V_m} = \frac{S\delta}{V_p}, \tag{C.6}$$

and

$$P_{bulk} = 1 - \frac{S\delta}{V_p}. \tag{C.7}$$

The correct analytical form of Equation C.1 is therefore

$$\boxed{R_{obs} = \left(1 - \frac{S\delta}{V_p}\right)R_{bulk} + \frac{S\delta}{V_p}R_{surf}.} \tag{C.8}$$

Appendix D

Supplementary DRIFTS data

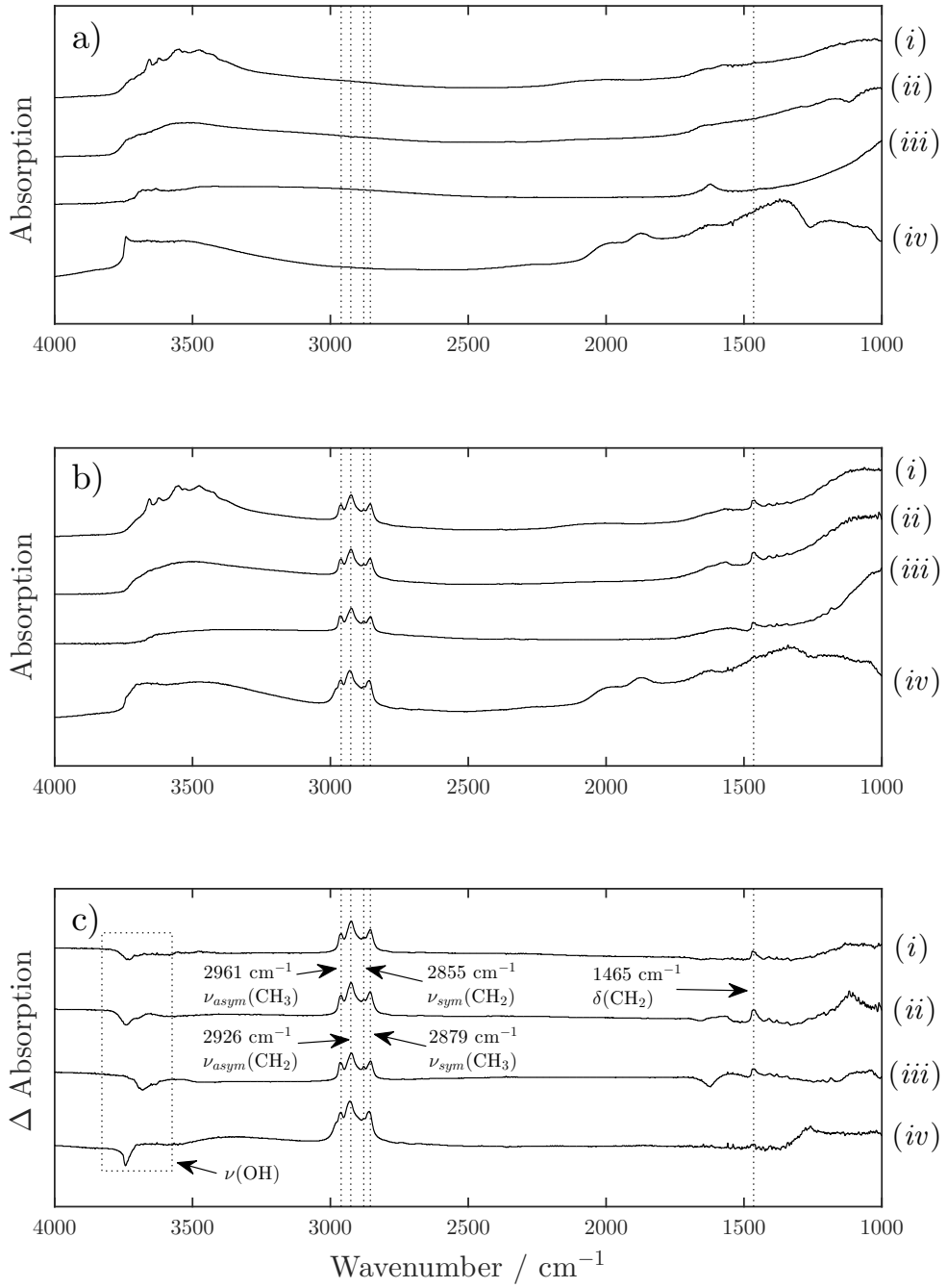

Figure D.1: Supplementary diffuse reflectance infrared data. Panels a) and b) show spectra acquired from unfunctionalised and TEOS-functionalised oxides, respectively, while panel c) illustrates the difference upon functionalisation. Datasets (*i*), (*ii*), (*iii*) and (*iv*) indicate data acquired from γ-Al_2O_3, θ-Al_2O_3, Anatase-TiO_2 and SiO_2, respectively.

Appendix E

Electronic structure theory

E.1 Molecular quantum theory

E.1.1 Eigenvalue equations

Let us briefly introduce the concept of an eigenvalue equation. Such expressions are central to the mathematical description of quantum mechanical phenomena and take the general form

$$\mathcal{A}\mathcal{F} = \alpha\mathcal{F}. \tag{E.1}$$

Here $\mathcal{A}$ is an operator and represents an observable (or measurable) quantity, such as energy, position or momentum. The value of this observable, represented here by the eigenvalue α, is retrieved through the operation of $\mathcal{A}$ on the eigenfunction $\mathcal{F}$, which is a function that describes the system under study. This operation produces the relevant eigenvalue multiplied by the original eigenfunction.

E.1.2 The wavefunction description

The quantum dynamics of a time-independent, position-dependent system are described their wavefunction (or statefunction) $\Psi(\mathbf{r})$. This function is related to the probability of finding a particle at a certain location $\mathbf{r} = (x, y, z)^{(1)}$ according to

$$P(\mathbf{r}) = \int_{\mathbf{r}}^{\mathbf{r}+d\mathbf{r}} \Psi^*(\mathbf{r})\Psi(\mathbf{r})\, d\mathbf{r}, \tag{E.2}$$

[1] As previously defined in Chapter 3 this thesis employs the mathematical convention that $(a, b, c) = a\hat{\mathbf{i}} + b\hat{\mathbf{j}} + c\hat{\mathbf{k}}$, where $\hat{\mathbf{i}}$, $\hat{\mathbf{j}}$ and $\hat{\mathbf{k}}$ are unit vectors in the x, y and z directions.

and is usually considered to be normalised such that

$$\int \Psi^*(\mathbf{r})\Psi(\mathbf{r})\, d\mathbf{r} = 1, \tag{E.3}$$

where the integral is over all of $\mathbf{r}$. Here Ψ^* is the complex conjugate of Ψ and allows us to consider mathematically complex wavefunctions.

For a given many-body system, such as a molecule or crystalline solid consisting of M nuclei surrounded by N electrons, we may extend this concept to that of a many-body wavefunction $\Psi(\{\mathbf{R}\},\{\mathbf{r}\})$, which is a function of both nuclear ($\{\mathbf{R}\} = \mathbf{R}_1, \mathbf{R}_2, ..., \mathbf{R}_M$) and electronic ($\{\mathbf{r}\} = \mathbf{r}_1, \mathbf{r}_2, ..., \mathbf{r}_N$) spatial coordinates. For stationary (time-independent) states, which are often the states of interest, this wavefunction is related to the energy of the system *via* the time-independent, many-body Schrödinger equation,

$$\mathcal{H}\Psi(\{\mathbf{R}\},\{\mathbf{r}\}) = E\Psi(\{\mathbf{R}\},\{\mathbf{r}\}). \tag{E.4}$$

This is an example of an eigenvalue equation; the Hamiltonian Operator (or Energy Operator) $\mathcal{H}$ operates on the wavefunction to produce the observable eigenvalue E, the energy of the system. The total Hamiltonian $\mathcal{H}$ has the form [1]

$$\mathcal{H} = \mathcal{T}_e + \mathcal{T}_n + \mathcal{V}_{nn} + \mathcal{V}_{ee} + \mathcal{V}_{en}, \tag{E.5}$$

and comprises kinetic energy operators ($\mathcal{T}$) for the constituent electrons (e) and nuclei (n), as well as potential energy operators ($\mathcal{V}$) for the electron-electron, electron-nuclear and nuclear-nuclear interactions These operators take the form

$$\mathcal{T}_e = -\sum_j^N \frac{\hbar^2}{2m_e}\nabla_j^2, \tag{E.6a}$$

$$\mathcal{T}_n = -\sum_J^M \frac{\hbar^2}{2m_J}\nabla_J^2, \tag{E.6b}$$

$$\mathcal{V}_{nn} = \frac{1}{2}\sum_{I\neq J}^M \frac{e^2}{4\pi\epsilon_0}\frac{Z_J Z_K}{|\mathbf{R}_J - \mathbf{R}_K|}, \tag{E.6c}$$

$$\mathcal{V}_{ee} = \frac{1}{2}\sum_{j\neq k}^N \frac{e^2}{4\pi\epsilon_0}\frac{1}{|\mathbf{r}_j - \mathbf{r}_k|}, \tag{E.6d}$$

$$\mathcal{V}_{en} = -\sum_j^N\sum_J^M \frac{e^2}{4\pi\epsilon_0}\frac{Z_J}{|\mathbf{r}_j - \mathbf{R}_J|}, \tag{E.6e}$$

where $\hbar = h/2\pi$ is the reduced form of Plank's constant, with $h = 6.626070 \times 10^{-34}$ J s, $m_e = 9.10938 \times 10^{-31}$ kg is the electron mass, m_J and Z_J are the mass and charge of the Jth nucleus and $\epsilon_0 = 8.85410\times10^{-12}$ s^4 A^2 m^{-2} kg^{-1} is the vacuum permittivity. $\nabla^2 = \nabla\cdot\nabla$ is the Laplacian operator where

$$\nabla = \left(\frac{\partial}{\partial x}, \frac{\partial}{\partial y}, \frac{\partial}{\partial z}\right), \tag{E.7}$$

and is directly related to the quantum mechanical momentum operator $\mathcal{P} = -i\hbar\nabla$.

E.1.3 The Born-Oppenheimer approximation

As the mass of even the lightest nucleus (the proton) is over 1000 times heavier than that of the electron, the time-scales of nuclear and electronic motion are significantly different. In fact electrons can be considered to respond almost instantaneously to nuclear motion; in this case the dependence of the many-body wavefunction on both nuclear and electronic dynamics can be decoupled,

$$\Psi(\{\mathbf{R}\},\{\mathbf{r}\}) \approx \psi_n(\{\mathbf{R}\})\psi_e(\{\mathbf{r}\}). \tag{E.8}$$

This concept is known as the Born-Oppenheimer approximation and allows us to consider electronic and nuclear motion separately. [2]

E.1.4 The electronic Schrödinger equation

As a result of the Born-Oppenheimer approximation we may neglect second term in Equation E.5 and consider electron dynamics within a frozen nuclear configuration. This allows us to state a purely electronic Schrödinger equation,

$$[\mathcal{H}_e + \mathcal{V}_{nn}]\psi_e(\{\mathbf{r}\}) = [E_e + \upsilon_{nn}]\psi_e(\{\mathbf{r}\}). \tag{E.9}$$

Here $\mathcal{H}_e$ is the electronic Hamiltonian and corresponds with the electronic energy E_e. The $\mathcal{V}_{nn}$ term remains only to provide a constant nuclear-nuclear potential ν_{nn} across the system. From hereon in we will consider only the electronic energy $E_e = E_{total} - \upsilon_{nn}$, whose expectation value may be obtained from the electronic Hamiltonian according to

$$E_e = \int \psi_e^*(\{\mathbf{r}\})\ \mathcal{H}_e\ \psi_e(\{\mathbf{r}\})\ d\{\mathbf{r}\}. \tag{E.10}$$

It is typical to express the electronic Hamiltonian in atomic (or Hartree) units, where we set the electronic mass m_e and charge e, as well as the reduced Plank constant $\hbar$ and the permittivity of free space ϵ_0 multiplied by 4π, to 1; $m_e = e = \hbar = 4\pi\epsilon_0 = 1$. In this case we find $\frac{e^2}{4\pi\varepsilon_0} = \hbar^2 = 1$, significantly simplifying the notation required for the following discussion. Within this formalism the electronic Hamiltonian for a many-electron system has the form

$$\begin{aligned}\mathcal{H}_e &= \mathcal{T}_e + \mathcal{V}_{ee} + \mathcal{V}_{en} \\ &= -\frac{1}{2}\sum_{j}^{N}\nabla_j^2 + \frac{1}{2}\sum_{j\neq k}^{N}\frac{1}{|\mathbf{r}_j - \mathbf{r}_k|} - \sum_{j}^{N}\sum_{J}^{M}\frac{Z_J}{|\mathbf{r}_j - \mathbf{R}_J|}.\end{aligned} \tag{E.11}$$

Unfortunately as the number of electrons within a given many-body system is usually significant ($\sim 10^{23}$), it becomes impossible to solve Equation E.9 for any but the most basic one- and two-electron systems due to the complex nature of the electron-electron potential operator $\mathcal{V}_{ee}$; this is known as the many-body problem and requires approximate methods – such as density functional theory (DFT) – to solve. [3]

E.2 Hartree-Fock theory

Before we detail the basic underpinnings of DFT it is useful to consider a simple wavefunction-based method known as Hartree-Fock (HF) theory. Let us temporarily neglect $\mathcal{V}_{ee}$ altogether and consider a system comprised of non-interacting electrons; the non-interacting nature means we may consider the energetics of each electron individually through a single-electron Hamiltonian $h(\mathbf{r})$ of the form

$$h(\mathbf{r}) = -\frac{1}{2}\nabla^2 - \sum_J^M \frac{Z_J}{|\mathbf{r} - \mathbf{R}_J|}. \tag{E.12}$$

From here we may envision a set of single-particle Schrödinger-like equations of the form

$$h(\mathbf{r})\phi_a(\mathbf{r}) = \varepsilon_a \phi_a(\mathbf{r}), \tag{E.13}$$

where, in a first approximation, the single-electron wavefuctions (or orbitals) $\phi_a(\mathbf{r}_j)$ $(a = 1, 2, ..., N; j = 1, 2, ..., N)$ can be considered to follow the Hartree product

$$\psi_e(\{\mathbf{r}\}) = \phi_1(\mathbf{r}_1)\phi_2(\mathbf{r}_2)...\phi_N(\mathbf{r}_N). \tag{E.14}$$

E.2.1 Slater determinants

We must also recognise that up until this point the spin of the electron $\sigma = \alpha, \beta$ has been neglected; we can include this parameter by redefining our orbitals as spin-orbitals $\phi(\mathbf{x})$, where $\mathbf{x} = \{\mathbf{r}, \sigma\}$. These spin-orbitals are constrained to be orthonormal such that[2]

$$\int \phi_a^*(\mathbf{x})\phi_b(\mathbf{x})\, d\mathbf{x} = \delta_{ab}. \tag{E.15}$$

Importantly, the fermionic (spin-$\frac{1}{2}$) nature of the electron means that the many-body electronic wavefunction ψ_e must satisfy the Pauli Exclusion Principle; this condition states that no two identical electrons may occupy the same space. Electrons are therefore required to be antisymmetric, such that the interchange of spin-position parameters $\mathbf{x}$ requires a change of sign; this antisymmetry is not satisfied by a simple product form of one-particle wavefunctions defined by Equation

[2]Here δ_{ab} is the Kronecker delta such that $\delta_{ab} = 1$ when $a = b$ and $\delta_{ab} = 0$ when $a \neq b$.

E.14. However, in the case of a simple two electron system the requirement that $\psi_e(\mathbf{x}_1, \mathbf{x}_2) = -\psi_e(\mathbf{x}_2, \mathbf{x}_1)$ can be satisfied by the 2×2 Slater determinant [4]

$$\begin{aligned}\psi_e(\mathbf{x}_1, \mathbf{x}_2) &= \frac{1}{\sqrt{2}} \begin{vmatrix} \phi_1(\mathbf{x}_1) & \phi_1(\mathbf{x}_2) \\ \phi_2(\mathbf{x}_1) & \phi_2(\mathbf{x}_2) \end{vmatrix} \\ &= \frac{1}{\sqrt{2}}[\phi_1(\mathbf{x}_1)\phi_2(\mathbf{x}_2) - \phi_1(\mathbf{x}_2)\phi_2(\mathbf{x}_1)],\end{aligned} \tag{E.16}$$

where the factor $1/\sqrt{2}$ is a normalisation constant which ensures Equation E.3 is satisfied. Equation E.16 may then be generalised to N electrons in the form of an $N \times N$ determinant

$$\psi_e(\mathbf{x}) = \frac{1}{\sqrt{N!}} \begin{vmatrix} \phi_1(\mathbf{x}_1) & \phi_1(\mathbf{x}_2) & \cdots & \phi_1(\mathbf{x}_N) \\ \phi_2(\mathbf{x}_1) & \phi_2(\mathbf{x}_2) & \cdots & \phi_2(\mathbf{x}_N) \\ \vdots & \vdots & \ddots & \vdots \\ \phi_N(\mathbf{x}_1) & \phi_N(\mathbf{x}_2) & \cdots & \phi_N(\mathbf{x}_N) \end{vmatrix}, \tag{E.17}$$

which enforces the antisymmetry of an electronic wavefunction of arbitrary complexity.

E.2.2 Electrostatics and exchange

We are now in a position to reconsider the influence of electron-electron interactions; HF theory reintroduces these interactions through the addition of both classical and quantum mechanical terms. The action of the classical electrostatic electron-electron interaction on the spin-orbital $\phi_a(\mathbf{x}_j)$ may be expressed in the form of the Hartree potential operator $\mathcal{J}$, [1]

$$\mathcal{J}(\mathbf{x}_j)\phi_a(\mathbf{x}_j) = \sum_b^N \int \frac{\phi_b^*(\mathbf{x}_k)\phi_b(\mathbf{x}_k)}{|\mathbf{r}_j - \mathbf{r}_k|}\, \phi_a(\mathbf{x}_j)\, d\mathbf{x}_k. \tag{E.18}$$

Recalling that $\mathbf{x}_j = \{\mathbf{r}_j, \alpha\}$ and $\mathbf{x}_k = \{\mathbf{r}_k, \alpha\}$ are different spatial-spin coordinates while ϕ_a and ϕ_b are different one-electron spin-orbitals, we note that the quantity $\phi_b^*(\mathbf{x}_k)\phi_b(\mathbf{x}_k)$ gives the electron charge density at $\mathbf{x}_k$ due to orbital ϕ_b. The integrand $\phi_b^*(\mathbf{x}_k)\phi_b(\mathbf{x}_k)/|\mathbf{r}_j - \mathbf{r}_k|$ therefore represents the potential energy at $\mathbf{x}_j$ due to the

charge density at $\mathbf{x}_k$; when evaluated over all $\mathbf{x}_k$ this gives the total potential energy at $\mathbf{x}_j$ due to all other electron spatial-spin coordinates. The summation over all other orbitals leads to an average Coulombic potential – or mean field – which is determined by every electron within the system.

A second energy is required to enforce the antisymmetry of the system; this purely quantum mechanical term has no classical analogue and is known as the Fock exchange potential operator $\mathcal{K}$; the operation of $\mathcal{K}$ on the spin-orbital $\phi_a(\mathbf{x}_j)$ is expressed as [1]

$$\mathcal{K}(\mathbf{x}_j)\phi_a(\mathbf{x}_j) = \sum_b^N \int \frac{\phi_b^*(\mathbf{x}_k)\phi_a(\mathbf{x}_k)}{|\mathbf{r}_j - \mathbf{r}_k|}\, \phi_b(\mathbf{x}_j)\, d\mathbf{x}_k. \tag{E.19}$$

In analogy to Equation E.18 the integrand $\phi_b^*(\mathbf{x}_k)\phi_a(\mathbf{x}_k)/|\mathbf{r}_j - \mathbf{r}_k|$ represents the potential energy at $\mathbf{x}_j$ due to overlap of the spin-orbitals ϕ_a and ϕ_b. However, unlike Equation E.18, the Fock exchange potential operator exchanges the electron at $\mathbf{x}_j$ from orbital ϕ_a to ϕ_b. This can be interpreted as a repulsive interaction between electrons of parallel spin due to the Pauli Exclusion Principle.

E.2.3 Self-consistent field theory

By combining Equations E.12, E.18 and E.19 we obtain the single-electron HF equation

$$\Big\{h(\mathbf{x}) + \mathcal{J}(\mathbf{x}) - \mathcal{K}(\mathbf{x})\Big\}\phi_a(\mathbf{x}) = \varepsilon_a\phi_a(\mathbf{x}), \tag{E.20}$$

where ε_a is the eigenvalue energy of the a^{th} spin-orbital ϕ_a. As the Fock operator $\big\{h(\mathbf{x}) + \mathcal{J}(\mathbf{x}) - \mathcal{K}(\mathbf{x})\big\}$ depends on the mean field generated by the single-particle orbitals this expression is an example of a non-linear eigenvalue equation, and can only be solved iteratively. This process is initiated by guessing the form of $\phi_a(\mathbf{x})$; solving the eigenvalue equation with this guess provides ε_a values for these initial orbitals together with a new set of orbitals. Equation E.20 is then re-solved with these new orbitals; this iterative cycle is repeated until the orbital energies from subsequent iterations converge to within a pre-set threshold value, at which point the system is said to have achieved a self-consistent field.

The total ground state HF energy $E_{HF}^{(0)}$ may then be calculated using the N

lowest ε_a values according to

$$\begin{aligned} E_{HF}^{(0)} = &\sum_{a}^{N} \varepsilon_a - \sum_{a,b}^{N} \int \frac{\phi_a^*(\mathbf{x}_j)\phi_b^*(\mathbf{x}_k)\phi_a(\mathbf{x}_j)\phi_b(\mathbf{x}_k)}{2|\mathbf{r}_j - \mathbf{r}_k|} \, d\mathbf{x}_j d\mathbf{x}_k \\ &+ \sum_{a,b}^{N} \int \frac{\phi_a^*(\mathbf{x}_j)\phi_b^*(\mathbf{x}_k)\phi_a(\mathbf{x}_k)\phi_b(\mathbf{x}_j)}{2|\mathbf{r}_j - \mathbf{r}_k|} \, d\mathbf{x}_j d\mathbf{x}_k + \upsilon_{nn} \end{aligned} \tag{E.21}$$

where the second and third terms as necessary to avoid double-counting the Coulomb ($\mathcal{J}$) and Exchange ($\mathcal{K}$) energy contributions.

E.3 Density functional theory

Density functional theory (DFT) is the most widely applied electronic structure method in surface chemistry. [5, 6] The defining approach of DFT is that it determines energetics from the ground state electron density of a system $n(\mathbf{r})$, rather than attempting to perform any direct evaluation of the many-body electronic wavefunction ψ_e. It is useful to consider the integral

$$n(\mathbf{r}) = N \int ... \int |\psi_e(\mathbf{x}_1, ..., \mathbf{x}_N)|^2 \, d\sigma_1 d\mathbf{x}_2 ... d\mathbf{x}_N, \tag{E.22}$$

which defines $n(\mathbf{r})$ in terms of the many-body electronic wavefunction ψ_e. This expression states that $n(\mathbf{r})$ is equal to the probability of finding N electrons within the volume $\mathbf{r} + d\mathbf{r}$, one of which has an arbitrary position and well defined spin σ_1, while the other $N - 1$ electrons have arbitrary positions but spins defined by the constraints of ψ_e, given that $\mathbf{x}_1 = \{\mathbf{r}_1, \sigma_1\}$. The number of electrons N is related to $n(\mathbf{r})$ according to

$$N = \int n(\mathbf{r}) \, d\mathbf{r}. \tag{E.23}$$

E.3.1 Hohenberg-Kohn theorem

The basis for a density-based approach comes from the proof by Hohenberg and Kohn that the ground state electronic density is a unique functional of the ground state energy, [7]

$$E_e = E_{HK}[n(\mathbf{r})]. \tag{E.24}$$

In consequence, all that is required to calculated the ground state energy of a system is exact knowledge of the ground state electron density $n(\mathbf{r})$, and the form of the energy functional $E_{HK}[n(\mathbf{r})]$. We shall not reproduce the full Hohenberg-Kohn proof here for reasons of brevity; however, we highlight the following key points which direct us towards Equation E.24: [6]

1. The Hohenberg-Kohn theorem considers the energetics of a homogeneous electron gas under the influence of Coulombic interactions and an external potential υ_{ext}. The authors demonstrate *reductio ad absurdum*[3] that the electron density determines uniquely the external potential of the nuclei; $n \rightarrow \upsilon_{ext}$.

2. As any change to the external potential will alter the many-body electronic wavefunction ψ_e, it follows that υ_{ext} uniquely determines ψ_e; $\upsilon_{ext} \rightarrow \psi_e$.

3. The total energy is a direct response to ψ_e, as defined by Equation E.10; $\psi_e \rightarrow E_e$

As the density functional $E_{HK}[n(\mathbf{r})]$ is dependent on the 3-dimensions of real space rather than the $3N$ coupled variables which determine ψ_e, this approach suggests that DFT may be utilised computationally to evaluate large systems consisting of many electrons. This is indeed the case, and DFT calculations involving hundreds of atoms (and therefore hundreds – if not thousands – of electrons) are now commonplace, in turn allowing theoreticians to simulate molecular systems of direct relevance to complex chemical phenomena. There now exists a plethora of excellent textbooks which detail the application of such calculations to chemical and condensed matter problems. [3, 5, 6, 8, 9]

Unfortunately the exact form of the $E_{HK}[n(\mathbf{r})]$ functional is unknown; however, the variational principal – also known as the second Hohenberg-Kohn theorem – states the successful minimisation of an approximate energy functional $E[n(\mathbf{r})]$ will give the correct ground state energy and electron density, [7]

[3]The literal meaning of this phrase is to argue something to absurdity. In our case the authors show that any other case leads to a clear mathematical impossibility. [7]

$$E_e = E_{HK}[n(\mathbf{r})] \leq E[n(\mathbf{r})], \tag{E.25}$$

It therefore falls to us to find and minimise an adequate energy functional $E[n(\mathbf{r})]$ for molecular or solid-state electronic systems.

E.3.2 Kohn-Sham DFT

A sensible first attempt at an expression for $E[n(\mathbf{r})]$ can be obtained by consulting the above discussion on many-body electronic theory, such that

$$E[n(\mathbf{r})] = T_e[n(\mathbf{r})] + V_{ee}[n(\mathbf{r})] + V_{en}[n(\mathbf{r})]. \tag{E.26}$$

Here $T_e[n(\mathbf{r})]$, $V_{ee}[n(\mathbf{r})]$ and $V_{en}[n(\mathbf{r})]$ are density functionals representing the electronic kinetic energy, electron-electron interaction potential and electron-nuclear interaction potential, respectfully. By considering Equations E.11 and E.22 a density-based expression for the electron-nuclear potential can be obtained in the form of

$$V_{en}[n(\mathbf{r})] = \int n(\mathbf{r}) \upsilon_{ext}(\mathbf{r})\, d\mathbf{r}, \tag{E.27}$$

where the so-called external potential $\upsilon_{ext}(\mathbf{r})$ is dictated by the nuclear geometry according to [6]

$$\upsilon_{ext}(\mathbf{r}) = -\sum_J \frac{Z_J}{|\mathbf{r} - \mathbf{R}_J|}. \tag{E.28}$$

Unfortunately the many-body nature of the electron-electron interactions mean the terms $T_e[n]$ and $V_{ee}[n]$ are more difficult to define. Hohenberg and Kohn showed that $E[n(\mathbf{r})]$ can be expressed as [7]

$$E[n(\mathbf{r})] = V_{en}[n(\mathbf{r})] + F[n(\mathbf{r})], \tag{E.29}$$

where the functional $F[n(\mathbf{r})]$ is valid for any number of electrons and any external potential.[4] Kohn and Sham approached this problem by considering a fictitious system of non-interacting electrons of equivalent density to that of the interacting

[4] In this capacity $F[n(\mathbf{r})]$ is often referred to as a universal functional. [7]

system; in this case the functional $F[n(\mathbf{r})]$ may be expressed as [10]

$$F[n(\mathbf{r})] = V_H[n(\mathbf{r})] + T'_e[n(\mathbf{r})] + E_{xc}[n(\mathbf{r})], \tag{E.30}$$

where $V_H[n]$ is the Hartree (or Coulomb) energy functional, which takes a similar form to Equation E.18,

$$V_H[n(\mathbf{r})] = \frac{1}{2}\iint \frac{n(\mathbf{r})n(\mathbf{r}')}{|\mathbf{r}-\mathbf{r}'|}\, d\mathbf{r}d\mathbf{r}'. \tag{E.31}$$

$T'_e[n]$ is the kinetic energy functional of the non-interacting electrons. Finally $E_{xc}[n(\mathbf{r})]$ is the infamous exchange-correlation functional, and contains all the complex many-body effects not accounted for by $T'_e[n(\mathbf{r})]$ or $V_H[n(\mathbf{r})]$, [10]

$$E_{xc}[n(\mathbf{r})] = \big(T_e[n(\mathbf{r})] - T'_e[n(\mathbf{r})]\big) + \big(V_{ee}[n(\mathbf{r})] - V_H[n(\mathbf{r})]\big). \tag{E.32}$$

The addition of this functional transforms Equation E.30 from a description of non-interacting electrons to that of a many-body system; clearly from the name of this functional $E_{xc}[n(\mathbf{r})]$ contains an energetic contribution from exchange, as introduced above with reference to Hartree-Fock theory. It also contains the remnants of a second quantum mechanical energy known as correlation energy. The movement of one electron can have signficant effects on the behaviour of others. Electrons are therefore clearly highly correlated particles; this concept can be considered in terms of the classical repulsion between negative charges, as well as quantum mechanical effects such as the exchange energy repulsion between parallel spin states. Unfortunately this correlation energy is not adequately treated within Hartree-Fock theory; in fact the term correlation energy has become synonymous with the difference between the true energy of a system and the energy calculated using Hartree-Fock theory. This energy difference has two major contributions, known as dynamic and static correlation, respectively. Dynamic correlation is defined by the instantaneous motion electrons take to avoid one another; while this is partially accounted for by adequate evaluation of the exchange energy,[5] the mean-field nature

[5]Indeed the concept of exchange is also sometimes referred to as Fermi correlation.

of Hartree-Fock calculations lead to an overestimation of Coulombic correlation arising from electrostatics. The Hartree-Fock energy is therefore always higher than the actual energy. [6] Static correlation is more subtle and arises from the inability of a single stater determinant (Equation E.17) to fully describe a given many-body electronic wavefunction. [3]

The key approach of Kohn-Sham DFT is to realise that $E[n(\mathbf{r})]$ can be minimised through a single-particle approach. The effective potential υ_{eff} is given by[6]

$$\begin{aligned} \upsilon_{eff}(\mathbf{r}) &= \frac{\delta\big\{V_{en}[n(\mathbf{r})] + V_H[n(\mathbf{r})] + E_{xc}[n(\mathbf{r})]\big\}}{\delta n(\mathbf{r})} \\ &= \upsilon_{ext}(\mathbf{r}) + \int \frac{n(\mathbf{r}')}{|\mathbf{r}-\mathbf{r}'|}\, d\mathbf{r}' + \upsilon_{xc}(\mathbf{r}), \end{aligned} \tag{E.33}$$

where $\upsilon_{xc}(\mathbf{r}) = \frac{\delta E_{xc}[n(\mathbf{r})]}{\delta n(\mathbf{r})}$ is an exchange-correlation potential. We may then define a single-particle eigenvalue equation as

$$\left\{ -\frac{1}{2}\nabla + \upsilon_{eff}(\mathbf{r}) \right\} \phi_a^{KS}(\mathbf{r}) = \varepsilon_a \phi_a^{KS}(\mathbf{r}), \tag{E.34}$$

where the one-electron Kohn-Sham orbitals define the electron density according to

$$n(\mathbf{r}) = \sum_a |\phi_a^{KS}(\mathbf{r})|^2. \tag{E.35}$$

Equations E.33, E.34 and E.35 are the well-known Kohn-Sham equations. Equation E.34 is clearly similar to the single-particle equation employed within HF theory (Equation E.20), such that the eigenvalue energies ε_a must be minimised through a similar iterative approach.

E.3.3 Approximations for the exchange-correlation functional

Unfortunately an exact, closed form mathematical expression for the exchange-correlation functional remains unknown. The adequate approximation of $E_{xc}[n(\mathbf{r})]$, and by extension $\upsilon_{xc}(\mathbf{r})$, is therefore central to the accuracy of a given DFT calculation.

[6] Here $\frac{\delta f[x]}{\delta x}$ is the functional derivative, which relates a change in a functional to a change in the function on which that functional depends.

Local density approximation

The most basic approximation of the exchange-correlation functional considers the exchange and correlation present within a uniform electron gas. In order to apply this approach to real systems, the inhomogeneous density under study is divided into infinitesimal volumes to which this approximation is applied. This approximation calculates the exchange and correlation energies at each coordinate $\mathbf{r}$, but makes no consideration of the gradient of the density; this approach is therefore known as the local density approximation (LDA), [11] and is considered a reasonable approach only in the case of very slowly-varying electron densities $n(\mathbf{r})$. Here $E_{xc}[n(\mathbf{r})]$ may be expressed by

$$E_{xc}^{\mathrm{LDA}}[n(\mathbf{r})] = \int n(\mathbf{r})\epsilon_{xc}^{unif}\big(n(\mathbf{r})\big)\, d\mathbf{r}, \tag{E.36}$$

where $\epsilon_{xc}^{unif}(n(\mathbf{r}))$ is the exchange-correlation energy *per* electron of a uniform electron gas of density $n(\mathbf{r})$. In practice the exchange and correlation contributions are calculated separately, such that $E_{xc}[n(\mathbf{r})] = E_x[n(\mathbf{r})] + E_c[n(\mathbf{r})]$. In the case of the homogeneous electron gas the exchange energy is known exactly, [3]

$$E_x^{\mathrm{LDA}}[n(\mathbf{r})] = -\frac{3}{4}\left(\frac{3}{\pi}\right)^{1/3} \int n^{4/3}(\mathbf{r})\, d\mathbf{r}, \tag{E.37}$$

while the correlation energy $E_c^{\mathrm{LDA}}[n(\mathbf{r})]$ is approximated from the works of Gell-Mann and Brueckner [12] and Ceperley and Alder. [13]

Generalised gradient approximation

The term generalised gradient approximation (GGA) describes second generation exchange correlation functionals which also take account of the gradient of the electron density $\nabla n(\mathbf{r})$. GGA exchange-correlation functionals have the general form

$$E_{xc}^{\mathrm{GGA}}[n(\mathbf{r})] = \int n(\mathbf{r})\epsilon_{xc}^{unif}\big(n(\mathbf{r})\big)F_{xc}\big(n(\mathbf{r}), \nabla n(\mathbf{r})\big)\, d\mathbf{r}, \tag{E.38}$$

where $F_{xc}\big(n(\mathbf{r}), \nabla n(\mathbf{r})\big)$ is an enhancement factor that incorporates the effects of the density gradient at each coordinate. [3] Multiple GGAs exist throughout the literature; in this work the GGA of Perdew, Burke and Ernzerhof (PBE) is employed.

[14]

E.3.4 Basis sets and Bloch's theorem

In order to solve Equation E.34 it is necessary to expand the Kohn-Sham orbitals using an appropriate set of basis functions $\chi_p(\mathbf{r})$, [9]

$$\phi_a(\mathbf{r}) = \sum_{p=1}^{P} c_{a,p}\chi_p(\mathbf{r}). \tag{E.39}$$

This process is of critical importance to the accuracy of a particular quantum mechanical calculation and allows the single-particle eigenvalue equations to be solved through efficient computational matrix techniques. Here $c_{a,p}$ are a set of P expansion coefficients which facilitate the definition of ϕ_a as a linear combination of basis functions. In principle $P \to \infty$, in which case $\phi_a^{KS}(\mathbf{r})$ are said to be described by a complete basis set; however, in order to approach such calculations computationally it is necessary to truncate P and work with a finite number of basis functions. [9]

The form of the basis functions $\chi_p(\mathbf{r})$ is often chosen the reflect the physics of the system under study. For instance, the orbitals of molecular systems are usually described using the well-known linear combination of atomic orbitals (LCAO) approximation, such that the basis functions comprise a set hydrogenic atomic orbitals. When considering solid systems, however, it is typical that the basis functions are chosen to reflect the periodic nature of the crystalline wavefunction; basis functions based on plane-waves are therefore a natural choice.

Some notes on lattice structures

Before we detail an appropriate set of basis functions for use in solid state DFT calculations it is necessary to briefly introduce some of the terminology used in the description of solid state structures. [15, 16]

Our calculations here will be based on the evaluation of crystalline structures and surfaces; crystalline structures are defined by a repeating arrangement of atoms or ions known as a unit cell. The smallest possible repeating segment from which

we may define an entire crystalline structure is known as the primitive unit cell; this cell is a parallelepiped[7] structure whose edges are the primitive lattice vectors $\mathbf{a}_1$, $\mathbf{a}_2$ and $\mathbf{a}_3$. The volume of this primitive unit cell Ω is defined by the triple product rule

$$\Omega = |\mathbf{a}_1 \cdot \mathbf{a}_2 \times \mathbf{a}_3|, \tag{E.40}$$

while the macroscopic crystal may be defined through translation of the primitive cell according to

$$\mathbf{T} = n_1\mathbf{a}_1 + n_2\mathbf{a}_2 + n_3\mathbf{a}_3, \tag{E.41}$$

where n_1, n_2 and n_3 are integers. The translation vectors $\mathbf{T}$ connects all equivalent points in real space, known as the Bravais lattice.

It is also of importance to define a reciprocal lattice defined by the lattice vectors

$$\mathbf{b}_1 = 2\pi\frac{\mathbf{a}_2 \times \mathbf{a}_3}{\mathbf{a}_1 \cdot \mathbf{a}_2 \times \mathbf{a}_3}, \tag{E.42a}$$

$$\mathbf{b}_2 = 2\pi\frac{\mathbf{a}_3 \times \mathbf{a}_1}{\mathbf{a}_2 \cdot \mathbf{a}_3 \times \mathbf{a}_1}, \tag{E.42b}$$

$$\mathbf{b}_3 = 2\pi\frac{\mathbf{a}_1 \times \mathbf{a}_2}{\mathbf{a}_3 \cdot \mathbf{a}_1 \times \mathbf{a}_2}, \tag{E.42c}$$

and reciprocal cell of volume

$$\bar{\Omega} = |\mathbf{b}_1 \cdot \mathbf{b}_2 \times \mathbf{b}_3| = \frac{(2\pi)^3}{\Omega}. \tag{E.43}$$

This primitive reciprocal lattice is known as the first Brillouin zone and is of fundamental importance to solid state electronic structure theory. Furthermore, we may define a reciprocal translation vector

$$\mathbf{G} = m_1\mathbf{b}_1 + m_2\mathbf{b}_2 + m_3\mathbf{b}_3, \tag{E.44}$$

where m_1, m_2 and m_3 are also integers; the reciprocal translation vectors $\mathbf{G}$ connect all equivalent points within reciprocal space. The primitive cell vectors are orthogonal,

[7] A parallelepiped is a three-dimensional structure, each face of which takes the form of a parallelogram.

$$\mathbf{a}_j \cdot \mathbf{b}_k = 2\pi\delta_{jk}, \tag{E.45}$$

where δ_{jk} is the Kronecker delta function, and the translation vectors $\mathbf{T}$ and $\mathbf{G}$ satisfy

$$\mathbf{T} \cdot \mathbf{G} = 2\pi l, \tag{E.46}$$

where $l = n_1 m_1 + n_2 m_2 + n_3 m_3$, and

$$\exp(i\mathbf{G} \cdot \mathbf{T}) = 1. \tag{E.47}$$

Finally we note that any function $f(\mathbf{r}) = f(\mathbf{r} + \mathbf{T})$ which has the periodicity of the Bravais lattice can be expressed as

$$f(\mathbf{r}) = \sum_{\mathbf{G}} \exp(i\mathbf{G} \cdot \mathbf{r}) f(\mathbf{G}), \tag{E.48}$$

where $f(\mathbf{G})$ are the Fourier components of $f(\mathbf{r})$.

Bloch's theorem

Within a periodic potential $v(\mathbf{r}) = v(\mathbf{r} + \mathbf{T})$ of periodicity $\mathbf{T}$ (Equation E.41), Bloch's theorem states that the single-particle wavefunctions $\phi_a(\mathbf{r})$ will have the same periodicity to within a phase factor $\exp(i\mathbf{k} \cdot \mathbf{T})$, [17]

$$\phi_{a,\mathbf{k}}(\mathbf{r} + \mathbf{T}) = \phi_{a,\mathbf{k}}(\mathbf{r}) \exp(i\mathbf{k} \cdot \mathbf{T}). \tag{E.49}$$

The wavevector $\mathbf{k}$ which indexes $\phi_a(\mathbf{r})$ can be considered to denote a coordinate within reciprocal space – specifically within the first Brillouin zone – and has the general form

$$\mathbf{k} = \kappa_1 \mathbf{b}_1 + \kappa_2 \mathbf{b}_2 + \kappa_3 \mathbf{b}_3, \tag{E.50}$$

where κ_1, κ_2 and κ_3 are constants. Equation E.49 is more usually defined in terms of the periodic function

$$\mu_{a,\mathbf{k}}(\mathbf{r}) = \frac{\phi_{a,\mathbf{k}}(\mathbf{r})}{\exp(i\mathbf{k} \cdot \mathbf{r})}, \tag{E.51}$$

such that

$$\phi_{a,\mathbf{k}}(\mathbf{r}) = \exp(i\mathbf{k}\cdot\mathbf{r})\mu_{a,\mathbf{k}}(\mathbf{r}). \tag{E.52}$$

Following Equation E.48, and noting that $\mu_{a,\mathbf{k}}(\mathbf{r})$ must have the same periodicity as $v(\mathbf{r})$, we may express this periodic function as Fourier series in the form of a discrete summation of plane-waves,

$$\mu_{a,\mathbf{k}} = \sum_{\mathbf{G}} c_{a,\mathbf{G}} \exp(i\mathbf{G}\cdot\mathbf{r}), \tag{E.53}$$

where the summation is over all possible combinations n_1, n_2 and n_3 in Equation E.44. By combining Equations E.52 and E.53 it follow that Bloch's theorem allows us to express the crystalline wavefunction $\phi_{a,\mathbf{k}}$ as

$$\phi_{a,\mathbf{k}} = \sum_{\mathbf{G}} c_{a,\mathbf{k}+\mathbf{G}} \exp\big(i(\mathbf{k}+\mathbf{G})\cdot\mathbf{r}\big), \tag{E.54}$$

which is clearly similar in structure to Equation E.39.

k-point sampling

The reciprocal points (**k**-points) which occur in Equation E.54 are of significant importance to solid-state electronic theory. The electronic states within a particular periodic structure are allows only at a particular set of **k**-points, as determined by the boundary conditions of the bulk solid. The infinite number of electrons within an infinitely repeating solid are accounted for by an infinite number of **k**-points, but there exist only a finite number of occupied electronic states at each point.

Bloch's theorem described above alters the problem of calculating an infinite number of electronic wavefunctions to a problem of calculating a finite number of wavefunctions at an infinite number of **k**-points. [18] This problem can be further reduced by realising that **k**-points very close together are almost identical. It is therefore the case that only a finite number of these points are required for a particular electronic calculation. The most widely-applied **k**-point sampling method is that of Monkhorst and Pack. [19] Using this method the Brillouin zone is sampled by a special set of **k**-points which are distributed uniformly according to

$$\mathbf{k}_{prs} = \kappa_p \mathbf{b}_1 + \kappa_r \mathbf{b}_2 + \kappa_s \mathbf{b}_3, \tag{E.55}$$

where

$$\kappa_{prs} = \frac{2r - q - 1}{2q}, \tag{E.56}$$

and $r = 1, 2, 3, ..., q$; here q is an integer that determines the number of special **k**-points to be used in each direction, leading to q^3 uniformly spaced points throughout the first Brillouin zone. Such an array of **k**-points is usually referred to as a Monkhorst-Pack grid.

Energy cutoff

Equation E.54 illustrates that the electronic wavefunction at each **k**-point can be expanded in the form of a discrete set of plane-waves; unfortunately it also suggests that an infinite number of plane-waves is required to fully expand each wavefunction (equivaent to $P \to \infty$ in Equation E.39). In reality this plane-wave basis set can be truncated by recognising that expansion coefficients with small kinetic energy $(\hbar^2/2m_e)|\mathbf{k}+\mathbf{G}|^2$ will be more important than those of large kinetic energy. [18] The plane-wave expansion may therefore be truncated by the expression of a particular energy cutoff E_{cut} in the form

$$E_{cut} = \frac{\hbar^2}{2m_e}|\mathbf{k} + \mathbf{G}|^2, \tag{E.57}$$

such that

$$|\mathbf{k} + \mathbf{G}|_{max} = \frac{\sqrt{2m_e E_{cut}}}{\hbar}. \tag{E.58}$$

This cut-off fixes the largest reciprocal lattice vector **G** used within the plane-waved expansion (Equation E.54), providing us with a finite basis set.

E.3.5 Pseudopotentials

The wavefunction associated with tightly bound core atoms near the nucleus typically oscillates rapidly across real space. To satisfactorily capture the electronic structure of this region it is therefore necessary to employ large E_{cut} values to

describe plane-waves with high spatial frequency. We note, however, that such states are typically unimportant in terms of chemical bonding, which is dictated by smoothly-varying valence electron density further from the nucleus. As the computational cost of a given plane-wave DFT calculation is inversely proportional to the length scale which need be described, a significant computational saving can be made by realising that these high spatial-frequency core regions can often be replaced with a smoothly varying function of electron density associated with an appropriate charge; this region is known as a pseudopotential. [9]

In this work we have employed ultrasoft pseudopotentials; [20] the ultrasoft term refers to the low E_{cut} value required by pseudopotentials which extend far from the nucleus. As such, this approach provides our plane-wave DFT calculations with a sizeable computation saving.

E.3.6 Dispersion energy corrections

A major drawback of the DFT methods described above lies in their inability to correctly handle long-range dispersion (van der Waals) interactions. This provides us with a significant issue as such interactions are known to be important in the accurate modelling of adsorption interactions as simulated in this thesis. [21–24] The failure of DFT energy calculations to capture these weak interactions arises from the inability of the exchange-correlation functional (even GGA) to capture the long-range electron correlation effects responsible. [25, 26] As such, it is necessary to correct the resulting energies; is the present work we do this *via* the addition of the semi-empirical dispersion energy by Grimme (D2). [27] This correction takes the form

$$E_{D2} = -s_6 \sum_{j=1}^{N-1} \sum_{k=j-1}^{N} \frac{C^{jk}}{R_{jk}^6} f_{damp}(R_{jk}) \tag{E.59}$$

which is calculated pair-wise between each atom pair jk. Here N is the number of atoms in the system under study, C_6^{jk} are the relevant dispersion coefficients which describe the long-range $-C_6^{jk}/R_{jk}^6$ attraction of each atom pair, R_{jk} is the interatomic distance and s_6 is a global scaling parameter which depends on the exchange-correlation functional employed. The damping function

$$f_{damp}(R_{jk}) = \frac{1}{1 + \exp\big(-d\{\frac{R_{jk}}{R_r - 1}\}\big)} \tag{E.60}$$

prevents E_{D2} tending to ∞ at small R_{ij}, and employs the distance R_r which is the sum of the van der Waals radii of the relevant atom pair, while the C_6^{jk} dispersion coefficients are defined as

$$C_6^{jk} = \sqrt{C_6^j C_6^k}, \tag{E.61}$$

where the relevant C_6 coefficients are provided in Table 1 of [27].

E.3.7 Forces and geometry optimisation

Following the calculation of the energy of a particular molecular or solid state structure it is of particular use to be able to optimise its nuclear geometry; such optimisation is almost always necessary given that the structural parameters which minimise the potential energy of particular geometry at a particular level of theory (exchange-correlation energy, basis set parameters, dispersion energy correction) will usually differ from experimental measurements to some degree. Furthermore, for the modelling of adsorption interactions it is necessary to allow an adsorbate to relax into a relevant potential well at the solid surface under investigation.

Geometry optimisation is achieved by considering the forces [6]

$$\mathbf{F}_J = -\frac{\partial E}{\partial \mathbf{R}_J}, \tag{E.62}$$

where E is the energy of the system and $\mathbf{R}_J$ defines the position of nucleus J. Clearly Equation E.62 provides a direct link between the equilibrium structure of the system and its energy. Geometry optimisation is achieved through the minimisation of $\mathbf{F}_J$ (to within some pre-set threshold value) through the application of a relevant optimisation algorithm. [9] In the present work our calcuations have been carried our using the plane-wave pseudopotential code CASTEP, [28] in which geometry optimisation calculations are performed using the BFGS (Broyden-Fletcher-Goldfarb-Shanno) energy minimiser. [29]

E.4 References

[1] P. W. Atkins and R. S. Friedman, *Molecular Quantum Mechanics*, OUP Oxford, 2011.

[2] M. Born and R. Oppenheimer, "Zur Quantentheorie Der Molekeln", *Ann. Phys.*, 1927, **389**, 457–484.

[3] R. M. Martin, *Electronic Structure: Basic Theory and Practical Methods*, Cambridge University Press, Cambridge, UK ; New York, 1 edition, 2008.

[4] J. C. Slater, "The Theory of Complex Spectra", *Phys. Rev.*, 1929, **34**, 1293–1322.

[5] A. Groß, *Theoretical Surface Science: A Microscopic Perspective*, Springer Science & Business Media, 2009.

[6] F. Giustino, *Materials Modelling Using Density Functional Theory: Properties and Predictions*, Oxford University Press, 2014.

[7] P. Hohenberg and W. Kohn, "Inhomogeneous Electron Gas", *Phys. Rev.*, 1964, **136**, B864–B871.

[8] W. Koch and M. C. Holthausen, *A Chemist's Guide to Density Functional Theory*, John Wiley & Sons, 2015.

[9] D. Sholl and J. A. Steckel, *Density Functional Theory: A Practical Introduction*, John Wiley & Sons, 2011.

[10] W. Kohn and L. J. Sham, "Self-Consistent Equations Including Exchange and Correlation Effects", *Phys. Rev.*, 1965, **140**, A1133–A1138.

[11] J. P. Perdew and A. Zunger, "Self-Interaction Correction to Density-Functional Approximations for Many-Electron Systems", *Phys. Rev. B*, 1981, **23**, 5048–5079.

[12] M. Gell-Mann and K. A. Brueckner, "Correlation Energy of an Electron Gas at High Density", *Phys. Rev.*, 1957, **106**, 364–368.

[13] D. M. Ceperley and B. J. Alder, "Ground State of the Electron Gas by a Stochastic Method", *Phys. Rev. Lett.*, 1980, **45**, 566–569.

[14] J. P. Perdew, K. Burke and M. Ernzerhof, "Generalized Gradient Approximation Made Simple", *Phys. Rev. Lett.*, 1996, **77**, 3865–3868.

[15] P. Hofmann, *Solid State Physics: An Introduction*, Wiley VCH, Weinheim, 2nd edition, 2015.

[16] A. R. West, *Solid State Chemistry and Its Applications*, Wiley, Chichester, West Sussex, 2nd Edition, Student edition, 2014.

[17] E. Kaxiras, *Atomic and Electronic Structure of Solids*, Cambridge University Press, 2003.

[18] M. C. Payne, M. P. Teter, D. C. Allan, T. A. Arias and J. D. Joannopoulos, "Iterative Minimization Techniques for Ab Initio Total-Energy Calculations: Molecular Dynamics and Conjugate Gradients", *Rev. Mod. Phys.*, 1992, **64**, 1045–1097.

[19] H. J. Monkhorst and J. D. Pack, "Special Points for Brillouin-Zone Integrations", *Phys. Rev. B*, 1976, **13**, 5188–5192.

[20] D. Vanderbilt, "Soft Self-Consistent Pseudopotentials in a Generalized Eigenvalue Formalism", *Phys. Rev. B*, 1990, **41**, 7892–7895.

[21] C. M. Nguyen, M.-F. Reyniers and G. B. Marin, "Theoretical Study of the Adsorption of C1–C4 Primary Alcohols in H-ZSM-5", *Phys. Chem. Chem. Phys.*, 2010, **12**, 9481–9493.

[22] C. M. Nguyen, M.-F. Reyniers and G. B. Marin, "Theoretical Study of the Adsorption of the Butanol Isomers in H-ZSM-5", *J. Phys. Chem. C*, 2011, **115**, 8658–8669.

[23] J. C. F. Rodriguez-Reyes, C. G. F. Siler, W. Liu, A. Tkatchenko, C. M. Friend and R. J. Madix, "Van Der Waals Interactions Determine Selectivity in Catalysis by Metallic Gold", *J. Am. Chem. Soc.*, 2014, **136**, 13333–13340.

[24] S. Karakalos, Y. Xu, F. Cheenicode Kabeer, W. Chen, J. C. F. Rodríguez-Reyes, A. Tkatchenko, E. Kaxiras, R. J. Madix and C. M. Friend, "Noncovalent Bonding Controls Selectivity in Heterogeneous Catalysis: Coupling Reactions on Gold", *J. Am. Chem. Soc.*, 2016, **138**, 15243–15250.

[25] S. Grimme, "Density Functional Theory with London Dispersion Corrections", *WIREs Comput. Mol. Sci.*, 2011, **1**, 211–228.

[26] S. Grimme, A. Hansen, J. G. Brandenburg and C. Bannwarth, "Dispersion-Corrected Mean-Field Electronic Structure Methods", *Chem. Rev.*, 2016, **116**, 5105–5154.

[27] S. Grimme, "Semiempirical GGA-Type Density Functional Constructed with a Long-Range Dispersion Correction", *J. Comput. Chem.*, 2006, **27**, 1787–1799.

[28] S. J. Clark, M. D. Segall, C. J. Pickard, P. J. Hasnip, M. I. J. Probert, K. Refson and M. C. Payne, "First Principles Methods Using CASTEP", *Zeitschrift für Kristallographie*, 2005, **220**, 567–570.

[29] B. G. Pfrommer, M. Côté, S. G. Louie and M. L. Cohen, "Relaxation of Crystals with the Quasi-Newton Method", *J. Comput. Phys.*, 1997, **131**, 233–240.

Appendix F

Supplementary relaxation correlations

Figure F.1 provides a comparison between the intermediate field $T_1 - T_2$ correlation plots discussed in Chapter 6 and supplementary experiments performed at high field. In this case hardware limitations allowed significantly shorter echo times to be investigated, facilitating a comparison of peak shape and relaxation characteristics across different field strengths and t_e values. Our high-field $T_1 - T_2$ relaxation correlation experiments were performed on Bruker DMX 300 NMR spectrometer equipped with a 7.1 T superconducting magnet, corresponding to a ^{1}H frequency of $\omega_0/(2\pi) = 300.13$ MHz; $T_1 - T_2$ correlation plots were again obtained by applying the inversion recovery - PROJECT pulse sequence detailed in Figure 3.17b. 16 τ_1 recovery delays were implemented ranging from 1 ms to $5T_1$ for each liquid. The PROJECT echo train consisted of either $n = 256$ echoes with $t_e = 10$ ms or $n = 2048$ echoes with $t_e = 3$ ms; t_e values are indicated by dotted lines on each correlation plot.

Qualitatively, Figure F.1 illustrates significant similarities between the two $t_e = 10$ ms data sets. Methanol relaxation data acquired at both 85 and 300 MHz shows 2 correlation peaks, while ethanol and 1-propanol exhibit a single correlation peak. At 85 MHz 1-butanol exhibits only a single peak, while at 300 MHz a small secondary peak at $T_2 \approx t_e$ has appeared. In all cases large (primary) peaks are labelled peak I, while smaller (secondary) peaks are labelled II. High-field data

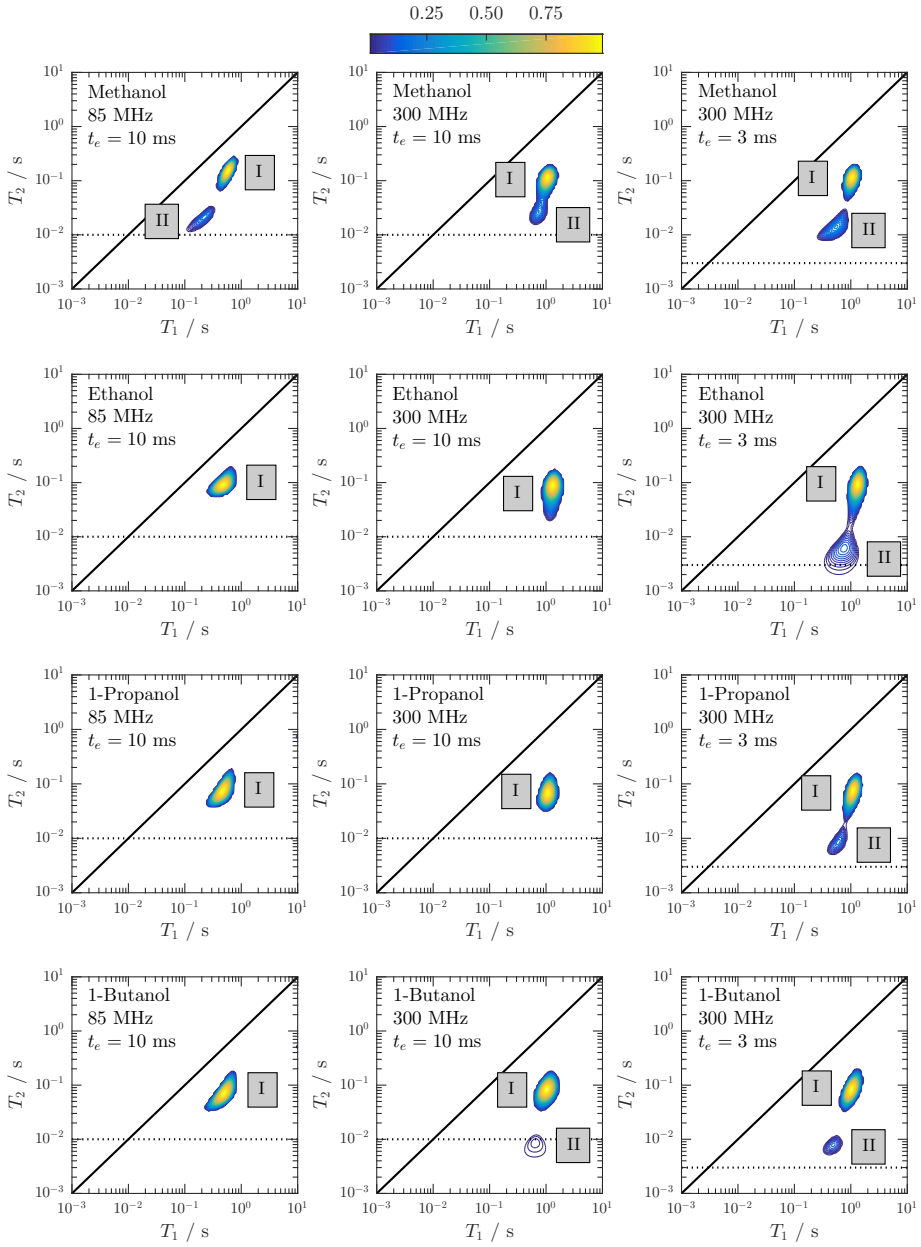

Figure F.1: ^{1}H $T_1 - T_2$ relaxation correlation plots of short chain primary alcohols in mesoporous silica, obtained at 85 MHz and 300 MHz. Dotted horizontal lines indicate the echo time t_e.

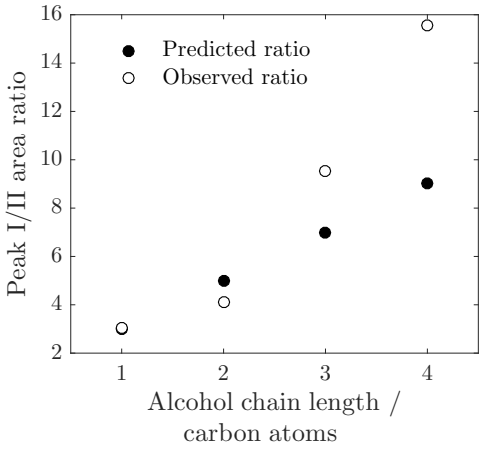

Figure F.2: Ratio of peak areas from the 300 MHz $t_e = 3$ ms relaxation correlation plots in Figure F.1, compared with the alkyl/hydroxyl ^{1}H number ratio within $C_1 - C_4$ primary alcohols.

acquired with $t_e = 3$ ms show significant differences from that obtained with $t_e = 10$ ms. Most prominently, a second correlation peak at short T_2 and is observed for all alcohols. Figure F.2 illustrates the ratio of the integrated areas of these peaks as a function of carbon chain length, and provides a comparison with that expected from the number ratio of alkyl and hydroxyl ^{1}H within each alcohol. The resultant trend provides strong evidence that peaks I and II correspond to alkyl and hydroxyl relaxation ^{1}H, respectively. It is further apparent from Figure F.1 that observation of the hydroxyl peak is strongly dependent on the echo time employed; indeed at 300 MHz the ethanol and 1-propanol hydroxyl peaks clearly fall at $T_2 < 10$ ms, and are therefore only visible in the $t_e = 3$ ms data sets. The 1-butanol hydroxyl peak falls at $T_2 \sim 10$ ms and is apparent in the $t_e = 10$ ms data as a small peak, while the methanol hydroxyl peak appears abridged. Importantly, a comparison of these data with our 85 MHz correlation plots - together with the results of Chapter 5 - provides significant confidence in our interpretation that i) the observed ethanol, 1-propanol and 1-butanol correlation peaks may be attributed to alkyl ^{1}H relaxation, and ii) the lack of hydroxyl signal may be attributed to the echo time employed.

The 300 MHz data in Figure F.1 suggests that the T_2 – therefore T_1/T_2 – of the alkyl peak is unaffected by the echo time employed. It is a reasonable assumption that this is also the case at 85 MHz, such that the relatively long t_e has no bearing on the observed relaxation characteristics of the alkyl environment. To confirm

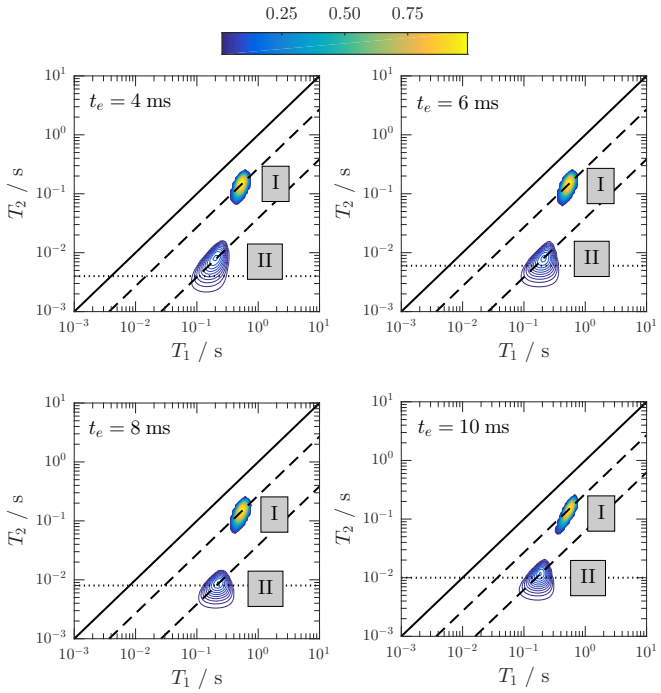

Figure F.3: 85 MHz ^{1}H $T_1 - T_2$ relaxation correlation plots of methanol in mesoporous silica, obtained through application of the inversion recovery - CPMG with variable echo times t_e. Dashed diagonal lines indicate the $\langle T_1/T_2 \rangle$ of each peak (labelled I and II). Dotted horizontal lines indicate the echo time applied in each case.

this assumption we have performed addition relaxation correlation experiments on methanol-saturated silica, utilising the inversion recovery – CPMG pulse sequence (Figure 3.17b). The CPMG echo train is advantageous here given its $t_e = 2\tau_2$ scaling. Methanol is a prototypical molecule for CPMG T_2 analysis as – unlike the other primary alcohols in this study – it is the subject of no ^{1}H J-coupling interactions. Figures F.3 and F.4 provide a comparison between methanol relaxation characteristics acquired with t_e in the range 4 ms – 10 ms, and confirm that the alkyl relaxation characteristics are insensitive to echo time changes within this range. The hydroxyl peak is shown to be depended on t_e when $t_e \sim T_2$, as expected.

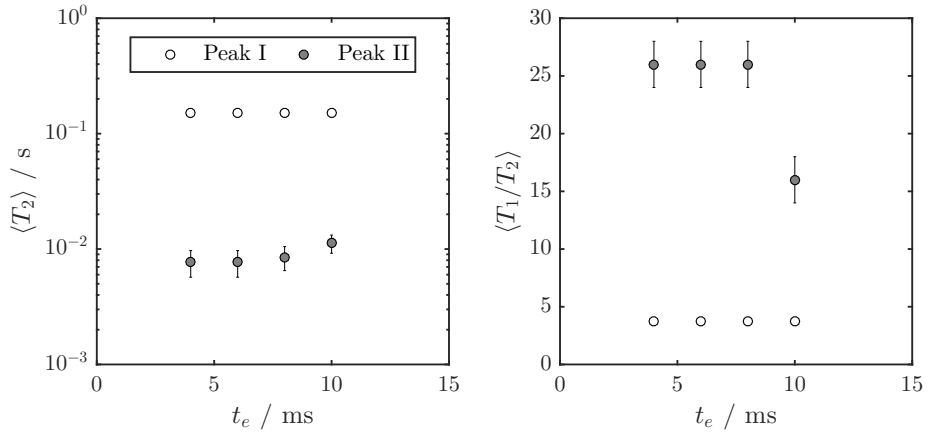

Figure F.4: Illustration of the modal relaxation characteristics $\langle T_2 \rangle$ and $\langle T_1/T_2 \rangle$ as a function of echo time t_e, as obtained from Figure F.3. Peaks I and II are attributed to methanol methyl and hydroxyl ^{1}H relaxation, respectively.

Appendix G

Nomenclature

Acronyms

Acronym	Definition
APGSTE	Alternating pulsed gradient stimulated echo
BET	Brunauer-Emmett-Teller
BFGS	Broyden-Fletcher-Goldfarb-Shanno
BJH	Barrett-Joyner-Halenda
BPP	Bloembergen-Purcell-Pound
CASTEP	Cambridge serial total energy package
CPMG	Carr-Purcell-Meiboom-Gill
DFT	Density functional theory
FID	Free induction decay
GGA	Generalised gradient approximation
IUPAC	International Union of Pure and Applied Chemistry
LDA	Local density approximation
LS	Lipari-Szabo
PBE	Perdew-Burke-Ernzerhof
PFG	Pulsed field gradient
PGSE	Pulsed gradient spin echo
PGSTE	Pulsed gradient stimulated echo
PROJECT	Periodic refocussing of J evolution by coherence transfer
NMR	Nuclear magnetic resonance
RF	Radio frequency
ppm	Parts *per* million

Constants

Constant	Symbol	Value (6 d.p.)	Units
Avogadro's number	N_A	$6.02214086 \times 10^{23}$	mol^{-1}
Boltzmann constant	k_B	$1.38064852 \times 10^{-23}$	J K^{-1}
Electron mass	m_e	$9.10938356 \times 10^{-31}$	kg
Elemental charge	e	$1.60217663 \times 10^{-19}$	C
Euler's number	e	2.71828183	-
Gas constant	R	$N_A k_B$	$\text{J K}^{-1}\ \text{mol}^{-1}$
Imaginary unit	i	$\sqrt{-1}$	-
Permeability of free space	μ_0	$4\pi \times 10^{-7}$	$\text{J m}^{-1}\ \text{A}^{-2}$
Permittivity of free space	ε_0	$8.85418719 \times 10^{-12}$	$\text{A}^2\ \text{kg}^{-1}\ \text{J}^{-2}$
Planck's constant	h	$6.62607015 \times 10^{-34}$	J s
Pi	π	3.14592654	-
Proton mass	m_p	$1.67262190 \times 10^{-27}$	kg
Reduced Planck constant	$\hbar$	$h/(2\pi)$	J s

Roman symbols

Symbol	Definition	Units
a	Internal gradient composite parameter	various
a	Density operator constant of proportionality (x component)	-
$\mathbf{a}$	Surface cell vector	m
$\mathbf{a}'$	Surface cell vector	m
$\mathbf{a}_1$	Primitive lattice vector	m
$\mathbf{a}_2$	Primitive lattice vector	m
$\mathbf{a}_3$	Primitive lattice vector	m
A	Surface area	m^2
$\mathcal{A}$	Arrhenius pre-exponential factor	-
$\mathcal{A}$	Operator	various
b	Density operator constant of proportionality (y component)	-
b	Langmuir equilibrium constant	m^3 mol
b	Dipole-dipole coupling constant	s^{-1}
b	PFG NMR b-factor	s m^{-2}
$\mathbf{b}$	Surface cell vector	m
$\mathbf{b}'$	Surface cell vector	m
$\mathbf{b}_1$	Reciprical lattive vector	m^{-1}
$\mathbf{b}_2$	Reciprical lattive vector	m^{-1}
$\mathbf{b}_3$	Reciprical lattive vector	m^{-1}
B_{local}	Local magnetic field magnitude	T
$B_{induced}$	Induced magnetic field magnitude	T
B_z	Longitudinal magnetic field magnitude	T
B_0	Static magnetic field magnitude	T
B_1	Applied oscillating magnetic field magnitude	T
B_μ	Microscopic magnetic field amplitude	T
$\mathbf{B}$	Magnetic field vector	T
$\mathbf{B_{eff}}$	Effective magnetic field vector	T
$\mathbf{B_0}$	Static magnetic field vector	T
$\mathbf{B_1}$	Applied oscillating magnetic field vector	T
$\mathbf{B_{1+}}$	Counter-rotating applied magnetic field vector	T
$\mathbf{B_{1-}}$	Counter-rotating applied magnetic field vector	T
$\mathbf{B_\mu}$	Microscopic magnetic field	T
c	BET constant	-
c	Density operator constant of proportionality (z component)	-
c	Basis expansion coefficients	-
c	Concentration	mol m^{-3}
d_{kin}	Kinetic diameter	m
d_{pore}	Pore diameter	m
$\mathcal{D}$	Diffusion coefficient	m^2 s^{-1}
$\mathcal{D}_0$	Bulk diffusion coefficient	m^2 s^{-1}
$\mathcal{D}_0^{\mathrm{PFG}}$	$\mathcal{D}_0$ obtained from PFG diffusion measurements	m^2 s^{-1}
$\mathcal{D}_{0,0}$	Bulk diffusion pre-exponential	m^2 s^{-1}
$\mathcal{D}_\infty$	Effective diffusion coefficient in the long-time diffusion limit	m^2 s^{-1}
$\mathcal{D}_\infty^{\mathrm{PFG}}$	$\mathcal{D}_\infty$ obtained from PFG diffusion measurements	m^2 s^{-1}
$\mathcal{D}_{eff}$	Effective diffusion coefficient	m^2 s^{-1}
$\mathcal{D}_m$	Surface diffusion coefficient	m^2 s^{-1}
$\mathcal{D}_{m,0}$	Surface diffusion pre-exponential	m^2 s^{-1}
e^-	Electron	-
$E[n(\mathbf{r})]$	Electronic energy functional	J

$E_{xc}[n(\mathbf{r})]$	Exchange-correlation energy functional	J
$E_{HK}[n(\mathbf{r})]$	Hohenberg-Kohn electronic energy functional	J
E_a	Activation energy	J
E_a	Activation energy for adsorption	J
E_{ads}	Adsorption energy	J
E_{bulk}	Bulk unit cell energy	J
E_{bulk}^{corr}	Corrected bulk unit cell energy	J
E_{cut}	Cut-off energy	J
E_e	Electronic energy	J
E_{des}	Desorption energy	J
E_h	Activation energy for hole generation	J
E_j	Activation energy for surface jumping	J
E_m	Activation energy for surface migration	J
E_m^*	Macroscopic activation energy for surface migration	J
E_J	Energy of the scalar coupling interaction	J
E_Z	Nuclear Zeeman interaction energy	J
$E_{Z,J}$	Energy of the nuclear Zeeman and scalar coupling interactions	J
E_0	Activation energy for bulk diffusion	J
E_{slab}	Surface slab energy	J
E'_{slab}	Surface slab energy	J
f	Probability density (log scale)	-
F	Helmholtz free energy	J
$F[n(\mathbf{r})]$	Universal energy functional	J
$\mathcal{F}$	Eigenfunction	-
$\mathcal{F}$	Collision flux at the adsorbing surface	mol m^{-2} s^{-1}
$\mathbf{F}$	Force	J m^{-1}
g	Field gradient magnitude	T m^{-1}
g	Field gradient pulse axis	-
g^*	Effective field gradient magnitude	T m^{-1}
g^*	Effective gradient pulse axis	-
g_{eff}	Effective gradient magnitude due to $\Delta\chi$	T m^{-1}
g_{eff}^{max}	Maximum g_{eff}	T m^{-1}
g_x	Field gradient magnitude (x component)	T m^{-1}
g_y	Field gradient magnitude (y component)	T m^{-1}
g_z	Field gradient magnitude (z component)	T m^{-1}
g_0	Background field gradient magnitude	T m^{-1}
$\overline{g}$	Average effective gradient magnitude	T m^{-1}
$\mathbf{g}$	Magnetic field gradient vector	T m^{-1}
G	Gibbs free energy	J
G	Autocorrelation function	T^2
G_{inter}	Intermolecular autocorrelation function	T^2
G_{intra}	Intramolecular autocorrelation function	T^2
$G_{intra,int}$	Internal intramolecular autocorrelation function	T^2
$G_{intra,mol}$	Molecular intramolecular autocorrelation function	T^2
$\mathbf{G}$	Reciprocal translation vector	m^{-1}
h	Single-electron Hamiltonian operator	J
^{1}H	Proton	-
H	Enthalpy	J
H_m	Enthalpy of the mobile phase	J
H_{surf}	Enthalpy of the adsorbed phase	J
$\mathcal{H}$	Hamiltonian operator	J
$\mathcal{H}_e$	Electronic Hamiltonian operator	J

$\hat{\mathbf{i}}$	Unit vector (x direction)	-
I	Nuclear spin quantum number	-
$\mathbf{I}$	Nuclear spin angular momentum vector	J rad
I_x	Transverse nuclear spin angular momentum (x component)	J rad
I_y	Transverse nuclear spin angular momentum (y component)	J rad
I_z	Longitudinal nuclear spin angular momentum	J rad
j	Surface slab thickness	Unit cells
$\hat{\mathbf{j}}$	Unit vector (y direction)	-
J	Scalar coupling constant	s^{-1}
J	Spectral density function	T^2 s
J_{inter}	Intermolecular spectral density function	T^2 s
J_{intra}	Intramolecular spectral density function	T^2 s
J_{surf}	Surface spectral density function	T^2 s
J	Hartree potential operator	J
k	Echo time dependence power	-
k	Rate constant	s^{-1}
k_{ads}	Adsorption rate constant	s^{-1}
k_{ads}	Adsorption rate constant	$\mathrm{m}^3\ \mathrm{mol}^{-1}\ \mathrm{s}^{-1}$
k_{des}	Desorption rate constant	s^{-1}
k_+	Forward reaction rate constant	s^{-1}
k_-	Backward reaction rate constant	s^{-1}
$\mathbf{k}$	Wave vector	m^{-1}
$\hat{\mathbf{k}}$	Unit vector (z direction)	-
K	Equilibrium constant	-
$K^\ddagger$	Equilibrium constant between reagents and transition state	-
$\mathcal{K}$	Fock exchange potential operator	J
$\mathcal{K}$	Kernel function	-
$\mathcal{K}_1$	Kernel function for longitudinal relaxation	-
$\mathcal{K}_2$	Kernel function for transverse relaxation	-
ℓ	Average adsorbate jump length	m
ℓ_s	Structural length scale	m
ℓ_e	Diffusion path length scale	m
ℓ_g	Dephasing path length scale	m
ℓ_*	Critical length scale	m
ℓ_{direct}	Direct path length	m
$\ell_{indirect}$	Indirect path length	m
$\mathcal{L}$	Lorentzian function	-
m	Number of inversion recovery cycles	-
m_I	Magnetic quantum number	-
M	Adsorbate mass	kg
M_x	Transverse magnetisation (x component)	$\mathrm{A\ m}^{-1}$
M_y	Transverse magnetisation (y component)	$\mathrm{A\ m}^{-1}$
$M_{x,y}$	Transverse magnetisation	$\mathrm{A\ m}^{-1}$
M_z	Longitudinal magnetisation magnitude	$\mathrm{A\ m}^{-1}$
M_0	Equilibrium magnetisation magnitude	$\mathrm{A\ m}^{-1}$
$\mathbf{M}$	Bulk magnetisation vector	$\mathrm{A\ m}^{-1}$
$\mathbf{M}_0$	Equilibrium magnetisation vector	$\mathrm{A\ m}^{-1}$
n	Number of dimensions	dimensions
n	Electron density	$e^-\ \mathrm{m}^{-3}$
n	Nuclear spin density	spins m^{-3}
n	Number of echo cycles	cycles
N	Proportionality constant between surface slab and bulk unit cell	-

N	Number of electrons	e^-
N	Number of nuclear spins	spins
N_{abs}	Number of molecules absorbed	mol g^{-1}
N_{ads}	Number of adsorbates	mol
N_S	Number of adsorption sites	mol
N_{mon}	Monolayer capacity	mol g^{-1}
p	Pressure	Pa
p	Probability density (linear scale)	-
p_0	Saturation pressure	Pa
P	Diffusion propagator	-
P	Adsorbed spin population	-
P_{bulk}	Bulk molecular population	-
P_{surf}	Adsorbed molecular population	-
q	Wave number	m^{-1}
N_α	Number of spins in the α spin state	spins
N_β	Number of spins in the β spin state	spins
r_H	Hydrodynamic radius	m
r	Internuclear distance	m
$\mathbf{r}$	Position	-
$\mathbf{r}$	Electronic coordinates	-
R_{ads}	Rate of adsorption	mol m^{-2} s^{-1}
R_{ads}	Rate of adsorption	s^{-1}
R_{diff}	Relaxation rate due to diffusion through internal gradients	s^{-1}
R_{diff}^{max}	Maximum R_{diff}	s^{-1}
R_m	Rate of surface migration	s^{-1}
RF	Radio frequency pulse axis	-
R_1	Longitudinal relaxation rate	s^{-1}
R_2	Transverse relaxation rate	s^{-1}
$R_{1,bulk}$	Longitudinal relaxation rate of the bulk phase	s^{-1}
$R_{1,obs}$	Observed rate of longitudinal relaxation	s^{-1}
$R_{1,surf}$	Longitudinal relaxation rate of the adsorbed phase	s^{-1}
$R_{2,bulk}$	Transverse relaxation rate of the bulk phase	s^{-1}
$R_{2,obs}$	Observed rate of transverse relaxation	s^{-1}
$R_{1,surf}$	Longitudinal relaxation rate of the adsorbed phase	s^{-1}
$\mathbf{R}$	Nuclear coordinates	-
s	Sticking coefficient	-
s_0	Initial sticking coefficient	-
S	Entropy	J
S	Generalised order parameter	T^2
S	NMR signal	-
S_0	Initial NMR signal amplitude	-
S	Surface area	m^2 g^{-1}
S_{BET}	BET surface area	m^2 g^{-1}
t	Time	s
t_{eff}	Effective diffusion time	s
t_β	Pulse length for flip angle β	s
t_e	Echo time	s
t_g	Gradient pulse length	s
t_Δ	Diffusion observation time	s
$t_{\delta 1}$	Pre-gradient stabilisation time	s
$t_{\delta 2}$	Post-gradient stabilisation time	s
t_{90}	Pulse length for 90° pulse	s

t_{180}	Pulse length for 180° pulse	s
T	Longitudinal storage interval	s
T	Temperature	K
$T_e[n(\mathbf{r})]$	Electron kinetic energy functional	J
$T'_e[n(\mathbf{r})]$	Non-interacting electron kinetic energy functional	J
T_{surf}	Surface temperature	K
T_1	Longitudinal relaxation time constant	s
$T_{1,bulk}$	Longitudinal relaxation time constant of the bulk phase	s
$T_{1,inter}$	Intermolecular longitudinal relaxation time constant	s
$T_{1,intra}$	Intramolecular longitudinal relaxation time constant	s
$T_{1,obs}$	Observed longitudinal relaxation time constant	s
$T_{1,surf}$	Longitudinal relaxation time constant of the adsorbed phase	s
T_2	Transverse relaxation time constant	s
$T_2{}'$	Transverse relaxation time constant for ΔB_0 effects	s
$T_2{}''$	Transverse relaxation time constant for $\Delta\chi$ effects	s
T_2^*	Transverse dephasing time constant	s
$T_{2,bulk}$	Transverse relaxation time constant of the bulk phase	s
$T_{2,inter}$	Intermolecular transverse relaxation time constant	s
$T_{2,intra}$	Intramolecular transverse relaxation time constant	s
$T_{2,obs}$	Observed Transverse relaxation time constant	s
$T_{2,surf}$	Transverse relaxation time constant of the adsorbed phase	s
$T_{2,eff}$	Effective T_2 in the presence of internal gradients	s
$\mathcal{T}_e$	Electronic kinetic energy operator	J
$\mathcal{T}_n$	Nuclear kinetic energy operator	J
$\mathbf{T}$	Translational vector	m
U	Internal energy	J
U_m	Internal energy of the mobile phase	J
U_{surf}	Internal energy of the adsorbed phase	J
$V_{ee}[n(\mathbf{r})]$	Electron-electron potential energy functional	J
$V_{en}[n(\mathbf{r})]$	Electron-nuclear potential energy functional	J
$V_H[n(\mathbf{r})]$	Hartree energy functional	J
V_p	Pore volume	$m^3\ g^{-1}$
$V_{p,open}$	Open pore volume	$m^3\ g^{-1}$
$V_{p,closed}$	Closed pore volume	$m^3\ g^{-1}$
V_{BJH}	Pore volume	$m^3\ g^{-1}$
V_m	Molecular volume	m^3 molecule^{-1}
V_t	Total material volume	$m^3\ g^{-1}$
$\mathcal{V}_{ee}$	Electron-electron potential energy operator	J
$\mathcal{V}_{en}$	Electron-nuclear potential energy operator	J
$\mathcal{V}_{nn}$	Nuclear-nuclear potential energy operator	J
x	x-axis label	-
x'	x-axis label within the rotating frame of reference	-
$\mathbf{x}$	Spin-position vector, $\mathbf{x} = \{\mathbf{r}, \sigma\}$	-
y	y-axis label	-
y'	y-axis label within the rotating frame of reference	-
z	z-axis label	-
z	Spatial coordinate along the z-axis	-
z'	z-axis label within the rotating frame of reference	-
z_0	Initial spatial coordinate along the z-axis	-
z_1	Final spatial coordinate along the z-axis	-
Z	Nuclear charge	C

Greek symbols

Symbol	Definition	Units
α	α spin state	-
α	Pore shape parameter	-
α	Eigenvalue	various
α	Proportionality constant	-
α_1	Constant of proportionality relating E_j and E_{des}	-
α_2	Constant of proportionality relating E_h and E_{des}	-
β	β spin state	-
β	Flip angle	rad
γ	Gyromagnetic ratio	rad s^{-1} T^{-1}
γ	Surface energy	J m^{-2}
γ_{fixed}	Surface energy of the fixed surface	J m^{-2}
γ_{free}	Surface energy of the free surface	J m^{-2}
δ	Adsorbed surface layer thickness	molecules
δ	Adsorbed surface layer thickness	m
δ	Chemical shift	ppm
δ	Kronecker delta function	-
δ	Wave number (infrared bending mode)	cm^{-1}
ΔB	Reduced field	T
ΔB_0	Static field inhomogeneity	T
ΔE_z	Difference in Zeeman energy between α and β spin states	J
ΔF	Helmholtz free energy change	J
$\Delta^{\ddagger} F$	Helmholtz free energy change of activation	J
$\Delta^{\ddagger} F_m$	Helmholtz free energy change of activation for surface migration	J
ΔG	Gibbs free energy change	J
ΔG_{ads}	Gibbs free energy change of adsorption	J
ΔG_r	Gibbs free energy change of reaction	J
$\Delta^{\ddagger} G$	Gibbs free energy change of activation	J
$\Delta^{\ddagger} G_{des}$	Gibbs free energy change of activation for desorption	J
$\Delta^{\ddagger} G_h$	Gibbs free energy change of activation for hole generation	J
$\Delta^{\ddagger} G_m$	Gibbs free energy change of activation for surface migration	J
ΔH_{ads}	Enthalpy change of adsorption	J
$\Delta^{\ddagger} H$	Enthalpy change of activation	J
$\Delta^{\ddagger} H_{des}$	Enthalpy change of activation for desorption	J
$\Delta^{\ddagger} H_m$	Enthalpy change of activation for surface migration	J
ΔS_{ads}	Entropy change of adsorption	J
$\Delta^{\ddagger} S$	Entropy change of activation	J
$\Delta^{\ddagger} S_{des}$	Entropy change of activation for desorption	J
$\Delta^{\ddagger} S_m$	Entropy change of activation for surface migration	J
$\Delta^{\ddagger} U_m$	Internal energy change of activation for surface migration	J
$\Delta\nu$	Resonant frequency difference	s^{-1}
Δz	Displacement in the z-direction	m
$\Delta\phi_g$	Transverse phase shift	-
$\Delta\chi$	Magnetic susceptibility difference	-
∇	Divergence operator	-
∇^2	Laplacian operator	-
ε	Spin-orbital eigenvalue energy	J
ε	Experimental noise	-
ϵ_{xc}^{unif}	Exchange-correlation energy for the uniform electron gas	J
η_{surf}	T_1 surface interaction parameter	-

η^N_{surf}	Normalised T_1 surface interaction parameter	-
θ	Fractional surface coverage	-
θ	Rotation angle	rad
κ	Control parameter	-
κ	Transmission coefficient	-
κ_{des}	Transmission coefficient for desorption	-
κ_m	Transmission coefficient for surface migration	-
λ	Damping constant	s^{-1}
λ	Spin pair distance of closest approach	m
$\boldsymbol{\mu}$	Magnetic dipole moment vector	J T^{-1}
μ	Bloch function	-
μ_z	Longitudinal magnetic dipole moment	J T^{-1}
ν	Wave number (infrared spectroscopy)	cm^{-1}
ν_{sym}	Wave number (infrared symmetric stretching mode)	cm^{-1}
ν_{sym}	Wave number (infrared asymmetric stretching mode)	cm^{-1}
ν	Resonant frequency	s^{-1}
ν_{ref}	Reference frequency	s^{-1}
ν_0	Larmor frequency	s^{-1}
$\overline{\nu}$	Mean adsorbate velocity	m s^{-1}
ξ	PFG interaction parameter	-
ξ_n	Mesoscopic PFG interaction parameter	-
ξ_μ	Microscopic PFG interaction parameter	-
Ξ	Restricted diffusion parameter	-
ρ_{OH}	Surface hydroxyl coverage	m^{-2}
σ	Electron spin, $\sigma = \alpha, \beta$	-
σ	Nuclear shielding constant	-
σ	Density operator	J s
σ	Surface spin density	mol m^{-2}
σ	Areal density of adsorbed species	mol m^{-2}
σ_{mol}	Molecular crosssectional area	m^2
σ_0	Areal density of adsorption sites	mol m^{-2}
τ	Transverse evolution period	s
τ	Spin echo time	s
τ_c	Rotational correlation time	s
τ_d	Translational correlation time	s
τ_{int}	Internal rotational correlation time	s
τ_m	Adsorption site residence time	s
τ_{mol}	Molecular rotational correlation time	s
τ_s	Adsorbate surface lifetime	s
τ_t	Total rotational correlation time	s
τ_1	Longitudinal recovery period (T_1 measurements)	s
τ_2	Transverse recovery period (T_2 measurements)	s
$\hat{\tau}$	Tortuosity	-
$\hat{\tau}^{\mathrm{PFG}}$	Tortuosity obtained from PFG diffusion measurements	-
$\hat{\tau}_m$	Macroscopic tortuosity	-
$\hat{\tau}_n$	Mesoscopic tortuosity	-
$\hat{\tau}_{surf}$	Surface tortuosity	-
$\hat{\tau}_\mu$	Microscopic tortuosity	-
υ_{eff}	Effective potential	J
υ_{ext}	External potential	J
υ_{nn}	Nuclear-nuclear potential	J
υ_{xc}	Exchange-correlation potential	J

ϕ	spin-orbital	-
ϕ^{KS}	Kohn-Sham spin-orbital	-
ϕ_{corr}	Zero-order correction phase factor	-
ϕ_g	Transverse phase	-
ϕ_{rec}	Receiver phase factor	-
ϕ_{rf}	RF pulse phase	-
φ	Porosity	-
φ_{eff}	Effective porosity	-
χ	Basis function	-
χ	Magnetic susceptibility	-
ψ_e	Electronic wavefunction	-
ψ_n	Nuclear wavefunction	-
Ψ	Wavefunction	-
ω	Resonant frequency	rad s^{-1}
ω_a	IR beam frequency (SFG)	rad s^{-1}
ω_a	Visible beam frequency (SHG)	rad s^{-1}
ω_b	Visible beam frequency (SFG and SHG)	rad s^{-1}
ω_c	Reflected frequency (SFG)	rad s^{-1}
ω_{eff}	Effective resonant frequency	rad s^{-1}
ω_r	Frequency of the rotating frame of reference	rad s^{-1}
ω_0	Larmor frequency	rad s^{-1}
ω_1	RF transmitter frequency	rad s^{-1}
Ω	Primitive unit cell volume	m^3
Ω	Offset	rad s^{-1}
Ω_{eff}	Effective offset	rad s^{-1}
$\overline{\Omega}$	Reciprocal cell volume	m^{-3}